Characterization and Modeling of Moisture Flow through hydrating Cement-Based Materials under Early-Age Drying and Shrinkage Conditions

by

Mehdi Bakhshi

A Dissertation Presented in Partial Fulfillment
of the Requirements for the Degree
Doctor of Philosophy

Approved July 2011 by the
Graduate Supervisory Committee:

Barzin Mobasher, Chair
Subramaniam D. Rajan
Claudia E. Zapata

ARIZONA STATE UNIVERSITY

August 2011

ABSTRACT

Early-age cracks in fresh concrete occur mainly due to high rate of surface evaporation and restraint offered by the contracting solid phase. Available test methods that simulate severe drying conditions, however, were not originally designed to focus on evaporation and transport characteristics of the liquid-gas phases in a hydrating cementitious microstructure. Therefore, these tests lack accurate measurement of the drying rate and data interpretation based on the principles of transport properties is limited.

A vacuum-based test method capable of simulating early-age cracks in 2-D cement paste is developed which continuously monitors the weight loss and changes to the surface characteristics. 2-D crack evolution is documented using time-lapse photography. Effects of sample size, w/c ratio, initial curing and fiber content are studied. In the subsequent analysis, the cement paste phase is considered as a porous medium and moisture transport is described based on surface mass transfer and internal moisture transport characteristics. Results indicate that drying occurs in two stages: constant drying rate period (stage I), followed by a falling drying rate period (stage II). Vapor diffusion in stage I and unsaturated flow within porous medium in stage II determine the overall rate of evaporation. The mass loss results are analyzed using diffusion-based models. Results show that moisture diffusivity in stage I is higher than its value in stage II by more than one order of magnitude.

The drying model is used in conjunction with a shrinkage model to predict the development of capillary pressures. Similar approach is implemented in drying restrained ring specimens to predict 1-D crack width development. An analytical approach relates diffusion, shrinkage, creep, tensile and fracture properties to interpret the experimental data.

Evaporation potential is introduced based on the boundary layer concept, mass transfer, and a driving force consisting of the concentration gradient. Effect of wind velocity is reflected on Reynolds number which affects the boundary layer on sample surface. This parameter along with Schmidt and Sherwood numbers are used for prediction of mass transfer coefficient. Concentration gradient is shown to be a strong function of temperature and relative humidity and used to predict the evaporation potential. Results of modeling efforts are compared with a variety of test results reported in the literature.

Diffusivity data and results of 1-D and 2-D image analyses indicate significant effects of fibers on controlling early-age cracks. Presented models are capable of predicting evaporation rates and moisture flow through hydrating cement-based materials during early-age drying and shrinkage conditions.

To my family for their support, patience and understanding during the past four years

ACKNOWLEDGMENTS

I would like to start by expressing my gratitude to my advisor Professor Barzin Mobasher for giving me the opportunity to work with him and study at Arizona State University. His guidance and support are the reasons I was able to accomplish this work. Thank you to Professor Subramaniam D. Rajan and Dr. Claudia E. Zapata for serving on my defense committee. Thank you to Dr. M. Shekarchi and late Professor Ghalibafian for starting me on this trek of concrete at University of Tehran.

I would like to gratefully acknowledge financial support for this project received from the Arizona Department of Transportation under project number SR-633. This project was conducted in the Structural Mechanics and Materials Testing Laboratories at Arizona State University and as such I would like to acknowledge the support that has made these experiments possible. I would also like to acknowledge the assistance of Mr. Peter Goguen, the laboratories manager, Mr. Danny Clevenger and Mr. Jeff Long, for assistance in performance and preparation of experimental testing.

In addition, I want to acknowledge the assistance of my colleagues at Arizona State University including, Dr. Amir Bonakdar, Dr. Deju Zhu, Dr. Chote Soranakom, Dr. Flavio Silva, Geoffrey Minor, Christopher Barsby, Sean Krauss, and Nathan Rodriguez.

Thank you to all my friends who helped keep me sane during the process including Jonathan Fein, Erblina Vokshi, Vikram Dey, Aditya Vaidya, Kapil Krishnan, Pedram Shafieian, Shahrzad Badvipour and Kaveh Behbahani.

I would finally like to express my deepest appreciation and gratitude to my family. I would like to thank my parents for their love and support through my path of self-discovery. And finally I would like to thank my brothers for being a constant reminder to worry about the important things in life.

TABLE OF CONTENTS

Page

CHAPTER

CHAPTER Page

CHAPTER Page

APPENDIX

LIST OF TABLES

LIST OF FIGURES

Figure Page

Figure Page

Figure Page

Figure Page

Figure Page

Figure Page

NOMENCLATURE

B_m: mass transfer driving force for water vapor [kg.m^{-3}]

BF: blowing factor

c: mass concentration of water vapor [kg.m^{-3}]

c_{crit}: critical water vapor concentration for transition from stage I to II [kg.m^{-3}]

c_e: mass concentration of water vapor at the air stream [kg.m^{-3}]

c_s: mass concentration of water vapor at the interface [kg.m^{-3}]

D: diffusivity of the water vapor in the air [$\text{m}^2\text{.s}^{-1}$]

E: Rate of evaporation based on Menzel's equation [$\text{kg.m}^{-2}\text{.h}^{-1}$]

h_c: heat transfer coefficient by convection [$\text{W.m}^{-2}\text{.}^{\text{o}}\text{C}^{-1}$]

h_m: mass transfer coefficient for water vapor [m.s^{-1}]

$\overline{h_m}$: average low-rate mass transfer coefficient for water vapor [m.s^{-1}]

J_s: rate of diffusion of water vapor per unit area of the surface [$\text{kg.m}^{-2}\text{.s}^{-1}$]

K_H: drying coefficient per unit humidity difference [$\text{kg.s}^{-1}\text{.m}^{-2}$]

$l_{a,v}$: characteristic length of the mixture of air and water vapor, i.e. 3.176×10^{-10} [m]

L: total characteristic length in the direction of air flow [m]

M: molar mass of the water [kg.mol^{-1}]

M_a: molar mass of the air [kg.mol^{-1}]

m_s: mass fraction of water vapor at the surface

$\dot{m}''$: total mass flux of water vapor [$\text{kg.m}^{-2}\text{.s}^{-1}$]

$\dot{m}''_a$: total mass flux of all components in the humid air [$\text{kg.m}^{-2}\text{.s}^{-1}$]

p_{atm}: atmospheric pressure [kPa]

p: water vapor pressure [kPa]

p_{sat}: saturated water vapor pressure [kPa]

p_v: partial pressure of the water vapor in the air far from the surface [kPa]

Re_{crit}: critical Reynolds number

Re_L: Reynolds number for the characteristic length in the direction of flow

Re_x: local Reynolds number

Sc: Schmidt number

Sh_x: local Sherwood number

$\overline{Sh_L}$: average Sherwood number

T: absolute temperature [K]

T_a: temperature of the air far from the water surface [^{o}C]

T_c: temperature of the concrete surface [^{o}C]

T_{film}: temperature of the boundary layer (film)

T_{wb}: wet-bulb temperature of water [^{o}C]

t: transport time for the mass diffusion [s]

t_{trn}: time of transition from stage I to stage II drying [h]

u_∞ : free-stream velocity [m.s^{-1}]

v_s: velocity of water vapor at the interface [m.s^{-1}]

v_a: mass average velocity of all components in the humid air at interface [m.s^{-1}]

V: wind velocity [km.h^{-1}]

x: the distance from the leading edge [m]

x_{crit}: distance from leading edge at which critical Reynolds number is reached [m]

y: distance in the direction of diffusion [m]

δ_d : diffusion boundary layer thickness [m]

λ: latent heat of evaporation at T_{wb} [kJ.kg^{-1}]

μ : dynamic viscosity of the air [kg.m^{-1}.s^{-1}]

ν: kinematic viscosity of the air [m^{2}.s^{-1}]

ρ: density of the air [kg.m^{-3}]

ρ_a: total density of all components of the humid air at the interface [kg.m^{-3}]

ρ_s: density of the water vapor at the interface [kg.m^{3}]

φ: relative humidity of the air far from the surface

Ω_D : dimensionless collision integral for diffusion

1. Introduction

1.1. Motivation

The construction industry has to support continuing population growth and social and economic development. It is one of the largest industries in any country of the world with a vast number of participants. Only in the United States, there were 709,590 establishments with 6.57 million paid employees in 2000. The value of new construction put in place was $842.5 billion in 2001, or 8.4% of the U.S. gross domestic product (GDP) that year. Construction services contributed 4.7% to the GDP, i.e., over three times more than agriculture, forestry, and fishing, and almost four times more than motor vehicles and equipment manufacturing [1]. These numbers show that construction industry's contribution to the GDP in 2000 was larger than the GDP of 212 countries of the world [2]. Construction involves numerous manufacturing sectors such as construction materials, building systems, and service sectors. Among these sectors construction materials is very important as for almost a century, the construction industry uses the most materials by weight comparing to other industries [1]. Among all construction materials, crushed rock, gravel, sand, and cement are the ones which are used the most by volume. These data indicate that the materials that make up the bulk of Portland cement concrete and asphalt concrete are used in the largest volume and a special attention has to be given to concrete and cement industry.

Heavy civil construction is increasingly faced with considerable public opposition due to construction activities' environmental impacts. Although residential construction is still growing in the industrialized countries primarily owing to renovations and retrofits, suburban sprawl, and automobility [1], the growth cannot be maintained without tackling global economical and environmental issues namely the rising cost and demand of natural resources and energy and increasing environmental concerns due to industrial waste products. Focusing on building material sector, concrete and cement industry is considered as a large polluter of environment due to production of CO_2. It is now well-known that CO_2 as one of the main greenhouse gases traps some of the sun's heat energy causing a significant climate challenge called as 'global warming'. CO_2 production due to calcination of limestone is one way of CO_2 production ($CaCO_3 \rightarrow CaO + CO_2$) which leads to CO_2 emission of 525 kg per 1 ton of clinker [3]. On the other hand, the combustion of fossil fuels to heat up the clinker is another way of CO_2 production. Fossil fuels are hydrocarbons and burning process is the oxidation of carbon that leads to CO_2 emission ($C + O_2 \rightarrow CO_2 +$ thermal energy) by as much as 165 kg CO_2 per 1 ton of clinker [3]. Therefore, production of 1 ton clinker emits 0.69 ton CO_2. Altogether, the cement production contributes approximately 5% of the earth's CO_2 emissions which is a very significant number.

Different methods to reduce CO_2 emissions include but not limited to: improving energy efficiency, finding alternative fuels and energy, reformulation, capturing CO_2, and establishing tough regulations against CO_2 emissions. While these solutions are directly related to the production of cement, extending service life of cement-based materials and enhancing performance of cement systems also result in reduction of CO_2 emissions as well as reducing materials demand and economical benefits. This is a sustainable solution since it leads to environmental and social responsibility as well as economical performance and therefore meets the needs of the present without compromising the ability of future generations to meet their own needs. Using sustainable construction materials will eventually lead to structures which are more durable and economical, while meeting the ever increasing demand of the public. The main thrust of this effort is to use novel characterization and simulation techniques in the development of a range of materials for applications in various infrastructure systems. This research program will focus on addressing sustainability metrics through prolonging the service life of products currently used. This task can be achieved through a fundamental scientific understanding of degradation mechanisms in cement systems. The focus is on increasing durability of cement-based materials by controlling early-age shrinkage cracks. The main topic is the drying which is a major cause of early-age shrinkage.

Cementitious materials are weak against tensile stresses, especially during early hours after casting, and therefore they crack when restrained against shrinkage strains. Early-age shrinkage cracks in concrete reduce load carrying capacity, and accelerate deterioration, resulting in increased maintenance costs and reduced service life [4, 5]. These cracks are the main routes through which

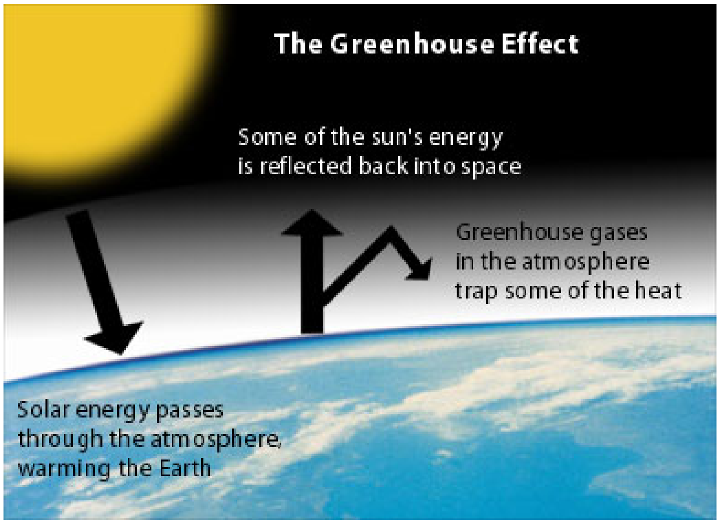

Figure 1.1.1. Greenhouse gases trap some of the heat causing global warming [6]

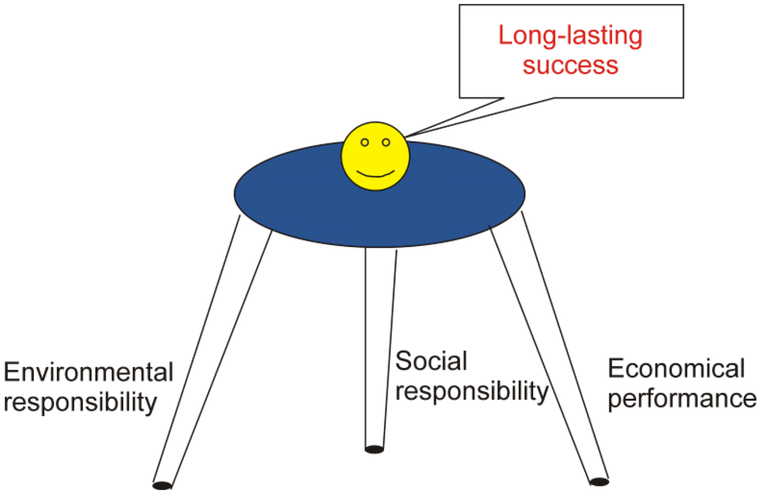

Figure 1.1.2. Sustainable development principle

aggressive agents such as chloride ions penetrate into the concrete mass and threaten the long-term durability of structures [7]. Plastic shrinkage in presence of restraints leads to tensile stresses which may easily exceed the low tensile strength of fresh concrete and result in cracking. Although attributed to several driving forces such as differential settlement, thermal dilation, and autogenous deformation [8], plastic shrinkage cracking in concrete occurs principally due to a high rate of water evaporation from the concrete surface [9, 10, 11]. The drying as the main cause of shrinkage is studied thoroughly.

1.2. Early-age Shrinkage Cracking Mechanisms

Early-age cracking is a threat to structural integrity of concrete structures and if not inhibited would lead to service life reduction and unsightliness. High rates of evaporation which depends on air and concrete temperature, wind speed and relative humidity increase the risk of early age cracking [11]. Due to evaporation, the solid particles at the surface of fresh concrete are no longer covered by the water and water menisci are formed in the inter-particle spaces because of adhesive forces and surface tension [12]. A negative pressure in the capillary water is built up due to the curvature of the water surface [13, 14] and continues to rise as the evaporation proceeds. The developed capillary pressure in drying fresh concrete can reach 50 kPa in less than few hours [10, 12, 15] and exceed 1MPa [16, 17]. This pressure acts on the solid particles resulting in the contraction of the still plastic material [18] ranging from strain levels of $1\text{-}4\text{x}10^{-3}$ [12, 14, 19, 20]. If concrete is restrained, the developed shrinkage strain may easily exceed low tensile strength of the fresh concrete [21] and cracking occurs.

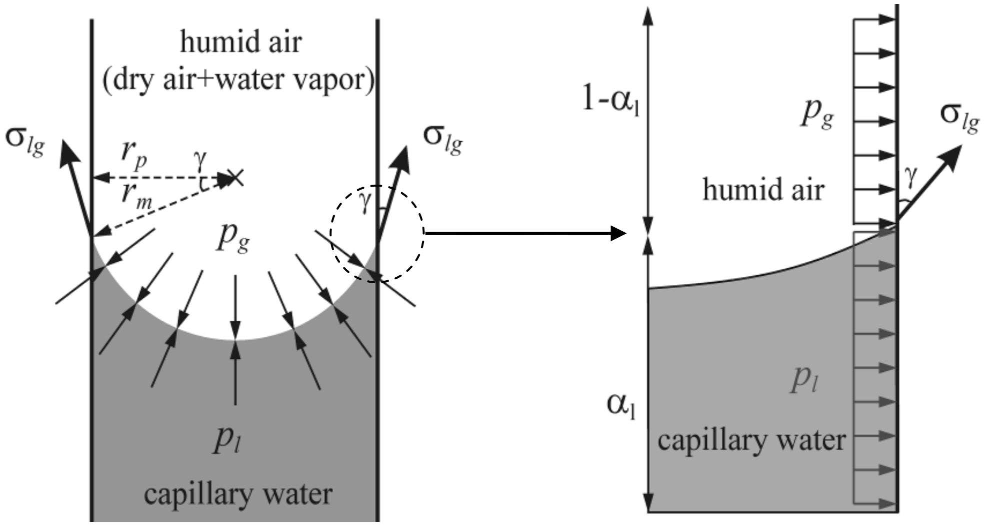

Figure 1.2.1. Equilibrium between liquid water and humid air at the interface of liquid/gas phase inside a pore and different pressures applied on solid skeleton [22]

1.3. Background in Shrinkage Testing and Modeling

1.3.1. Free Shrinkage Testing of Cement-based Materials

The free shrinkage test is performed according to ASTM standard C 157 [23]. This test method covers the determination of the length changes that are produced by causes other than externally applied forces and temperature changes in hardened hydraulic-cement mortar and concrete specimens made in the laboratory and exposed to controlled conditions of temperature and moisture. Measurement of length change permits assessment of the potential for volumetric contraction (shrinkage) of concrete due to drying. This test method is particularly useful for comparative evaluation of shrinkage potential in different hydraulic-cement mortar or concrete mixtures. In this test, specimens of 1” [25-mm] square cross-section and approximately 11⁄4” [285 mm] in length are casted for each mixture. Assuming the length of the specimen is much larger than the cross sectional dimensions, then shrinkage takes place only in the length direction. The measurement of change in length with time can then provide a measure of one-dimensional shrinkage of the material. In this method, the test specimens are cured in the molds covered with a plastic sheet for 24 hours while water dripping from specimen is protected. Upon removal of the specimens from the molds, the initial length reading is taken using a digital comparator dial. After the initial comparator reading, the specimens are stored in the drying room, so that the specimens have a clearance of at least 1” [25 mm] on all sides. Comparator readings of each specimen are taken every one or two days after initial reading. These readings are done in a room maintained at a relative humidity of 30% while the specimens are at a temperature of 73°F [23°C]. The difference between the average of readings on at least two specimens and the initial length of specimens is used to calculate shrinkage strain. Since the specimens are not restrained in this test method, this test cannot be an indicator of cracking performance of cement systems against shrinkage and does not differentiate the contribution of different materials such as fibers in controlling shrinkage cracks.

Figure 1.3.1.1. Molds, samples and digital comparator dial used in free shrinkage tests

1.3.2. Restrained Shrinkage Testing of Cement-based Materials

If the prismatic specimen is restrained on the length direction, uniaxial tensile stresses are produced which is similar to a uniaxial tensile test. The linear specimens have the advantage of the relatively straight-forward data interpretation, however, it is difficult to provide sufficient restraint to produce cracking with linear specimens, especially when cross sectional dimensions are large [24]. It is also difficult to restrain linear specimens, just as it is difficult to conduct a uniaxial tensile test for concrete [24]. Paillere, Buil, and Serrano [25] used long specimens (1.5 m) with flared ends that were restrained, and used small cross-sectional dimensions (70 x 100 mm) to produce shrinkage cracking. Other researchers have used similar methods and linear specimens to assess the shrinkage cracking potential of concrete mixtures [26, 27, 28, 29]. Unfortunately due to difficulties associated with providing sufficient end restraint, these test methods are generally not used for quality control procedures [28, 30]. Other investigators have used different types of specimens to simulate cracking due to restrained shrinkage. Plate-type specimens have been used by Kraai [31], Shaeles and Hover [32], Opsahl and Kvam [33], and Padron and Zollo [34]. When restraint to shrinkage is provided in two directions, a biaxial state of stress is produced. Consequently, the results obtained from plate-type specimens may depend on specimen geometry in addition to the material properties [24].

A restrained shrinkage test using a steel ring was done as early as 1939 to 1942 by Carlson and Reading [35]. They used a 25 mm thick and 38 mm wide concrete ring cast around a 25 mm thick steel ring with an external diameter of 175 mm. As a result of drying, a concrete ring would tend to shrink, but the steel ring would prevent this and cracking occurs. More recently, to better quantify early-age cracking tendency of cementitious material, instrumented rings have been used by researchers to measure the magnitude of tensile stresses that develop inside the material [24, 36, 37, 38, 39, 40]. Due to its simplicity and economy, the ring test has been developed into both AASHTO [41] and ASTM [42] standards. The main difference between these standards is the relative ratio of the concrete to steel ring thickness which influences the degree of restraint provided to the concrete. Although this test method can be used to study cracking tendency of different materials, the test is not applicable to fresh concrete when plastic cracking is the main concern.

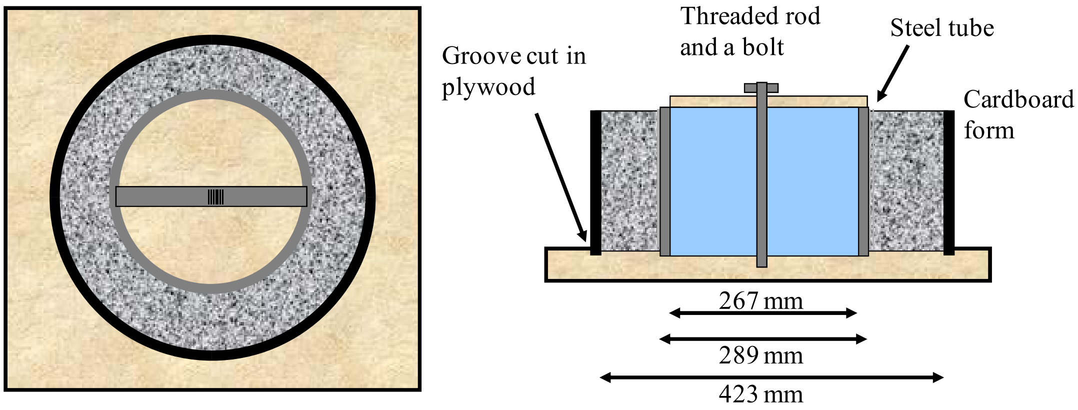

Figure 1.3.1.2. The configuration and geometry of restrained shrinkage ring specimen

1.3.3. Early-age (Plastic) Shrinkage Testing of Cement-based Materials

Several test methods have been implemented using fans [43, 44, 45], fans and heaters [46, 47], or heat lamps [48] to simulate severe evaporation conditions causing plastic shrinkage cracks in fresh concrete. Wind tunnel [49] and vacuum drying [50] have also been used to expedite the drying process. However, these tests were not designed to focus on evaporation characteristics of the drying material as the principal driving force of plastic shrinkage. Also, results of test methods in which the drying of fresh concrete have been studied lack accurate measurement of the evaporation rate and data interpretation based on transport characteristics. While Wongtanakitcharoen and Naaman [20] and Wang et al. [51] studied the effect of fiber content, w/c ratio, and fly ash on normalized cumulative moisture loss using fan, heater, and methanol treatment respectively, parameters addressing rates of evaporation were not utilized in their work. Samman et al. [52] used an electric fan to investigate the effect of w/c ratio, admixtures, and silica fume on the normalized cumulative moisture loss and maximum rate of evaporation. However, maximum rate of evaporation is not sufficient to characterize different materials characteristics. Berhane [53] evaluated the effect of w/c ratio and ambient relative humidity using evaporation rates obtained from moisture loss curves. However, the scale of data requires the evaporation rates to be interpreted based on mass transport parameters. Hall and Hoff [54] analyzed the drying of clay brick ceramics using two distinct stages: a constant drying rate period and a falling drying rate period. They then extended the results from porous media to stones and concrete. Analysis of the evaporation rates of cement-based materials with direct attention to stages of drying process has not been thoroughly investigated.

1.3.4. Modeling the Drying of Cement-based Materials

In existing literature, the moisture movement during drying of concrete is often described as a diffusion process where the diffusivity depends highly on the moisture content. Torrenti et al [55], West and Holmes [56], Garbalińska [57], Huldén and Hansen [58], Kim and Lee [59] modeled the moisture movement by the Fick's second law of diffusion without explanation of the physics of the problem. Most of these works refer to Bazant and Najjar [60, 61] who considered the drying of concrete as a nonlinear diffusion problem. Using an approach based on soil science, Kodikara and Chakrabarti [62] expressed the moisture movement during drying as a two separate stage mechanism [63], however, they modeled the phenomena as a one-stage diffusion process. Chen and Mahadevan [64] referred to Walton et al [65] in using diffusion as the dominant moisture transport mechanism in concrete. Shimomura and Maekawa [50] used mass conservation of the vapor and liquid water to derive a diffusion-type equation. Šelih and Bremner [66] concluded from the experimental results that the diffusion-driven moisture transport approach is appropriate only for the late stage of drying when the material is predominantly unsaturated, and the moisture movement in the form of vapor flux is dominant. Although Shimomura and Maekawa [50] discussed the movement of liquid water as governing mechanism regarding moisture movement near the saturated state, referring to Young [67], the concept was not implemented in their model. Šelih and Bremner [66] expressed the drying process as two different types of mechanisms of movement which can be described by a Darcy-type equation near saturation, succeeding by a diffusion-type equation. Nonetheless, their work was only limited to experimental observations.

The evaporation through the surface as a boundary condition is applied differently in available models. While ACI 305R-99 [68] and Uno [69] recommended a constant flux equal to evaporation rate of water surface for early-age hot weather concreting, a convective boundary condition proportional to the difference of internal and ambient moisture concentration was most often employed [50, 56, 58, 59]. Torrenti et al [55] and Shimomura and Maekawa [50] also used evaporative boundary conditions similar to convection. In another approach, Bazant and Najjar [60], and Garbalinska [57] applied a constant moisture concentration equal to ambient moisture concentration as the boundary condition in their models. However, the assumed boundary conditions are not supported by the physics and driving forces of surface evaporation process.

1.4. Objectives of the Dissertation

The objectives of this research are as follows:

(1) Build and calibrate an evaporation tests system to investigate evaporation characteristics of the drying cement-based material as the principal driving force of plastic shrinkage.

(2) Accurate measurement of the evaporation rates and data interpretation based on mass transport parameters.

(3) Investigate two distinct stages of drying which are generally proposed for drying of various capillary porous media.

(4) Equip the tests system with restraining methods and imaging device to impose and track 2-D shrinkage cracks from the early initiation stage to crack propagation and stabilization stages using time-lapse photography.

(5) Develop an image analysis technique to perform crack surface morphology and distinguish various surface crack patterns.

(6) Propose a simplified non-linear diffusion equation, which is accounted for all drying processes namely, Darcian transport of liquid water and diffusional transport of vapor water.

(7) Propose appropriate boundary conditions for different stages of drying based on the physics of the problem which is useful when modeling the drying process.

(8) Model early-age shrinkage from the drying model using the intermediate tools namely, desorption isotherms and capillary pressure-based models.

(9) Predict cracking tendency of cement-based materials from material models by comparing predicted developed shrinkage with strain capacity of the material.

1.5. Overview of Thesis

Chapter 2 describes testing methodology of a ring-type restrained drying shrinkage test. Materials and mixture properties of different concrete samples including plain and fiber reinforced concrete samples are investigated experimentally. Results of the tests including strain history in restraining steel captured by strain gauges attached to the mid-height of the steel ring is monitored as concrete is exposed to an arid environment. Also a systematic image analysis approach is followed to measure crack width growth in concrete ring specimen. Along with the experimental results, an analytical approach that relates key influential parameters of modeling including diffusion, shrinkage, creep, aging material properties, and restraining effect is presented.

Chapter 3 presents a test method for characterizing evaporation parameters and simulating the sequential formation of shrinkage cracks in two-dimensional cement paste samples under low-pressure condition. Effects of sample size, w/c ratio, initial curing and fiber content on weight loss and evaporation rates are explained. Two major stages of drying including a constant drying rate period (stage I) and a falling drying rate period (stage II) is investigated through experimental results. The results are interpreted based on mass transfer parameters using continuity of liquid and vapor phases.

Chapter 4 summarizes physics of water evaporation followed by a description of theory of evaporation from cementitious matrix that is represented as a capillary porous media. A dual-stage methodology for modeling the drying is introduced based on surface moisture transfer and internal moisture transport characteristics. After studying the effect of different parameters on the model, the methodology is applied to the results of drying experiments under low and normal pressure conditions. A 1-D Finite Element (FE) analysis code is also presented in order to verify the results of proposed analytical method. The FE method is further extended to 2-D analysis using ABAQUS v.6.10-1 [70] utilizing the analogy between the heat transfer and the moisture diffusion.

Chapter 5 suggests a new approach in the absence of other theoretical methods for calculation of initial rate of evaporation from cement-based materials. In this chapter theory of water evaporation is described based on the boundary layer theory, mass transfer, diffusion, and fluid mechanics. A driving force of concentration gradient is introduced as the main cause of mass transfer during the drying process. Mass transfer at low and high rates is discussed separately. The Schmidt number, Sc, which is a dimensionless number defined as the ratio of momentum diffusivity (ν) and mass diffusivity (D), physically relates the relative thickness of the hydrodynamic (velocity) and mass-transfer (concentration) boundary layers. On the other hand, the local Sherwood number,

Sh_x is a dimensionless number representing the effectiveness of mass convection at the surface. Using these parameters and Reynolds number, Re, which gives a measure of the ratio of inertial forces to viscous forces, mass transfer coefficient can be derived. An algorithm for determination of evaporation rate is suggested. Considering similarity between rate of evaporation from water surface and concrete surface during initial stage of drying, predicted evaporation rates are verified by the recent experiments. The results show that given the environmental parameters as inputs, the model is capable of predicting the evaporation rates with a good accuracy assuming surface cooling occurrence.

2. Restrained Shrinkage Cracking

2.1. Introduction

This chapter deals with the role of fibers in extending the cracking resistance of concrete subjected to drying shrinkage. In hot and low humidity environments, concrete shrinks due to loss of moisture from capillary and gel pore microstructure. When concrete is restrained from free shrinkage, tensile stresses develop and may result in cracking if the stress exceeds materials' low tensile strength. This is more dominant when at an early age the tensile strength is quite low and rate of moisture evaporation is high. The main objective of this chapter is to study effect of fibers on responses of a well-known restrained shrinkage test.

The methodologies of restrained drying shrinkage tests are described. Materials and mixture properties of different concrete samples including plain and fiber reinforced concrete samples are investigated experimentally. The experiments are performed according to the ring-type restrained shrinkage test method and strain history in the steel ring is monitored. A systematic methodology based on image analysis approach is used to measure crack width growth in concrete ring specimen. An analytical approach that relates key influential parameters of modeling including diffusion, shrinkage, creep, aging material properties, and restraining effect is presented.

2.2. Review of Drying Shrinkage Testing Methods

Understanding the mechanism of shrinkage cracking is essential to design of durable structures. Plastic shrinkage occurs during the early age period when the strength of the paste is quite low and drying volume changes occur due to depletion of water due to evaporation, chemical reactions, in addition to chemical shrinkage. While the fibers may not affect the evaporation rate, their addition increases the strength and strain capacity sufficiently during the early ages so that the potential for tensile cracking is minimized. Fiber addition to concrete therefore reduces cracking potential due to restrained shrinkage. As the concrete hardens, high stiffness fibers such as steel and macro synthetic fibers serve to increase the strength, crack growth resistance, and strain carrying capacity, providing a mechanism for additional restraint to distribute volumetric shrinkage and maintain a low crack width.

To measure free drying shrinkage, ASTM C 157 [23] recommends a prismatic specimen of 25, 75 or 100 mm square cross section and 285 mm in length. If it is assumed that the length of the specimen is much larger than the cross sectional dimensions, then shrinkage takes place only in the length direction. The measurement of change in length with time can then provide a measure of one-dimensional shrinkage of the material. In this test method no tensile stress and consequently no crack develops in the specimen. Therefore, this test method does not differentiate the contribution of fibers which reveals in the resistance of concrete to cracking.

If the prismatic specimen is restrained on the length direction, uniaxial tensile stresses are produced which is similar to a uniaxial tensile test. The linear specimens have the advantage of the relatively straight-forward data interpretation, however, it is difficult to provide sufficient restraint to produce cracking with linear specimens, especially when cross sectional dimensions are large [24]. It is also difficult to restrain linear specimens, just as it is difficult to conduct a uniaxial tensile test for concrete [24]. Paillere et al. [25] used long specimens (1.5 m) with flared ends that were restrained, and used small cross-sectional dimensions (70 x 100 mm) to produce shrinkage cracking. Other researchers have used similar methods and linear specimens to assess the shrinkage cracking potential of concrete mixtures [26, 27, 28, 29]. Unfortunately due to difficulties associated with providing sufficient end restraint, these test methods are generally not used for quality control procedures [28, 30].

Other investigators have used different types of specimens to simulate cracking due to restrained shrinkage. Plate-type specimens have been used by Kraai [31], Shaeles and Hover [32], Opsahl and Kvam [33], and Padron and Zollo [34]. When restraint to shrinkage is provided in two directions, a biaxial state of stress is produced. Consequently, the results obtained from plate-type specimens may depend on specimen geometry in addition to the material properties [24].

A restrained shrinkage test using a steel ring was done as early as 1939 to 1942 by Carlson and Reading [35]. They used a 25 mm thick and 38 mm wide concrete ring cast around a 25 mm thick steel ring with an external diameter of 175 mm. As a result of drying, a concrete ring would tend to shrink, but the steel ring would prevent this and cracking occurs. More recently, to better quantify early-age cracking tendency of cementitious material, instrumented rings have been used by researchers to measure the magnitude of tensile stresses that develop inside the material [24, 36, 37, 38, 39, 40]. Due to its simplicity and economy, the ring test has been developed into both AASHTO [41] and ASTM [42] standards. The main difference between these standards is the relative ratio of the concrete to steel ring thickness which influences the degree of restraint provided to the concrete. A ring-type restrained shrinkage testing method similar to AASHTO PP 34-99 is used in this chapter to study effects of fibers on shrinkage cracking.

2.3. Restrained Shrinkage Cracking

Uniaxial restrained shrinkage tests and tensile tests conducted on large-scale steel FRC specimens with fiber contents ranging from 0-100 kg/m^3 indicate that multiple cracking affects the overall response of the steel FRC in the hardened state [71]. The Ring test however is unable to capture the effect of multiple cracking simply because as a single crack forms the boundary conditions on the wall change. Several approaches to evaluate the influence of ring geometry and drying direction on the behavior of the restrain shrinkage test using the steel ring specimen have been proposed [72, 73, 39]. These studies demonstrate use of the steel ring in measuring the residual stress development as well as the stress relaxation once cracking occurs. Mane el al. [74] developed an experimental and analytical simulation algorithm to study the restrained shrinkage cracking in plain and FRC. A constant humidity chamber holding the restrained shrinkage specimens was utilized with a fan providing constant flow of air around the specimens. The strain in the restraining steel and the crack width in the concrete samples were monitored continuously. The results are correlated with the specimen geometry, humidity and temperature conditions, stiffness of the steel ring, and concrete stiffness, ductility, shrinkage, and creep characteristics.

Shah and Weiss [75] demonstrated that prior to cracking, the stresses that develop in a plain and a FRC are very similar. They also developed an analytical procedure for stress development in the steel ring, the stress transfer across the crack, and crack size [75]. Acoustic emission measurements indicated similar energy release in plain and fiber reinforced specimens; however, fibers appear to delay the development of a localized, visible crack [76]. In order to eliminate the influence of test conditions, an analytical approach is needed to incorporate influential parameters of shrinkage, creep, aging, and micro-cracking in the stress analysis of a restrained concrete section. Using the theoretical models, it is possible to calibrate and interpret the experimental test results.

2.4. Restrained Drying Shrinkage Test Methodology

Restrained shrinkage due to drying environment may cause cracking in concrete and cementitious materials. Shrinkage cracking can be a critical problem in concrete construction. One possible method to reduce the adverse effect of cracking is the addition of randomly distributed short fibers to the concrete mixture. An experimental study is conducted to evaluate effects of adding low contents of AR-glass fibers (1.5, 3, 4.5 and 6 kg/m3) on shrinkage cracking [77].

An instrumented ring specimen similar to AASHTO PP34-99 [41] has been used to quantify the restrained shrinkage and tensile creep behavior of concrete. The specimen consists of a 66.6 mm thick annulus of concrete cast around a rigid steel ring 11.2 mm in thickness with outer diameter of 289.4 mm and a height of 133.3 mm. A schematic configuration and geometry of shrinkage ring specimen is shown in Figure 1.3.1.2. In order to cast this sample, a cardboard form is used to hold the concrete from the outer sides. Since the height of specimen is two times to its thickness, it is assumed that uniform shrinkage takes place along the height of specimen. Two strain gauges are mounted on interior surface of steel ring at the mid height level and 90 degrees apart to measure developed strains in steel due to shrinkage of concrete. The width of the shrinkage cracks are measured at different ages using a high-resolution digital camera and implementing a systematic procedure of image analysis.

2.4.1. Mixture Properties, Casting and Specimen Preparation

To understand the drying shrinkage and cracking properties of glassfiber reinforced concrete (GRC), four concrete mix designs were developed with water-cement ratio of 0.55 and slump of 65- 90 mm. The cement content was 680 Kg/m^3 and only fine aggregates were used to cast concrete. Four mixtures of Control, GRC1.5, GRC3 and GRC4.5 are designed with 1.5, 3 and 4.5 kg/m^3 of glass fibers (24 mm long) respectively. These dosages are equivalent to 0.06%, 0.11%, 0.17% and 0% volumetric fractions, respectively. The Alkali-Resistant (AR) Glass fibers were provided by St. Gobain Vetrotex America Inc. as multi-fiber strand of 100 round filaments bonded together, with filament diameter of 14 micron. The length, elastic modulus and specific gravity of fibers are 24 mm, 72

GPa and 2.68, respectively. The AR glass fibers contain zirconium dioxide (ZrO2) which makes the glass composition resistant against alkaline environment, and thus stable in concrete [78, 79, 80, 81, 82]. The mixture proportions of all mixes are shown in Table 2.4.1.1 and include Type I/II Portland cement as the primary binding agent.

Table 2.4.1.1.
Mixture proportions of the Control and GRC samples (kg/m^3)

Mix ID	Control	GRC1.5	GRC3	GRC4.5
Portland cement	680	680	680	680
Fine aggregates	1360	1360	1360	1360
Water	374	374	374	374
AR glass fibers	0	1.5	3	4.5
w/c	0.55	0.55	0.55	0.55
Sand/cement	2.0	2.0	2.0	2.0

The following mixing procedure is adopted in this study. First half of dry materials including cement and fine aggregates are introduced into the mixer and blended for 2 minutes. Then, water is added to the mixer thoroughly and blended for 5 minutes before adding the rest of dry materials and mixing for an extra 5 minutes. Finally, glass fibers are added gradually to the GRC mixer and blended for 3 minutes. The dosage of AR glass fibers in GRC mixes are limited to the weight fractions of 4.5 kg/m^3 which is equivalent to very low volume fraction of 0.17%. All molds are filled in three layers with proper compaction by a thin rod in between the layers. Due to high fluidity of all mixes, no special technique such as vibration is used to help with the compaction of the fresh mixture in molds.

Four replicate specimens are made from each batch. The samples are kept in a moist curing room, covered with sealed plastic sheets for 24 hours. After 24 hours, the specimens are demolded and top surface of ring samples are sealed by a silicon rubber adhesive sealant to allow drying to occur only from the outer circumferential surface of the concrete specimen. Samples are placed in the shrinkage chamber shown in Figure 2.4.1.1.

Figure 2.4.1.1. Experimental setup of shrinkage test and recording strain gauge results

The rings are placed in a constant humidity chamber at the temperature of 40º C. The strain gauges attached to the inner surface of the steel ring are connected to the interface module and a dummy temperature compensating gauge in the form a half-bridge. The response from the strain gauges is collected using

SCXI-1321(16-channel, Half Bridge) module, SCXI-1000 carrier and NI data acquisition device and transferred into a LABVIEW programmed computer. The program records the strain gauges readings at specified intervals.

2.4.2. Results of Strain Gauges Attached to Steel Ring

The results of a typical strain gauge attached to steel ring for a plain concrete sample is shown in Figure 2.4.2.1. As shown in the figure, three stages can be seen in the response of strain gauge vs. time. The first stage which lasts 3 hours to less than 24 hours shows the effect of rising temperature and expansion of steel ring due to placement in chamber. After steel ring reaches the same constant temperature as the chamber, the strain gauge response reflects effect of shrinkage in concrete at stage 2. In this stage the response of concrete cast around the steel ring is linear elastic. When shrinkage strain in concrete exceeds ultimate tensile strength, concrete cracks and its effect on steel ring in plain concrete is a drop in the strain values. This drop in strain gauge results shows time of cracking due to very low residual post-crack tensile strength in plain concrete. In this stage (stage 3), strain in steel drop approximately to zero in plain concrete samples and visible crack width increases by the time. Strain gauge vs. time response can be used to detect time of cracking in the specimen, e.g. in the Figure 2.4.2.1, 6 days after drying in the chamber.

Two strain gauges mounted on each sample give different responses especially after cracking. Different responses before cracking can be related to different distances of strain gauges relative to heater location or source of temperature. In the post-crack response, the difference can be related to different distances of strain gauges from crack location in the sample. Results of two strain gauges mounted on a steel ring along with location of crack and strain gauges are shown in Figure 2.4.2.2 representing the strain responses of a plain concrete sample. A simple code is used to reduce and smooth the data. The raw and smoothened results of a strain gauge attached to steel ring are shown in Figure 2.4.2.3. The smoothened results of strain gauges were used to compare results of different mixtures.

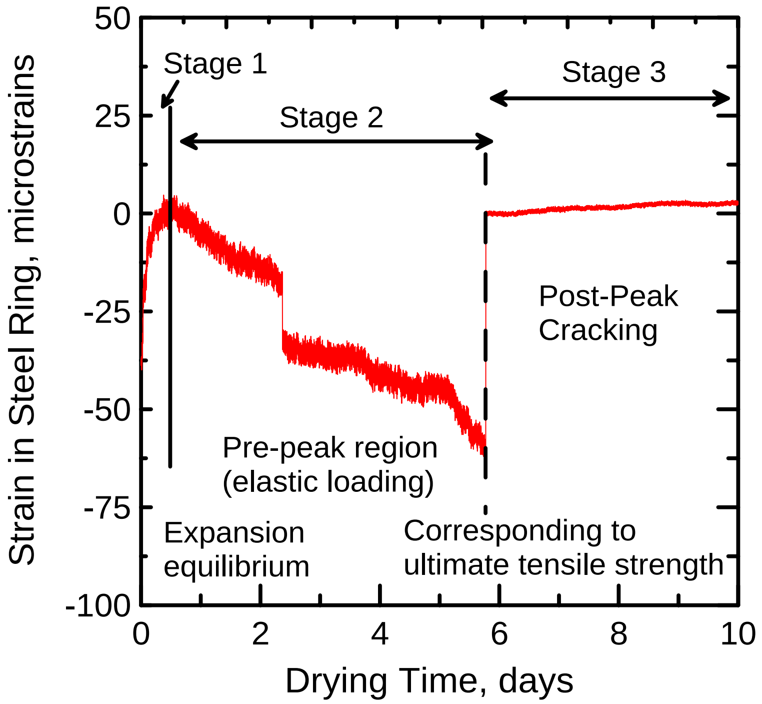

Figure 2.4.2.1. Typical result of an attached strain gauge for a plain concrete sample

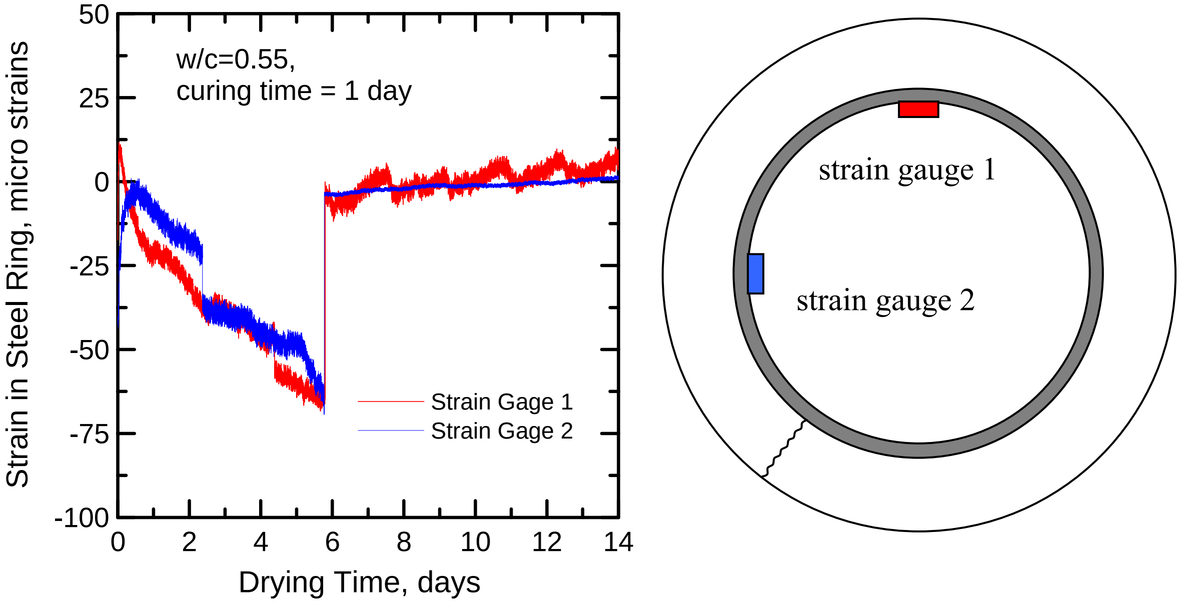

(a) (b)

Figure 2.4.2.2. (a) Results of two strain gauges mounted on a plain concrete sample, (b) Location of the crack and strain gauges

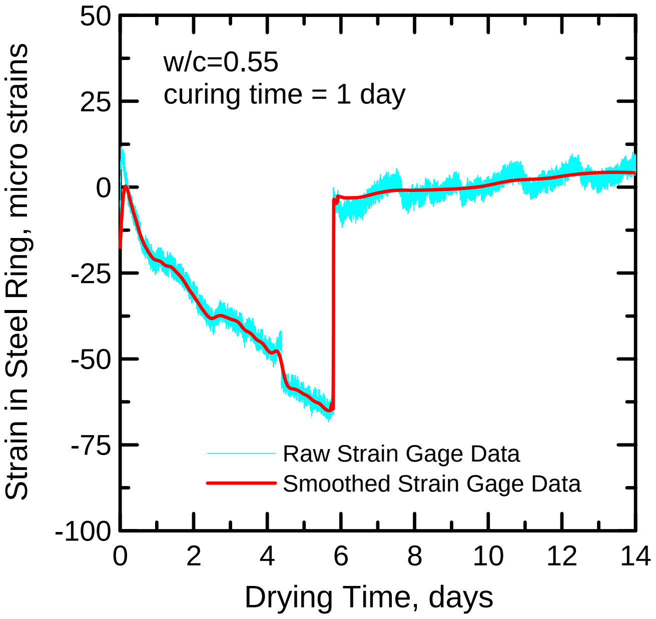

Figure 2.4.2.3. Smoothing typical results of a strain gauge attached to steel ring

From two strain gauges attached on each sample's steel ring, the results of the one showing more stability and not so close to the crack location was used to be compared with other samples. The results of strain gauges of different mixtures are shown in Figure 2.4.2.4. The figure clearly indicates that using AR-glass fibers delayed cracking in concrete samples for nearly 1 or 2 days. According to the figure, only Control sample and somehow GRC1.5, which are the samples with no or very low amount of fibers show abrupt drop in the strain gauge data due to cracking. Cracking happens between 6-8 days for all different samples, and the post-crack response of GRC samples with higher fiber dosages are significantly more than Control sample.

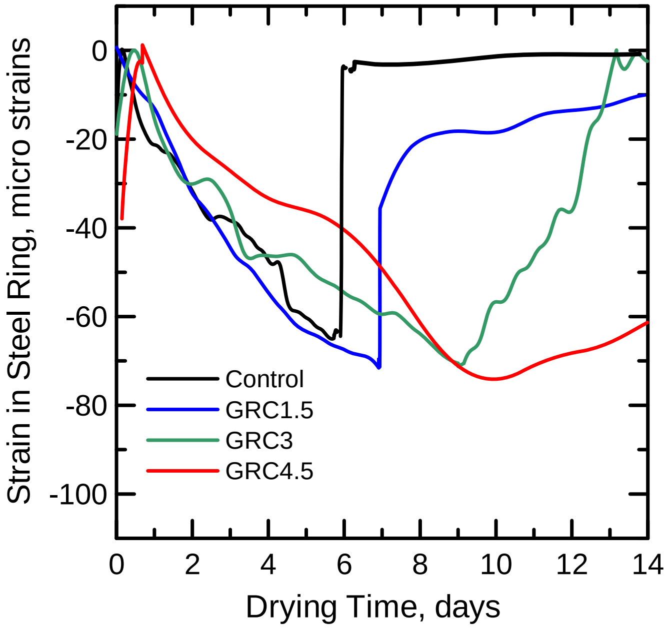

Figure 2.4.2.4. Effect of glass fibers on results of strain gauges attached to the rings

2.4.3. Capturing Shrinkage Cracks on the Ring Samples

In order to measure crack width, capturing digital images followed by image analysis approach is adopted in this study. Capturing is performed for all specimens after 14, 21 and 28 days of drying in the chamber. Since the average cracking time is 7 days, 14, 21 and 28 days are chosen as convenient ages that provide sufficient time for shrinkage cracks to extend along the height of samples. The samples were mounted on a traveling round plate and a 10x digital camera is used to take pictures. Using this setup, the entire surface of the specimen can be scanned and examined for new cracks and the measurements of the widths of already existing cracks. A view of the digital camera when taking picture of cracks of a concrete sample is shown in Figure 2.4.3.1. Images taken by this camera are grayscale images with RGB color format. In Figure 2.4.3.2, wide images of transversal shrinkage cracks in control and GRC3 samples are shown. As one can see, the difference between crack widths of different samples is obvious, but in order to quantitatively measure them, images are acquired along the crack length using a series of 8-12 images. To do reconstruction of whole image, overlapping portion of images is cut off and images are attached along the crack length. Figures 2.4.3.3 show that crack width in GRC3 sample is almost 3 times smaller than in control.

Figure 2.4.3.1. Imaging with the digital camera for crack investigations

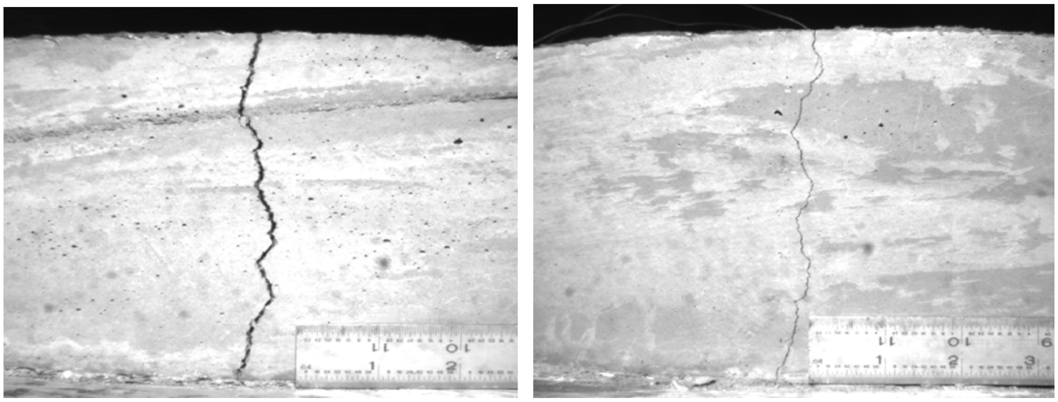

(a) (b)

Figure 2.4.3.2. Transverse cracks due to restrained drying shrinkage; a) control sample, b) GRC3 sample after 14 days of drying in the shrinkage chamber

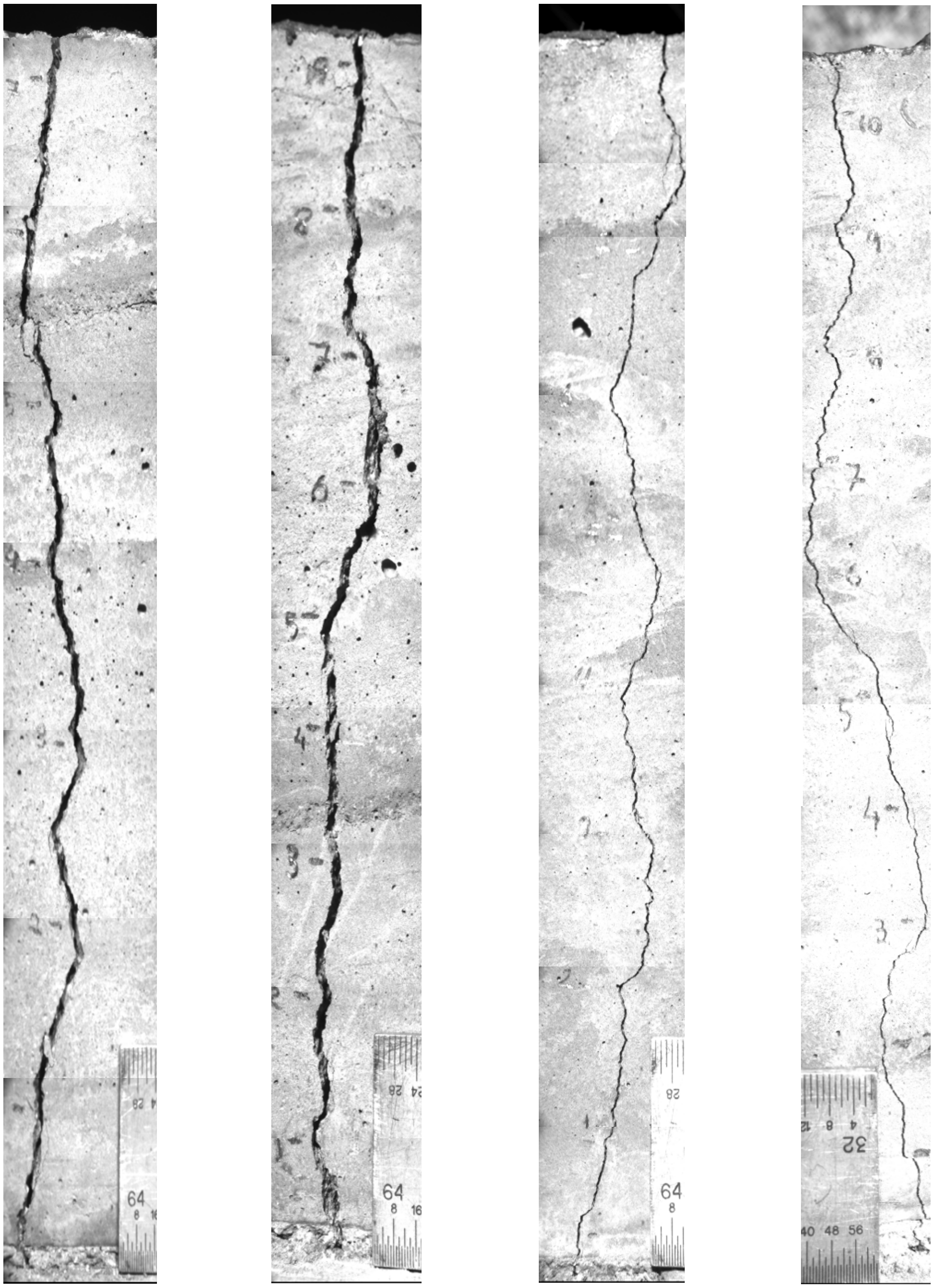

Control (Sample 1) Control (Sample 2) GRC3 (Sample 1) GRC3 (Sample 2)

Figure 2.4.3.3. Reconstructed shrinkage crack images of control and GRC3 samples

2.4.4. Image Analysis of Shrinkage Cracks

Image analysis technique is used to measure crack width of concrete samples precisely. First all images are converted from RGB color to 8-bit format. Then a code is developed to read the 8-bit images, ask the user of scale factor and crack boundaries and then makes a binary image of crack boundaries. In the next step, crack width is automatically measured by pixel counting at 64 different lines perpendicular to crack length and implementing the scale factor. Finally code calculates mean crack width, standard deviation, and demonstrates crack width histogram and normal probability density. Figure 2.4.4.1 shows image analysis process and output statistical results of a single crack image. To report crack width of a sample, average crack width and Standard Deviation (SD) obtained from 8-12 discrete images along the crack length are calculated. These values for four replicates of Control, GRC1.5, GRC3 and GRC4.5 mixes at 14, 21 and 28 days are shown in Table 2.4.4.1.

Crack width for each mixture is reported as an average crack width of four replicate samples. These results are shown in Table 2.4.4.1. Results indicate that in all shrinkage samples, crack width dimension increases by increasing drying time. Effect of fiber addition is so significant on reducing crack width dimension. By adding 1.5, 3 and 4.5 kg/m3 AR-glass fiber to the plain concrete (Control mix) crack width dimension at 14 days is reduced by 51%, 72% and 82%, respectively. Approximately the same trend is observed after 21 and 28 days of drying in shrinkage chamber.

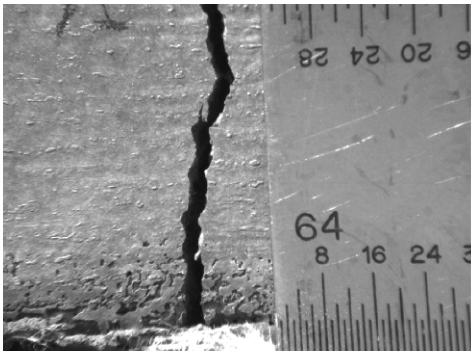

(a) Input grey scale image

(b) Binary image of crack region

(c) Crack width measurement along the crack length

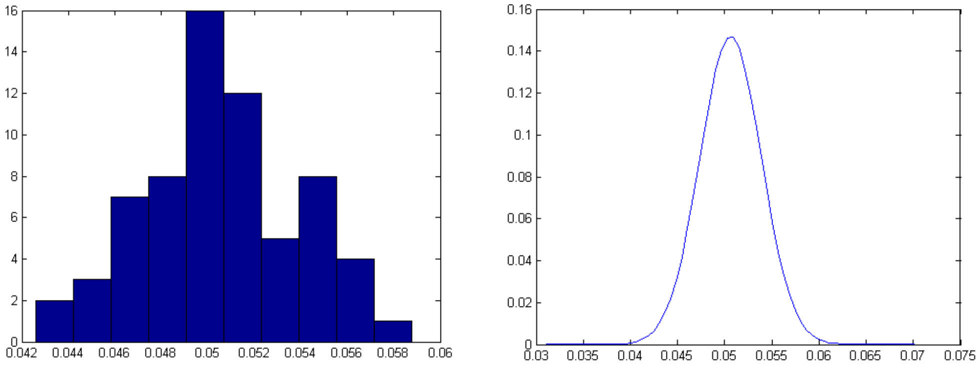

(d) Crack width histogram

(e) Crack width normal probability

Figure 2.4.4.1. Image analysis of a single image taken from a Control sample

Table 2.4.4.1.

Mean Crack width and standard deviation of samples (mm)

Sample Code	Crack Width at 14 Days		Crack Width at 21 Days		Crack Width at 28 Days	
	Average	SD	Average	SD	Average	SD
Control -1*	1.168	0.094	1.461	0.079	-	-
Control -2*	1.146	0.066	1.427	0.147	-	-
Control -3	1.280	0.064	1.534	0.084	1.742	0.069
Control -4	1.017	0.053	1.196	0.046	1.364	0.061
Average	1.153	0.069	1.405	0.089	1.553	0.065
GRC1.5 -1	0.340	0.104	0.470	0.168	0.528	0.104
GRC1.5 -2	0.551	0.010	0.704	0.061	0.823	0.046
GRC1.5 -3	0.343	0.041	0.391	0.023	0.488	0.048
GRC1.5 -4	0.993	0.048	1.189	0.041	1.227	0.048
Average	0.557	0.051	0.688	0.073	0.766	0.062
GRC3 -1*	0.363	0.046	0.445	0.020	-	-
GRC3 -2*	0.323	0.046	0.404	0.046	-	-
GRC3 -3	0.333	0.051	0.427	0.074	0.528	0.041
GRC3 -4	0.244	0.038	0.348	0.043	0.480	0.046
Average	0.316	0.045	0.406	0.046	0.504	0.043
GRC4.5 -1	0.229	0.033	0.307	0.033	0.386	0.038
GRC4.5 -2	0.216	0.048	0.300	0.020	0.351	0.020
GRC4.5 -3	0.157	0.028	0.218	0.015	0.246	0.025
GRC4.5 -4	0.114	0.025	0.173	0.043	0.229	0.020
Average	0.179	0.034	0.250	0.028	0.303	0.026

* Crack width dimension of these samples were not measured at 28ays.

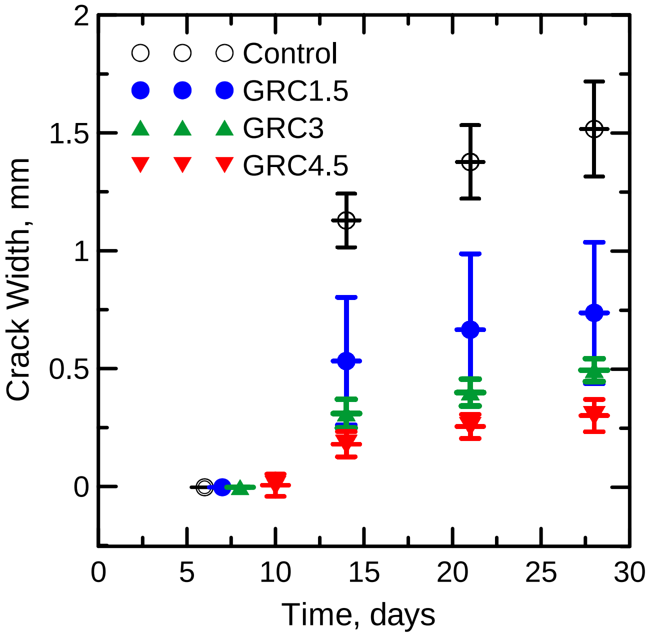

Figure 2.4.4.2. Mean and SD of shrinkage crack widths at different times of drying

According to Figure 2.4.4.2 and Table 2.4.4.2, standard deviation of the crack widths for GRC1.5 samples is higher than that of Control and other GRC mixtures. The resistance of GRC1.5 samples against crack extension can be similar to both plain concrete (plain sample) and other GRC samples with higher fiber dosage. It is concluded that glass fiber dosage of 1.5 kg/m^3 is not enough to ensure of crack controlling. However, addition of 3 kg/m^3 glass fibers or more to the plain mixture results in much lower deviation in the results and reduction of crack width dimension by 70%.

2.5. Theoretical Modeling of Restrained Shrinkage

Various theoretical approaches for modeling the restrained shrinkage cracking of concrete have been developed [40, 83, 84]. These models try to address the interaction between materials properties and the shrinkage characteristics of concrete. Meanwhile, there is no model to properly predict post-crack behavior of plain concrete and GRC in the restrained shrinkage test based on the experimentally obtained tensile stress-strain response of the material. The simulation of crack width opening which is of great importance from the aspects of durability and serviceability is also lacking.

A research attempt to develop an analytical approach that relates key influential parameters of modeling including diffusion, shrinkage, creep, aging material properties and restraining effect is presented in this section [74]. The theoretical model is used to calibrate and interpret the experimental test results, which provides better understanding on how drying environment generates tensile stress and cracks in a restrained concrete specimen. This model is capable of showing effects of adding fiber on the restrained shrinkage and cracking of concrete. Finally a summary of results concluding significant effect of AR-glass fibers on minimizing crack width dimension supported by both experimental and analytical data are presented.

2.5.1. Moisture Diffusion and Free Shrinkage

As concrete loses its moisture to the environment, free shrinkage is taken place and the humidity profile *h(z)* through the thickness of the concrete section is simplified to follow the Fick's law of diffusion:

$$h(z) = h_s - (h_s - h_i) erf(z) \tag{2.5.1.1}$$

where z is the distance measured from the outside surface inward the specimen, h_s and h_i represent the humidity (fraction) at the outside surface and interior section and *erf(z)* represents the error function [85].

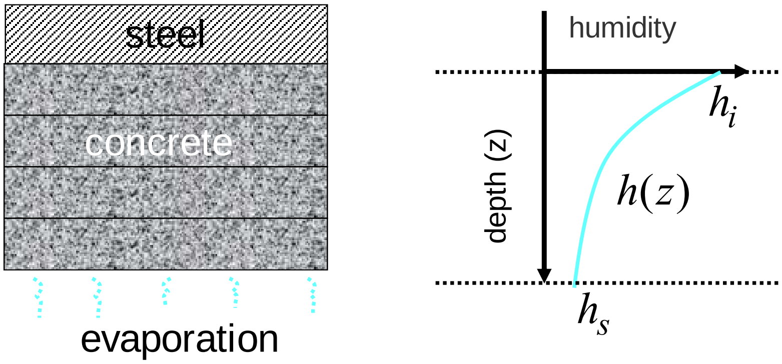

Figure 2.5.1.1. Fick's law of diffusion is used to simulate humidity profile through the thickness of the concrete section using an error function

A cubic function is used to relate the free shrinkage strain as a function of the humidity profile throughout the thickness.

$$\varepsilon_{sh}(z)=\varepsilon_{sh(t)}(1-h(z)^3) \tag{2.5.1.2}$$

where $\varepsilon_{sh(t)}$ is the free drying shrinkage strain at any time. Free drying shrinkage can be obtained by experiments or from the empirical relationships proposed by Bazant-Panula [86] for drying shrinkage at infinite time ($\varepsilon_{sh\infty}$) and time-dependent shrinkage formulation suggested by ACI 209 [87] as;

$$\varepsilon_{sh(t)}=\frac{t^{\xi}}{f+t^{\xi}}\varepsilon_{sh\infty} \tag{2.5.1.3}$$

where f and ξ are constants and t is time in days. ACI 209R-92 recommends an average value for f of 35 for 7 days of moist curing, while an average value of 1.0

is suggested for ξ. In this study, free drying shrinkage is obtained by experiments performed according to ASTM standard C 157-04. Meanwhile, the experimental data of free shrinkage is fitted by the ACI equation as shown in Figure 2.5.1.2, and the proper values of f and ξ are selected as 28 days and 1.5, respectively. As shown in the figure, the best fitted values for drying shrinkage at infinite time ($\varepsilon_{sh\infty}$) for Control, GRC1.5, GRC3 and GRC 4.5 samples are 2160, 2052, 1944 and 1836 micro strains, respectively.

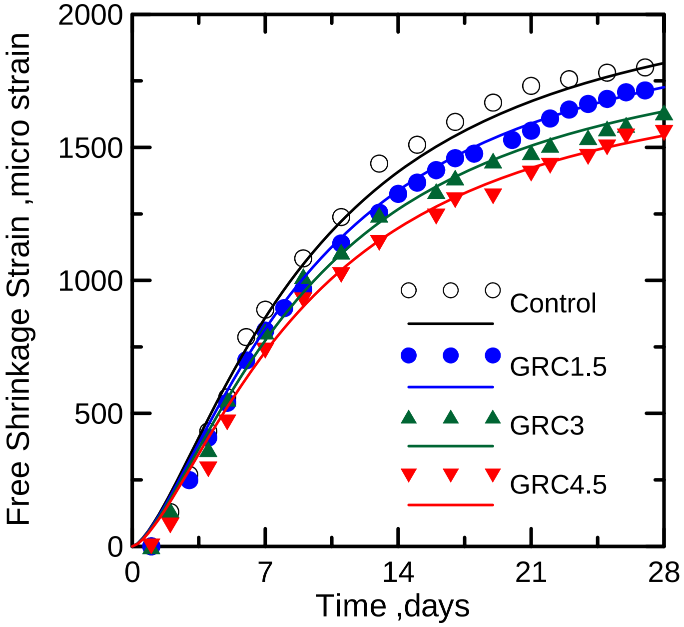

Figure 2.5.1.2. Fitted free shrinkage results by the modified ACI 209R-92 model

2.5.2. Creep of Concrete

As concrete is subjected to tensile stress, it produces creep strain with time and offset the strain due to free shrinkage, resulting in relaxation of the elastic stresses in the material. Due to lacking of early age tensile creep model, it is assumed that the creep coefficient of concrete in compression $v(t)$ used in ACI 209 report [87] is applicable to the present tensile mode of loading.

$$v(t) = \frac{t^{\psi}}{d + t^{\psi}} v_u \tag{2.5.2.1}$$

where v_u is the ultimate creep coefficient, d and ψ are constants and t is time in days. In this study v_u is assumed as 12 for all samples. ACI-209R-92 recommends an average value of 10 and 0.6 for d and ψ, respectively. However, since the recommendation is for the plain concrete under compression tests, the values of d and ψ are modified to 6 and 1 respectively for the tensile creep behavior of Control mixture. For the case of GRC1.5, 3 and 4.5, values of d are chosen as 4, 3 and 1.5 and values of ψ are chosen as 1.1, 1.3 and 0.5, respectively. Note that the presented creep model needs further studies to be verified by experimental data.

2.5.3. Age Dependent Concrete Strength

To obtain tensile strength properties of the mixtures along the time, monotonic three-point bending tests are performed on the Control and GRC3 samples at 1, 3, 7 and 28 days. Figure 2.5.3.1 shows the flexural responses of these two mixtures at 1 and 7 days.

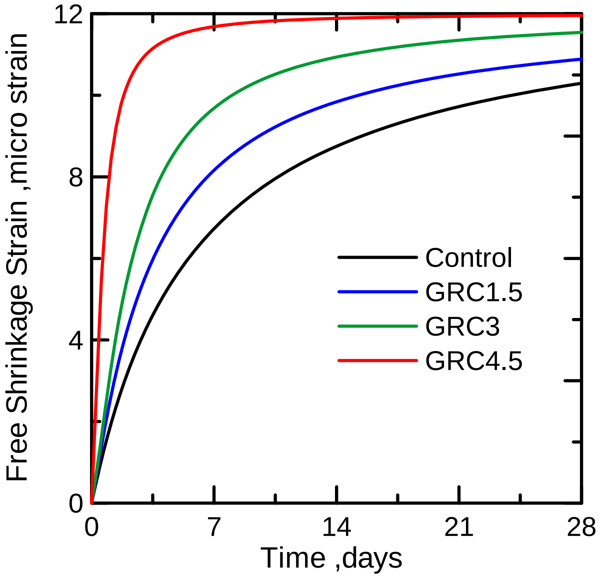

Figure 2.5.2.1. Creep model for Control and GRC mixes

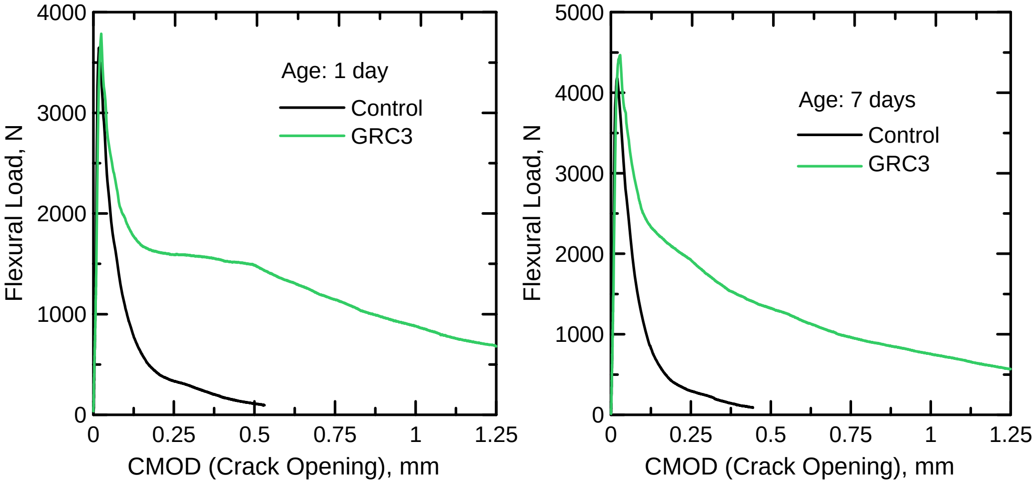

Figure 2.5.3.1. Flexural response of concrete samples under three-point bending tests

To calculate tensile stress-strain parameters of the samples from three-point bending tests, a model shown in below figure, which is properly applicable to both plain and GRC samples is hired.

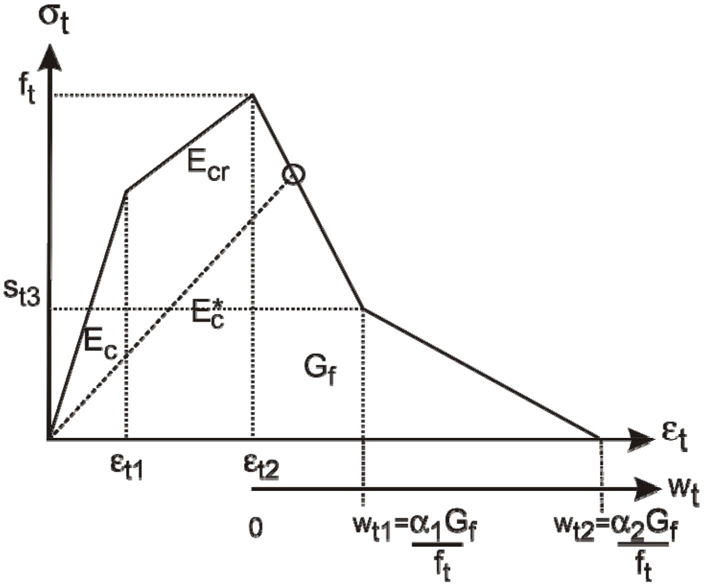

Figure 2.5.3.2. Tensile stress-strain and crack width model

The parameters of stress-strain back-calculations model of Control and GRC3 samples at 1, 3, 7 and 28 days are summarized in the following Table 2.5.3.1.

Similar to ACI time-dependent compressive strength development function, back calculated tensile strength, ft, residual strength, st3, fracture energy, Gf and young's modulus, Ec are assumed to follow these functions:

$$f_t(t) = f_{t28}\left(\frac{t}{a+bt}\right), \qquad s_{t3}(t) = s_{t3-28}\left(\frac{t}{a+bt}\right)$$

$$G_f(t) = G_{f28}\left(\frac{t}{a+bt}\right), \qquad E_c(t) = E_{c28}\left(\frac{t}{a+bt}\right) \tag{2.5.3.1}$$

Table 2.5.3.1.
Back-calculated parameters of Control and GRC3 samples at different ages

Mix ID	Age (days)	ε_{t1}	ε_{t2}	w_{t1} (mm)	w_{t2} (mm)	f_t (MPa)	S_{t3} (MPa)	G_f (MPa. mm)	E_c (GPa)
Control	1	0.00012	0.00020	0.02794	0.1524	1.758	0.246	0.041	11.264
	3	0.00012	0.00019	0.0254	0.1524	2.034	0.270	0.043	13.141
	7	0.00011	0.00017	0.02286	0.1143	2.068	0.310	0.046	15.019
	28	0.00011	0.00017	0.02286	0.10922	2.103	0.315	0.048	15.770
GRC3	1	0.00017	0.00026	0.04064	1.0668	1.758	0.475	0.255	8.448
	3	0.00012	0.00019	0.03048	0.889	2.034	0.529	0.269	13.141
	7	0.00011	0.00017	0.0254	0.8128	2.068	0.538	0.275	15.019
	28	0.00011	0.00017	0.0254	0.762	2.103	0.547	0.289	15.770

where, f_{t28}, $s_{t3\text{-}28}$, G_{f28} and E_{c28} are tensile strength, residual strength, fracture energy and Young's modulus of concrete at 28 days, respectively. t is the time in days, a and b are material parameters. ε_{t1} and ε_{t2}, are the tensile strains at limit of proportionality and peak stress respectively, and w_{t1} and w_{t2}, are the transition and ultimate crack widths, are assumed to follow these functions:

$$\varepsilon_{\mathrm{t1}}(\mathrm{t}) = \mathrm{a} \cdot e^{bt} + \mathrm{c}, \qquad \varepsilon_{\mathrm{t2}}(\mathrm{t}) = \mathrm{a} \cdot e^{bt} + \mathrm{c}$$
$$w_{\mathrm{t1}}(\mathrm{t}) = \mathrm{a} \cdot e^{bt} + \mathrm{c}, \qquad w_{\mathrm{t2}}(\mathrm{t}) = \mathrm{a} \cdot e^{bt} + \mathrm{c} \qquad (2.5.3.2)$$

In the above mentioned functions, t is time in days, a, b and c are constant material parameters. The best values for the coefficients a, b, and c after fitting equation (2.5.3.1) and equation (2.5.3.2) with the values of Table 2.5.3.1 are being used in this modeling approach.

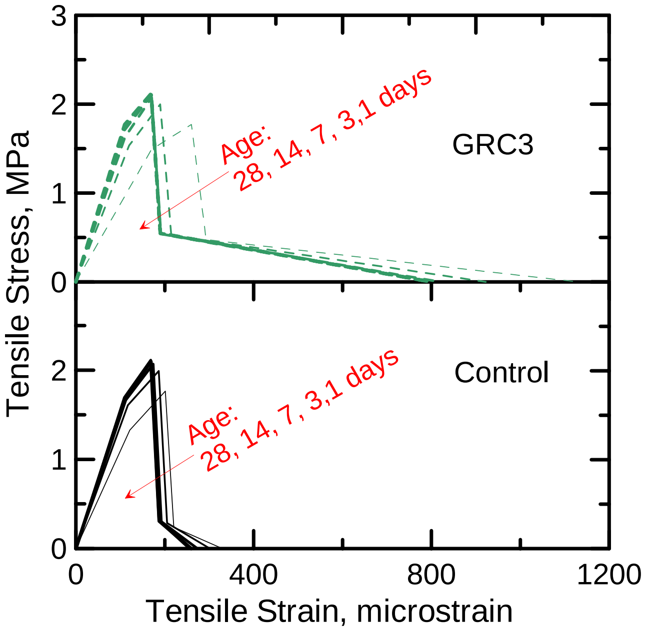

Figure 2.5.3.3. Back-calculated tensile stress strain model at different ages

2.5.4. Restraining Effect

In this model, tensile strain is positive while compressive and shrinkage strains are negative. Other related terms such as forces and stresses follow the same sign as strains. Symbol Δ is used for the incremental change of quantities between previous time step t_{j-1} and the current time step t_j and index i is used for the layer number at particular location z_i. The restraining effect provided by steel ring that prohibits concrete to shrink freely can be determined by equilibrium of force between the tension force in concrete ΔF_c (positive) and compression force in steel (negative) ΔF_{st}.

$$\Delta F_c + \Delta F_{st} = 0 \qquad (2.5.4.1)$$

In the equilibrium, only the elastic tensile strain component of the concrete $\Delta\varepsilon_{el}$ produces stress and it is balanced with the compressive stress in steel, which has elastic compressive strain $\Delta\varepsilon_{st}$. Using modulus of materials, the equilibrium of force in (2.5.4.1) can be written as

$$\Delta\varepsilon_{el}\overline{E_c^*}(t_{j-1})A_c + \Delta\varepsilon_{st}E_sA_s = 0 \tag{2.5.4.2}$$

where, $\overline{E_c^*}(t_{j-1})$ is the secant modulus of the concrete at previous time step averaged from all discretized concrete layers. This is only an approximation since the modulus at the current time step is not yet known. E_s is the young modulus of steel, A_c and A_s are area of concrete and steel, respectively. Rearrange the terms in equation (2.5.4.2), the incremental compressive steel strain $\Delta\varepsilon_{st}$ is obtained:

$$\Delta\varepsilon_{st} = -\frac{\overline{E_c^*}(t_{j-1})A_c}{E_sA_s}\Delta\varepsilon_{el} \tag{2.5.4.3}$$

2.5.5. Stress Strain Development

Figure 2.5.5.1(a) shows a concrete ring specimen subjected to moisture loss until it cracks. An arch segment of the ring as shown in a dash box can be approximated to 1D problem depicted in Figure 2.5.5.1(b); the thickness is assumed to be flat. The figure represents a schematic drawing of strain components developed in the concrete ring specimen. The free shrinkage strain $\Delta\varepsilon_{sh}$ (negative) will be restrained by steel ring creating compressive strain in the steel $\Delta\varepsilon_{st}$ (negative) and the steel compressive force must be balanced with the tension force in concrete, which immediately generates elastic strain in concrete

$\Delta\varepsilon_{el}$ (positive). For time interval Δt, the concrete tensile stress will generate creep strain $\Delta\varepsilon_{cp}$ (positive). In addition, the previous stress history before time t_{j-1} also contributes to the creep strain increment between time t_{j-1} and t_j, $\Delta\varepsilon_{cp}^{(prev\sigma)}$, which can be calculated by using Bolzmann's superposition principle:

$$\Delta\varepsilon_{cp}^{(prev\sigma)} = \left\{ \sum_{k=2}^{j-1} \left| \frac{1}{2} \frac{\sigma_{el_k} - \sigma_{el_{k-1}}}{E_{c28}} \right| v(t_j - t_{k-1}) \right\} - \varepsilon_{cp}(t_{j-1}) \qquad (2.5.4.4)$$

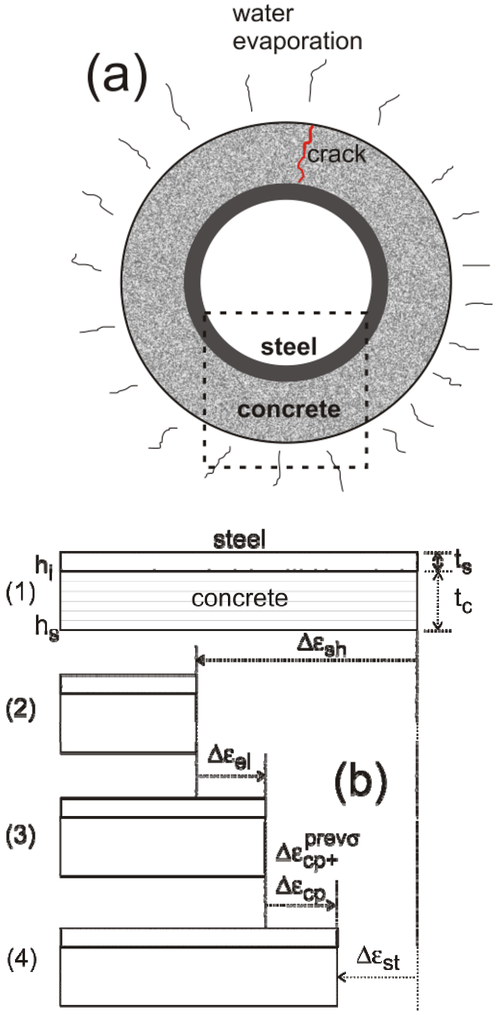

Figure 2.5.5.1. Schematic drawing for the proposed drying shrinkage model; (a) ring specimen; (b) strain components

Therefore, the equilibrium of incremental strains developed between time step t_{j-1} and t_j can be written as:

$$-\Delta\varepsilon_{sh} = \Delta\varepsilon_{el} + \Delta\varepsilon_{cp} + \Delta\varepsilon_{cp}^{(prev\sigma)} - \Delta\varepsilon_{st} \qquad (2.5.4.5)$$

Substitute the restraining steel strain $\Delta\varepsilon_{st}$ from equation (2.5.4.3) into equation (2.5.4.5), yields

$$-\Delta\varepsilon_{sh} = \frac{\overline{E_c^*}(t_{j-1})A_c}{E_s A_s}\Delta\varepsilon_{el} + \Delta\varepsilon_{el} + \Delta\varepsilon_{cp} + \Delta\varepsilon_{cp}^{(prev\sigma)} \qquad (2.5.4.6)$$

Use the relationship between tensile stress and creep coefficient $\Delta\varepsilon_{cp} = \Delta\sigma_{el}C(dt)/E_{c28}$ to determine creep strain, and substitute in equation (2.5.4.6) results in:

$$-\Delta\varepsilon_{sh} = \frac{\overline{E_c^*}(t_{j-1})A_c + E_s A_s}{E_s A_s}\Delta\varepsilon_{el} + \Delta\sigma_{el}\frac{v(dt)}{E_{c28}} + \Delta\varepsilon_{cp}^{(prev\sigma)} \qquad (2.5.4.7)$$

To obtain stress and strain distribution, the thickness of concrete is discretized into N_c sub layers while steel has only one layer. The incremental elastic stress in layer i located at z_i can be expressed as:

$$\begin{aligned}\Delta\sigma_{el}(z_i) &= [\varepsilon_{el}(z_i,t_j) - \varepsilon_{el}(z_i,t_{j-1})]E_c^*(z_i,t_{j-1}) \\ &= \Delta\varepsilon_{el}(z_i)E_c^*(z_i,t_{j-1})\end{aligned} \qquad (2.5.4.8)$$

Substitute incremental stress $\Delta\sigma_{el}(z_i)$ defined in equation (2.5.4.8) into equation (2.5.4.8) and rearrange the terms, the incremental concrete elastic strain at each sub layer can be expressed as:

$$\Delta\varepsilon_{el}(z_i) = \frac{-\Delta\varepsilon_{sh}(z_i) - \Delta\varepsilon_{cp}^{(prev\sigma)}(z_i)}{Q + \dfrac{E_c^*(z_i, t_{j-1})}{E_{c28}} v(dt)}; \qquad Q = \frac{\overline{E_c^*}(t_{j-1}) A_c + E_s A_s}{E_s A_s}$$

(2.5.4.9)

It should be noted that the concrete is considered as a whole thickness with an average secant modulus $\overline{E_c^*}(t_{j-1})$ in accounting for the restraining effect from steel while concrete is treated individually with its secant modulus at each layer $E_c^*(z_i, t_{j-1})$ for the effect of free shrinkage and creep.

2.5.6. Algorithm for Strain History in Steel Ring and Crack Width at Concrete Surface

1) Calculate free shrinkage strain distribution at each layer *i* from equation (2.5.1.2) and equation (2.5.1.3), and its increment by:

$$\Delta\varepsilon_{sh}(z_i) = \varepsilon_{sh}(z_i, t_j) - \varepsilon_{sh}(z_i, t_{j-1}) \tag{2.5.6.1}$$

2) Calculate incremental elastic tensile strain at each layer due to free shrinkage, restraining effect and creep from equation (2.5.4.9).

3) Update total elastic strain, stress and secant modulus using concrete model described in Figure 2.5.3.2.

$$\varepsilon_t(z_i, t_j) = \varepsilon_t(z_i, t_{j-1}) + \Delta\varepsilon_{el}(z_i) \tag{2.5.6.2}$$

$$\sigma_t(z_i, t_j) = function[\varepsilon_t(z_i, t_j)] \ from \ Figure\, 2.5.3.2$$

(2.5.6.3)

$$E_c^*(z_i, t_j) = \frac{\sigma_t(z_i, t_j)}{\varepsilon_t(z_i, t_j)} \tag{2.5.6.4}$$

4) If the updated strain $\varepsilon_t(z_i,t_j)$ exceeds the strain at peak stress $\varepsilon_{t2}(t_j)$, the crack width at each layer of concrete is calculated by:

$$w_t(z_i,t_j) = \left[\varepsilon_t(z_i,t_j) - \varepsilon_{t\_unload}(z_i,t_j)\right]\pi D(z_i) \qquad (2.5.6.5)$$

where $\varepsilon_{t\_unload}(z_i,t_j)$ is the unloading strain in the pre-peak stress strain curve corresponding to the same stress level as the strain in post peak response $\varepsilon_t(z_i,t_j)$ and $D(z_i)$ is the diameter of the concrete ring at location z_i.

5) Sum concrete force at each concrete layer A_{ci} to obtain the total tensile force, which the magnitude equals to compressive the force in steel.

$$F_c(t_j) = \sum_{i=1}^{N_c} A_{ci}\sigma_t(z_i,t_j) \text{ and } F_s(t_j) = -F_c(t_j) \qquad (2.5.6.6)$$

6) Calculate nominal stress and strain in steel, defined by:

$$\sigma_{ns}(t_j) = \frac{F_s(t_j)}{A_s}; \qquad \varepsilon_{ns}(t_j) = \frac{\sigma_{ns}(t_j)}{E_s} \qquad (2.5.6.7)$$

7) A complete strain history at steel ring and crack width at concrete surface can be obtained by repeating steps 1-6 until the time t_j reaches the specified age.

2.6. Comparing Experimental Data and Simulations

Results of simulation by this model and comparison with the experimental data are shown in Figure 2.6.1. The results show a good correlation between the experimental data including strain in steel ring and crack width opening histories and simulation data. While the best correlation of the simulation with experimental data is for Control sample, the model overestimates the crack widths of GRC samples after 14 days. However, the model is capable of capturing significant effects of adding glassfibers to control shrinkage cracking in concrete.

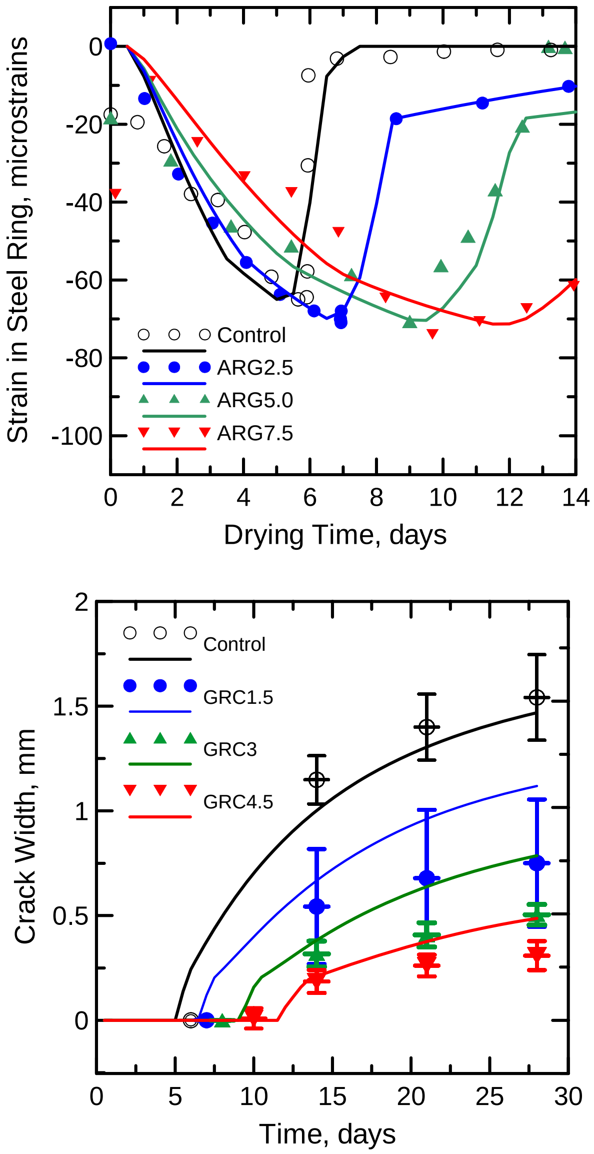

Figure 2.6.1. Comparison of experimental results and model simulation; (a) history of strain in steel ring; and (b) crack width dimension history at the outer concrete surface

2.7. Conclusion

Reducing crack width dimension by 3 times by using low content of AR-glassfibers is the most significant effect of adding fibers to the mixture in controlling shrinkage cracking. This effect in addition to delaying crack occurrence by 1 or 2 days represent the low dosage glassfiber concrete as an appropriate construction material to be used in dry and hot regions with the risk of high drying shrinkage. The analytical model for predicting steel strain history and concrete crack width dimension for restrained shrinkage test shows a relatively good correlation with the experimental data. This model is capable of capturing significant effects of fiber addition in order to control cracking of shrinkage. Collectively speaking, ring-type restrained shrinkage test method is a good method to capture the behavior of concrete materials against restrained drying shrinkage.

3. Experimental Observations of Early-Age Drying

3.1. Introduction

Plastic shrinkage cracks in concrete reduce load carrying capacity, and accelerate deterioration, resulting in increased maintenance costs and reduced service life [4, 5]. These cracks are the main routes through which aggressive agents such as chloride ions penetrate into the concrete mass and threaten the long-term durability of structures [7]. Plastic shrinkage in presence of restraints leads to tensile stresses which may easily exceed the low tensile strength of fresh concrete and result in cracking. Although attributed to several driving forces such as differential settlement, thermal dilation, and autogenous deformation [8], plastic shrinkage cracking in concrete occurs principally due to a high rate of water evaporation from the concrete surface [9, 10, 11].

Several test methods have been implemented using fans [43, 44, 45], fans and heaters [46, 47], or heat lamps [48] to simulate severe evaporation conditions causing plastic shrinkage cracks in fresh concrete. Wind tunnel [49] and vacuum drying [50] have also been used to expedite the drying process. However, these tests were not designed to focus on evaporation characteristics of the drying material as the principal driving force of plastic shrinkage. Also, results of test methods in which the drying of fresh concrete have been studied lack accurate measurement of the evaporation rate and data interpretation based on transport characteristics. While Wongtanakitcharoen and Naaman [20] and Wang et al. [51] studied the effect of fiber content, w/c ratio, and fly ash on normalized cumulative moisture loss using fan, heater, and methanol treatment respectively, parameters addressing rates of evaporation were not utilized in their work. Samman et al. [52] used an electric fan to investigate the effect of w/c ratio, admixtures, and silica fume on the normalized cumulative moisture loss and maximum rate of evaporation. However, maximum rate of evaporation is not sufficient to characterize different materials characteristics. Berhane [53] evaluated the effect of w/c ratio and ambient relative humidity using evaporation rates obtained from moisture loss curves. However, the scale of data requires the evaporation rates to be interpreted based on mass transport parameters. Hall and Hoff [54] analyzed the drying of clay brick ceramics using two distinct stages: a constant drying rate period and a falling drying rate period. They then extended the results from porous media to stones and concrete. Analysis of the evaporation rates of cement-based materials with direct attention to stages of drying process has not been thoroughly investigated.

Evaporation is viewed as the diffusion of water molecules through the boundary layer at the surface to maintain the equilibrium of liquid-gas phase transition [88, 89, 90, 91, 92, 93]. During the drying phase, moisture flows through the porous material toward the evaporative surface to supply the necessary surface flux. The relationship between unsaturated flow within concrete pores and evaporation rate on the surface can be used to measure moisture diffusivity [94, 95]. By analyzing moisture loss data during the drying of well hydrated cement paste samples, Garbalińska used desorptive measurement techniques to determine moisture diffusivity [57]. A Similar analytical method is proposed to measure moisture diffusivity in drying fresh cement pastes.

Plastic shrinkage cracks due to a high rate of evaporation are two-dimensional [96]. However, a majority of recent publications have focused on one-dimensional cracking of the concrete by utilizing special restraints [8, 9, 10, 47, 97]. Characterization of images taken from a drying surface helps in understanding crack initiation, propagation, and stabilization during the drying process.

A test method to monitor the drying of fresh cement paste and the formation of plastic two-dimensional cracks is presented in this work. This test method allows measuring material properties that characterize mass transfer during the early stages of fresh paste drying. A drying technique based on a low-pressure condition was employed to cause a rapid rate of evaporation while weight loss was measured. This drying method imposes a one-dimensional moisture flow through the thickness and facilitates parameter estimation from the mass transfer data. The test method was applied to a variety of samples in order to evaluate the impact of sample thickness, surface area, w/c ratio, duration of initial curing and fiber content on the evaporation characteristics being tested. An analytical method to determine moisture diffusivity using experimental data is presented and the effects of different testing parameters on diffusion coefficients are investigated. The development of crack patterns during drying is documented using time-lapse photography. The images have been used to determine the ability of the fibers in controlling shrinkage cracking in drying cement pastes.

3.2. Testing methodology

Apparatus of the developed low-pressure drying test method is shown in Figure 3.2.1a. A prismatic sample is filled with fresh paste such that its face is exposed and all other sides are sealed. The mold consists of interlocking pieces made of polycarbonate as shown in Figure 3.2.1b and uses anchor hooks to connect the fresh paste with the mold, providing shrinkage restraint in two directions. The sample is placed on a load cell which serves as a digital scale, and the entire assembly is placed inside a glass desiccator. The weight of the sample is continuously monitored throughout the drying cycle. Using a vacuum pump and a pressure regulator the air pressure inside the desiccator is lowered to absolute 1700 Pa (0.5 inHg) and maintained at this pressure throughout the test. This level of air pressure was selected as a system level parameter after extensive pressure calibration procedures. If the pressure is too low, evaporation occurs at normal rates, and if it is too high, microstructural damage due to cavitation occurs. A controlled test condition therefore requires evaporation rates which simulate the range of severe atmospheric conditions. A condensing system including a D-Drying apparatus is used similar to Copeland and Hayes [98] to remove the water vapor from the desiccator. Similar preliminary results from comparison of the weight of the condensed water in the flask with the total moisture loss at the end of the test show the efficiency of the condensing system. The weight loss measured was recorded using a computer interface unit. The specimen surface was photographed at 15 min intervals using a digital camera mounted 10 cm above the sample. To avoid excessive moisture removal at the beginning of the test, a calibration procedure was developed using a cement paste exposed to several vacuum pressures such that the rate of evaporation was maintained at a constant rate. Based on this procedure, a test procedure consisting of 30 minutes at 34 kPa (10 inHg), followed by a decrease in pressure to 1700 Pa (0.5 inHg) for the remainder of the test was selected. The test procedure was subjected to additional calibration using liquid water as the evaporating material. This indicated the free water evaporation rate of the test setup.

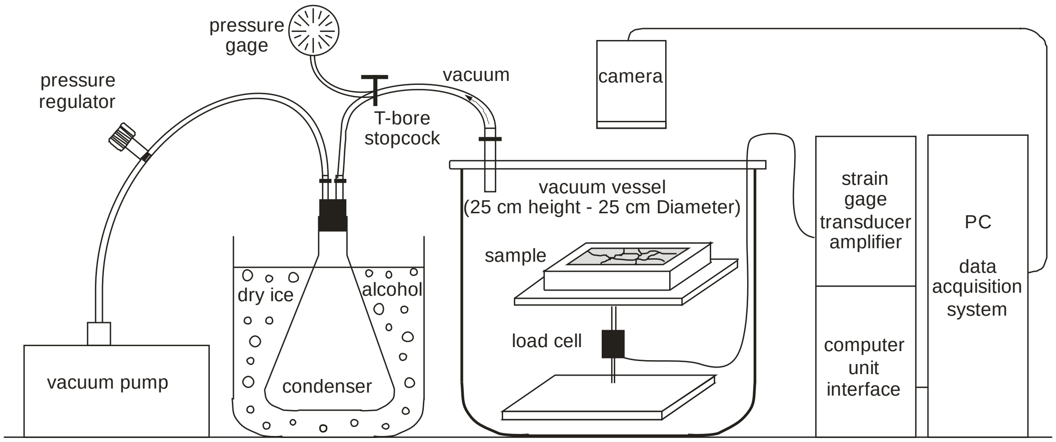

Figure 3.2.1a. Schematic of vacuum drying test setup

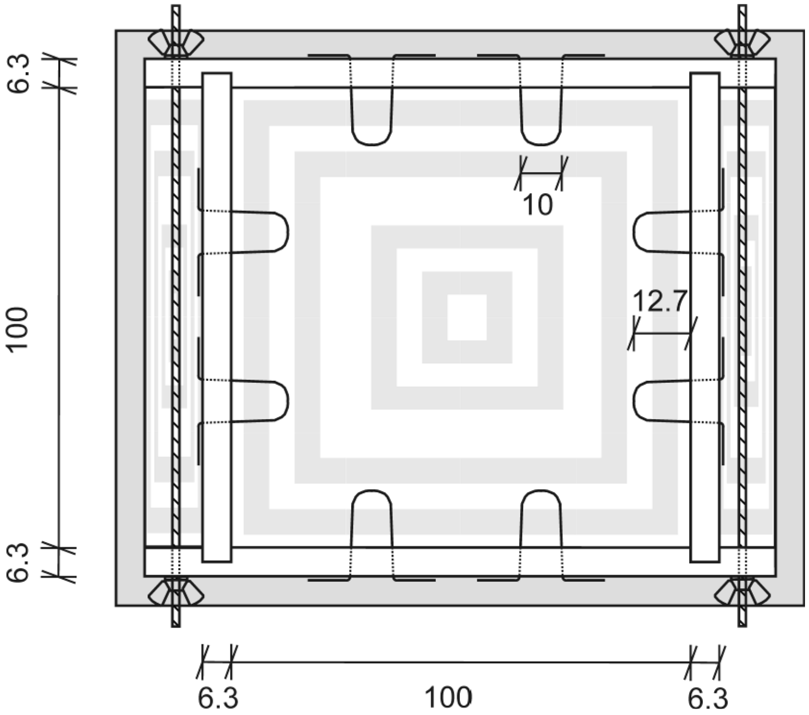

Figure 3.2.1b. Plan view of the mold (numbers in mm)

3.3. Analysis of typical evaporation data under low pressure test condition

3.3.1. Cumulative moisture loss and evaporation rate versus time

The cumulative moisture loss curve was obtained for periods of up to 24 hours or more, and adjusted by means of a baseline calibration curve. Cumulative moisture loss data were subjected to a numerical differentiation procedure in order to measure the evaporation rate. Results were expressed with respect to the exposed surface area in accordance to equation (3.3.1.1).

$$J = \frac{\Delta M}{A \Delta t} = \frac{1}{A}\frac{dM}{dt} \tag{3.3.1.1}$$

where J is the evaporation rate (kg/m^{2}s), ΔM is the mass change at specified time steps (kg), Δt is the time step (s) and A is the surface area of the original sample (m^2).

Cumulative moisture loss and evaporation rate curves for a typical cement paste sample are shown in Figure 3.3.1.1a. Under constant drying condition, the drying rate of cement paste at the beginning is roughly constant with an evaporation rate of 0.42 kg/(m^{2}hr) during first 10 hours, and gradually reduces to 0.05 kg/(m^{2}hr) afterwards. This change in the evaporation rate is also presented in log format. Figure 3.3.1.1b shows the evaporation rate versus log of drying time which is in accordance with results obtained by Hall et al. [99], Cooling [100] for clay brick ceramics, and Kowalski [101] for wet capillary-porous materials such as paper, leather, ceramics and clay. Similar to their observations, drying of cement pastes under constant external conditions occurs in two distinct stages of a constant drying rate period (stage I), and a falling drying rate period (stage II).

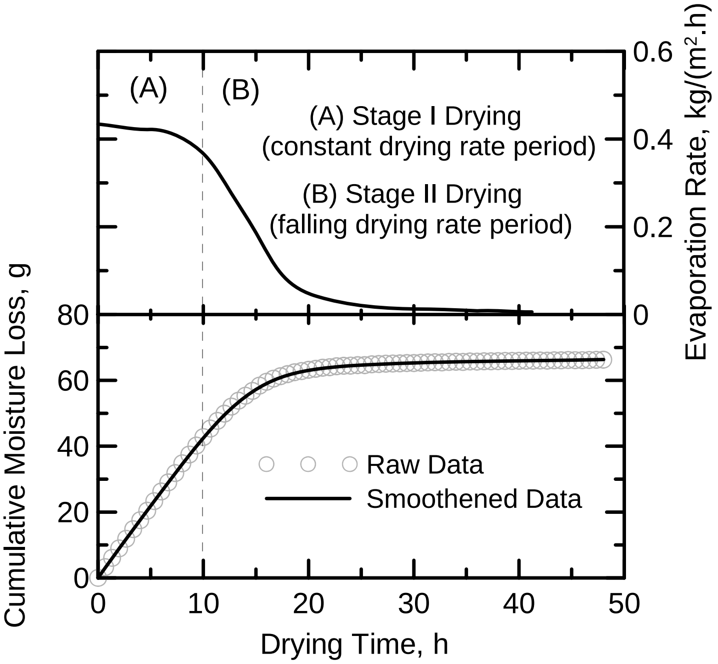

Figure 3.3.1.1a

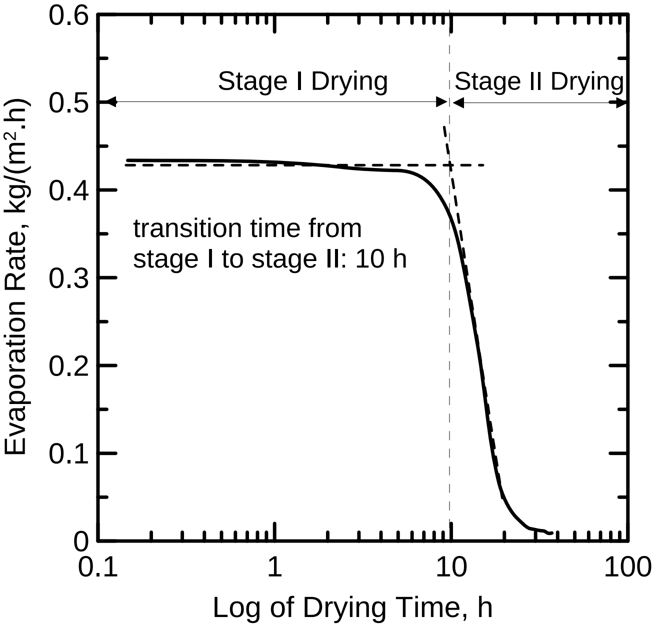

Figure 3.3.1.1b

Figure 3.3.1.1. Typical cumulative moisture loss and evaporation rate of a cement paste sample versus time, (a) in linear scale, (b) in log scale

Different stages of drying can be described based on the degree of continuity between liquid and vapor phases. Schematics of state phases and moisture transport during drying process of porous media according to Scherer [102] and Plumb [103] are presented in Figures 3.3.1.2a-c. During stage I drying, the main phase transitions occur at the boundary surface and vapor phase diffusion into the air is determining rate of evaporation. Hall and Hoff [54] referred to several experimental data showing that stage I behavior is independent of capillary processes inside the material. Drying rate at early time is constant and about the same as rate of evaporation from water surface exposed to the same conditions [8, 99]. This was verified by the evaporation tests on water samples. Results of water surface evaporation compared with a plain cement paste sample are shown in Figure 3.3.1.3.

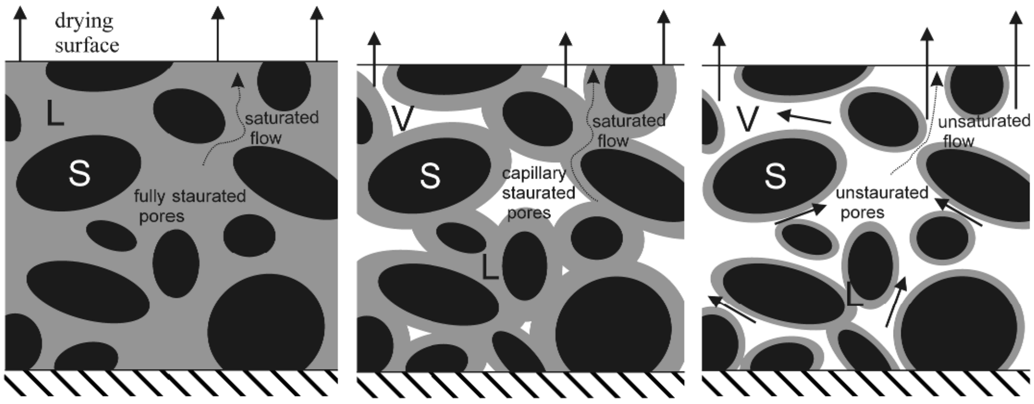

(a) (b) (c)

Figure 3.3.1.2. Schematics of moisture transport during drying process of porous media representing solid (S), liquid (L) and vapor phases (V): (a) initial condition (full saturation), (b) capillary saturation (continuous liquid phase), (c) hygroscopic state (continuous vapor phase)

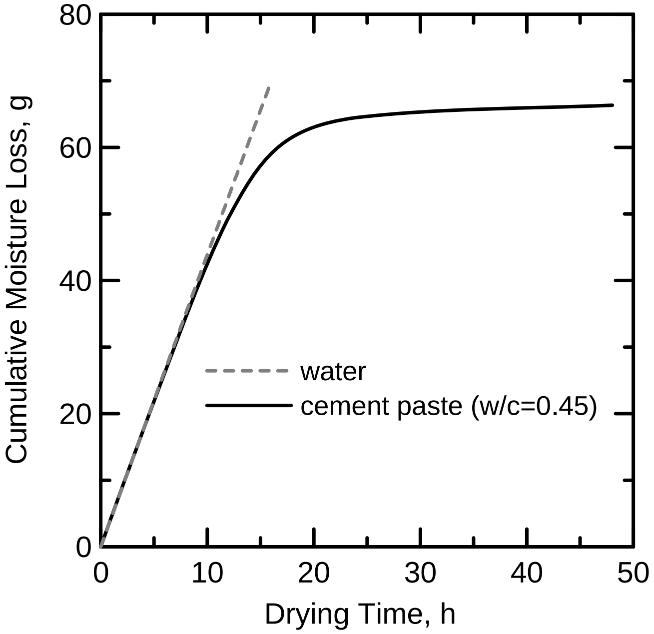

Figure 3.3.1.3a

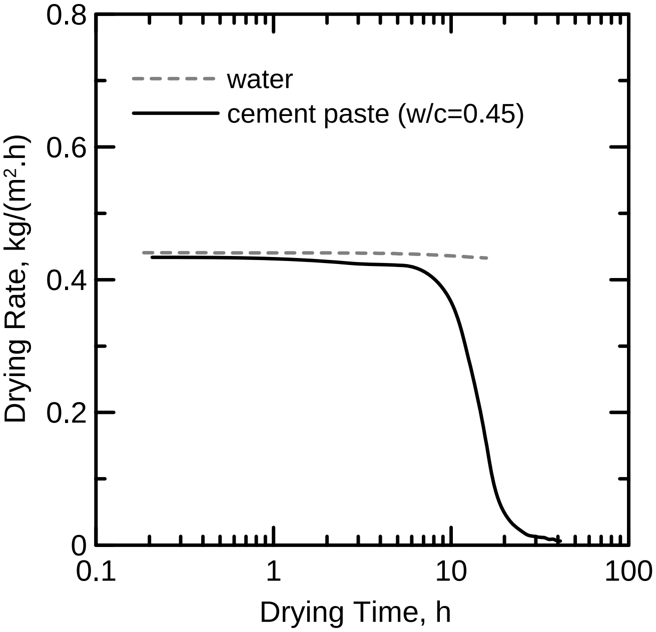

Figure 3.3.1.3b

Figure 3.3.1.3. Evaporation test results from water surface comparing to cement paste

Both samples show evaporation rates in the range of 0.45 kg/(m^2hr). It is therefore postulated that within stage I drying, a continuous liquid phase is present in the pore structure and external evaporative flux away from the surface causes a gradient in capillary pressure in the pores which is the main mechanism of liquid migration from inside toward the boundary [104]. Note that visible plastic cracks were seen as early as 3 h as shown in Figure 3.3.1.3, and fully developed up to 4 h, a time period well within the stage I drying. Since in this stage, drying takes place under external mass transfer control, potential cracking could have no significant effect in increasing evaporation rate which was the same before and after cracking.

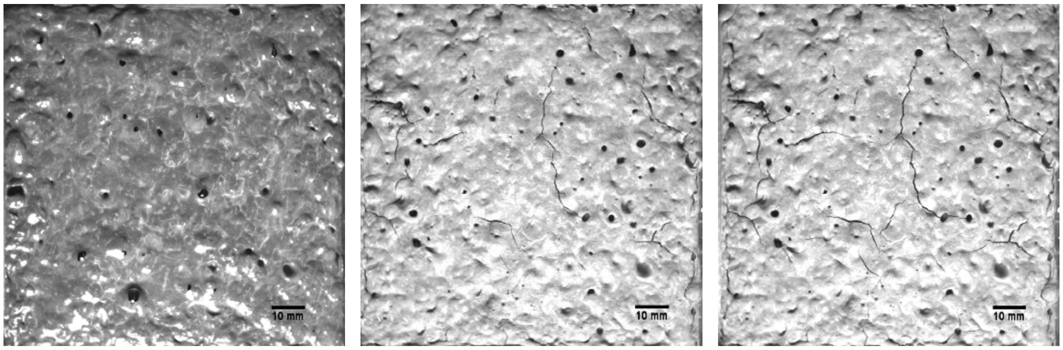

Drying time: 15 min, 3h, 3h 15min

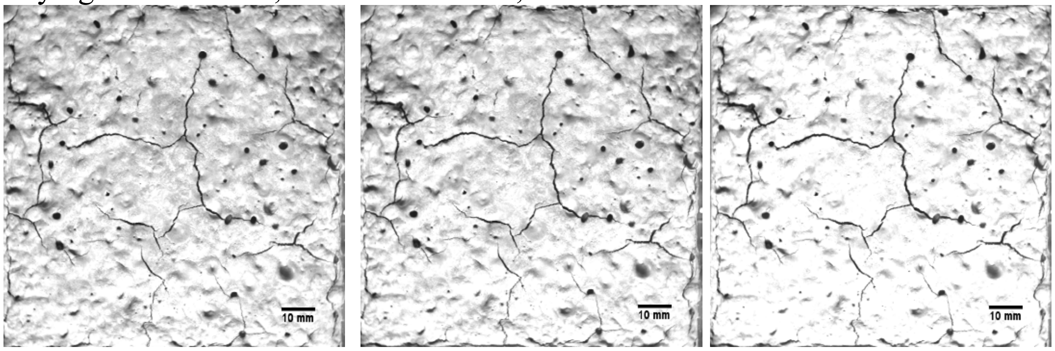

Drying time: 3h 30min, 4h, 24h

Figure 3.3.1.4. 2-D Crack development during drying of a fresh plain cement paste

As the liquid phase water moves to the surface and evaporates with a constant rate during stage I drying, the moisture content drops continuously. The moisture content at the surface reaches a critical value at and below which the material is unable to support the necessary flux to the surface to satisfy the potential evaporation [105]. At this time, stage II drying begins and rate of evaporation starts to fall. Referring to the results presented in Figure 3.3.1.1b, this transition in drying stage is gradual. An empirical definition of transition time is defined by the intersection point of two asymptotic linear approximations to the evaporation rate data at stage I and stage II. As shown in Figure 3.3.1.1b, this transition time for a plain cement paste sample is determined as 9.7 h. Figure 3.3.1.2c shows that in stage II drying, the liquid phase becomes discontinuous while vapor phase becomes continuous within the matrix. Therefore, phase transitions take place within capillary pores and mass transfer begins to occur through the pore vapor phase. Thus, unsaturated capillary flow determines the rate of evaporation and drying happens under internal mass transfer control [105]. In stage II drying, the removal of moisture is mainly controlled by diffusion which dominates the capillary forces [106]. During this period, the moisture content decreases slowly until it reaches the equilibrium value below which the material cannot be dried.

3.3.2. Calculation of Moisture Diffusivity

Evaporation from water surface can be treated as a boundary layer problem, in which the water vapor diffuses from a saturated state on the surface to the ambient moisture concentration [88-93]. Rate of evaporation is controlled by two parameters of binary air-water vapor diffusivity and the concentration gradient. Evaporation from a fresh cement paste at stage I is quite similar to the case of clay, ceramics, and other capillary porous media [107]. It consists of a boundary layer identical to water evaporation boundary, and an unsaturated flow for transfer of liquid water from within the material to supply the flux. The focus of this work is on calculation of diffusivity of water within the cement paste rather than air-water vapor diffusivity at the boundary layer. The calculated diffusivities at stage I and II show the potential for moisture conductivity through the fresh cement paste.

Flow within the porous medium can be described by the extended Darcy equation for unsaturated flow [99, 104] which in the case of a one-dimensional expression is written as:

$$\frac{\partial \theta}{\partial t} = \frac{\partial}{\partial x}\left(K \frac{\partial \psi}{\partial x} \right) \qquad (3.3.2.1)$$

where θ is the volume fraction moisture content (-), ψ is the hydraulic or capillary potential (m), K is moisture conductivity (m/s), x is the pass of moisture transfer (m), and t is the time (s).

Definition of capillary diffusivity (m^2/s) as $D = K(\partial \psi / \partial \theta)$ leads us to Fick's second law of diffusion which governs a majority of moisture transfer problems in porous media [50, 58, 108].

$$\frac{\partial C}{\partial t} = D \frac{\partial^2 C}{\partial x^2} \qquad (3.3.2.2)$$

where C is the moisture concentration (kg/m^3), D is the moisture (liquid and vapor) diffusion coefficient (m^2/s) and t is the time (s).

In order to simulate the drying test results using a dual-stage drying concept, two different boundary conditions at the top surface are required. For the first stage, boundary condition of constant flux at the surface can be applied which is obtained directly from experimental data. Boundary condition for the second stage which is a constant concentration at the surface is set to ambient moisture concentration. At ambient pressure of 1 atm, the water vapor pressure is the product of relative humidity and the saturated water vapor pressure. However, in this low pressure test condition, the sum of the partial pressure of all the species in the air including dry air and water vapor is 1700 Pa. Assuming the percentage of water vapor remains the same after running the vacuum pump, water vapor pressure can be estimated as 2% of barometric pressure which is 34 Pa. The corresponding moisture content defined as $\omega = M_{water} / M_{Dry\ Air} = 0.622 \times P_{water} /(1700 - P_{water})$ is equal to 0.0127 kg of Water/ Kg of Air. Therefore, moisture concentration can be assumed to be zero as a reasonable approximation. Using the experimental evaporation rate during stage I drying, and zero moisture concentration at stage II, the two required boundary conditions are:

$$\begin{array}{lll} \text{Stage I drying:} & \text{at } x = L, & J = F_0 \\ \text{Stage II drying:} & \text{at } x = L, & C_s = C_* = C_{w,low\ pressure} \end{array} \tag{3.3.2.3}$$

where, x is the pass length of diffusion, measured from the bottom face (m), L is the thickness of sample (m), F_0 is the constant flux in stage I drying (kg/(m^{2}s)), and C_* is the ambient moisture concentration (kg/m^3).

Considering C_i as the initial moisture concentration (kg/m^3), the initial boundary condition is

$$t = 0, \quad C = C_i \qquad 0 \le x \le L \tag{3.3.2.4}$$

Since the bottom surface is impermeable, the boundary condition at the bottom is

$$J = -D\frac{\partial C}{\partial x} = 0 \qquad \text{at } x = 0 \tag{3.3.2.5}$$

The analytical solution of equation (3.3.2.2), for the initial and boundary conditions of stage I drying, assuming a constant diffusivity is given by equation (3.3.2.6) [109].

$$C(t,x) = C_i + \frac{F_0 L}{D_I}\left\{\frac{D_I t}{L^2} + \frac{3x^2 - L^2}{6L^2} - \frac{2}{\pi^2}\sum_{n=1}^{\infty}\frac{(-1)^n}{n^2}\exp\left(\frac{-D_I n^2 \pi^2 t}{L^2}\right)\cos\frac{n\pi x}{L}\right\} \tag{3.3.2.6}$$

where, D_I is the diffusivity in stage I drying.

Using equation (3.3.2.6), moisture concentration at the top surface is obtained providing constant F_0 and D_I values. Since stage I drying ends when the surface reaches equilibrium moisture concentration, moisture diffusivity at stage I drying is calculated as long as the time of transition from stage I to stage II has not lapsed. Applying this method on a typical result of a plain cement paste sample results in calculating a diffusivity value of 5.15x10^{-7} m^2/s at stage I drying. Unlike the stage I drying, diffusion coefficients in Stage II drying depend on moisture concentration [110]. For simplicity, diffusivity in stage II is taken constant resulting in calculation of an average diffusivity, which is averaged over space and time. Analytical solution for the boundary conditions of stage II drying subjected to constant concentration, C_*, at the surface is [109]:

$$\frac{C - C_i}{C_* - C_i} = 1 - \frac{4}{\pi} \sum_{n=0}^{\infty} \frac{(-1)^n}{2n+1} \exp\{-D_{II}(2n+1)^2 \pi^2 t / 4l^2\} \cos \frac{(2n+1)\pi x}{2L} \qquad (3.3.2.7)$$

where, D_{II} is the diffusivity in stage II drying.

By integrating equation (3.3.2.7) over the thickness of sample, total amount of diffusing moisture in stage II drying, which has left the sample at time t, M_t (kg), can be obtained and related to its corresponding quantity after infinite time, M_∞ (kg). Therefore, moisture loss during the advanced phase of drying is given by

$$\frac{M_t}{M_\infty} = 1 - \sum_{n=0}^{\infty} \frac{8}{(2n+1)^2 \pi^2} \exp\{-D_{II}(2n+1)^2 \pi^2 t / 4L^2\} \qquad (3.3.2.8)$$

Results of analyses performed by Garbalińska [57] on cement based materials show that in the expansion of equation (3.3.2.8), the higher terms with $n>0$ can be neglected after releasing 40% of the total mass change. As discussed in the following sections, for almost all samples tested in this study, stage II drying begins when more than 60% of the moisture is lost. By considering only first term of the series, moisture diffusivity, D_{II} (m^2/s), can be derived by rearranging equation (3.3.2.8) as

$$D_{II} \cdot \frac{\pi^2}{-4L^2} = \frac{\ln\left(1 - \frac{M_t}{M_\infty}\right) - \ln \frac{8}{\pi^2}}{t} \qquad (3.3.2.9)$$

Assuming the logarithmic terms on the right hand side of the equation are following a linear relationship with the time, slope of the curve, $a_{\ln}$, can be used to determine moisture diffusivity during stage II drying.

$$\ln\left(1-\frac{M_t}{M_\infty}\right)-\ln\frac{8}{\pi^2}=a_{\ln}\,t \qquad (3.3.2.10)$$

$$D_{II}=\frac{-4L^2}{\pi^2}\cdot a_{\ln} \qquad (3.3.2.11)$$

Procedures for obtaining the slope, $a_{\ln}$ for a plain cement paste sample is shown in Figure 3.3.2.1a. This process results in calculation of diffusivity as 3.33x10^{-9} m^2/s at stage II drying. Using calculated values of diffusivity from stage I and stage II drying, total amount of moisture loss at any time can be predicted. Comparison of the simulation and experimental data for a drying cement paste sample is shown in Figure 3.3.2.1b. This figure shows that dual-stage drying model and corresponding moisture diffusivity values can be used to predict drying characteristics of cement-based materials in this low pressure condition. Since two different boundary conditions are applied in stage I and stage II, the continuity of the slope is not completely achieved as shown by the slight bump in the simulation data. Further studies on variable diffusion coefficients and applying different boundary conditions such a convective-diffusive boundary condition at stage II are required in order to better fit the results.

Note that the evaporation rate in the normal room pressure is different than that in the low pressure desiccator, where rate of water vapor diffusion in the desiccator controls the rate of vaporization and drying. The reason is that diffusion rates of water vapor in low pressure are much higher than that under normal room pressure, because the diffusion coefficient of gasses is roughly inversely proportional to the gas pressure at constant temperature [111].

Therefore, the calculated diffusion coefficients for stage I and II drying are only representatives for this low pressure drying condition. However, the analysis is applicable to drying at normal room pressure providing evaporation rates and ambient moisture concentration of that test condition.

3.4. Experimental program

3.4.1. Scope of Test Program

Effects of different variables including sample size, w/c ratio, duration of initial curing, and fiber content were studied. The scope of the test program is shown in Table 3.4.1.1 and includes a test matrix consisting of twelve sets of evaporation tests conducted on different portland cement pastes. Variables of the study included sample thickness, surface area, w/c ratio, duration of initial curing and fiber content. Two sample thicknesses of 11 and 21 mm, and two surface dimensions of 127 mm x 127 mm and 100 mm x 100 mm were used. w/c ratios of 0.45, 0.5, 0.55 and 0.6 were chosen as material variables. Effect of fibers was investigated by adding 1.5, 3, 4.5 and 6 kg/m^3 Alkali Resistant (AR) glass fibers (St. Gobain Vetrotext) to the plain cement paste, equivalent to 0.06%, 0.11%,

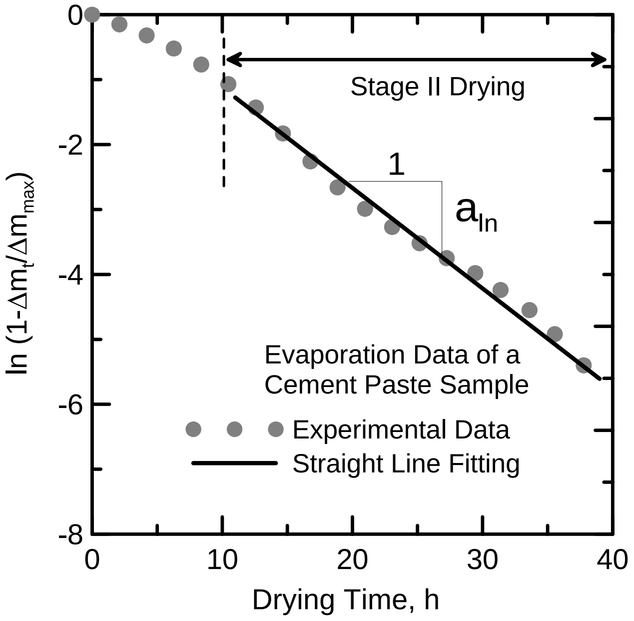

Figure 3.3.2.1a

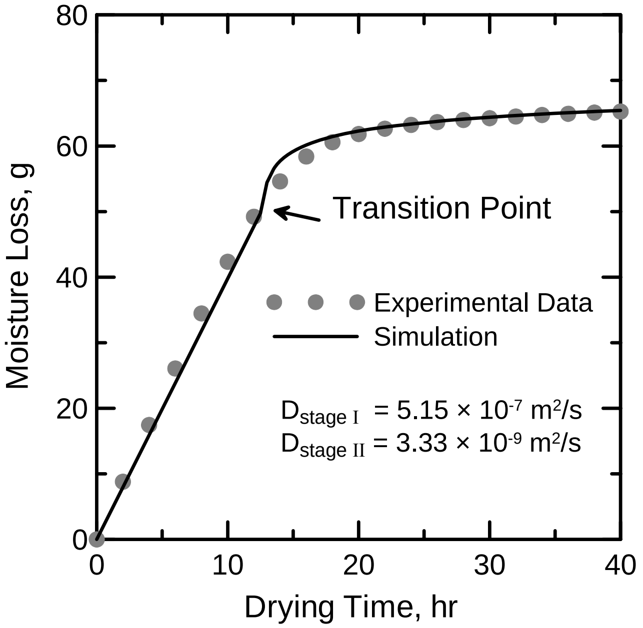

Figure 3.3.2.1b

Figure 3.3.2.1. (a) Deriving aln by fitting a straight line to the curve of $\ln\left(1-\Delta M_t/\Delta M_{\max}\right)$ vs. time in stage II, (b) Simulation of cumulative moisture loss vs. experimental data for a cement paste sample

Table 3.4.1.1.
Scope of the test program

Test series	w/c	Initial curing (h)	Fiber content (kg/m^3)	Thickness (mm)	Surface area (m^2)
P0.45-IC0-F0 (control)	0.45	0	0	11	0.01
P0.45-IC0-F0-Th21	0.45	0	0	21	0.01
P0.45-IC0-F0-SA0.016	0.45	0	0	11	0.016
P0.50-IC0-F0	0.50	0	0	11	0.01
P0.55-IC0-F0	0.55	0	0	11	0.01
P0.60-IC0-F0	0.60	0	0	11	0.01
P0.45-IC3-F0	0.45	3	0	11	0.01
P0.45-IC24-F0	0.45	24	0	11	0.01
P0.45-IC0-F1.5	0.45	0	1.5	11	0.01
P0.45-IC0-F3	0.45	0	3	11	0.01
P0.45-IC0-F4.5	0.45	0	4.5	11	0.01
P0.45-IC0-F6	0.45	0	6	11	0.01

0.17% and 0.23% volumetric fractions. Cement paste samples with initial curing of 0, 3 and 24 hours were also tested to evaluate effect of curing duration.

3.4.2. Materials, Mixing, Placing and Curing procedures

The test program consisted of variations in the physical parameters of testing such as sample area, depth, and materials mixture variations. The mixture proportions for cement pastes are provided in Table 3.4.2.1 and include Type I/II portland cement as the primary binding agent. In fiber reinforced cement pastes, Alkali-Resistant (AR) glass fibers of 24 mm in length and aspect ratio of 150 were used. The fibers are multi-fiber strand of 100 round filaments bonded together. The filament diameter is 14 microns and fiber has elastic modulus of 72 GPa, specific gravity of 2.68 and tensile strength of 1,700 MPa. After mixing in accordance with ASTM C 1116 [112], samples were cast in the molds immediately and subjected to test within 15 minutes. No curing was applied except for samples of two test series which were covered with a plastic sheet for 3 and 24 h at the room temperature before running tests.

Table 3.4.2.1.
Mix proportions of the test series

Test series	Portland cement	Water	AR-glass fiber	w/c
P0.45-ICxx-F0*	1450	650	0	0.45
P0.50-IC0-F0	1400	700	0	0.50
P0.55-IC0-F0	1355	745	0	0.55
P0.60-IC0-F0	1310	790	0	0.60
P0.45-IC0-F1.5	1450	650	1.5	0.45
P0.45-IC0-F3	1450	650	3	0.45
P0.45-IC0-F4.5	1450	650	4.5	0.45
P0.45-IC0-F6	1450	650	6	0.45

* This mix proportion was used for P0.45-IC0-F0, P0.45-IC3-F0, P0.45-IC24-F0, P0.45-IC0-F0-Th21 and P0.45-IC0-F0-SA0.016 samples

3.5. Parameter Estimation

Parameters obtained from evaporation tests includes aspects of initial rate of evaporation, time of transition from stage I to stage II drying, evaporation rate at 24 h, cumulative moisture loss at 24 h and moisture diffusivities. Results are compiled in Table 3.5.1 and are discussed in the following sections.

Table 3.5.1.
Initial evaporation rates, transition time, evaporation rate at 24 h, cumulative moisture loss, and diffusivities of tested samples

Test series	Initial evaporation rate (kg/(m^2.h))	Transition time of drying stages (h)	Evaporation rate at 24 h (kg/(m^2.h))	Cumulative moisture loss at 24 h (g)	Moisture diffusivity at stage I (m^2/s)	Moisture diffusivity at stage II (m^2/s)
P0.45-IC0-F0	0.42	9.7	0.024	65	5.15E-07	3.33E-09
P0.45-IC0-F0-	0.44	18.9	0.300	127	5.27E-07	3.61E-09
P0.45-IC0-F0-	0.37	12.8	0.079	108	4.91E-07	3.25E-09
P0.50-IC0-F0	0.44	9.8	0.031	68	5.27E-07	3.50E-09
P0.55-IC0-F0	0.45	11.0	0.039	74	5.33E-07	4.03E-09
P0.60-IC0-F0	0.46	12.3	0.033	78	5.27E-07	4.16E-09
P0.45-IC3-F0	0.39	7.3	0.017	49	1.94E-07	1.25E-09
P0.45-IC24-F0	0.34	3.0	0.019	26	2.78E-08	2.36E-10
P0.45-IC0-	0.42	10.0	0.043	64	5.05E-07	3.27E-09
P0.45-IC0-F3	0.41	11.2	0.036	65	5.19E-07	2.64E-09
P0.45-IC0-	0.40	11.5	0.028	65	5.15E-07	2.22E-09
P0.45-IC0-F6	0.38	11.3	0.087	66	5.11E-07	2.08E-09

3.5.1. Effect of sample size

Evaporation characteristics of samples with the two different thicknesses and surface areas were studied. Two sample thicknesses of 11 mm and 21 mm in addition to two exposed surface dimensions of 100 mm x 100 mm and 127 mm x 127 mm were used. Cumulative moisture loss and evaporation rates of these test series are shown in Figure 3.5.1.1. As expected, increasing sample thickness and surface area, increased the cumulative moisture loss at the end of the test. Results indicate a 95% increase in the total moisture loss due to doubling of the thickness. A 66% increase in the total moisture loss was observed as the surface area was increased by 62%. Initial evaporation rates changed slightly from 0.42 kg/(m^2.hr) to 0.44 and 0.37 kg/(m^2.hr) for thicker sample and sample with larger surface area, respectively. Thicker sample has a slightly higher initial evaporation rate (~4%) and if this is attributed to within sample variation, then the initial evaporation is primarily a surface phenomenon. Larger sample however has a lower evaporation rate by 12% during stage I. The difference may be attributed to the side and edge effects, as in the vacuum evaporation the mass flux is only a function of total pressure gradient and the water vapor diffusion coefficient is not related to the size of evaporative surface [113, 114, 115]. Since control and thicker samples have approximately the same initial evaporation rates as shown in Table 3.5.1, critical moisture concentration reached later for thicker sample due to higher initial moisture content. Therefore the transition time changes from 9.7 h for control to 18.9 h for the thicker sample. This indicates that the critical moisture concentration was reached after

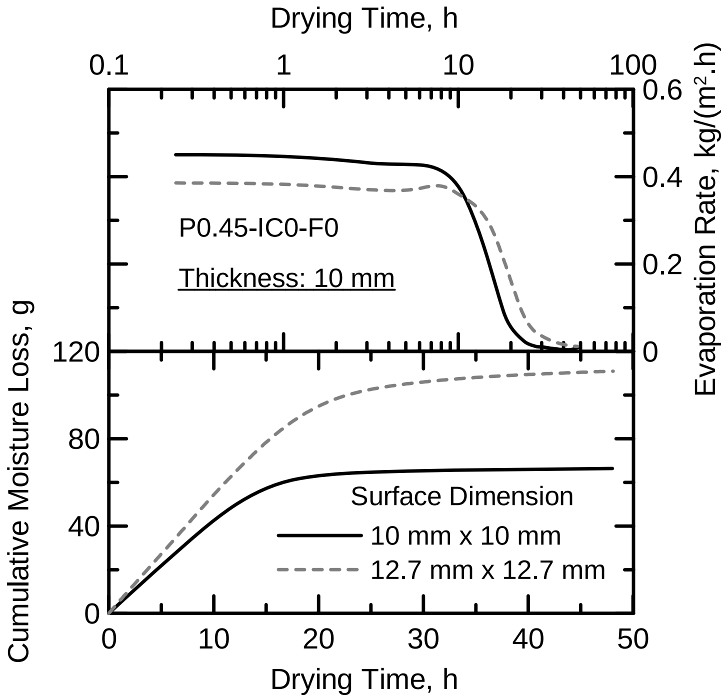

Figure 3.5.1.1a

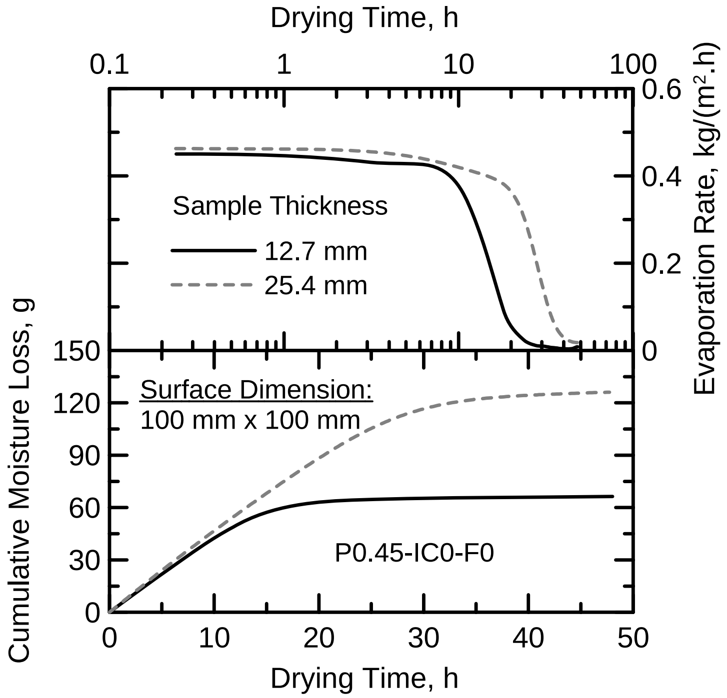

Figure 3.5.1.1b

Figure 3.5.1.1. Effects of surface area and thickness on results of evaporation tests on plain cement paste

losing 63%-65% of the initial moisture content. Similarly, the transition time for larger sample was obtained as 12.8 h which refers to the time when 68% of initial moisture is lost. The values of diffusivity at stage I and stage II drying determined for these three samples are shown in Table 3.5.1. Values of moisture diffusivities at stage I drying is within range of 4.91×10^{-7} to 5.27×10^{-7} m^2/s. Moisture diffusivity at stage II is calculated as 3.33×10^{-9} m^2/s for the control sample (P045-IC0-F0), while for thicker (P045-IC0-F0-Th21) and larger (P045-IC0-F0-SA0.016) is determined as 3.6×10^{-9} and 3.25×10^{-9} m^2/s, respectively. Such similar values for moisture diffusivity of Portland cement paste mixture validate the range of accuracy of the analytical method.

3.5.2. Effect of w/c ratio

Figure 3.5.2.1a shows the cumulative moisture loss-time curves for water cement ratios of 0.4, 0.45, 0.5, and 0.6 after a 24 h drying period, which range from 0 to 65, 68, 74 and 78 g respectively. As expected, the initial rate of evaporation is rather the same for all samples, however higher w/c ratio resulted in a higher cumulative moisture loss. An increase in w/c from 0.45 to 0.6 led to 20% increase in total moisture loss. On the other hand, initial drying rate as shown in Figure 3.5.2.1a was slightly affected by increasing w/c ratio. Average rates of evaporation at first drying stage were 0.42, 0.44, 0.45 and 0.46 $kg/(m^2.hr)$ for samples with w/c ratio of 0.45, 0.50, 0.55 and 0.60, respectively. These magnitudes are sufficiently close to the rate of evaporation from water surface (i.e. 0.45 $kg/(m^2.hr)$) as the upper limit, hence increasing w/c ratio does

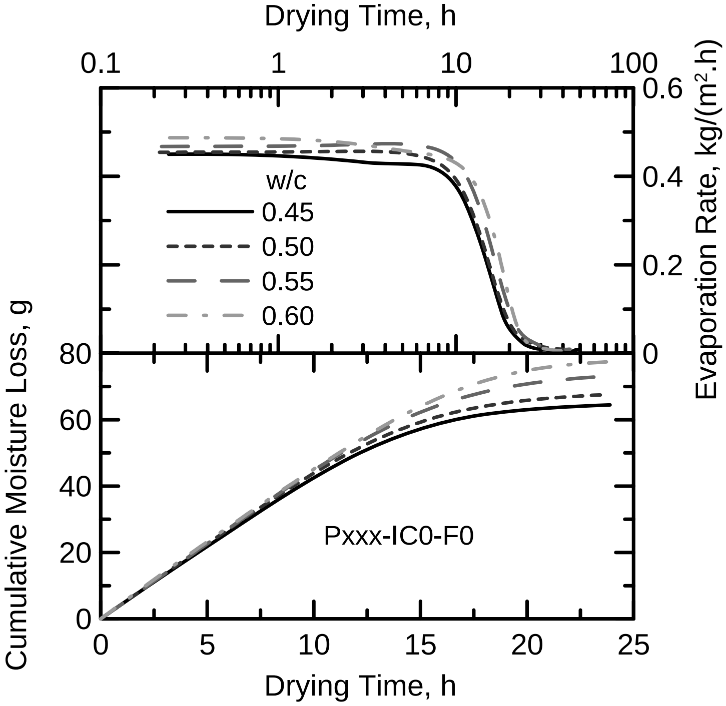

Figure 3.5.2.1a

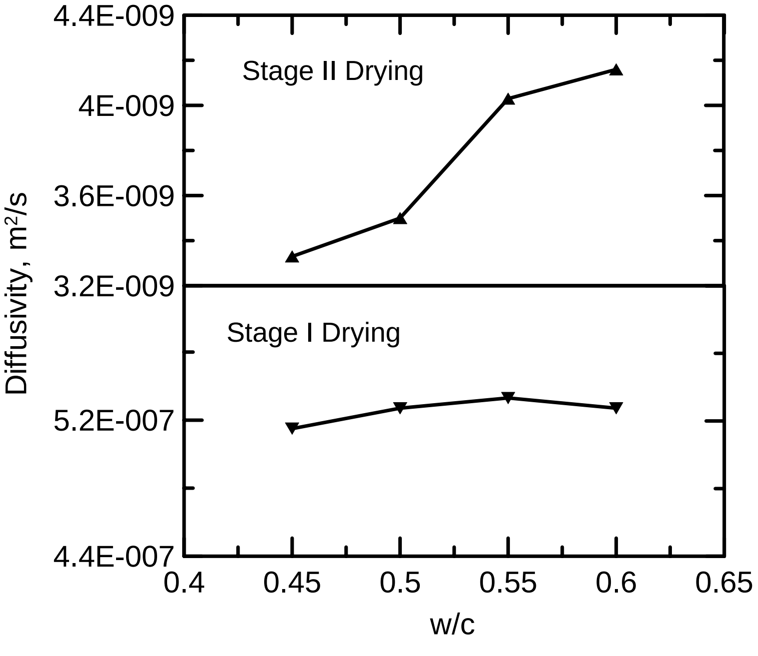

Figure 3.5.2.1b

Figure 3.5.2.1. Effects of w/c ratio on evaporation results of plain cement pastes

not significantly increase the initial evaporation rate. Rates of evaporation at the second drying stage indicate that samples with higher w/c ratios have consistently higher evaporation rates. After 24 h of drying, evaporation rates dropped to 0.03 kg/(m^2.hr) for all samples. But the transition time changes from 9.7 h for the series with w/c ratio of 0.45 to 9.8 h, 11 h, and 12.3 h for series with w/c ratios of 0.5, 0.55 and 0.6, respectively. Diffusivity values determined for different w/c ratios are shown in Figure 3.5.2.1b and indicate that moisture diffusivities of different samples at stage I drying are very similar. However, at stage II drying moisture diffusivities increased by 5%, 21% and 25% when w/c ratio varied from 0.45 to 0.5, 0.55 and 0.6.

3.5.3. Effect of duration of initial curing

Effect of duration of curing prior to initiation of drying was studied by test series P0.45-IC0-F0, P0.45-IC3-F0 and P0.45-IC24-F0. These samples had the same mix proportions and differed only in duration of initial curing which ranged from 0, to 3, and to 24 h. Figure 3.5.3.1 shows the results of the cumulative moisture loss and evaporation rates versus time. The cumulative moisture loss after 24 h of drying was substantially
reduced by increasing the duration of initial curing. This parameter fell from 65 g for the non-cured cement paste to 49 g and 26 g for cement pastes with initial curing of 3 and 24 h, respectively translating into 24% and 60% reduction in cumulative moisture loss of cement paste. This transition can only be justified by the change of microstructure, pore size distributions and physical properties of the

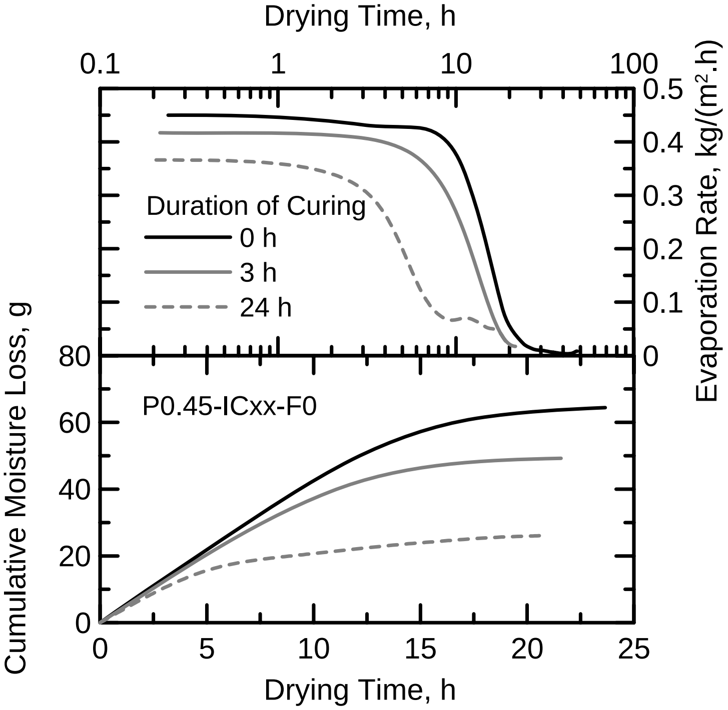

Figure 3.5.3.1a

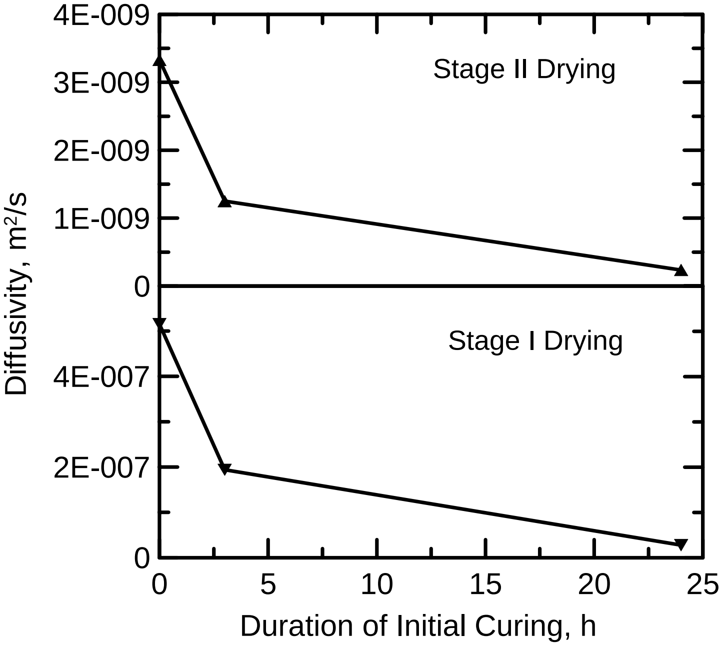

Figure 3.5.3.1b

Figure 3.5.3.1. Effect of curing duration on results of evaporation tests on plain cement pastes

transition layer through which evaporation occurs [114]. Results of stage I drying indicate considerable reduction in initial evaporation rates from a control of 0.42 to 0.39 and 0.34 kg/(m^2.hr) for 3 and 24 h cured samples. However, the reduction of drying rates in second stage of drying is more significant, i.e. after 12 h drying when all three test series were on stage II drying, evaporation rates dropped from 0.3 kg/(m^2hr) for control sample to 0.2 kg/(m^2.hr) and 0.07 kg/(m^2.hr) for 3 h-cured and 24 h-cured samples, respectively. The transition time from stage I to stage II drying decreased from 9.7 h to 7.3 h for the 3 h-cured specimens and down to 3 h for the 24 h-cured sample. The reduction is clearly attributed to the reduction of moisture diffusivities at stage I by increasing curing duration. As shown in Table 3.5.1, moisture diffusivity of control sample is 2.7 and 18.5 times than diffusion coefficients of 3h- and 24h-cured samples, respectively. Increasing curing duration led to decreasing stage II diffusion coefficient of 3 h-cured and 24 h-cured samples comparing to the control sample by as much as 62% and 93%, respectively.

3.5.4. Effect of fiber content and cracking

Effect of fiber addition and its volume fraction was studied by utilizing AR-glass fiber in the mixture. The effect of fiber reinforcement is compared with the plain cement paste in Figure 3.5.4.1. Fiber addition to the cement paste did not result in any significant reduction in cumulative moisture loss at the end of the test. This is in agreement with the result of Naaman et al. [47] which shows fibers result in the reduction of the cumulative moisture loss by only 5% or less.

However, AR-glass fibers caused slight reduction of evaporation rates at the first drying stage. The initial evaporation rate dropped from 0.42 kg/(m^2hr) for plain sample to 0.42, 0.41, 0.40 and 0.38 kg/(m^2.hr) associated with samples with 1.5, 3, 4.5 and 6 kg/m^3 AR-glass fiber additions, respectively. A more significant effect of fiber addition was observed in the manner of transition from the first stage of drying to the second. Addition of fibers resulted in a gradual transition of the modes of drying which could be attributed to the effect of fibers in controlling early-age cracks. As shown in the micrographs of Figure 3.5.4.2, fiber addition reduced the maximum crack width and cracking area of the cement paste. Since early-age cracks cause the evaporative surface to be more exposed to the low pressure condition in the desiccator, they may contribute to higher evaporation rates than uncracked surfaces. The transition time from stage I to stage II drying increased by the addition of fiber for all fiber reinforced paste samples to ranges of 10 to 11.5 h compared to 9.7 h for the control sample.

According to Figure 3.5.4.1b, diffusivity results at stage I drying do not vary significantly by the change of fiber dosage. Since fiber controls plastic shrinkage cracking during early hours (see Figure 3.5.4.2), results support the minimal effect of cracks on drying rate in stage I. However, results show a decreasing trend for the diffusivities at stage II by increasing fiber dosage as shown in Figure 3.5.4.1b. The diffusivities of fiber reinforced cement paste samples with fiber content of 1.5, 3, 4.5 and 6 kg/m^3 are 2%, 20%, 33% and 38% less than corresponding value for plain control sample, respectively. This

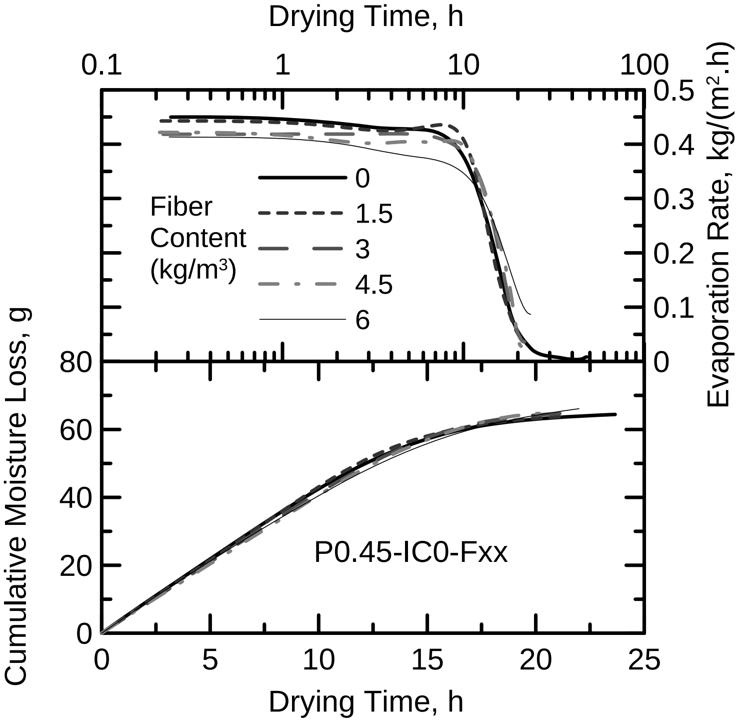

Figure 3.5.4.1a

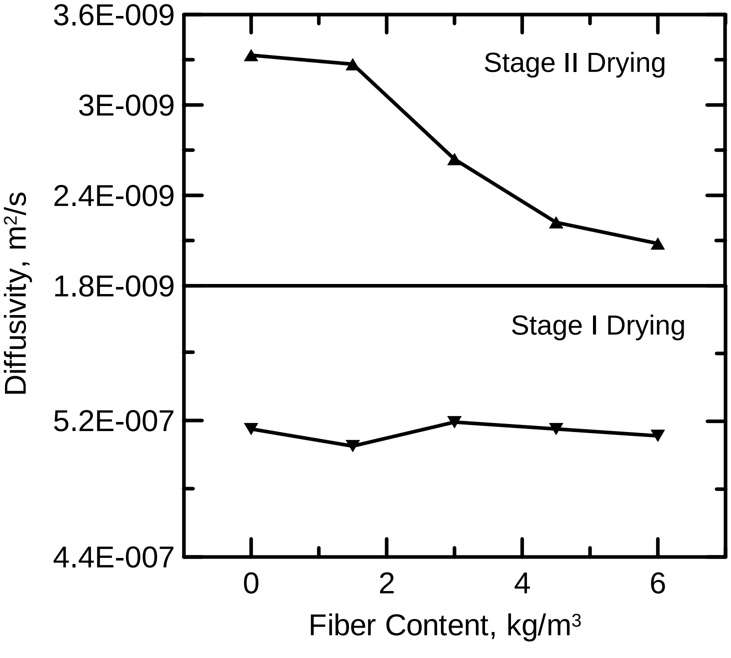

Figure 3.5.4.1b

Figure 3.5.4.1. Results of drying tests on cement paste with different content of AR-glass fibers

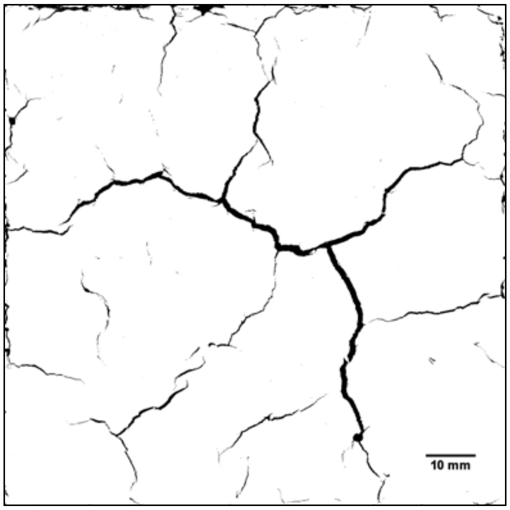

P0.45-IC0-F0

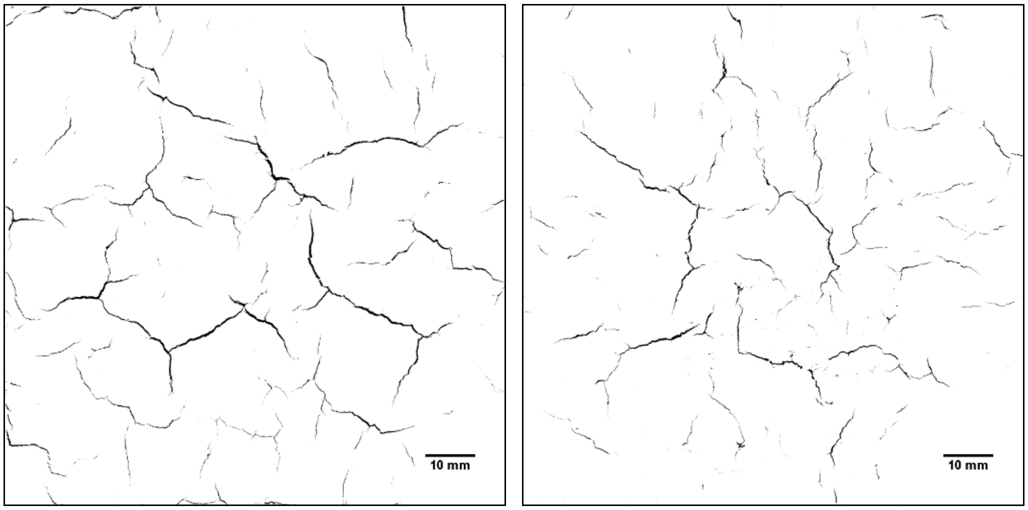

P0.45-IC0-F3 P0.45-IC0-F6

Figure 3.5.4.2. Crack pattern of cement paste specimens with and without AR-glass fibers after 24 hours of drying under low-pressure test condition

effect can be explained by the higher degree of surface cracking in the presence of fibers which reduces the mean path length of moisture transfer to reach the surface. The result can thus be interpreted as the effect of cracking on the drying rate in stage II when unlike to stage I, the restraint of cracks by fibers, the increased number of microcracks, and reduced crack widths are effective on lowering moisture diffusivity. This explanation can be supported by the fact that in stage II, drying happens under internal mass transfer control and the microstructure plays a significant role on the drying process. As shown in Figure 3.5.4.2, 22% and 61% reduction in areal fraction of cracks were observed by adding 3 and 6kg/m^3 fibers to cement paste, respectively. Also, maximum crack widths of samples associated with 3 and 6kg/m^3 fibers were 47% and 71% less than corresponding value for the control sample, respectively. The length of microcracks however was increased by addition of fibers. Higher moisture diffusivities at stage II in plain pastes with wider cracks compared to fiber reinforced pastes with narrower but more plentiful cracks are in accordance with the studies performed by Bažant and Raftshol [116] and Aldea et al. [117]. While they found the moisture diffusivity and the water permeability are proportional to the crack width cubed, results of another experimental study [118] indicated that diffusivity of concrete increased 2.25 times by shrinkage cracks with a width of 0.1 mm and a spacing of 70 mm. Also, the recent experimental data reported by Vejmelková et al. [119] show that moisture diffusivity of high performance concrete and cement pastes increased by one order of magnitude due to the cracking. In addition, Torrijos et al. [120] reported the increase of water permeability by one order of magnitude due to increase of crack density from 0.25 to 0.45 cm/cm^2. Considering all these results, it can be concluded that fibers reduce moisture diffusivities of cracked samples at stage II by reducing crack width and crack density which results in the durability improvement of cement-based materials.

3.6. Conclusion

A test method capable of characterizing evaporation parameters and simulating sequential formation of shrinkage cracks in two-dimensional samples under low-pressure condition was developed. The cumulative moisture loss and evaporation rates were calculated. Based on the results of experiments and analyses in this study, following conclusions may be drawn:

(1) Drying of cement pastes can be segmented into two distinct stages: constant drying rate period (stage I) and falling drying rate period (stage II). During stage I drying, evaporation rate is constant, main phase transitions take place at the surface and vapor phase diffusion process is rate-determining. At the transition time, moisture content at the surface reaches a critical value. During stage II drying, phase transitions take place within capillary pores and unsaturated capillary flow is rate-determining. During this stage, moisture content decreases slowly until reaching the equilibrium value below which the material cannot be dried.

(2) The cumulative moisture loss and evaporation rate curves can be used to differentiate evaporation characteristics of different cement pastes. Parameters including thickness and surface area of samples, w/c ratio,

and duration of initial curing have significant effects on evaporation results.

(3) A dual-stage drying model based on two different boundary conditions at the top surface and a diffusional moisture transfer within the pores can be used to simulate experimental results. The model can be used to determine moisture diffusivity of the samples during drying process. Moisture diffusivity is higher in stage I by more than one order of magnitude than its values in stage II.

(4) Fibers contribute to the control of plastic shrinkage cracks. However, presence of fibers and cracking control do not affect the drying rate in stage I drying. In stage II drying, the presence of fibers reduces the diffusivity values. This could be due to the restraint of cracks by fibers which is effective in stage II when internal mass transfer controls the drying. Results show that 22% and 61% reduction in areal fraction of cracks were observed by adding 3 and 6kg/m^3 fibers to cement paste, respectively. Also, maximum crack widths of samples associated with 3 and 6kg/m^3 fibers were 47% and 71% less than corresponding value for the control sample, respectively. Since there is a cubic relationship between permeability rate and the crack width, effect of fibers in controlling the plastic crack width results in significant durability enhancement.

(5) Among several different parameters investigated in this study, duration of curing has the most significant effect on the reduction of drying rate and moisture diffusivities.

4. Theory and Modeling of Early-Age Drying

4.1. Introduction

Drying of cementitious materials is a preventable, but often inevitable phenomenon during early age. With regard to long-term durability, shrinkage cracking is the most anticipated consequence of drying due to low early-age strength of cement based materials. Therefore, understanding the physics of drying and modeling the process is of great importance.

In existing literature, the moisture movement during drying of concrete is often described as a diffusion process where the diffusivity depends highly on the moisture content. Torrenti et al [55], West and Holmes [56], Garbalińska [57], Huldén and Hansen [58], Kim and Lee [59] modeled the moisture movement by the Fick's second law of diffusion without explanation of the physics of the problem. Most of these works refer to Bazant and Najjar [60, 61] who considered the drying of concrete as a nonlinear diffusion problem. Using an approach based on soil science, Kodikara and Chakrabarti [62] expressed the moisture movement during drying as a two separate stage mechanism [63], however, they modeled the phenomena as a one-stage diffusion process. Chen and Mahadevan [64] referred to Walton et al [65] in using diffusion as the dominant moisture transport mechanism in concrete. Shimomura and Maekawa [50] used mass conservation of the vapor and liquid water to derive a diffusion-type equation. Šelih and Bremner [66] concluded from the experimental results that the diffusion-driven moisture transport approach is appropriate only for the late stage of drying when the material is predominantly unsaturated, and the moisture movement in the form of vapor flux is dominant. Although Shimomura and Maekawa [50] discussed the movement of liquid water as governing mechanism regarding moisture movement near the saturated state, referring to Young [67], the concept was not implemented in their model. Šelih and Bremner [66] expressed the drying process as two different types of mechanisms of movement which can be described by a Darcy-type equation near saturation, succeeding by a diffusion-type equation. Nonetheless, their work was only limited to experimental observations.

The evaporation through the surface as a boundary condition is applied differently in available models. While ACI 305R-99 [68] and Uno [69] recommended a constant flux equal to evaporation rate of water surface for early-age hot weather concreting, a convective boundary condition proportional to the difference of internal and ambient moisture concentration was most often employed [50, 56, 58, 59]. Torrenti et al [55] and Shimomura and Maekawa [50] also used evaporative boundary conditions similar to convection. In another approach, Bazant and Najjar [60], and Garbalinska [57] applied a constant moisture concentration equal to ambient moisture concentration as the boundary condition in their models. However, the assumed boundary conditions are not supported by the physics and driving forces of surface evaporation process.

In this chapter, physics of water evaporation is presented followed by a description of theory of evaporation from cementitious matrix that is represented as a capillary porous media. A dual-stage methodology for modeling the drying is introduced based on surface moisture transfer and internal moisture transport characteristics. After studying the effect of different parameters on the model, the methodology is applied to the results of drying experiments under low and normal pressure conditions and is further verified by a Finite Element (FE) analysis.

4.2. Physics of water evaporation

Water evaporation is a phase transition process by which molecules are converted from the liquid state into a vapor state. It usually occurs at the water surface exposed to the atmosphere as the vapor is carried away by the air flow [121, 91]. This process in the atmosphere arises from the action of molecular diffusivity, since water vapor concentration at the water surface is higher than its concentration away from the surface [88, 89, 90, 92, 93]. This concentration gradient drives water vapor from higher concentration to lower. Vapor is transferred through molecular exchange in the same manner as heat and momentum are transferred, as most of transfer takes place within a few molecular free path lengths of the surface [89]. According to Fick's first law, the net flux of a material (e.g. vapor) in any direction is proportional to its concentration gradient in that direction and therefore the rate of evaporation at a horizontal surface is given by [122]

$$J = -D_w \frac{dC_w}{dx} \tag{4.2.1}$$

where J is the mass flux (kg/(m^{2}s)) or drying rate in evaporation problems, D_w is the molecular diffusivity of water vapor in air (m^2/s), C_w is the water vapor concentration (kg/m^3) and x is diffusion distance (m). Assuming water vapor as an ideal gas ($p_w = C_w RT / M$), evaporation rate can be described by:

$$J = -\frac{D_w M}{RT}\frac{dp_w}{dx} \tag{4.2.2}$$

where p_w is the water vapor pressure (Pa), M is the molar mass of water (Kg/mol), R is the universal gas constant (m^3Pa/mol.K) and T is the absolute temperature (^oK).

At the water surface of an open dish, the partial pressure of water vapor, p_w, is fixed by the saturated vapor pressure of water, p_{w0}, since the air in direct contact with the water is saturated [54]. Based on definition of fractional relative humidity as $H = p_w / p_{w0}$, local relative humidity at water surface is 1 (100%). If relative humidity of the air well away from the surface is below 100%, water vapor moves upwards from the surface and evaporation rate can be obtained as

$$J = -\frac{p_{w0} D_w M}{RT} \cdot \frac{dH}{dx} \tag{4.2.3}$$

The approach based on equation (4.2.3) has been suggested in studying the evaporation processes and determining diffusion coefficients of volatile liquids diffused into air [123, 124, 125, 126].

In mass transfer problems, the air near the surface may be regarded as a boundary layer, a concept set forth by Prandtl [127] for the momentum transport in the neighborhood of a solid wall. Bringing the concept to the evaporation problem, as shown in Figure 4.2.1, a thin interfacial layer covering the water surface is considered as the boundary layer through which the vapor molecules transfer to the surrounding air. The thickness of the boundary layer is of the order of 1mm [128] and the movement through this boundary layer is presumed to be governed by the molecular diffusivity [129].

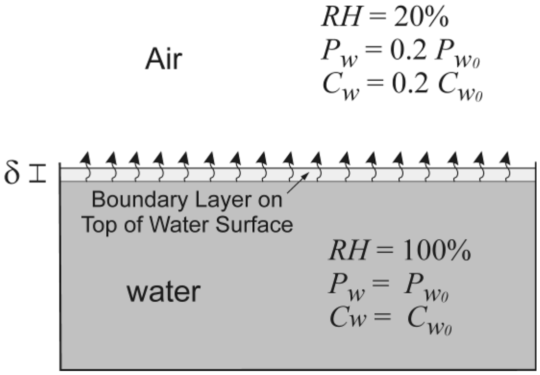

Figure 4.2.1. Schematics of the interfacial boundary layer during evaporation from free water surface

For simplicity we assume linear variation of vapor pressure across the boundary layer which is of thickness δ, so that from equation (4.2.2) we have

$$J = \frac{D_w M}{RT}\frac{p_{w0} - p_{w*}}{\delta} \tag{4.2.4}$$

where p_{w0} is the saturation vapor pressure and p_{w*} is the ambient vapor pressure and J is the mass flux or rate of evaporation (kg/m^{2}s). Since $H = p_w/p_{w0}$, moisture flux can be expressed as

$$J = \frac{D_w M}{RT}\frac{p_{w0}(1-H)}{\delta} \tag{4.2.5}$$

This equation shows that rate of evaporation is a function of relative humidity, H, saturated water vapor pressure, P_{w0}, and boundary layer thickness, δ. Since saturated water vapor pressure is a function of temperature itself [130] and boundary layer thickness is affected by the air flow, this equation reflects the effects of relative humidity, temperature and wind velocity on the evaporation rate. Following equation proposed by Wiederhold [130] relate saturation water vapor pressure to the temperature.

$$p_{w0} = 611.21(1.0007 + 3.46 \times 10^{-8}\, p)\, e^{\frac{17.502(T-273.15)}{T-32.18}} \tag{4.2.6}$$

where p_{w0} is saturated vapor pressure of water (Pa), p is the ambient pressure (Pa), and T is the absolute temperature (K). The relationship between saturated water vapor pressure and temperature is shown in Figure 4.2.2. Also, diffusion coefficient of water vapor in air is a function of temperature which can be obtained by a regression curve fit to data from Bolz and Tuve [131, 132].

$$D_w = -2.775 \times 10^{-6} + (4.479 \times 10^{-8})T + (1.656 \times 10^{-10})T^2 \tag{4.2.7}$$

where D_w is the diffusion coefficient of water vapor in the air (m^2/s) and T is the absolute temperature (°K). This relationship is shown in Figure 4.2.2 as well.

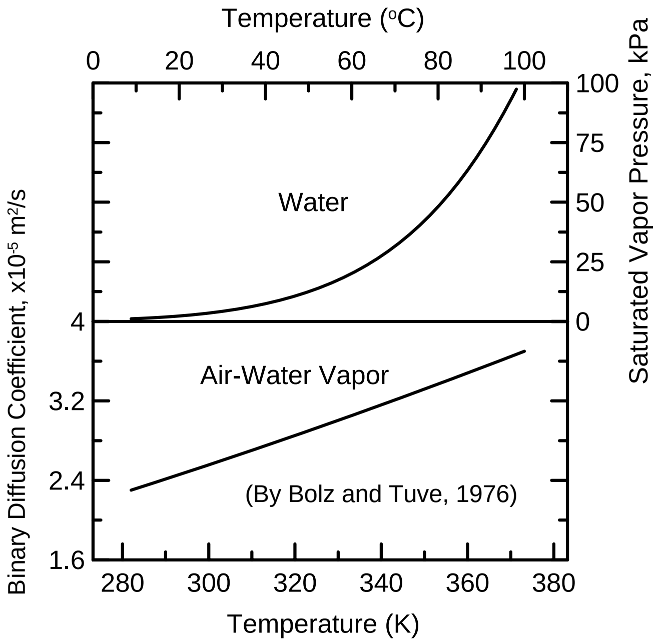

Figure 4.2.2. Variation of diffusion coefficient and saturated vapor pressure vs. temperature

Having molar mass of water vapor as M=18.016 x 10^{-3} kg/mol and the universal gas constant as R= 8.314472 m^3Pa/mol.K and using equations (4.2.4) to (4.2.7), effects of temperature, relative humidity and boundary layer thickness on rate of evaporation is studied and shown in Figures 4.2.3a and 4.2.3b. As shown in the figures, increasing ambient temperature leads to increase in the rate of evaporation, which more significantly increases by lowering ambient relative humidity and boundary layer thickness. Increasing boundary layer thickness however results in decreasing the evaporation rate, e.g., in an ambient temperature and relative humidity of 40°C and 50%, an increase in the boundary layer thickness from 0.2 mm to 3 mm translate into a reduction of evaporation rate from 13.4 to 0.9 kg/(m^2h). Similar to the effect of the boundary layer thickness, increasing the ambient relative humidity cause a drastic reduction in the rate of moisture evaporation. For instance assuming a boundary layer thickness of 0.7 mm, the evaporation rate at 40°C decreases from 6.8 to 0.7 kg/(m^2h) when the relative humidity increases from 10% to 90%.

4.3. Theory of evaporation from cementitious materials

Moisture evaporation of Portland cement paste and concrete can be explained by the concept of moisture transfer through porous media using an isothermal drying model. Since drying of porous media includes complex moisture transfer in both liquid and vapor states, the driving force of vapor pressure gradient which is the case in water vapor evaporation cannot be used directly here. Instead, a general concept of hydraulic potential ψ, applicable to

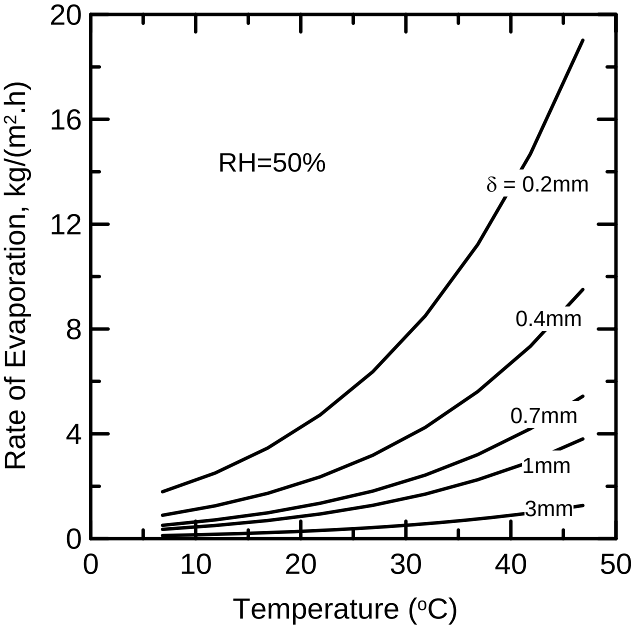

(a)

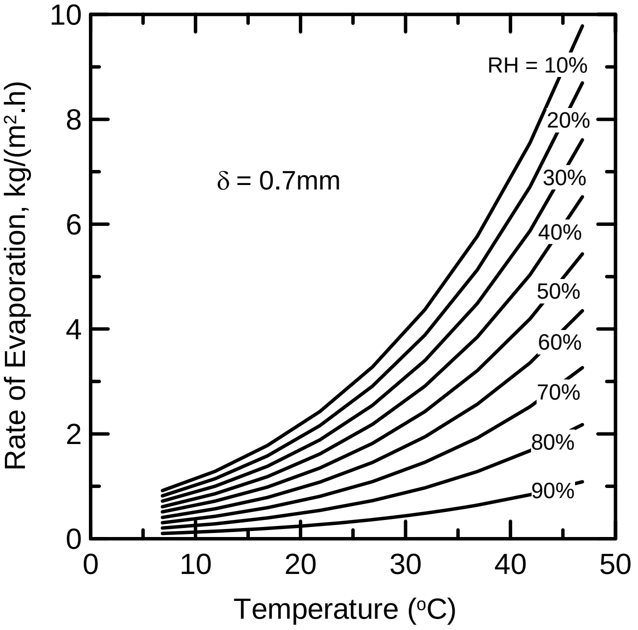

(b)

Figure 4.2.3. Parametric study on the effects of temperature, boundary layer thickness and relative humidity on evaporation rate from water surface

both vapor phase transfer and water liquid transfer through unsaturated porous medium is used. The concept comes from unsaturated flow which is governed by extended Darcy law, where unsaturated flow rate, u (m/s) is related to the hydraulic potential ψ (m) by a liquid conductivity coefficient K (m/s) [133, 134, 135].

$$u = -K \, \nabla \psi \tag{4.3.1}$$

Hydraulic potential is indeed the energy required to transfer unit weight of liquid from the porous materials to a reservoir of the same liquid at the same temperature and elevation, and hence it can be called capillary potential as well. In this approach u is the mass-averaged velocity which stands for the water in both liquid and vapor states. The drying of porous media has been recently analyzed with multiphase approaches considering the moisture transfer through porous space partially saturated by liquid water, water vapor and dry air [136, 137, 138, 139]. However, it has been shown that by introducing certain assumptions above formulation in terms of one single driving force can be retrieved [140, 141, 142]. The validity of this hypothesis was discussed by Mainguy et al. [139]. Equation (4.3.1) together with continuity equation leads to fundamental Richards equation as [135, 143, 144]

$$\frac{\partial \theta}{\partial t} = \nabla \cdot (K \, \nabla \psi) \tag{4.3.2}$$

where θ is the volume fraction moisture content (-), and t is the time (s).

Note that in this approach of drying, ψ depends on only one state variable, namely θ, as well as K which also depends explicitly on θ. Equation (4.3.2) shows that gradient of hydraulic or capillary potential is the main cause of moisture migration through capillary media [104]. Kelvin equation relates capillary potential to capillary pressure or vapor pressure by:

$$\psi = \frac{RT}{M} \ln \frac{P_{ws}}{P_{w0}} \tag{4.3.3}$$

This relationship shows that unsaturated flow in porous media can be expressed either by hydraulic potential gradient or by vapor pressure gradient. Accordingly, Coussot [145] discussed the cause of moisture motion through the porous network by the difference in capillary pressure between the top and the bottom of the sample. In this study, variation of both parameters as the driving force from the interior of material through ambient with no discontinuity is used to explain the drying process. Nonetheless, the focus of the work is on moisture loss analysis and therefore to calculate moisture content, ψ is replaced by θ in equation (4.3.2) using the definition of capillary diffusivity as $D = K(d\psi/d\theta)$, and we have

$$\frac{\partial \theta}{\partial t} = \nabla \cdot (D \nabla \theta) \tag{4.3.4}$$

where D is the moisture (liquid and vapor) diffusion coefficient (m^2/s). Equation (4.3.4) can also be derived from the mass conservation and transport laws for vapor and liquid water in concrete [50, 141]. This equation turns out to be a non-linear diffusion equation, with D depending on θ.

Studies of drying behavior of clay brick ceramics by Hall et al. [99], Platten [146], Cooling [100], and different wet capillary-porous materials by

Kowalski [147] as shown in Figure 4.3.1 indicate that evaporative flux at the boundary is roughly constant for a period of time at the beginning of the drying referred to as stage I and then falls significantly by the time in the second period or stage II. The same drying behavior was observed for the Portland cement pastes in recent experimental works by authors [148], as well as in mortar [149] and light-weight concrete [66]. These two stages of drying based on variation of driving forces and degree of continuity between liquid and vapor phases are discussed individually in the following sections.

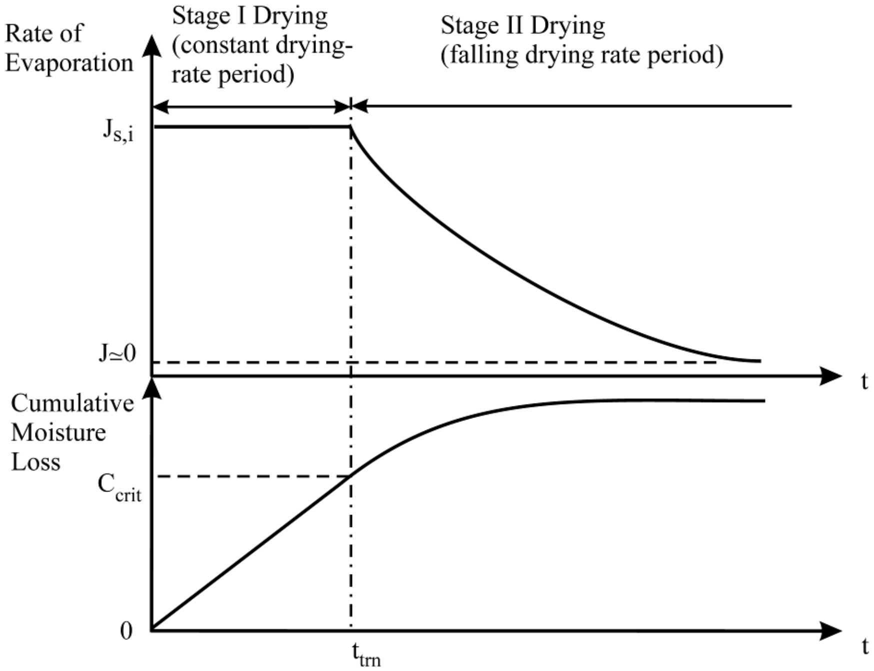

Figure 4.3.1. Two stages of drying during evaporation of capillary porous materials

4.3.1. Stage I Drying

Mass loss experiments of cement paste subjected to low pressure has been recently conducted [148]. Results show that the external evaporation potential is independent of internal capillary microstructure, and this aspects controls the moisture transport within the material in stage I drying. The phenomenon can be described by the variation of hydraulic potential or vapor pressure and the degree of continuity between liquid and vapor phases. As shown in Figure 4.3.1.1a at the beginning of drying, the porous media (i.e. cementitious materials) are fully saturated and therefore, the vapor pressure inside the open cell microstructure is equal to the saturated vapor pressure. There is no vapor pressure or hydraulic potential gradient to drive the moisture inside the porous body, but the gradient of vapor pressure at the boundary layer, which varies from saturated vapor pressure just on top of the material to the ambient vapor pressure, drives the moisture to the ambient. In analogy to vapor pressure, the hydraulic potential inside the porous body is also uniform and surface hydraulic potential is equal to initial value, $\psi_s = \psi_i$, which for a saturated material is $\psi = 0$, referring to equation (4.3.3) and varies to ψ_* as the ambient hydraulic potential. Variation of hydraulic potential and vapor pressure from the interior of material through ambient is depicted in Figure 4.3.1.1c.

A drying begins, the moisture evaporates at the surface and the surface vapor pressure falls slightly from the initial value. Although the vapor pressure is still approximately equal to the saturated vapor pressure, $p_s \approx p_i$, but the moisture concentration and hydraulic diffusivity are sufficiently high that an adequate capillary flow to the surface can be generated by small value of vapor pressure gradient or water content gradient [54]. Continuation of drying leads to continuous decrease of moisture concentration deep inside the material. The material is not fully saturated as shown in Figure 4.3.1.1b but the liquid phase is still continuous, and therefore, the porous material remains capillary saturated. The drying is in stage I while the material is capillary saturated, vapor pressure is approximately equal to saturated vapor pressure, and the profile of internal water concentration remains flat [54, 105]. This drying scenario is referred to as the funicular drying regime [150].

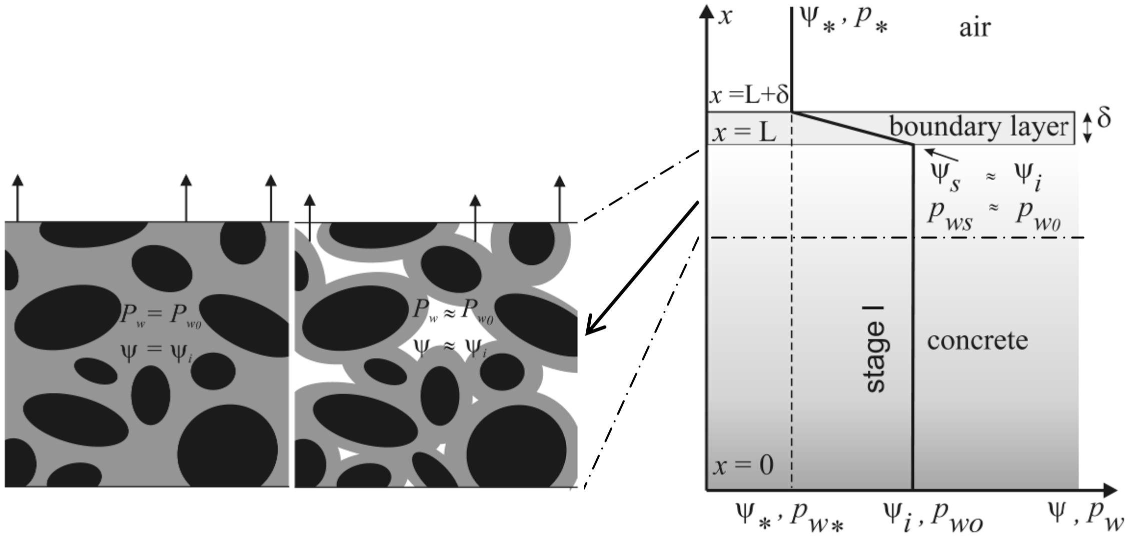

(a) **(b)** **(c)**

Figure 4.3.1.1. (a) Fully saturation state of porous material as the initial condition, (b) capillary saturation of porous material as a later stage of drying, (c) variation of hydraulic potential and vapor pressure from the interior of the material through ambient in stage I drying.

4.3.2. Stage II Drying

As drying continues, the moisture concentration in liquid phase decreases and reaches the insular saturation which is associated with the transition time from stage I to stage II, when the liquid phase becomes discontinuous [105]. As shown in Figure 4.3.2.1a, at this stage of drying, the diffusion of water vapor through continuous vapor space becomes the dominant mechanism for moisture transport [105]. Since moisture transfer is limited only to the diffusion of water vapor generated by local evaporation of bound liquid water, and not liquid water movement, the evaporation rate falls and drying happens under internal mass transfer control [106]. From the driving force aspect, at this stage, the saturation level is lower than capillary saturation and therefore, the vapor pressure falls from saturated vapor pressure to a lower value. During this period, the evaporation continues until vapor pressure reaches ambient vapor pressure or hydraulic potential balance created which can be referred to as hygroscopic equilibrium. At this stage, two different theories can be suggested for the variation of hydraulic potential or vapor pressure at the surface. As shown in Figure 4.3.2.1b, based on first theory designated by stage II(A), water vapor pressure can fall almost to the ambient vapor pressure instantaneously to reach hygral equilibrium with the environment. On the other hand, the second theory suggests a gradual decrease for the water vapor pressure from the saturated pressure to the ambient vapor pressure as shown in Figure 4.3.2.1c and designated by stage II (B) modeling. The former condition in terms of moisture concentration can be expressed as equal moisture concentration between surface and ambient levels [148]. The latter condition is tantamount to imposing a convective-diffusive transfer of vapor at the surface for modeling stage II drying.

4.4. Two-Stage Modeling of the Drying of Cementitious Materials

4.4.1. Governing Equations and Geometry of the Problem

A model is developed to address the moisture transport properties of cement pastes during drying tests under low pressure condition [148]. The moisture transport through the sample ($0 \le x \le L$) is assumed to be one-directional (1-D) because of high surface area-to-depth ratio, and exposing only top surface to the drying condition.

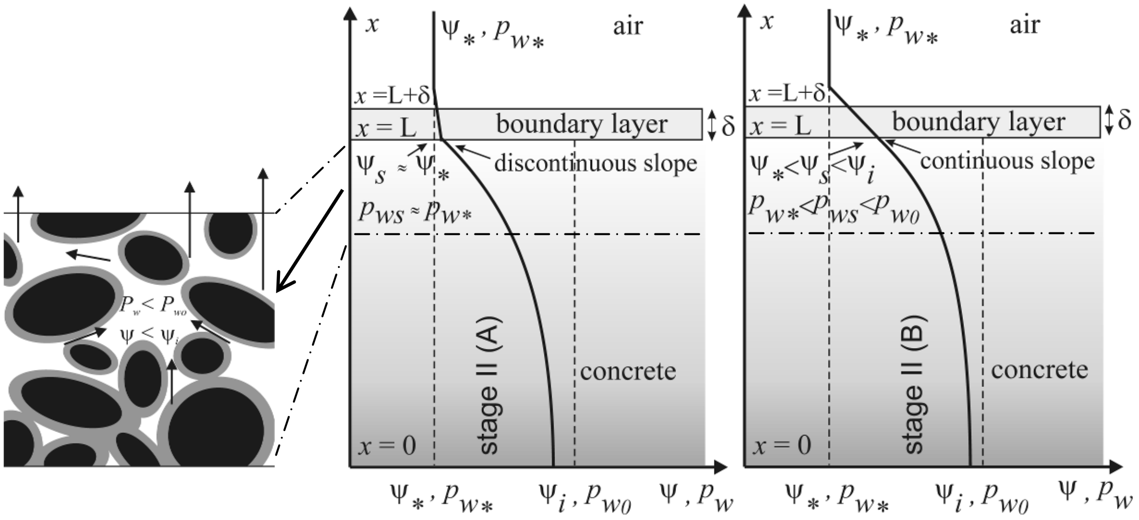

(a) **(b)** **(c)**

Figure 4.3.2.1. (a) Low saturation state of porous material as the advanced stage of drying, (b) variation of hydraulic potential and vapor pressure from the interior of the material through ambient in stage II using simplified model (model A), (c) variation of hydraulic potential and vapor pressure from the interior of the material through ambient in stage II using convection model (model B)

By assuming an isothermal condition, effects of change in temperature during drying process is negligible. For modeling the internal moisture transport in both stage I and stage II drying, 1-D form of equation (4.3.4) is used with the replacement of dimensionless moisture concentration variable, θ (-), with the dimensional variable C (kg/m^3) [55, 61, 63, 110, 151].

$$\frac{\partial C}{\partial t}=\frac{\partial}{\partial x}\left[D(C)\frac{\partial C}{\partial x}\right]=\frac{dD}{dC}\left(\frac{\partial C}{\partial x}\right)^2+D\frac{\partial^2 C}{\partial x^2} \tag{4.4.1.1}$$

The only difference in applying this formula in stage I and II, is the assumption of constant diffusivity at stage I, while diffusivity can be variable at stage II drying. The assumption is based on Garrabrants and Kosson's experimental observations [105] which support relatively constant moisture diffusivity in the early stage of drying, followed by variable moisture diffusivity at later stages of drying. While the first term in the right hand side of equation (4.4.1.1) is zero in the stage I drying, it is non-zero at stage II [141], although it looks very small considering higher order terms. For simplification, dD/dC can be assumed to be zero during stage II as well. However, since

$$\frac{\partial D}{\partial t}=\frac{dD}{dC}\frac{\partial C}{\partial t} \tag{4.4.1.2}$$

the assumption would lead to $\frac{\partial D}{\partial t}=0$, which contradicts the experimental observations. To take care of this problem, the time of drying was divided into several time steps at stage II and constant diffusivity was applied at each time step with respect to the time and the location. Therefore, the time-varying diffusivity values at stage II are only averaged over the space. This can be acceptable considering high evaporative surface-to-depth ratio of the samples. Consequently, equation (4.4.1.1) can be simplified to equation (4.4.1.3) for stage I as well as each time step for stage II.

$$\frac{\partial C}{\partial t} = D\frac{\partial^2 C}{\partial x^2} \tag{4.4.1.3}$$

Hydration of cement and its implications on transport properties need to be taken into account during early-age drying of cementitious materials. With time, liquid water will be chemically bounded into hydration products as well as physically bound water to increasing internal solid surfaces. Both chemically and physically bound water may be assumed to be in local equilibrium with free water due to rapid rate of hydration at the early age. To simplify the concept, the concentration of bound water, *S*, is directly taken proportional to the concentration of the free water, *C*, the substance free to diffuse.

$$S = RC \tag{4.4.1.4}$$

During early-age drying when the moisture diffusion is accompanied by immobilization of bound water, equation (4.4.1.3) is modified as:

$$\frac{\partial C}{\partial t} = D\frac{\partial^2 C}{\partial x^2} - \frac{\partial S}{\partial t} \tag{4.4.1.5}$$

Equation (4.4.1.5) can be presented in a new form by substituting for *S* from equation (4.4.1.4).

$$\frac{\partial C}{\partial t} = \frac{D}{1+R}\frac{\partial^2 C}{\partial x^2} = D'\frac{\partial^2 C}{\partial x^2} \tag{4.4.1.6}$$

Replacing the term *D/(1+R)* with *D'* as the effective moisture diffusion coefficient, the equation is seen in the usual form of diffusion equations.

Therefore, *D'* presents the potential for conductivity of free water through the fresh cementitious materials.

The cement paste is assumed to be homogeneous at initial conditions with an impermeable bottom surface. Therefore, the initial and boundary conditions are

$$t=0, \quad C=C_i \qquad 0 \leq x \leq L \tag{4.4.1.7}$$

$$J=-D'\frac{\partial C}{\partial x}=0 \qquad \text{at } x=0 \tag{4.4.1.8}$$

where C_i is the initial moisture concentration (kg/m^3), and J is the moisture flux (kg/m^2).

Moisture transport during stage I drying is considered as an external mass transfer control process with a constant drying rate. Thus, the boundary condition at the top surface is

$$J=F_0 \qquad \text{at } x=L \tag{4.4.1.9}$$

where, F_0 is the constant flux in stage I drying (kg/m^{2}s). Solution to moisture concentration values as a function of time and location during stage I drying based on equation (4.4.1.6-4.4.1.9) is [109]

$$C\left(t,x\right)=C_i+\frac{F_0\,L}{D'}\left\{\frac{D't}{L^2}+\frac{3x^2-L^2}{6L^2}-\frac{2}{\pi^2}\sum_{n=1}^{\infty}\frac{(-1)^n}{n^2}\exp\left(\frac{-D'n^2\pi^2t}{L^2}\right)\cos\frac{n\pi x}{L}\right\} \tag{4.4.1.10}$$

In this model transition time from stage I to stage II, referring to the loss of continuity in the liquid phase, is defined by the user which may be obtained from experimental data. Prediction of the transition time based on physical grounds requires further studies. For modeling stage II drying based on the concept of convective-diffusive transfer of vapor at the surface, the exchanged flux of moisture, J, can be characterized by the convection equation [109, 152].

$$J = -D'\frac{\partial C}{\partial x} = k\,(C_s - C_*) \qquad (4.4.1.11)$$

where k (m/h) is convective moisture transfer coefficient or surface factor, C_s is the surface moisture concentration and C_* is the ambient moisture concentration (kg/m^3). k parameter takes into account the wind velocity, the surface temperature, and the relative humidity for drying to the atmosphere or in the case of low-pressure drying encompasses vacuum condition and temperature. The analytical solution for equations (4.4.1.6-4.4.1.9) during each time step at stage II drying with the convective boundary condition as of equation (4.4.1.11) is given by [153]

$$C(t,x) = C_* + \left(C_i - C_*\right) + \sum_{n=1}^{\infty} \frac{2\sin(\lambda_n)}{\lambda_n + \sin(\lambda_n)\cos(\lambda_n)} \cos(\lambda_n \frac{x}{L})\, e^{\left(-\lambda_n^2 \frac{D't}{L^2}\right)} \qquad (4.4.1.12)$$

Where,

$$\lambda_n \tan(\lambda_n) = \frac{kL}{D'} \qquad (4.4.1.13)$$

Geometry, governing equations and boundary conditions during stages I and II drying are presented in Figure (4.3.2.2).

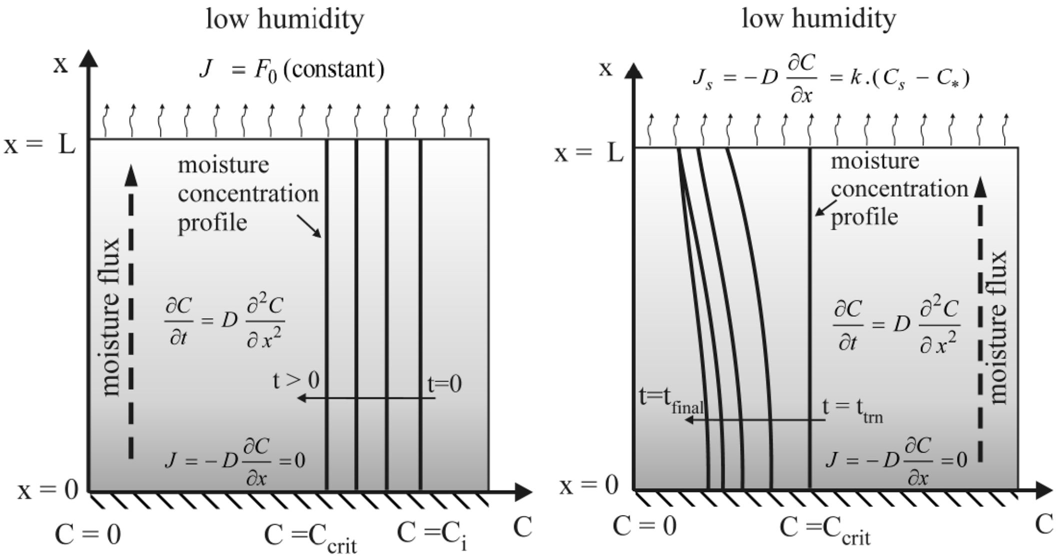

Figure 4.3.2.2a **Figure 4.3.2.2b**

Figure 4.3.2.2. Geometry, governing equations and boundary conditions during: (a) stage I drying, (b) stage II drying assuming convective moisture flow on the top surface

4.4.2. Simulation and Parametric Studies

Modeling of the drying process is presented based on dual-stage moisture movement through the porous media and imposing a constant flux and convective boundary conditions at stage I and II, respectively. Model simulates the evaporation process using equation (4.4.1.10) as the solution for stage I drying, and equation (4.4.1.12) as the solution for each time step at stage II drying. In the code, an extra function is developed to find sufficient number of solutions of λ_n in equation (4.4.1.13) and return them to the main code. The code calculates moisture concentration profile over the volume. The difference between integration of moisture concentration and initial total moisture yields the cumulative moisture loss, a variable that is measured during a drying test. The code calculates flux at the surface according to equation (4.4.1.11).

Parametric studies are performed to verify capability of the model in capturing effects of major moisture transport parameters, including effective diffusivity, *D'*, and surface factor, *k*. Parametric studies also include effects of initial external rate of evaporation, F_0, transition time, t_{trans}, and sample thickness, *L*, on the cumulative moisture loss and evaporation rates. Throughout the parametric study, a cement paste with w/c ratio of 0.45 is considered as the drying material. A drying surface area of 100 mm x 100 mm and thickness of 10 mm are used as the size of specimen, except for study of the depth in which the thickness is variable.

As expected, at stage I drying, diffusivity does not control cumulative moisture loss and evaporation rates due to the imposed boundary condition at this stage, but it controls moisture concentration profiles. Effect of diffusivity at stage I, D'_I, on moisture concentration profiles are studied at 1 h intervals with three orders of magnitude in diffusion coefficients of $5\text{x}10^{-9}$, $5\text{x}10^{-8}$ and $5\text{x}10^{-7}$ m^2/s as shown in Figure 4.4.2.1, assuming an initial evaporation rate of 0.4 $kg/(m^2.h)$ and a transition time of 10 h. As shown in Figure 4.4.2.1a and 4.4.2.1b, moisture concentrations reach negative values or large moisture concentration gradients show up imposing 0.4 $kg/(m^2.h)$ as the initial evaporation rate. It can be concluded that assumed diffusivities are too low to balance the flux on the top surface. Although in gravimetrical methods, moisture concentration profiles are not obtained, but funicular flow, the natural internal moisture flow in stage I, leads to values of initial diffusivity of the order of 5x10^{-7} m^2/s which satisfy the flux with small values of internal moisture concentration gradients. In Figure 4.4.2.2a effect of diffusivity at stage II drying, D'_{II}, on cumulative moisture loss and evaporation rates is studied with five different diffusivity values increasing from 5x10^{-10} m^2/s to 5x10^{-8} m^2/s, assuming D'_I as 5x10^{-7} m^2/s, k as 0.001 m/h, F_0 as 0.4 kg/(m^2.h) and t_{trans} as 5 h. These results reflect increases in the cumulative moisture loss from 44 g to 63 g translating into a 28% increase in total moisture loss after 40 h of drying, and also significant increase in evaporation rates after 10 h of drying as shown in Figure 4.4.2.2a. The results of simulation are in agreement with the concept of diffusivity which is moisture transport conductivity through capillary medium under driving force of a concentration gradient. As shown in the figure, an increase in moisture diffusivity translates into higher evaporation rate and higher cumulative moisture loss at stage II drying.

Effect of convective moisture transfer coefficient, k, is studied with increasing this parameter from 0.0005 m/h to 0.002 m/h assuming D'_I as 5x10^{-7} m^2/s, D'_{II} as 1.5x10^{-8} m^2/s, F_0 as 0.5 kg/(m^2.h) and t_{trans} as 5 h. As shown in Figure 4.4.2.2b, an increase in cumulative moisture loss from 55 g to 64 g, equivalent to an increase by 13% in total moisture loss, is simulated after 40 h of drying. A significant increase in evaporation rates at early hours of stage II drying is also simulated by increasing this parameter. A much smoother fall in evaporation rates are observed at the beginning of stage II drying by assuming

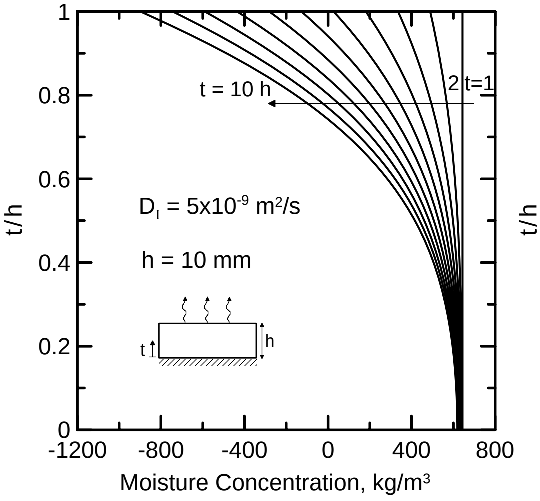

Figure 4.4.2.1a

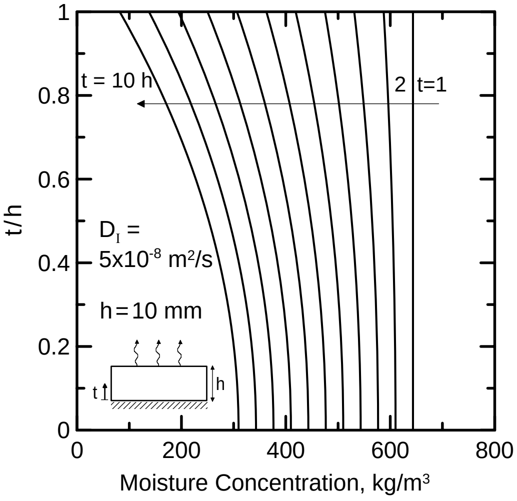

Figure 4.4.2.1b

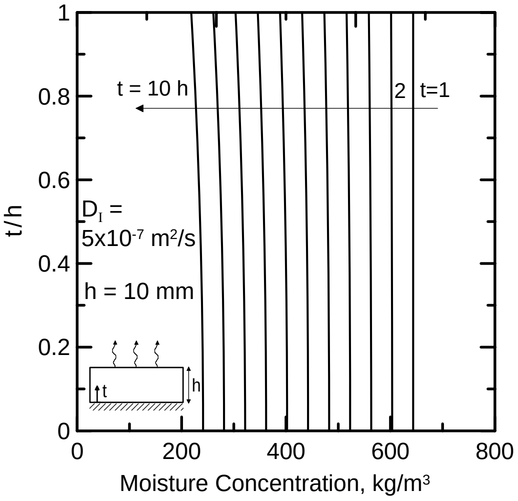

Figure 4.4.2.1c

Figure 4.4.2.1. Parametric study on the effect of moisture diffusivity at stage I on profiles of moisture concentration drawn at 1 h intervals during drying of cement paste samples

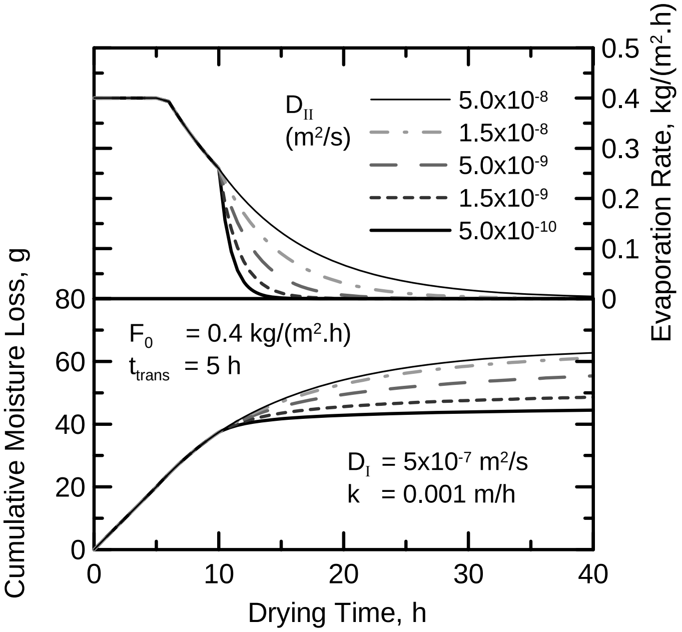

Figure 4.4.2.2a

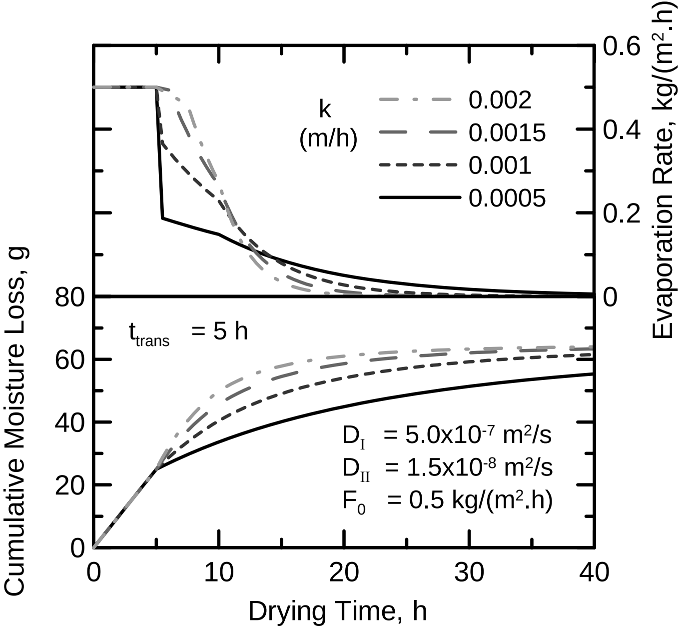

Figure 4.4.2.2b

Figure 4.4.2.2. Parametric study of moisture diffusivity at stage II drying and convective moisture transfer coefficient on cumulative moisture loss and evaporation rates of cement paste samples

higher values of k such as 0.002 m/h, while low k values such as 0.0005 m/h results in a marked drop in evaporation rates at the beginning of stage II.

Figure 4.4.2.3a and Figure 4.4.2.3b show parametric studies on initial external evaporation rate, F_0, and time of transition from stage I to stage II, t_{trans}, respectively. In both simulations, D'_I, D'_{II}, and k are given as 5x10^{-7} m^2/s, 1.5x10^{-8} m^2/s, and 0.001 m/h, respectively. As expected, increasing F_0 from 0.3 to 0.5 kg/(m^2.h) reflects in higher cumulative moisture loss and evaporation rates at early hours of drying, but has minimal effects on cumulative moisture loss after 24 h. However, at stage II drying, lower evaporation rates along with a large fall from initial values are simulated by increasing F_0, which is due to lower surface moisture concentration.

Effect of transition time is studied by five different values from 6 to 14 h. As shown in Figure 4.4.2.3b, higher values result in longer period of stage I and more significant fall in evaporation rate between stage I and II, which is expected due to lower surface moisture concentrations.

The specimen thickness is the last parameter studied by increasing from 5 to 25 mm in five intervals, assuming D'_I, D'_{II}, k, F_0 and t_{trans} are given as 5x10^{-7} m^2/s, 1.5x10^{-8} m^2/s, 0.001 m/h, 0.5 kg/(m^2.h) and 5 h, respectively. As shown in Figure 4.4.2.4, cumulative moisture loss after 40 h drying increases from 32 to 92 g and also evaporation rates at the beginning of stage II drying increase by increasing sample thickness, make drying stage transition smoother.

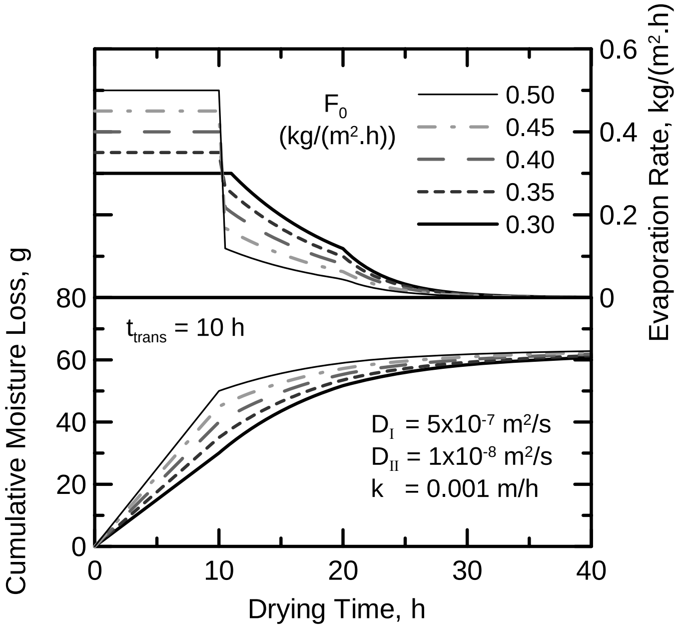

Figure 4.4.2.3a

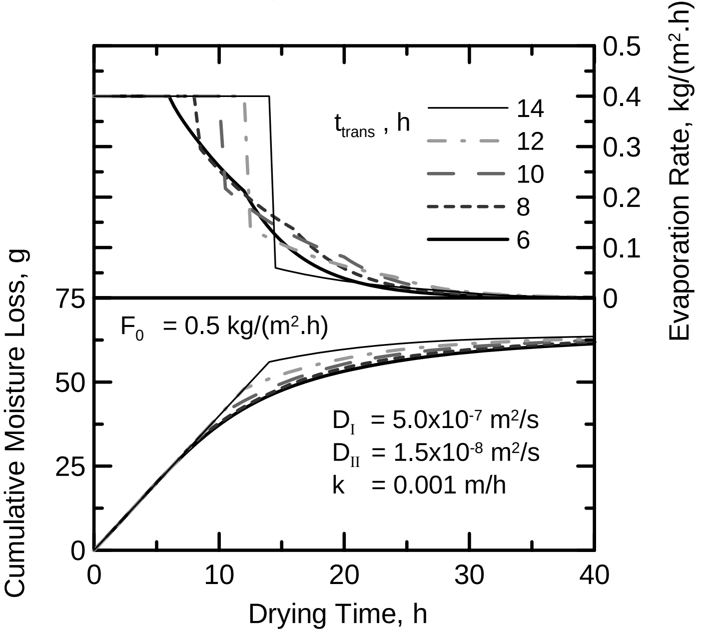

Figure 4.4.2.3b

Figure 4.4.2.3. Parametric study on the effect of initial evaporation rate, F0, and transition time, t_{trans}, on cumulative moisture loss and evaporation rates during drying of cement paste samples

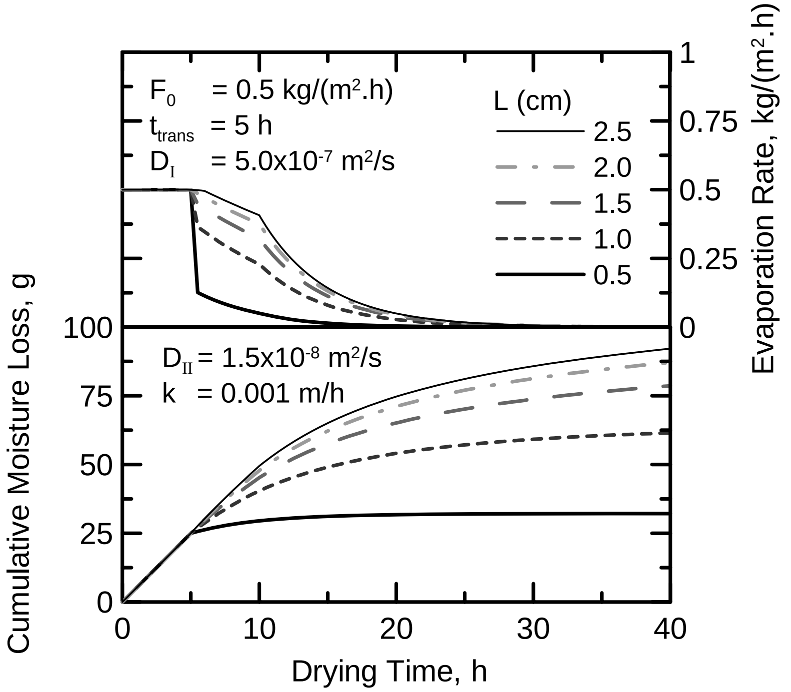

Figure 4.4.2.4. Parametric study on the effect of moisture transfer coefficient, *k*, on cumulative moisture loss and evaporation rates during drying of cement pastes

4.4.3. Back-Calculation Procedures for Modeling of Stage II Drying

A back calculation model is used to predict diffusivity and moisture transfer coefficient at any time step based on given cumulative moisture loss and evaporation rate curves. Optimization is implemented to find two best fit parameters, $D'(t)$ and $k(t)$ to predict the experimental results. The objective function for minimization is the weighted sum of two errors of cumulative moisture loss and flux. In optimization algorithm, normalized design variables (D' and k) are used to avoid numerical problems caused by mixing big and small numbers in numerical operations. Thus, diffusion coefficient at the current time step is normalized with its value at previous time step, $D_{norm}=D'_i/D'_{i-1}$, so does the mass transfer coefficient $k_{norm}= k_i/k_{i-1}$. Once the optimal solution D_{norm} and

k_{norm} are found, they are reverted back to *D'* and *k*. Inequality constraints are imposed to the design variables *D'* and *k* in terms of lower and upper bounds. Initial values for *D'* are obtained from analysis of stage I drying, while initial values for *k* are estimated from equation (4.4.3.1) which is derived by rearranging equation (4.4.1.11).

$$k^{(est)} = \frac{J^{(\exp)}(t = t_{trans})}{C_{crit} - C_*} \tag{4.4.3.1}$$

where, $k^{(est)}$ is the estimated surface factor (m/h) and $J^{(\exp)}(t = t_{trans})$ is the experimental rate of evaporation at the transition time which is roughly equal to initial evaporation rate. C_{crit} is the surface moisture concentration at end of stage I or critical moisture concentration (kg/m^3) and C_* is the ambient moisture concentration. For other time steps, initial *D'* values for optimization process, $D^{(est)}$ are estimated by the assumption of proportional decrease of diffusivity with the flux, while initial *k* values, $k^{(est)}$ are estimated by a convection transport formula.

$$D^{(est)} = D_{i-1} \frac{J^{(\exp)}(t^{(i)})}{J^{(\exp)}(t^{(i-1)})} \tag{4.4.3.3}$$

$$k^{(est)} = \frac{J^{(\exp)}(t^{(i)})}{C(t^{(i-1)}, x = L) - C_*} \tag{4.4.3.3}$$

In equation (4.4.3.1) and equation (4.4.3.3), $t^{(i)}$ is the current time step, while $t^{(i-1)}$ is the previous time step. At each time step, these two initially estimated parameters, $D^{(est)}$ and $k^{(est)}$ are passed to the optimizer and the optimizer calls the function evaluation to calculate the error and update these two parameters several times until optimal solution for *D'* and *k* are found. Results are discussed in the following section and shown in Figures 4.4.3.1a and 4.4.3.1b.

4.5. Comparison with Experimental Data and Finite Element (FE) Analysis

An experimental procedure for drying under low-pressure conditions was developed by authors that is capable of characterizing evaporation parameters using measurement of mass change during drying process [148]. Experimental data including cumulative moisture loss and evaporation rates of a drying Portland cement paste with w/c ratio of 0.45 are used in the back-calculation procedures. Results of prediction of experimental data and the best solutions for *D'* and *k* parameters are shown in Figure 4.4.3.1a and 4.4.3.1b. The model fits cumulative moisture loss and evaporation rates accurately throughout the drying period, while diffusion and moisture transfer coefficients are constant through the initial stage of drying and variable during stage II. As shown in Figure 4.4.3.1b, diffusivity fell almost at the beginning of stage II drying, but the moisture transfer coefficient remains constant even in the first 7 h of stage II before it gradually reduced from 0.0017 m/h to 0.0011 m/h. The reduction of moisture diffusivity at stage II drying is much more significant when this parameter reduced from initial value of $5.15\text{x}10^{-7}$ m^2/s to $1.18\text{x}10^{-8}$ m^2/s. This is in agreement with the literature where diffusivity after being relatively constant during early stages of drying, falls by decreasing moisture content below mid-range saturation [105].

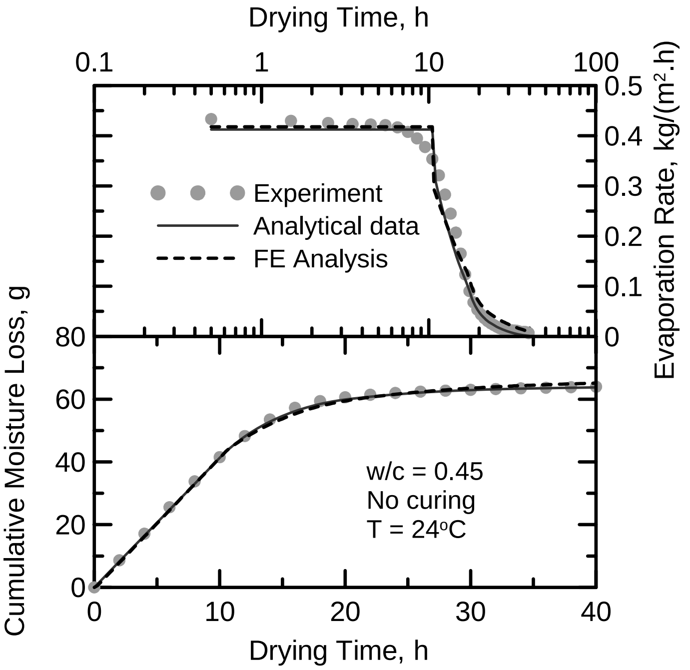

Figure 4.4.3.1a

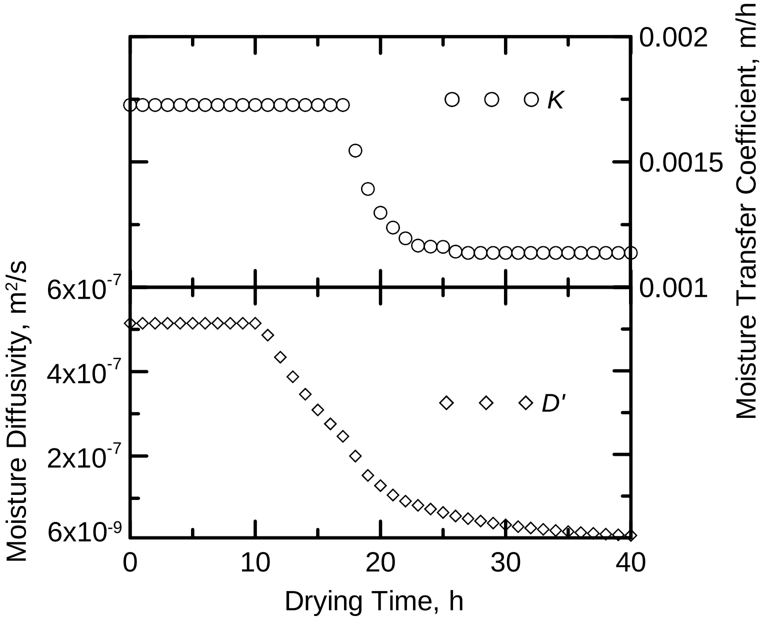

Figure 4.4.3.1b

Figure 4.4.3.1. (a) Prediction of cumulative moisture loss and evaporation rate as a function of time for the experimental data of an evaporation test, (b) Back-calculated D and k for the best fit of data

From the physical point of view, time is not the natural parameter for characterization of moisture diffusivity, hence it was related to the average moisture concentration to obtain an intrinsic characterization. This relationship is presented in Figure 4.5.1 which can be fitted by a model similar to CEB-FIP [154]. While in CEB-FIP model, the moisture diffusivity is related to the relative humidity [56, 155], in this work the moisture diffusivity is modeled versus average normalized moisture concentration.

$$D(C_{norm}) = D_1\left(\alpha + \frac{1-\alpha}{1+\left(\frac{1-C_{norm}}{1-C_c}\right)^n}\right) \tag{4.5.1}$$

where, D_1 represents $D(C_{norm})$ when the samples is initially fully saturated and normalized moisture concentration is 1, D_0 is the minimum $D(C_{norm})$ and α is the parameter that represents the ratio D_0/D_1. In this equation, C_c is the normalized moisture concentration at $D(C_{norm}) = 0.5D_1$ characterizing the location of the drop in the curve $D(C_{norm})$. According to Bazant and Najjar [60], Baluch et al [156] and Kim and Lee [155], calculated moisture diffusivity for well-hydrated and cured concrete samples is within range of $3\text{x}10^{-10}$ to $5.4\text{x}10^{-8}$ m^2/s. Comparing the values with the results of this analysis which ranges from $1.86\text{x}10^{-8}$ to $5.15\text{x}10^{-7}$ m^2/s, it may be concluded that very early-age moisture diffusivity of a poorly-cured cement paste is more than tenfold of the moisture diffusivity of a cured concrete. However, the results are well within the range of the data recently reported by Vejmelková et al. [119] which range from $1.78\text{x}10^{-8}$ to $2.53\text{x}10^{-8}$ m^2/s

for non-cracked and 5.46x10^{-7} to 2.00x10^{-7} m^2/s for cracked cement paste samples. On the other hand, the moisture diffusivity ratio, α, was obtained as 0.036 which is in accordance with the results of Bazant and Najjar [60], who reported values in the range of 0.025 to 0.10 for different types of concrete.

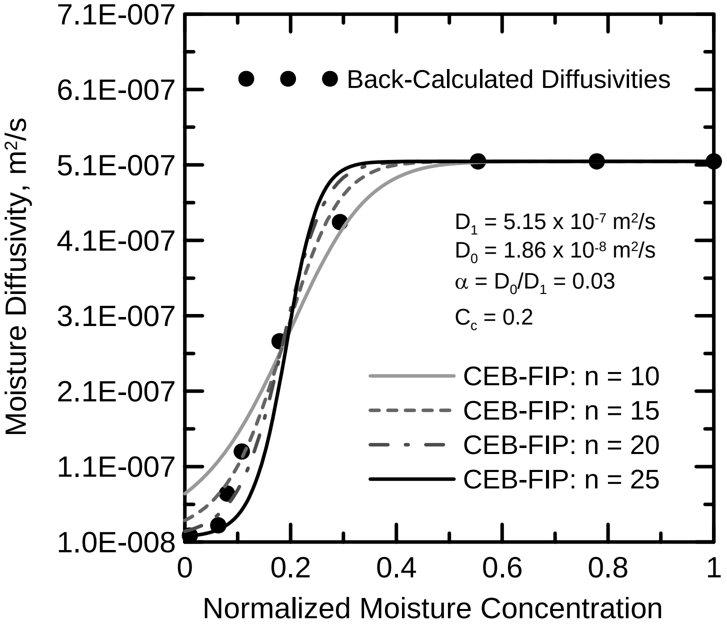

Figure 4.5.1. Back-calculated moisture diffusivity of an early-age non-cured cement paste as a function of normalized moisture concentration expressed by CEB-FIP models

As shown in Figure 4.5.1, among different values for variable *n*, *n = 15* gives the best fit to the calculated diffusivity results. On the other hand, the calculated values of parameter *k*, the convective moisture transfer coefficient, are within the range of the data reported in the literature [156, 157] varying from 0.0003 to 0.003 m/h.

A Finite Element (FE) analysis was carried out using ABAQUS v.6.10-1 [70] to verify the results of proposed analytical method including the flux at the top surface and the integration of the surface flux or cumulative moisture loss. The technique utilizes the analogy between the heat transfer and the moisture diffusion. In equivalent transient thermal problem in 2-D space, the corresponding equations are

$$\frac{\partial T}{\partial t}=\left(\frac{k}{\rho c}\right)\left[\frac{\partial^2 T}{\partial x^2}+\frac{\partial^2 T}{\partial y^2}\right] \tag{4.5.2}$$

$$\frac{\partial T}{\partial n}=h_{fT}\,(T_*-T_s) \tag{4.5.3}$$

whrere, $T(x,y,t)$ is the temperature varying in the domain with the time. k is the isotropic thermal conductivity which may be a function of T, and ρ and c are the density and the specific heat, respectively. $\frac{\partial T}{\partial n}$ is the thermal gradient with a unit normal "n", h_{fT} is the convective transfer coefficient for thermal problem, T_s is the temperature at the boundary, and T_* is the ambient temperature. While equation (4.5.3) is for the heat convection at the boundary, analogous to moisture convection during stage II at the boundary, boundary conditions for stage I can be introduced as a constant heat flux. Comparing equations (4.5.2 and 4.5.3) with equations (4.4.1.6) and (4.4.1.11) leads to the conclusion of one-to-one analogy between these two boundary value problems where C, D, and k in the diffusion problem are corresponding to T, $k/\rho c$ and h_{fT} in the heat transfer problem. In this analysis, the boundary condition of stage I drying is defined as a load at surface with the magnitude of initial evaporation rate. The other boundary conditions which are impermeable surfaces on the sides and bottom of the sample are ignored, since no load corresponds to zero flux or impermeability. Also an interaction was created for the purpose of imposing a convective boundary condition during stage II drying. For the sake of comparison with the results of analytical method, the same number of layers (100 layers) is used along y-direction which is along the direction of external flux. Since there is no heat transfer corresponding to moisture transfer along the x-direction which is perpendicular to the direction of external flux, the domain is divided by only 20 layers. The type of analysis was an implicit heat transfer analysis, and since there was no interest on the edge effects, a uniform mesh with 4-node linear heat transfer quadrilateral elements (DC2D4) was used. Results of FE analysis for the flux at different drying times are shown in Figure 4.5.2. The comparison between results of the surface flux by FE analysis and the analytical and experimental results are shown in Figure 4.4.3.1a. Cumulative moisture loss can also be obtained as the product of the integration of the flux obtained from FE analysis and the surface area. As shown in Figure 4.4.3.1a, the FE results show a good agreement with analytical and experimental data.

In order to further confirm the soundness of this analytical method, the method can be applied to different sets of drying data with available experimental moisture profiles. The experimental data of Šelih et al. [66, 158, 159] were chosen for this purpose which involve one-dimensional drying of concrete cylinders under normal room pressure, temperature of 22^{o}C and relative humidity of 50%. Among different drying tests

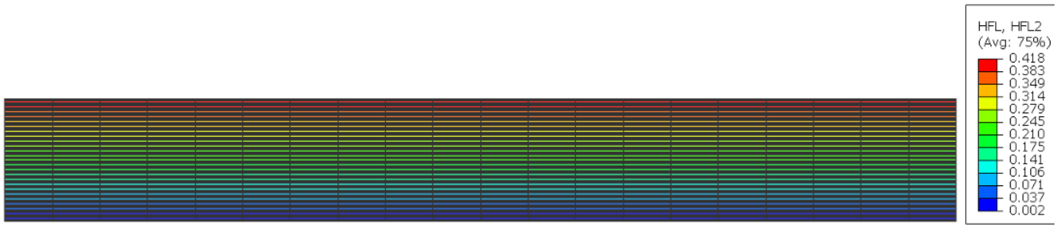

(a) t = 2 h

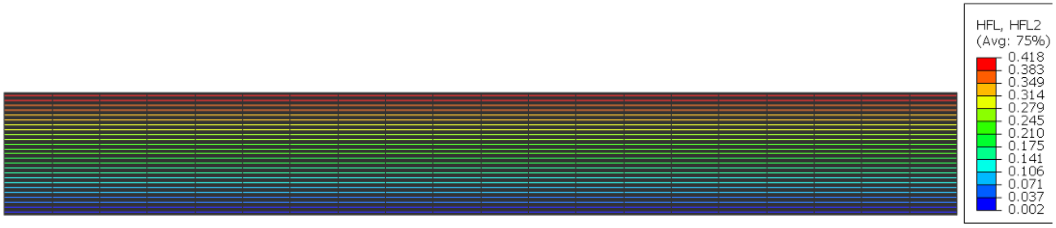

(b) t = 10 h

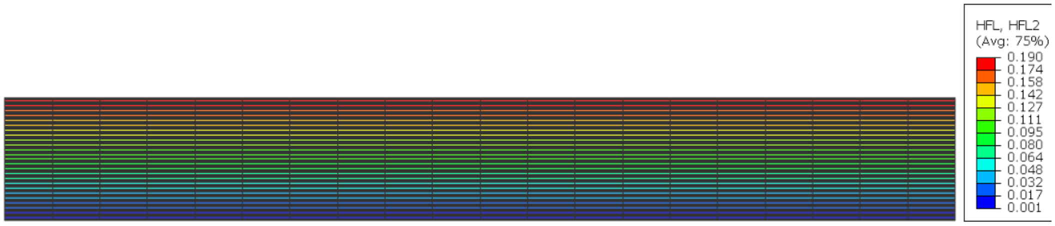

(c) t = 14 h

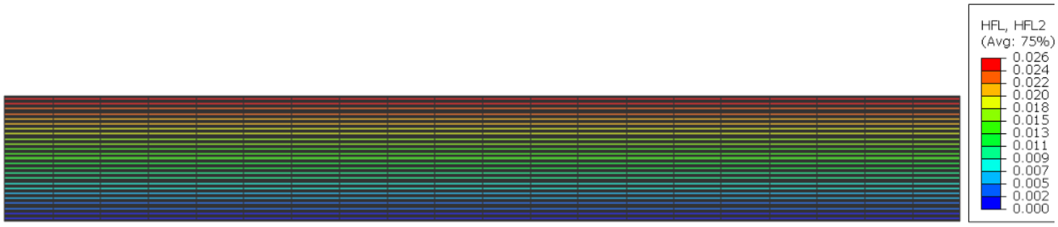

(d) t = 20 h

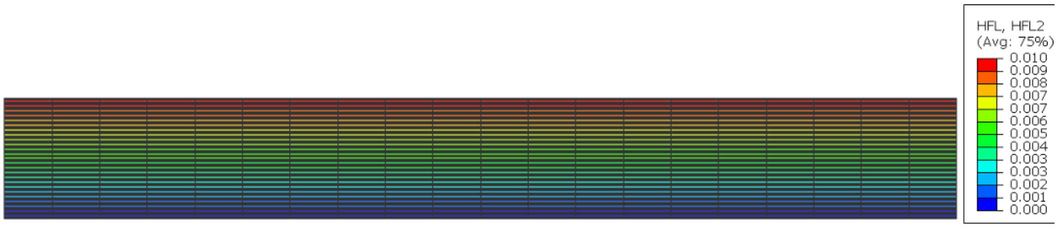

(e) t = 40 h

Figure 4.5.2. Distribution of moisture flux (kg/(m2h)) at: a) t = 2 h, b) t = 10 h, c) t = 14 h, d) t = 20 h, e) t = 40 h.

performed by Šelih et al., results of drying tests on non-cured normal aggregate concrete with w/c ratio of 0.40 was chosen [159] as a representative data set for drying of early-age cementitious materials. The amounts of Portland cement, water, coarse and fine aggregate in this mixture were 489.5, 195.8, 912.3 and 804.9 kg/m^3, respectively. The ambient moisture concentration, C_* , can be obtained from the desorption isotherm curves which relate relative humidity to the water content. Using the BSB model [110], C_* was obtained 49 kg/m^3. As shown in Figure 4.5.3a, the evaporation rates were computed from cumulative moisture loss data using a numerical differentiation procedure. The drying results were used to back-calculate diffusion and convective moisture transfer coefficients as shown in Figure 4.5.3b, and expressed as a function of average moisture concentration in accordance to the CEB-FIP model as shown in Figure 4.5.4a. The distribution of moisture concentration is compared with the experimental data as shown in Figure 4.5.4b, indicating a good agreement between the simulation and the experimental results.

4.6. Conclusion

Results of modeling moisture evaporation from the water surface and cement-based materials based on the physics of drying. Evaporation from free water surface is modeled implementing Prandtl’s interfacial boundary layer concept through which the water vapor molecules diffuse to the surrounding air due to gradient of moisture concentration. The model shows direct relationship of water evaporation rate to relative humidity, along with saturated vapor pressure,

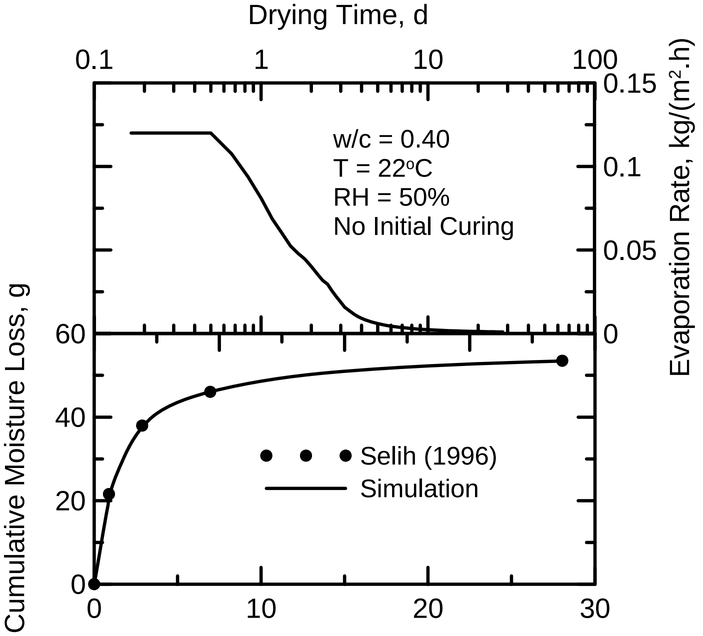

Figure 4.5.3a

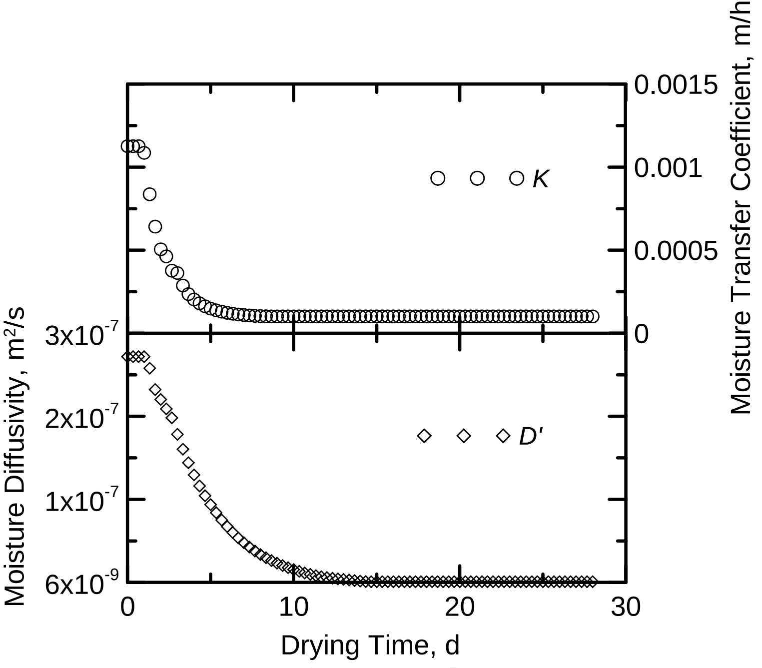

Figure 4.5.3b

Figure 4.5.3. (a) Prediction of cumulative moisture loss and evaporation rate as a function of time for the experiment performed by Šelih (1996), (b) Back-calculated D' and k for the best fit of data

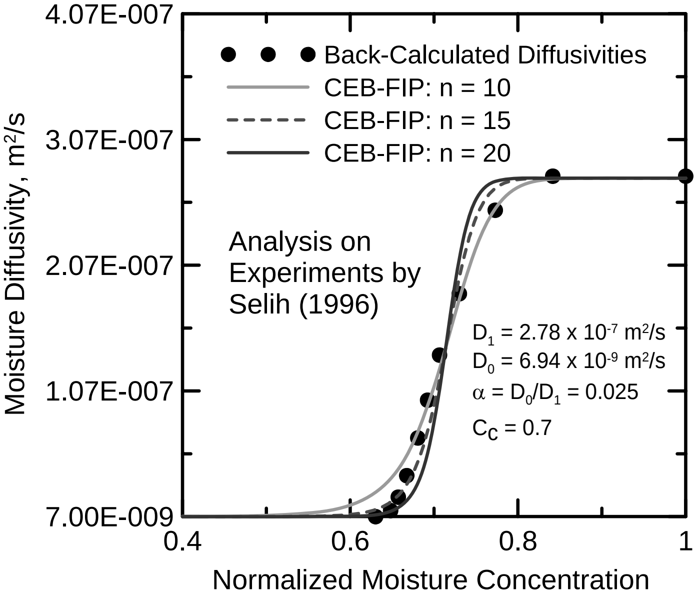

Figure 4.5.4a

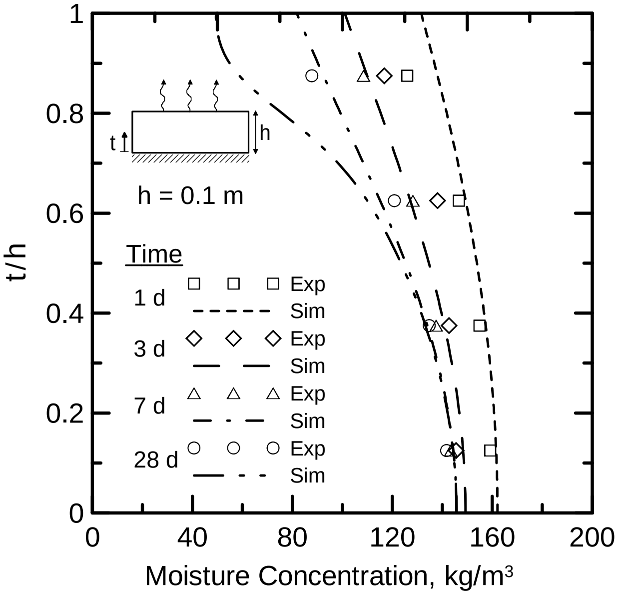

Figure 4.5.4b

Figure 4.5.4. Results of analysis on drying data by Šelih (1996): (a) Moisture diffusivity as a function of normalized moisture concentration expressed by CEB-FIP models, (b) moisture concentration distributions through the thickness of the sample in comparison with experimental results

and boundary layer thickness, which are functions of temperature and wind velocity themselves. Water evaporation is used as a boundary condition for the initial stages of drying. The moisture movement inside is modeled based on moisture transfer theories of capillary porous media. The initial constant drying rate period (stage I) is modeled as a funicular liquid water transport stage and falling drying rate period (stage II) as a vapor diffusion transport stage. While Fick's second law of diffusion is used for modeling moisture movement in both stages, it can be concluded that the moisture diffusivity indicates liquid water conductivity at stage I, rather than vapor diffusion at stage II. Physics of drying allows applying a constant flux boundary condition and a convective boundary condition at stage I and II, respectively. Results of applying the methodology to the drying experiments of cement-based materials under low and normal room pressure shows that calculated moisture diffusivities reduce drastically from stage I to stage II. The agreement between the results of the proposed analytical method and an FE analysis and also experimental profiles of moisture distribution verifies the soundness of this analytical method. Results of the analysis show that proposed analytical method is capable of predicting experimental data during drying process of cement-based materials and presenting the variation of introduced internal and surface moisture transfer parameters by the time.

5. Modeling Rate of Evaporation Potential during Early Stage of Drying

5.1. Introduction

Early-age cracking is a threat to structural integrity of concrete structures and if not inhibited would lead to service life reduction and unsightliness. High rates of evaporation which depends on air and concrete temperature, wind speed and relative humidity increase the risk of early age cracking [11]. Due to evaporation, water menisci are formed in the interparticle spaces [12] and a negative pressure in the capillary water is built up [13, 14] and continues to rise as the evaporation proceeds. The developed capillary pressure in drying fresh concrete reaching 50 kPa in few hours [10, 12, 15] and exceeding 1MPa in less than 8 h [16, 17] acts on the solid particles and results in the contraction of the still plastic material [18] ranging from strain levels of 1 to $3x10^{-3}$ [12, 14, 19]. If concrete is restrained, the developed shrinkage strain may easily exceed low tensile strength of the fresh concrete [21] and cracking occurs (see Figure 5.1.1).

The initial rate of evaporation is very significant from the capillary pressure point of view as comparably small changes in the evaporation rate noticeably influence the capillary pressure versus time curve [12]. The differences in crack tendency are most likely a consequence of the initial rate of evaporation [15]. As shown in Figure 5.1.2, results of drying experiments on fresh cement-based materials reveals that the initial evaporation rate remains roughly constant during a period, before beginning of a succeeding falling rate period [19, 66, 148, 149]. Visible plastic cracks are observed few hours after placing, a time period well within the initial stage of drying [148].

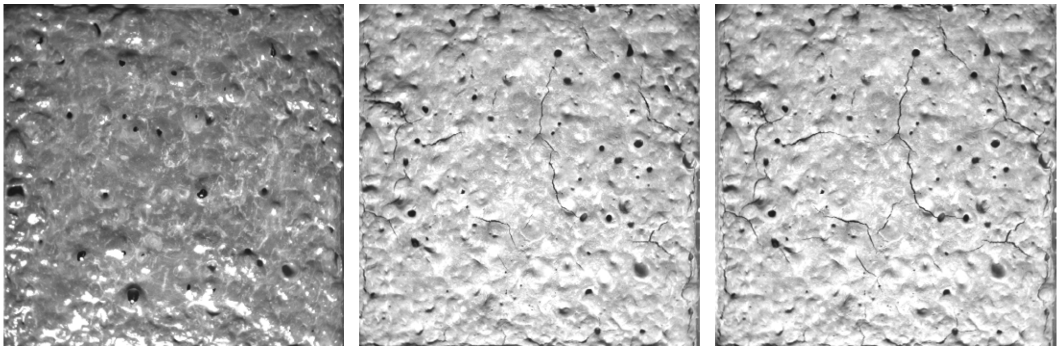

Drying time: 15 min, 3h, 3h 15min

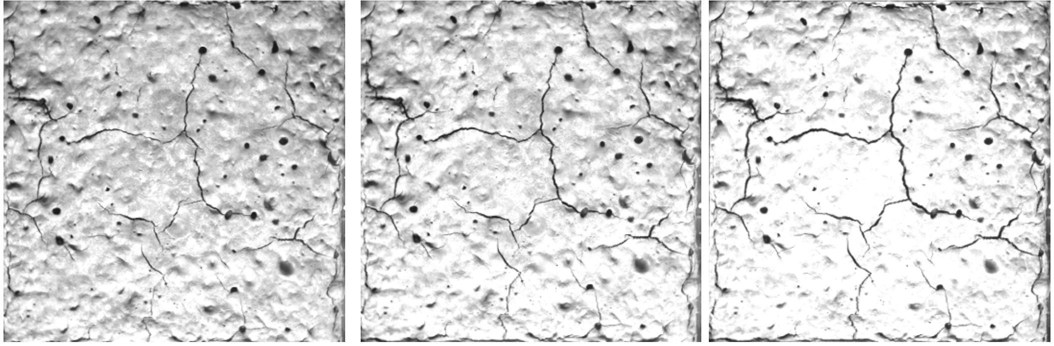

Drying time: 3h 30min, 4h, 24h

Figure 5.1.1. Development of 2-D plastic shrinkage cracks during drying of a fresh plain cement paste

It was found that the initial rate of evaporation from concrete surface is the same as rate of evaporation from water surface exposed to the same condition [8, 10, 148]. Moisture transport during initial stage of drying when concrete is still plastic is controlled by the external evaporation potential. Therefore, the rate of water evaporation is required for modeling the moisture transport at this initial stage [148, 160] which can be found by either experiments [161] or using a mass transfer approach.

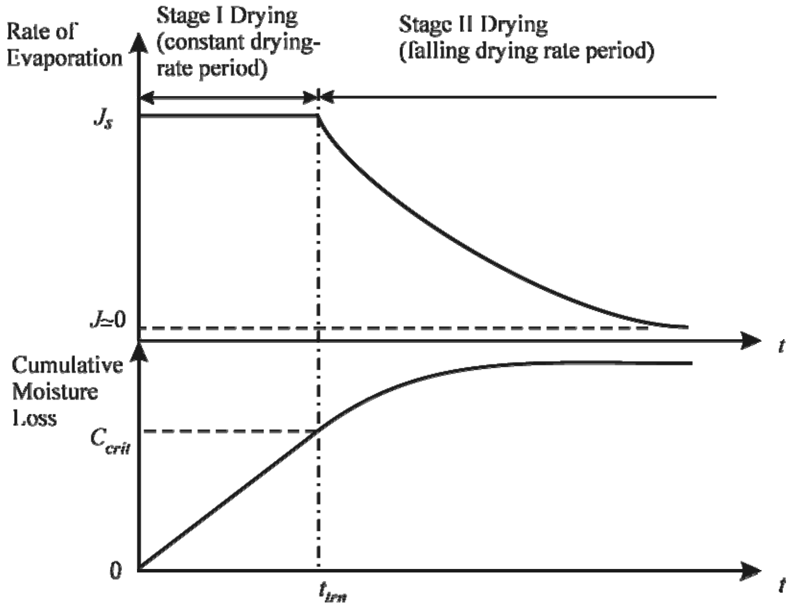

Figure 5.1.2. Two stages of drying during evaporation of capillary porous materials

In the absence of a theoretical method to estimate initial rate of evaporation from cement-based materials, a nomograph based on an empirical equation is used [68] which was calibrated by the data from Lake Hefner. In this paper theory of water evaporation based on the boundary layer theory, mass transfer, diffusion, and fluid mechanics is described. A driving force of concentration gradient is introduced as the main cause of mass transfer during the drying process. Mass transfer at low and high rates is discussed separately along with other related parameters such as mass transfer coefficient. An algorithm for determination of evaporation rate is suggested. Considering similarity between rate of evaporation from water surface and concrete surface during initial stage of drying, predicted evaporation rates are verified by the recent experimental data from concrete surfaces.

5.2. Available Method to Estimate Initial Rate of Evaporation

From the mechanical point of view, rate of evaporation can be related to plastic cracking only when there is a model to predict capillary pressure and pressure on solid skeleton due to moisture loss and the early-age tensile properties of the material is available. In the absence of such a model, available standards and specifications such as ACI 305.1 [68], USACE TM 5-822 [162], Canadian CSA Standard A23.1 [163] and Australian Technical Bulletin 95/1 [164] set requirements on evaporation rates below 1, 0.75, 0.75 and 0.5 kg/(m^2h), respectively to prevent plastic shrinkage cracking. As shown in Figure 5.2.1, the evaporation rate in the atmospheric pressure is commonly estimated using a nomograph in ACI 305 [68] given inputs for temperature, relative humidity, and wind velocity. According to Hover [165] the underlying relationship for Menzel's equation [166] which is the source of ACI nomograph is 200 years old Dalton's law [167].

$$E = 0.313(p_{sat} - p_v)\,(0.253+0.06V) \tag{5.2.1}$$

where E is the rate of evaporation [$kg.m^{-2}.h^{-1}$], p_{sat} is the saturated water vapor pressure [kPa] at the surface temperature of concrete T_c, p_v is the partial pressure of the water vapor in the air [kPa] and V is the wind velocity [$km.h^{-1}$].

Uno [69] used the relationship between temperature and saturation vapor pressure to replace saturation vapor pressure in Menzel's equation by the temperature.

$$p_{sat} = 0.61\exp(17.3\ T_c /(237.3+ T_c)) \tag{5.2.2}$$

where T_c is the temperature of the concrete surface [^oC].

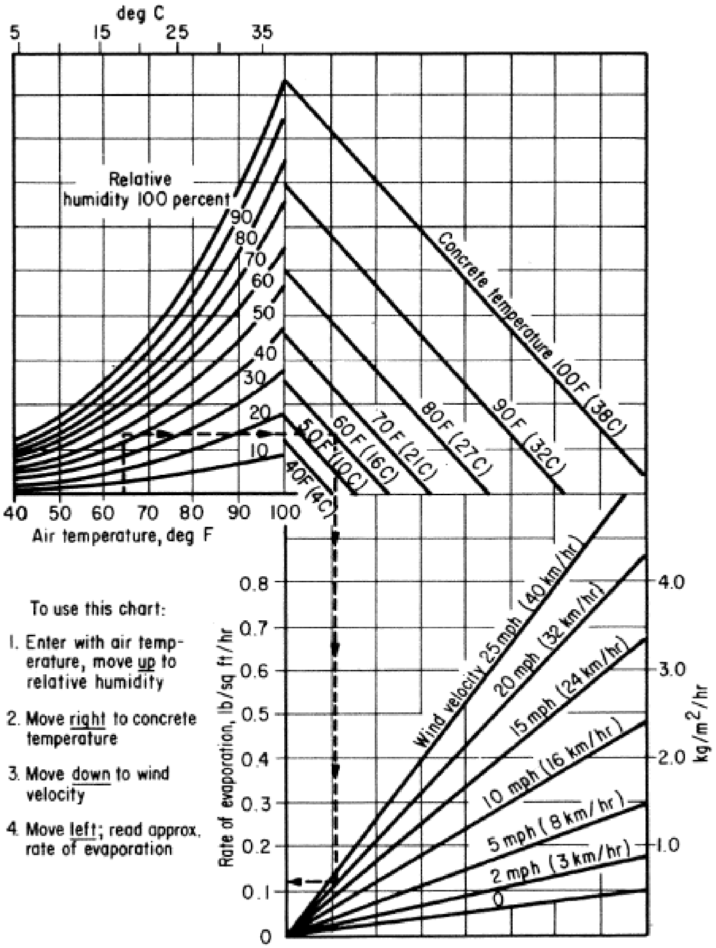

To use this chart:

1. Enter with air temperature, move up to relative humidity
2. Move right to concrete temperature
3. Move down to wind velocity
4. Move left; read approx. rate of evaporation

Figure 5.2.1. ACI nomograph for estimating rate of evaporation of surface moisture from concrete (ACI 305.1-06)

Using equation (5.2.1) and (5.2.2), Uno [69] developed a single equation which captures effect of temperature, relative humidity and wind velocity.

$$E = 5\left(\left[T_c+18\right]^{2.5} - \varphi.\left[T_a+18\right]^{2.5}\right)\left(V+4\right)\times 10^{-6} \tag{5.2.3}$$

where E is the rate of evaporation [kg.m^{-2}.h^{-1}], T_c is the (surface) temperature of concrete [^{o}C], T_a is the air temperature [^{o}C], φ is the relative humidity and V is the wind velocity [km.h^{-1}].

However, ACI 308R-01 [168] reported that the accuracy of the prediction is within ±25% for actual evaporation rates up to 1 kg/(m^{2}h) and consistently overestimates at higher evaporation rates by 50% or more. A Similar conclusion was reached by Al-Fadhala and Hover [169] who found that the nomograph is accurate for evaporation rates up to 0.5 kg/(m^{2}h). This inaccuracy can be due to the source of evaporation data used for deriving Menzel's equation which is Lake Hefner in Oklahoma in 1950 to 1951 [165]. Different lakes such as Lake Meade, AZ., Fort Collins, CO., and Lake Kickapoo, TX. have different evaporation equations [170, 171, 172, 173] which may be due to wind speed gradient, cloudiness, sunlight intensity and water quality [165]. On the other hand, the rate of evaporation which is the diffusion of water vapor through the boundary layer covering the water surface is directly related to the characteristic length of the surface [122, 128]. Menzel's equation completely ignores this effect and therefore the predicted evaporation rate can be used only when evaporation surface is about the same size as of BPI (Bureau of Plant Industry) evaporation pan, i.e. 6' in diameter and 2' deep [170].

5.3. Evaporation as a Mass Transfer Problem

Mass transfer is mass in transit as the result of a species concentration difference in a mixture. Evaporation is not a mass transport by bulk fluid motion, but rather a transport of one component, i.e. water vapor within a mixture of components, i.e. humid air that occurs as result of a concentration gradient. Humid air is a mixture of dry air containing a mixture of oxygen, nitrogen and other inert gases and the water vapor which is saturated very close to the water surface. Further from the surface, the humid air has lower water vapor concentration and the non-uniformity of water vapor concentration near the surface causes a mass transfer due to the effect of diffusion. The total rate of mass transfer of component *i* (i.e. water vapor) is:

$$\dot{m}_i'' = \rho_{i,s}\, v_{i,s} \tag{5.3.1}$$

where $\dot{m}_i''$ [kg.m^{-2}.s^{-1}] is the total mass flux, $\rho_{i,s}$ is the density of the component *i* at the interface [kg.m^{3}], and $v_{i,s}$ is the velocity component *i* at the interface [m.s^{-1}]. Mass flux due to diffusion, $J_{i,s}$ [kg.m^{-2}.s^{-1}] is related to the variation in the distance between molecules of the component *i* due to change in concentration of the component with time and can be expressed as:

$$J_{i,s} = \rho_{i,s}\,(v_{i,s} - v_s) \tag{5.3.2}$$

where v_s is the mass average velocity of all components [m.s^{-1}]. Combining equation (5.3.1) and equation (5.3.2) leads to a general equation for the total mass flux as:

$$\dot{m}_i'' = \rho_{i,s}\,(v_{i,s} - v_s) + \rho_{i,s}\, v_s = \underbrace{J_{i,s}}_{\text{diffusion}} + \underbrace{\rho_{i,s}\, v_s}_{\text{convection}} \tag{5.3.3}$$

The first term on the right-hand side of equation (5.3.3), $J_{i,s}$ is the mass diffusional flux at the interface and the second term represents the transfer of component *i* by the accompanying flow due to diffusional flux at the interface, which is called the convective mass flux. Considering these two terms, the mass transfer due to the evaporation can be studied separately in regard to the flow rate.

5.3.1. Mass Transfer at Low Rates

All mass transfer processes including evaporation generate flow at the interface. Nonetheless, when the mass transfer rates are sufficiently low, the velocities caused by mass transfer are negligible. Thus, a stationary medium will remain at rest and a flowing fluid will have the same velocity field as if there were no mass transfer. More generally, when concentration of the diffusing component is low and diffusional mass flux is low enough that it does not affect the imposed velocity field, the total mass flux is principally carried only by diffusion as given in the following equation:

$$\dot{m}_i'' = \rho_{i,s}\,(v_{i,s} - v_s) = J_{i,s} \tag{5.3.1.1}$$

According to Fick's law of diffusion, diffusional flux can be represented by:

$$J_i = -D_i \frac{\partial c_i}{\partial y} \tag{5.3.1.2}$$

where, c_i is the concentration of component *i* [kg.m^{-3}], D_i is the diffusivity [m^{-2}.s^{-1}], J_i is the rate of diffusion of component *i* per unit area of the surface [kg.m^{-2}.s^{-1}], and *y* is the distance in the direction of diffusion [m].

Therefore in the low rate mass transfer condition, the mass flux is:

$$\dot{m}_i'' = J_{i,s} = -D_i \left. \frac{\partial c_i}{\partial y} \right|_{y=0} \tag{5.3.1.3}$$

Figure 5.3.1.1 shows a schematic representation of the concentration distribution near an interface for the case of evaporation from a flat plate.

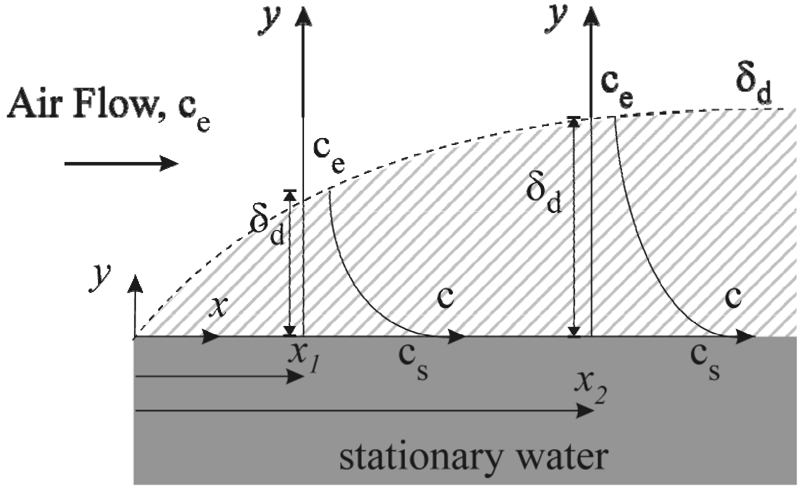

Figure 5.3.1.1. Schematic representation of the concentration distribution near an interface

Although the variation in the concentration near the interface is very sharp, it becomes more gradual in the region slightly above the interface and the concentration slowly approaches that in bulk fluid. The gradient of concentration near the interface is directly related to δ_d, the diffusion boundary layer thickness [m], which is also shown in Figure 5.3.1.1 for the case of evaporation due to laminar stream flow over a flat plate. This gradient can be written as:

$$\left. \frac{\partial c_i}{\partial y} \right|_{y=0} \approx \frac{(c_{i,e} - c_{i,s})}{\delta_d} \tag{5.3.1.4}$$

where, $c_{i,e}$ and $c_{i,s}$ are the concentration of component i at the air stream and interface [kg.m^{-3}], respectively. This equation is not exact because the gradient is not constant throughout the boundary layer. However, it does correctly reflect the fact that the concentration of component i (i.e. water vapor) will change from $c_{i,s}$ to $c_{i,e}$ in the region between the surface of the plate and the edge of the diffusion boundary layer. Therefore, using equation (5.3.1.3) and equation (5.3.1.4), the rate of mass transfer can be taken to be proportional to the concentration difference between the interface and the bulk fluid.

$$J_i \approx D_i \frac{(c_{i,s} - c_{i,e})}{\delta_d} \tag{5.3.1.5}$$

In mass transfer problems, the diffusional mass flux from a surface, $J_{i,s}$, can be expressed as the product of a mass transfer coefficient and the concentration difference between the surface and the fluid bulk (air flow). Hence, the mass transfer coefficient for component i, $h_{m,i}$ [m.s^{-1}] can be defined as:

$$\dot{m}_i'' = J_i = h_{m,i}\,(c_{i,s} - c_{i,e}) \approx D_i \frac{(c_{i,s} - c_{i,e})}{\delta_d} \tag{5.3.1.6}$$

Rearranging this equation leads to:

$$h_{m,i} \approx \frac{D_i}{\delta_d} \tag{5.3.1.7}$$

To find the mass transfer coefficient for water vapor in the case of evaporation, we need to solve an "external forced convection mass transfer" problem. Conceptually, the free stream behaves much like a semi-infinite body that experiences a step-change in its surface vapor concentration at the instant that fluid encounters the leading edge of the plate. The disturbance associated with the change in the surface vapor concentration diffuses as a mass wave into the free stream. This diffusion process takes time and, for the external flow problem, the fluid motion transports the wave downstream from the leading edge. Therefore, as shown in Figure 5.3.1.1, at $x = x_2$, the mass wave has propagated further into the free stream than it had at $x = x_1$. The motion of mass diffusion wave can be characterized by a mass diffusion boundary layer thickness given approximately by

$$\delta_d \approx 2\sqrt{D_{vapor}\, t} \tag{5.3.1.8}$$

Where D_{vapor} is the diffusivity of the water vapor [$m^2.s^{-1}$], and t is the time relative to the disturbance at the surface [s]. The transport time for the mass diffusion is approximately related to the distance from the leading edge, x [m], and the free-stream velocity, u_∞ [$m.s^{-1}$], according to:

$$t \approx \frac{x}{u_\infty} \tag{5.3.1.9}$$

Combining equation (5.3.1.9) and equation (5.3.1.8) gives:

$$\delta_d \approx 2\sqrt{\frac{D_{vapor}\, x}{u_\infty}} \tag{5.3.1.10}$$

To use dimensionless quantities to reduce number of independent variables, equation (5.3.1.10) can be re-arranged as:

$$\frac{\delta_d}{x} \approx \frac{2}{x}\sqrt{\frac{D_{vapor}x}{u_\infty}} = 2\sqrt{\frac{D_{vapor}}{u_\infty x}} = 2\sqrt{\frac{D_{vapor}}{u_\infty x}\frac{\nu}{\nu}} = \frac{2}{\sqrt{\frac{u_\infty x}{\nu}\frac{\nu}{D_{vapor}}}} \tag{5.3.1.11}$$

where ν is the kinematic viscosity of the water vapor [$m^2.s^{-1}$]. Substituting the definition of kinematic viscosity into equation (5.3.1.11) leads to:

$$\frac{\delta_d}{x} \approx \frac{2}{\sqrt{\frac{u_\infty x\rho}{\mu}\frac{\nu}{D_{vapor}}}} \tag{5.3.1.12}$$

where μ is the dynamic viscosity [$kg.m^{-1}.s^{-1}$], and ρ is the density of water vapor [$kg.m^{-3}$].

Since Reynolds number is defined generally as $Re = \frac{u_{char} L_{char} \rho}{\mu}$, for the flow over a flat plate, the characteristic length is the distance from the leading edge, x [m], and the characteristic velocity is the free-stream velocity, u_∞ [$m.s^{-1}$]. Therefore, the Reynolds number for the flow over a flat plate is defined according to:

$$Re_x = \frac{u_\infty x \rho}{\mu} \tag{5.3.1.13}$$

Also the Schmidt number, *Sc*, which provides a measure of the relative ability of the fluid to transport momentum and mass of component, is defined as:

$$Sc = \frac{\nu}{D_{vapor}} \tag{5.3.1.14}$$

Inserting equation (5.3.1.13) and equation (5.3.1.14) into equation (5.3.1.12) leads to:

$$\frac{\delta_d}{x} \approx \frac{2}{\sqrt{Re_x Sc}} \tag{5.3.1.15}$$

Combining equation (5.3.1.7) and equation (5.3.1.15), an approximate equation is provided for the local mass transfer coefficient associated with the laminar flow over a flat plate as:

$$h_{m,vapor} \approx \frac{D_{vapor}}{\delta_d} = \frac{D_{vapor}}{2x}\sqrt{Re_x Sc} \tag{5.3.1.16}$$

The mass transfer is typically made dimensionless using the Sherwood number, *Sh*. The Sherwood number is defined in general according to:

$$Sh = \frac{h_{m,i}\, L_{char}}{D_{vapor}} \tag{5.3.1.17}$$

where L_{char} is the characteristic dimension of the problem [m]. For stream flow over a flat plate, the characteristic dimension is the distance from the leading edge, x [m]. Therefore, the Sherwood number for flow over a flat plate is defined according to:

$$Sh_x = \frac{h_{m,vapor}\, x}{D_{vapor}} \tag{5.3.1.18}$$

Substituting equation (5.3.1.16) which is derived from conceptual model of the mass diffusion boundary layer thickness, into equation (5.3.1.18) provides an approximate equation for the local Sherwood number associated with the laminar flow over a flat plate as:

$$Sh_x = \frac{h_{m,vapor}\, x}{D_{vapor}} \approx 0.5\sqrt{Re_x Sc} \qquad (5.3.1.19)$$

Although above equation is only an approximate solution for a laminar flow, the exact analytical solution of local Sherwood number for laminar and turbulent flows over a smooth isothermal flat plate which are correlated based on experimental data can be found elsewhere [132, 174, 175].

$$Sh_x = \frac{0.3387\, Re_x^{1/2}\, Sc^{1/3}}{\left[1+\left(\frac{0.0468}{Sc}\right)^{2/3}\right]^{1/4}} \qquad \text{for } Re_x < Re_{crit} \qquad (5.3.1.20)$$

$$Sh_x = 0.0296\, Re_x^{4/5}\, Sc^{1/3} \qquad \text{for } Re_x > Re_{crit} \qquad (5.3.1.21)$$

where Re_{crit} is the critical Reynolds number for flow passing a flat plate of water. The critical Reynolds number for the transition from laminar to turbulent flow varies with experimental conditions. The reported data [176, 177, 178, 179, 180] are in the range of 10^4-10^6. In this study, $5\text{x}10^5$ was used for critical Reynolds number.

The values of Sherwood numbers in equation (5.3.1.20) and equation (5.3.1.21) are local, while an average Sherwood number associated with average mass transfer coefficient is more useful to specify the boundary conditions. For a stream flow over a flat plate, the average mass transfer coefficient is given by:

$$\overline{h_{m,vapor}} = \frac{1}{L}\int_0^L h_{m,vapor}\, dx \qquad (5.3.1.22)$$

and average Sherwood number is defined as:

$$\overline{Sh}_L = \frac{\overline{h_{m,vapor}}\, L}{D_{vapor}} \tag{5.3.1.23}$$

Inserting equation (5.3.1.22) into equation (5.3.1.23) and using equation (5.3.1.18) leads to:

$$\overline{Sh}_L = \frac{\int_0^L h_{m,vapor}\, dx}{D_{vapor}} = \frac{\int_0^L \frac{Sh_x\, D_{vapor}}{x}\, dx}{D_{vapor}} = \int_0^L \frac{Sh_x}{x}\, dx \tag{5.3.1.24}$$

Since the Sherwood number correlations are expressed in terms of the Reynolds number, it is convenient to change the coordinates of integration in equation (5.3.1.24) from x to Re_x by substituting equation (5.3.1.13) and its derivative in equation (5.3.1.24):

$$\overline{Sh}_L = \int_0^{Re_L} \frac{Sh_x}{Re_x}\, dRe_x \tag{5.3.1.25}$$

Equation (5.3.1.25) can be integrated using any correlation or set of correlations for the local Sherwood number [132]. In the laminar region, equation (5.3.1.20) is substituted into equation (5.3.1.25) in order to obtain:

$$\overline{Sh}_L = \frac{0.6774\, Re_L^{1/2}\, Sc^{1/3}}{\left[1 + \left(\frac{0.0468}{Sc}\right)^{2/3}\right]^{1/4}} \qquad \text{for } Re_L < Re_{crit} \tag{5.3.1.26}$$

The average Sherwood number for the combined laminar and turbulent regions as shown in Figure 5.3.1.2 is obtained by integrating equation (5.3.1.25) in two parts; equation (5.3.1.20) is used in the laminar region, from $Re_x < Re_{crit}$, and equation (5.3.1.21) is used in the turbulent region, for $Re_{crit} < Re_x < Re_L$ to obtain:

$$\overline{Sh}_L = \frac{0.6774\, {Re_{crit}}^{1/2}\, Sc^{1/3}}{\left[1+\left(\frac{0.0468}{Sc}\right)^{2/3}\right]^{1/4}} + 0.037\, Sc^{1/3}({Re_L}^{0.8} - {Re_{crit}}^{0.8}) \qquad \text{for } Re_L > Re_{crit}$$

(5.3.1.27)

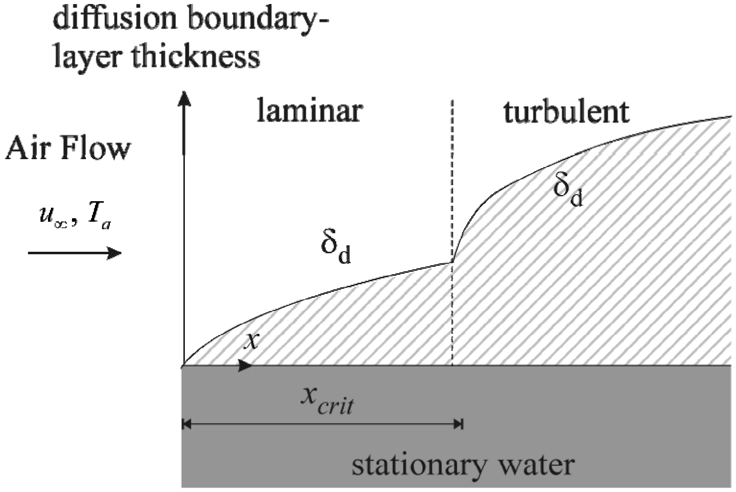

Figure 5.3.1.2. Diffusion boundary layer thickness in a mixed laminar and turbulent regions for free stream flow over a smooth isothermal flat plate

Finally, having average Sherwood number using equation (5.3.1.26) and equation (5.3.1.27) would lead us to obtain average mass transfer coefficient according to equation (5.3.1.23):

$$\overline{h_{m,vapor}} = \frac{\overline{Sh}_L\, D_{vapor}}{L} \tag{5.3.1.28}$$

This average mass transfer coefficient can be used directly by equation (5.3.1.6) to obtain average rate of evaporation at low rates:

$$\dot{m}''_{vapor} = J_{vapor} = \overline{h_{m,vapor}}\,(c_{vapor,s} - c_{vapor,e}) \tag{5.3.1.29}$$

5.3.2. Mass Transfer at High Rates

For assuming low rate mass transfer, it required that the velocity field be unaffected by mass transfer and that the transferred components be dilute. When those conditions are not met, the mass transfer coefficient will be different than the value given for low rate mass transfer. The difference can be either an increase or a decrease and can range from a few percent to an order of magnitude or more, depending upon the concentrations of the diffusing components. In addition to the diffusive transport represented by the mass transfer coefficient, convective transport can contribute substantially to the total mass flux.

Mass transfer driving force at high rates

Figure 5.3.2.1 shows a boundary layer over a flat surface through which there is a net mass transfer, $\dot{m}''$ [kg.m^{-2}.s^{-1}] of the various components in the direction normal to the surface [181]. The mass flux of component i with concentrations of $c_{i,e}$ [kg.m^{-3}] and $c_{i,s}$ [kg.m^{-3}] at the free stream and the surface is:

$$\dot{m}''_i = J_{i,s} + \rho_{i,s}\, v_s \tag{5.3.2.1}$$

where, $\dot{m}''_i$ is the total mass flux of component i [kg.m^{-2}.s^{-1}], $J_{i,s}$ is the mass diffusional flux at the interface [kg.m^{-2}.s^{-1}], $\rho_{i,s}$ is the density of the component i at the interface [kg.m^{-3}], and v_s is the mass average velocity of all components [m.s^{-1}].

As defined earlier, the mass transfer coefficient for component *i*, $h_{m,i}$ [kg.m^{-2}.s^{-1}] is:

$$J_{i,s} = h_{m,i}\,(c_{i,s} - c_{i,e}) \tag{5.3.2.2}$$

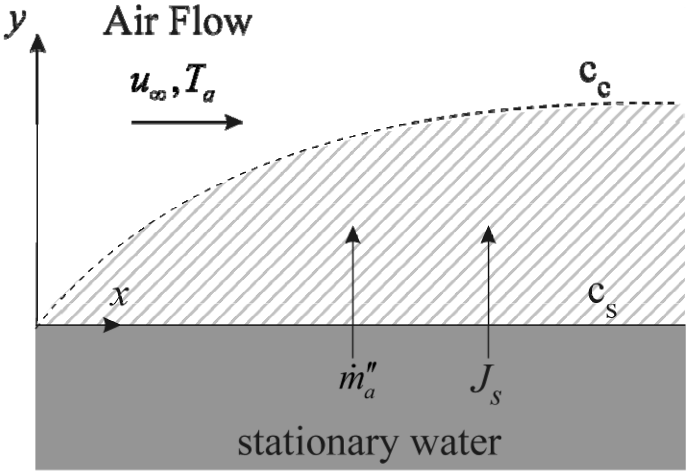

Figure 5.3.2.1. The mass concentration boundary layer in the high-rate mass transfer problem

Total mass flux of component *i* in terms of the concentrations $c_{i,s}$ and $c_{i,e}$ are:

$$\dot{m}''_i = \underbrace{h_{m,i}\,(c_{i,s} - c_{i,e})}_{J_{i,s}} + \rho_{i,s}\, v_s \tag{5.3.2.3}$$

Since the density of the component *i* at the interface, $\rho_{i,s}$, can be presented as $\rho_{i,s} = m_{i,s}\,\rho_s$ where $m_{i,s}$ is the mass fraction of component *i* at the surface, and ρ_s is the total density of all components at the interface [kg.m^{-3}], equation (5.3.2.3) can be rewritten as

$$\dot{m}''_i = \underbrace{h_{m,i}\,(c_{i,s} - c_{i,e})}_{J_{i,s}} + m_{i,s}\,\rho_s\, v_s \tag{5.3.2.4}$$

ρ_s v_s is the definition of total mass flux [kg.m^{-2}.s^{-1}], $\dot{m}''$, which is inserted in equation (5.3.2.4).

$$\dot{m}_i'' = h_{m,i}\,(c_{i,s} - c_{i,e}) + m_{i,s}\,\dot{m}'' = J_{i,s} + m_{i,s}\,\dot{m}'' \tag{5.3.2.5}$$

Although the mass transfer coefficient is based on diffusive transfer from the water surface, it may now differ considerably from the value for low-rate transport. Equation (5.3.2.5) may be rearranged as:

$$m_{i,s}\,\dot{m}'' - \dot{m}_i'' = h_{m,i}\,(c_{i,e} - c_{i,s}) \;\Rightarrow\; \dot{m}''\,(m_{i,s} - \dot{m}_i''/\dot{m}'') = h_{m,i}\,(c_{i,e} - c_{i,s}) \;\Rightarrow$$

$$\dot{m}'' = h_{m,i}\left(\frac{c_{i,e} - c_{i,s}}{m_{i,s} - \dot{m}_i''/\dot{m}''}\right) \tag{5.3.2.6}$$

Equation (5.3.2.6) expresses the total mass flux of all components through the interface, $\dot{m}''$, as the product of the mass transfer coefficient and a ratio of concentrations. This ratio is called the *mass transfer driving force* for component *i*:

$$B_{m,i} = \left(\frac{c_{i,e} - c_{i,s}}{m_{i,s} - \dot{m}_i''/\dot{m}''}\right) \tag{5.3.2.7}$$

The ratio of mass fluxes in the denominator is called the *mass fraction in the transferred state*, denoted as $m_{i,t}$ [181]:

$$m_{i,t} \equiv \dot{m}_i''/\dot{m}'' \tag{5.3.2.8}$$

The mass fraction in the transferred state is simply the fraction of the total mass flux, $\dot{m}''$, which is made up of component *i*. It is not really a mass fraction since it can have any value from $-\infty$ to $+\infty$, depending on the relative magnitudes of

$\dot{m}''$ and $\dot{m}''_{i,s}$. Equation (5.3.2.6) and equation (5.3.2.7) provide a formulation of mass transfer problems in terms of the mass transfer coefficient, $g_{m,i}$, and the driving force for mass transfer, $B_{m,i}$:

$$\dot{m}'' = h_{m,i} \, B_{m,i} \tag{5.3.2.9}$$

In many situations such as evaporation, only one component (i.e. water vapor) is transferred through the interface, since the second component (i.e. air) is not strongly absorbed into liquid (i.e. water) under normal conditions. If component *i* is the only one passing through the surface, then $\dot{m}'' = \dot{m}''_i$, so that $c_{i,t} = 1$. The mass transfer driving force is simply

$$B_{m,i} = \left(\frac{c_{i,e} - c_{i,s}}{m_{i,s} - 1} \right) \tag{5.3.2.10}$$

<u>The effect of mass transfer rates on the mass transfer coefficient</u>

Mass transfer coefficient, $g_{m,i}$ at high rates mass transfer problem is often found through applying solution of the momentum and component equations or through correlation of mass transfer data which are complicated approaches since the flow field and mass transfer rate are coupled [181]. $g_{m,i}$ can be obtained from the low-rate mass transfer coefficient by applying a correction for the effect of finite mass transfer rates. Lienhard IV and Lienhard V [181] isolated effect of $\dot{m}''$ on the mass transfer coefficient by approximating the boundary layer as a stagnant film and allowing for the possibility of the counter-diffusion, so that both diffusion and vertical convection may occur. They solved the partial differential equation of component conservation in the molar form with appropriate molar boundary condition assuming the mass transfer as a one-dimensional steady mass diffusion in stationary media without reactions. The solution of the rate of mass transfer considering vertical convective transport in the mass-based form is:

$$\dot{m}'' = \frac{D_i}{\delta_d} \ln\left(1 + \frac{c_{i,e} - c_{i,s}}{m_{i,s} - \dot{m}_i''/\dot{m}''}\right) \tag{5.3.2.11}$$

Recalling the definition of *mass transfer driving force* from equation (5.3.2.7), equation (5.3.2.11) is presented as:

$$\dot{m}'' = \frac{D_i}{\delta_d}\left[\frac{\ln\left(1 + B_{m,i}\right)}{B_{m,i}}\right] B_{m,i} \tag{5.3.2.12}$$

Equation (5.3.2.9) and equation (5.3.2.12) lead to:

$$h_{m,i} = \frac{D_i}{\delta_d}\left[\frac{\ln\left(1 + B_{m,i}\right)}{B_{m,i}}\right] \tag{5.3.2.13}$$

Now low-rate mass transfer coefficient of vapor can be obtained when $\dot{m}''$ approaches zero.

$$h^*_{m,vapor} \equiv \lim_{\dot{m}''\to 0} h_{m,vapor} = \lim_{B_{m,vapor}\to 0} h_{m,vapor} = \frac{D_{vapor}}{\delta_d} \tag{5.3.2.14}$$

Therefore, equation (5.3.2.13) can be rewritten as

$$h_{m,vapor} = h^*_{m,vapor}\left[\frac{\ln\left(1 + B_{m,vapor}\right)}{B_{m,vapor}}\right] \tag{5.3.2.15}$$

Since the group of $\left[\ln\left(1 + B_{m,vapor}\right)/B_{m,vapor}\right]$ is called the blowing factor (BF), the total mass flow rate of water vapor due to both diffusion and convective mass flux is calculated according to low-rate mass transfer coefficient, blowing factor and mass transfer driving force using

$$\dot{m}''_{vapor} = h^*_{m,vapor} \,.\, BF \,.\, B_{m,vapor} \qquad (5.3.2.16)$$

5.3.3 Algorithm for determination of evaporation rate

Considering the evaporation as a mass transfer problem, the following algorithm for determination of evaporation rate is suggested:

1) Calculate temperature of the film (boundary layer) as $T_{film} = \frac{T_c + T_a}{2}$
2) Determine the required air properties at the film temperature (μ, ρ, and v) [182]
3) Calculate binary diffusion coefficient for the water vapor in the air (D_{vapor}) by Chapman and Enskog formula [183]
4) Compute Schmidt number as: $Sc = \frac{v}{D_{vapor}}$
5) Compute Reynolds numbers as: $Re = \frac{u_\infty L \rho}{\mu}$
6) Calculate average Sherwood number $\overline{Sh}_L$ from equation (5.3.1.26) and equation (5.3.1.27)
7) Calculate average low-rate mass transfer coefficient $h^*_{m,vapor} = \frac{\overline{Sh}_L D_{vapor}}{L}$

8) Compute mass transfer driving force $B_{m,vapor} = \left(\dfrac{c_{vapor,e} - c_{vapor,s}}{m_{vapor,s} - 1} \right)$ from the change of water vapor concentration near the surface and the mass fraction of vapor at surface

9) Compute blowing factor as $BF = \ln\left(1 + B_{m,vapor}\right) / B_{m,vapor}$

10) Calculate total mass flux of water vapor due to evaporation according to

$$\dot{m}''_{vapor} = h^{*}{}_{m,vapor} \,.\, BF \,.\, B_{m,vapor}$$

5.4. Parametric Studies

Effects of boundary layer temperature, relative humidity and wind velocity on the rate of evaporation were studied and shown in Figure 5.4.1a-c. As shown in the figures, increasing ambient temperature leads to increase in the rate of evaporation, which more significantly increases by increasing wind speed and lowering ambient relative humidity. Increasing wind velocity, as shown in Figure 5.4.1a, results in decreasing boundary layer thickness which leads to an increase in the evaporation rate, e.g., in an ambient temperature and relative humidity of 40°C and 50%, a decrease in the wind velocity from 10 to 0.5 [m.s^{-1}] translate into a reduction of evaporation rate of a water surface with 0.3 m characteristic length from 1.3 to 0.3 [kg.m^{-2}h^{-1}]. According to the proposed mass transfer model, in both cases, the Schmidt number, *Sc*, is constant and equal to 0.72. However, the Reynolds number, Re_L, decreases from 174622 to 8731 leading to a decrease in the average Sherwood number, $\overline{Sh_L}$, from 244 to 55 and therefore, the average mass transfer coefficient, $\overline{h_m}$, falls from 0.0194 to 0.0043 [m.s^{-1}]. Having the same values for ambient and interface moisture concentration in both cases as c_s is 0.0514 and c_e is 0.0313, the difference in the average mass transfer coefficient can be held accountable for the reduction of evaporation rate by more than four times.

Increasing the ambient relative humidity, on the other hand, causes a drastic reduction in the rate of moisture evaporation. As shown in Figure 5.4.1b, assuming a wind velocity of 4 [m.s^{-1}], the evaporation rate at 40°C from a surface with 0.3 m characteristic length decreases from 2.0 to 0.2 [kg.m^{-2}h^{-1}] when the relative humidity increases from 10% to 90%. In these cases, the Schmidt (*Sc*), the Reynolds (Re_L) and the Sherwood ($\overline{Sh_L}$) numbers are constant and equal to 0.72, 70632 and 155, respectively, leading to a calculation of an average mass transfer coefficient ($\overline{h_m}$) of 0.0122 [m.s-1]. While the mass concentration of water vapor at the interface, c_s is also constant and equal to saturated concentration of 0.0514 [kg.m^{-3}], the mass concentration of water vapor at the air stream, c_e, increases from 0.0051 to 0.0463 [kg.m^{-3}] due to increasing relative humidity which causes a 10 time reduction in the value of the evaporation rate.

The size of sample in the direction of wind flow (characteristic length) also plays a significant role in the change of evaporation rates. The reduction of evaporation rates at the relative humidity of 50% and the wind velocity of 4 [m.s^{-1}] due to increasing characteristic length from 0.1 to 1 m was shown in Figure 5.4.1c. For example the results indicate that the evaporation rate at 40°C and relative humidity of 50% decreases from 2.0 to 0.6 [kg.m^{-2}h^{-1}] when the characteristic length increases from 0.1 to 1 m. In both cases, the Schmidt number, Sc, and the Reynolds number, Re_L, are constant and equal to 0.72 and 23544, while the average Sherwood number, $\overline{Sh_L}$, increases from 90 to 284 resulting in a decrease of the average mass transfer coefficient, $\overline{h_m}$, from 0.0211 to 0.0067 [m.s^{-1}]. When ambient and interface moisture concentrations are constant in both cases as c_s is 0.0514 and c_e is 0.0257, the difference in the average mass transfer coefficient leads into the reduction of evaporation rate by more than three times.

5.5. Model Comparison with Experimental Results of Concrete Evaporation

Results of recent evaporation tests from several references [8, 12, 19, 149] and one set of data from the authors tests were used to validate the model. The characteristic length which is defined as the length of specimen in the direction of the air flow was not given in most cases and therefore, an equivalent dimension which is the diameter of the equivalent circle to that area was used in calculations. Since the evaporating surface temperature was not reported, the rate of evaporation was calculated, first assuming the evaporating surface has the same temperature as the air and second, assuming surface cooling occurrence by the order of 3-4^{o}C. On the other hand, since the model cannot accept the air flow velocity of 0, it was approximated with a very small wind velocity of 0.5 m/s in those cases.

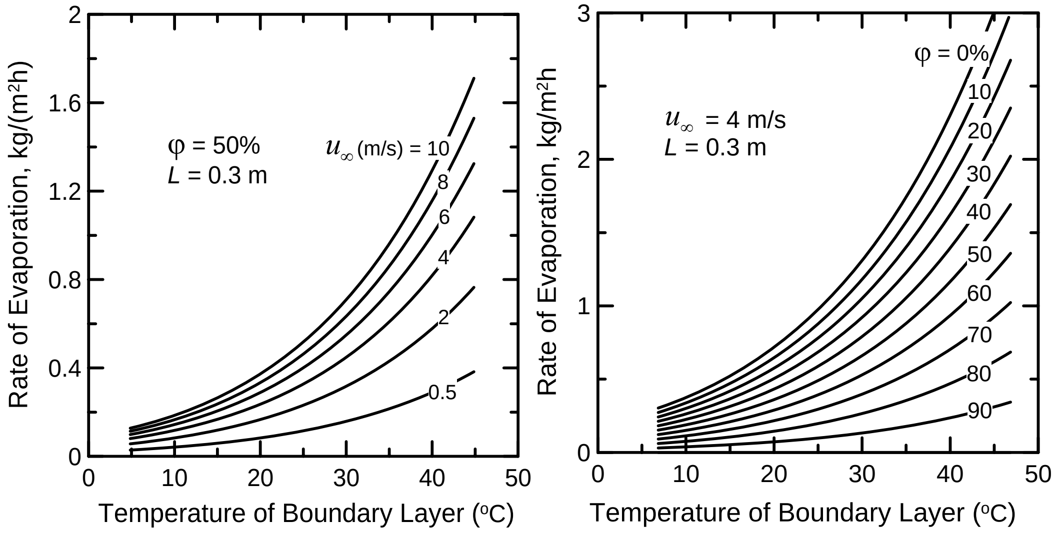

(Figure 5.4.1a) **(Figure 5.4.1b)**

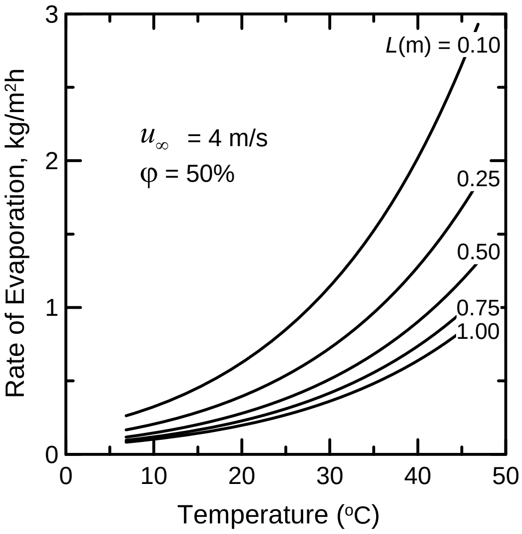

(**Figure 5.4.1c)**

Figure 5.4.1. Effect of temperature, relative humidity, wind velocity and characteristic length on the rate of evaporation from water surfaces.

The environmental parameters and predicted evaporation rates, as well as the parameters used for calculation of evaporation rates based on mass transfer and boundary layer theory are shown in Table 5.5.1 and 5.5.2. As shown in the Table 5.5.1, calculated evaporation rates assuming identical temperature for the air and evaporative surface overestimates the experimental results by 30-300%. However, evaporation rates estimated assuming surface cooling are very close to the experimental reported data. Except in two cases of wind velocity of zero, the other estimations are well within 0-30% of the experimental data. According to Poole [184], the assumption that concrete temperature represents the temperature at the evaporating surface is not strictly true because of the surface cooling occurrence during evaporation. A dynamic equilibrium between the rate of heat supply and the rate of liquid removal can explain the phenomena of evaporative cooling. The surface temperature can be compared with the wet-bulb temperature defined as the equilibrium temperature which liquid water attains when heat is transferred to it by contact with the air as an infinitely large quantity of gas. Taking psychrometry into consideration, the mass transfer from the liquid by evaporation is exactly balanced by the heat supply from the gas and can be represented by a heat and mass transfer equilibrium [185].

$$\dot{m}''_{vapor} = h_c(T_a - T_{wb})/\lambda = K_H(\varphi_s - \varphi_a) \;\Rightarrow\; \frac{(\varphi_s - \varphi_a)}{(T_a - T_{wb})} = \frac{-h_c}{K_H \lambda} \qquad (5.5.1)$$

where h_c is the heat transfer coefficient by convection [W.m^{-2} ^{o}C^{-1}], T_a is the temperature of the air [^{o}C], T_{wb} is the wet-bulb temperature of water [^{o}C], λ is the latent heat of evaporation at T_{wb} [kJ.kg^{-1}], K_H is the drying coefficient per unit humidity difference [kg.s^{-1}.m^{-2}], φ_s is the saturation humidity of water vapor, i.e. 1, and φ_a is the humidity of the air.

To verify the surface cooling, the input data of the evaporation tests by Azenha et al (2007) is compared with the data on usual psychrometric charts [186] and as a conclusion a wet-bulb temperature of 16°C is obtained. This result is in agreement with the magnitude of assumed surface cooling of about 3-4°C. Finally, the experimental data of Azenha et al. (2007) have been used to verify the effect of wind velocity. As shown in Figure 5.5.1, the experimental data are well predicted by the theory of boundary layer mass transfer. The comparison between experimental data and the theoretical modeling is shown in Figure 5.5.2 for all 9 cases. Considering all results and analyses, it may be concluded that the suggested model can well predict the initial rate of evaporation in the cement-based materials in the range of 0-0.5 [kg.m^{-2}h^{-1}]. While the results of modeling for higher evaporation rates were also verified using the test data reported by Lura (2007), more experimental data are required for further verification of the model in the evaporation rates higher than 0.5 [kg.m^{-2}h^{-1}].

Table 5.5.1.
Results of the evaporation rate in comparison with the experiments

Reference	Surface Dimensions, (m)	Characteristic Length, L (m)	Air Temp., T_a (^{o}C)	Relative Humidity, φ (-)	Wind Velocity, u_∞ (m/s)	Evaporation Rate assuming T_c=T_a, $\dot{m}''$ (kg/m^2/h)	Evaporation Rate assuming surface cooling, $\dot{m}''$ (kg/m^2/h)	Exp. Rate of Evaporation, $\dot{m}''$ (kg/m^2/h)
Case1: Azenha et al (2007)	0.051x0.073	0.0688	20	0.6	0	0.21	0.01	0.07
Case 2: Azenha et al (2007)	0.051x0.074	0.0688	20	0.6	1.8	0.40	0.19	0.17
Case 3: Azenha et al (2007)	0.051x0.075	0.0688	20	0.6	3.3	0.54	0.25	0.26
Case 4: Azenha et al (2007)	0.051x0.076	0.0688	20	0.6	4.2	0.61	0.28	0.31
Case 5: Lura et al (2007)	d=0.1	0.1	30	0.50	6.8	1.65	1.17	1.30
Case 6: Slowik et al. (2008)	0.3x0.3	0.3385	20	0.45	4.8	0.40	0.32	0.24
Case 7: Slowik et al. (2008)	0.3x0.3	0.3385	22	0.3	4.8	0.58	0.44	0.43
Case 8: Hammer (2001)	0.1x0.1	0.1128	20	0.5	0	0.29	0.12	0.08
Case 9: Authors	0.1x0.1	0.1128	24	0.34	0.5	0.34	0.23	0.20

Table 5.5.2.
Parameters used for calculation of evaporation rates

Parameters	Case1	Case 2	Case 3	Case 4	Case 5	Case 6	Case 7	Case 8	Case 9
boundary layer temperature, T_{film} [K]	291	291	291	291	303	291	294	291	295
dynamic viscosity, μ [kg.m^{-1}.s^{-1}]	1.81E-05	1.81E-05	1.81E-05	1.81E-05	1.87E-05	1.81E-05	1.82E-05	1.81E-05	1.83E-05
density of the air, ρ [kg.m^{-3}]	1.212	1.212	1.212	1.212	1.166	1.212	1.202	1.212	1.196
kinematic viscosity, ν [m^2.s^{-1}]	1.49E-05	1.49E-05	1.49E-05	1.49E-05	1.60E-05	1.49E-05	1.52E-05	1.49E-05	1.53E-05
diffusivity, D [m^2.s^{-1}]	2.04E-05	2.04E-05	2.04E-05	2.04E-05	2.20E-05	2.04E-05	2.08E-05	2.04E-05	2.10E-05
Schmidt number, Sc	0.7315	0.7315	0.7315	0.7315	0.7262	0.7315	0.7303	0.7315	0.7296
Reynolds number, Re_L	2304	8293	15204	19350	43762	108803	107166	3777	3686
avergae Sherwood number, $\overline{Sh_L}$	28	54	73	82	123	194	192	36	36
average low-rate mass transfer coefficient, $\overline{h_m}$ [m.s^{-1}]	8.38E-3	1.59E-2	2.15E-2	2.43E-2	2.7E-2	1.17E-2	1.18E-2	6.54E-3	6.63E-3
saturated water vapor pressure, p_{sat} [Pa]	1825	1825	1825	1825	3796	1825	2206	1825	2347
partial pressure of the vapor in air, p_v [Pa]	1408	1408	1408	1408	2256	1056	796	1174	1019
vapor concentration at the interface, c_s [kg.m^{-3}]	0.0137	0.0137	0.0137	0.0137	0.0273	0.0137	0.0164	0.0137	0.0174
mass fraction of the vapor at the interface, m_s	0.0113	0.0113	0.0113	0.0113	0.0234	0.0113	0.0136	0.0113	0.0145
vapor concentration in the air stream, c_e [kg.m^{-3}]	0.0104	0.0104	0.0104	0.0104	0.0161	0.0078	0.0058	0.0087	0.0074
mass transfer driving force, B_m [kg.m^{-3}]	0.0033	0.0033	0.0033	0.0033	0.0115	0.0060	0.0107	0.0051	0.0101
blowing factor, BF	0.998	0.998	0.998	0.998	0.994	0.997	0.995	0.997	0.995

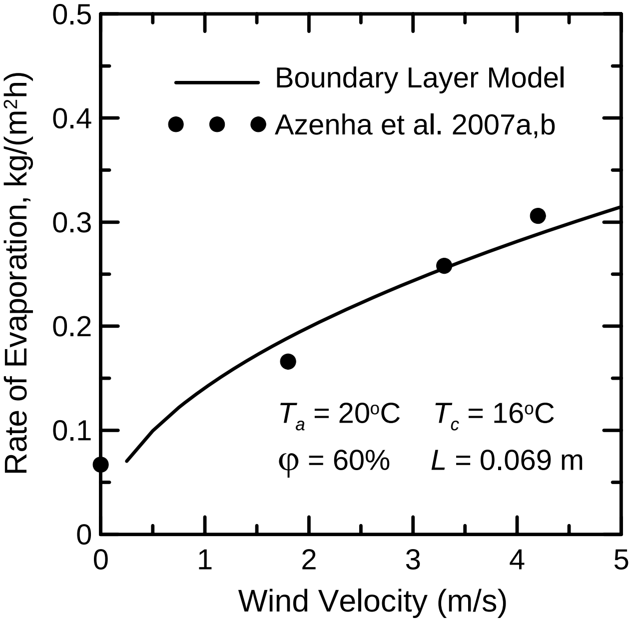

Figure 5.5.1. Prediction of experimental data of Azenha et al. (2007a,b) by a method based on a boundary layer mass transfer concept

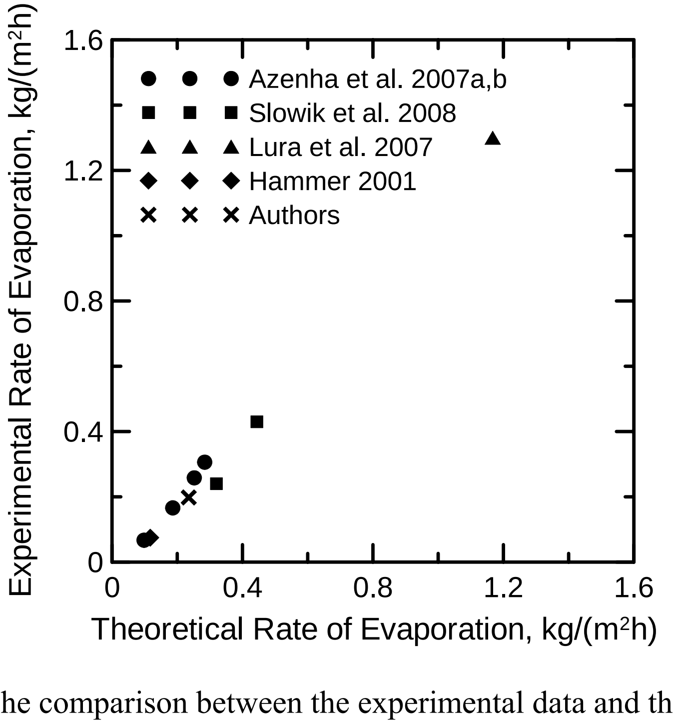

Figure 5.5.2. The comparison between the experimental data and the theoretical modeling of initial rate of evaporation based on a boundary layer mass transfer theory

5.6. Conclusion

Plastic shrinkage crack, a threat to structural integrity of concrete structures, are often observed in the first few hours after placing which is a time period well within the initial stage of drying. During stage I drying, rate of evaporation from concrete surfaces is roughly constant and similar to the external potential evaporation rate from water surfaces which controls the drying process. The theory of water evaporation based on the boundary layer theory, mass transfer, diffusion, and convection is described and a driving force of concentration gradient is introduced as the main cause of mass transfer. Mass transfer at low and high rates is discussed separately along with other related parameters such as mass transfer coefficient and a method for determination of evaporation rate is suggested. Results of parametric studies show that increasing ambient temperature leads to an increase in the rate of evaporation, which more significantly increases by increasing wind speed and lowering ambient relative humidity. Results of parametric studies also show that the size of sample in the direction of wind flow (characteristic length) plays a significant role in the change of evaporation rates. The proposed method is verified by the recent experimental data from several researchers on cement-based materials. The results show that given the environmental parameters as inputs, the model is capable of predicting the evaporation rates with a good accuracy.

APPENDIX A

FRee Shrinkage Test Results

An experimental study was conducted to evaluate the effects of adding low content of AR-glass fibers (5, and 10 lb/yd^3) on the free shrinkage of cement pastes. The free shrinkage tests were performed according to ASTM standard C 157-04. This test method covers the determination of the length changes that are produced by causes other than externally applied forces and temperature changes in hardened hydraulic-cement mortar and concrete specimens made in the laboratory and exposed to controlled conditions of temperature and moisture. Measurement of length change permits assessment of the potential for volumetric contraction (shrinkage) of concrete due to drying. This test method is particularly useful for comparative evaluation of this potential in different hydraulic-cement mortar or concrete mixtures. In this test, specimens of 1" [25-mm] square cross-section and approximately 11-1⁄4" [285 mm] in length are casted for each mixture. The test specimens are cured in the molds covered with a plastic sheet for 24 hours while water dripping from specimen is protected. Upon removal of the specimens from the molds, the initial Length reading is taken using a digital comparator dial. After the initial comparator reading, the specimens stored in the drying room, so that the specimens have a clearance of at least 1 in. [25 mm] on all sides. Comparator readings of each specimen are taken every one or two days after initial reading. These readings were done in a room maintained at a relative humidity of 30% while the specimens are at a temperature of 73°F [23°C]. The comparator dial were read with both test specimen and the reference bar in the comparator and the difference between the two readings and initial length of specimens were used to calculate shrinkage strain.

The effect of AR-glass fibers on free shrinkage was investigated by ASTM standard C 157-04. Three different cement paste mixtures were designed including 2 mixtures with AR-glass fibers and one control mixture with only plain cement paste and no fiber. All mixtures were designed with the water-cement ratio of 0.45 and a high slump (6 in.) such as slurry. The cement content was 2080 lb/yd^3 (1450 Kg/m^3) and only Portland cement, type I/II and water were used to cast the paste. The only difference between these mixtures, Control, ARG5.0, and ARG10 was due to adding 0, 5, and 10 lb/yd^3 fibers respectively. In all ARG mixes, Anti-Crak® HP-glass fibers with 24 mm length were used. The mix proportions of sample are resented in Table A.1.

Table A.1.

Mixture proportions of the ARGs and Control samples (lb/ft^3)

Mix ID	Control	ARG5.0	ARG10
Portland Cement	90	90	90
Water	41	41	41
Glass Fiber (HP-Glass)	0.0	0.19*	0.37*
w/c	0.45	0.45	0.45

* The fiber content of 0.19, and 0.37 lb/ft^3 is equivalent to 5, and 10 lb/yd^3

Tow prism specimens of 1” [25-mm] square cross-section and approximately 11 1⁄4” [285 mm] in length are cast for each mixture. For making each sample, Portland cement were added to the mixer and blended for 60 seconds. Then, water poured gradually to the mixer and blended for 5 minutes before adding the glass fibers only to the ARG mixtures and mixing for 5 additional minutes to thoroughly mix all the ingredients. After mixing concrete in a suitable laboratory mixer, the concrete is placed in the mold in two approximately equal layers and each layer compacted with the tamper. We worked with the concrete until a homogeneous specimen is obtained. After the top layer has been compacted, we strike off the mortar flush with the top of the mold, and smooth the surface with a few strokes of a trowel. The test specimens are cured in the molds covered with plastic sheet and then removed from the molds at an age of 24 hours after mixing. After length measurement at the end of the curing period using a digital comparator dial, the samples are stored in a drying room until next reading. The lengths of samples are read in 1 or 2 days intervals up to 28 days and the difference between the reading and initial reading (at 24h) used to calculate free shrinkage. The results of experimental tests are shown in Figures A.1. The results show that adding low content AR-glass fibers (5 to 10lb/yd^3) to the Portland cement paste reduces the free shrinkage by about 5% and 10%, respectively.

Experimental data were analyzed using ACI 209R-92 shrinkage model. This model is an empirical model developed by Branson and Christiason [187], with minor modifications introduced in ACI 209R-82 [188]. ACI Committee 209 incorporated the developed model in ACI 209R-92 [87]. The model for predicting shrinkage strains as a function of time have a simple principle: a hyperbolic curve that tends to an asymptotic value called the ultimate value. The shrinkage strain $\varepsilon_{sh}(t,t_c)$ at age of concrete t (d), measured from the start of drying at t_c (d), is calculated by equation (A.1).

$$\varepsilon_{sh}(t,t_c) = \frac{(t-t_c)^{\alpha}}{f+(t-t_c)^{\alpha}} \cdot \varepsilon_{shu} \tag{A.1}$$

where, f (in days) and α are considered constants for a given member shape and size that define the time-ratio part, ε_{shu} is the ultimate shrinkage strain, and $(t - t_c)$ is the time from the end of the initial curing. The shape and size effect can be totally considered on the time-ratio by replacing $\alpha = 1.0$, and f as given by equation (A.2) in in-lbs units.

$$f = 26.0e^{[0.36(V/S)]} \tag{A.2}$$

where, V/S is the volume-surface ratio in inches.

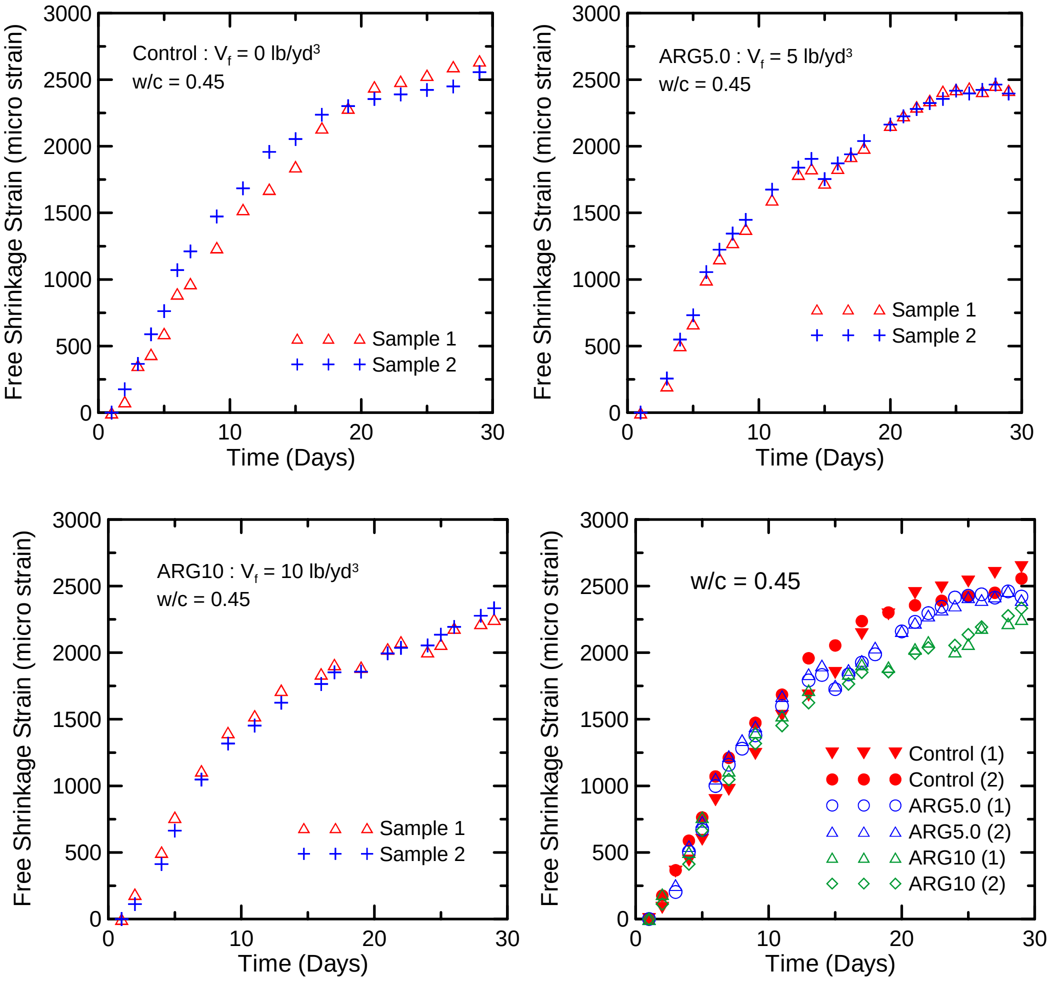

Figure A.1. Free shrinkage results of Control and ARG samples and their comparison

Hence, equation (A.1) is transformed to:

$$\varepsilon_{sh}(t,t_c) = \frac{(t-1)^{1.5}}{28+(t-1)^{1.5}} \cdot \varepsilon_{shu} \tag{A.3}$$

ACI 209R-92 suggests multiplying ε_{shu} by seven factors, depending on particular conditions

$$\varepsilon_{shu} = 780\,\gamma_{sh} \times 10^{-6}\ in./in. \tag{A.4}$$

with

$$\gamma_{sh} = \gamma_{sh,tc}\,\gamma_{sh,RH}\,\gamma_{sh,vs}\,\gamma_{sh,s}\,\gamma_{sh,\psi}\,\gamma_{sh,c}\,\gamma_{sh,\alpha} \tag{A.5}$$

where, γ_{sh} represents the cumulative product of the applicable correction factors. $\gamma_{sh,tc}$ represents the initial moist curing coefficient for curing times different from

7 days for moist-cured concrete. $\gamma_{sh,\,RH}$ is the ambient relative humidity coefficient while Coefficient $\gamma_{sh,vs}$ allows adjustment for the size of the member in terms of the volume-surface ratio. $\gamma_{sh,s}$ and $\gamma_{sh,\psi}$ are the slump the fine aggregate factors respectively. $\gamma_{sh,c}$ represents effect of cement content and $\gamma_{sh,\alpha}$ is air content factor.

In order to use ACI 209R-92 shrinkage model to analyze our free shrinkage data, α is chosen as 1.5, t_c equals to 1 day, and f is chosen as 28 days since V/S ratio is equal to 0.25 in. The values of $\gamma_{sh,tc}$, $\gamma_{sh,\,RH}$, $\gamma_{sh,vs}$, $\gamma_{sh,s}$, $\gamma_{sh,c}$, $\gamma_{sh,\alpha}$ are considered as 1.2, 1.094, 1.164, 1.136, 1.498 and 0.99 respectively since t_c equals to 1 day, RH is 30%, V/S ratio is equal to 0.25 in, slump is 6 in. and air content is about 5%. $\gamma_{sh\psi}$ referring to fine aggregate content factor is not applicable here since no aggregate was used in cement paste samples. With a good adjustment, the value of 1.5 is replaced $\gamma_{sh,\psi}$ factor and as shown in Figure A.2, the data show a good correlation with ACI model. ε_{shu} for plain cement paste or Control samples was calculated as 3012 x 10^{-6} in/in.

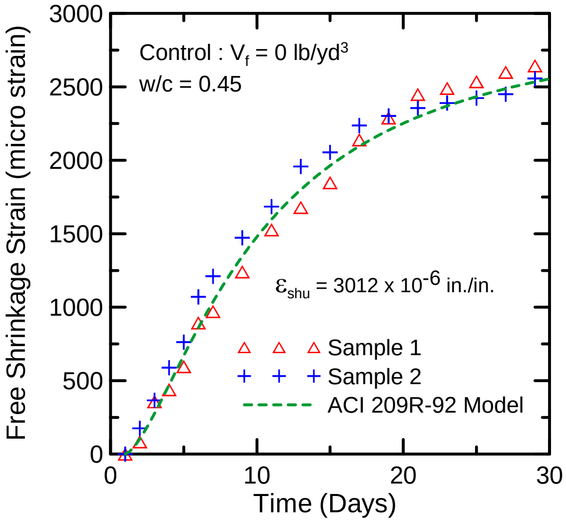

Figure A.2. Modeling free shrinkage data of Control sample using ACI 209R-92 model

To model ARG samples, a factor as γ_f is presented to include in cumulated correction factors, γ_{sh} in order to reduce ultimate shrinkage, ε_{shu} and modify ACI model for fiber effect. Then the shrinkage formula turned out as;

$$\varepsilon_{shu} = 780\ (\gamma_{sh,tc}\,\gamma_{sh,RH}\gamma_{sh,vs}\,\gamma_{sh,s}\,\gamma_{sh\psi}\,\gamma_{sh,c}\,\gamma_{sh,\alpha}\,\gamma_f) \times 10^{-6}\ in./in. \tag{A.6}$$

Using γ_f as 0.96 and 0.9 for paste samples with 5 lb/yrd^3 and 10 lb/yrd^3 respectively, our modified ACI model fitted experimental data appropriately. Using these fiber correction factors ε_{shu} is calculated as 2890 x 10^{-6} in/in for ARG5.0 and 2710 x 10^{-6} in/in for ARG10 samples. The results of fitting data with modified ACI model are shown in Figure A.3.

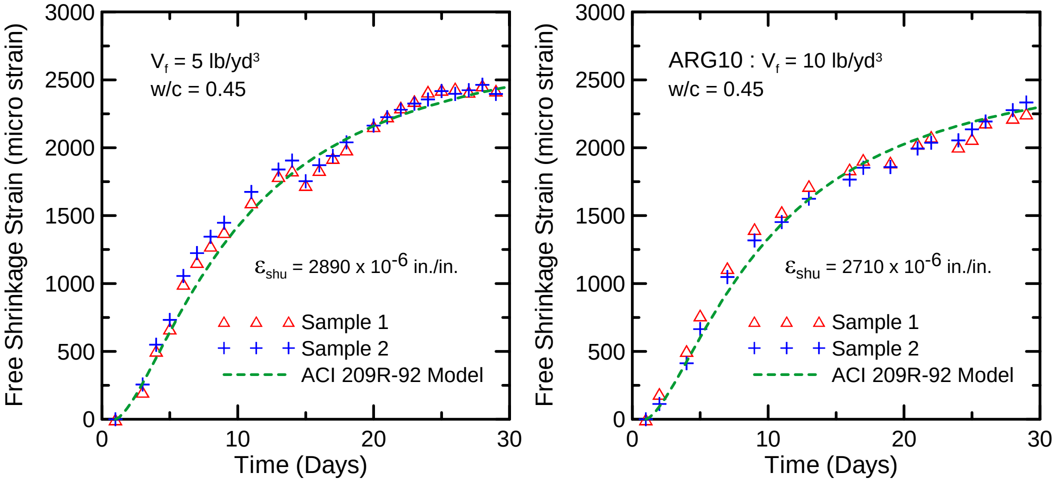

Figure A.3. Fitting experimental free shrinkage data of ARG samples with modified ACI 209R-92 model

Experimental and modeling free shrinkage data indicate that adding low dosage of AR-glass fibers to concrete samples reduced the free shrinkage strains so slightly. The results show that ultimate free shrinkage of cement pastes can reduce by almost 4% and less than 10% when adding 5 and 10 lb/yrd^3 AR-glass fibers to the batch. The final conclusion is that free shrinkage parameters do not significantly differentiate the contribution of fiber.

APPENDIX B

Vacuum Evaporation Test Method and Data Transfer Description

The author developed a new test method which is capable of characterizing evaporation parameters and simulating severe conditions to create 2D shrinkage cracks. This test method is based on the vacuum drying technique and test results can be used to analyze evaporation and cracking. A schematic of test setup is shown in Figure B.1.

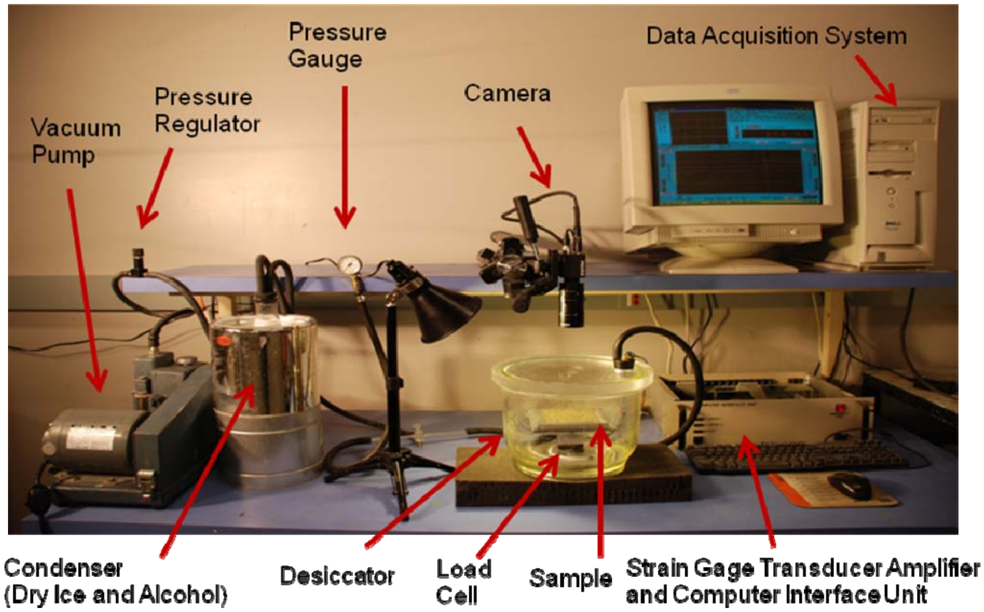

Figure B.1. 2D shrinkage cracking test setup based on vacuum technology

Note that before running an evaporation test, the following items have to be checked.

1. Oil level and quality (oil has to be changed after 4-5 complete tests)
2. Dry ice (10-15 lbs of dry ice is required for a single 48 h test)
3. Mold (to make sure is ready and cleaned-up)
4. Initial pressure inside the desiccator (adjust it at 20 in Hg before starting the test)
5. Load cell (Offset the load cell before starting a test)
6. Output file header (to be filled up in details and completed in GCTS software)

Testing equipments

Various components of the setup are described.

Equipped Vacuum Vessel

A Pyrex vacuum vessel covered with a transparent Acrylic lid was used to maintain vacuum pressure. As shown in the Figure B.1, the lid has a valve to induce vacuum pressure. There is another hole on the other side of lid used to pass load cell wires from inside of the vessel to the outside. The vessel was equipped with a scale system. In order to weigh samples continuously, an accurate load cell with capacity of 5440 g (12 lb) and accuracy of 0.05g (0.0001 lb) was hired. Two Plexiglas plates were attached to both end of the load cell to make weight measurement as convenient as possible. The load cell was calibrated by a precise digital scale (0.01g accuracy) using more than 30 different weights up to 1500 g. The calibration formula was derived and the obtained voltage gain was used for recording moisture loss.

Mold

As shown in Figure 3.2.1b, Plexiglas parts were used to make a 10×10×1.3 cm (4”×4”×0.5”) low-weight mold. This thin mold is proper to make samples with high specific surface area exposed to the external evaporation condition. In order to restrain the sample and cause early-age 2D cracks, two pairs of holes were drilled in each side of the mold and paper clips were passed through them and bended at the outer side by the right angle to stay fixed during the test.

Vacuum Pump

A belt-drive two-stage pump was used as the vacuum equipment operated at its ultimate blankoff pressure, 1700 Pa (0.017 atm) for a long period of time. The pump is designed to remove air from a vacuum system at atmospheric pressure to a deep vacuum.

Condenser System

A condenser system including a vessel, alcohol, dry ice and flask was used in this test method. Condenser vessel is a 15.2×30.5 cm (6”×12”) cylinder made up of double layer glass materials with a cylindrical hole of 12.7×25.4 cm (5”×10”) inside it. The dry ice was fallen first inside the trap up to 1/3 of the height. Then alcohol was added to the trap to decrease the atmosphere temperature to -70^{o}F to condense the moisture. Double layer glass vessel used as heat insulator to prevent fast evaporation of the dry ice. A 1000mL glass flask was acquired as a trap to collect condensed moisture and prevent water vapor to flow through the pump.

T-Bore Stopcock, Pressure Gage, Regulator and Hose

T-Bore stopcock was used to split and conduct vacuum flow of the vessel between condenser and pressure gage. The pressure gage was required to control the negative pressure inside the vessel and insure of ultimate pressure. All the components of the vacuum drying system including vacuum pump, condenser system, T-Bore stopcock, pressure gage and vacuum vessel are connected by high pressure hoses.

Data Collection System

The load cell was connected to a computer using a strain gage transducer amplifier and a simple computer interface unit. Computer has an acquisition card and equipped with a testing software to read and collect test data. The software is capable of getting calibration formula and read the data as weight in grams. The procedure was set to collect the data every single minute and stop collecting the data at the specified 24 or 48hrs.

Camera

In order to analyze several characteristics of early-age cracks developed by drying of the cement paste and clay samples, a digital camera (Pulnix TM1325CL) was provided. The camera mounted 10 cm away from the top surface of vessel lid facing the center of the sample inside the vessel. The camera was set automatically to take pictures of the top surface of the sample every 15 min through end of the test.

Testing procedure

After a number of preliminary trial tests, the following procedure was established to run evaporation test using vacuum technique. First, the mold was prepared and weighed using an accurate digital scale (0.01g accuracy). The cement paste was then made according to the mix design table and poured into the mold. Total weight of the sample including weight of mold and cement paste was measured using the digital scale. Note that the recorded weight was the same as or within the accuracy range of the weighing system inside the vessel. The condenser vessel was filled up to 1/3 of the height with alcohol. 10-12 pounds of dry ice was hooked up and crushed into small chunks before placing inside the condenser vessel. After some hours, the initial added dry ice may evaporate being exposed to the air in room temperature. In such a case, more dry ice is needed during the test to maintain its equilibrium with alcohol. T-Bore stopcock was opened to let the negative pressure flow from vacuum valve at top of the vessel when the pump is on. The cement paste sample was then placed inside the vacuum vessel attached to the load cell. The weight was measured by continuous recording of the load cell and the camera was powered on to capture images at 15 minutes interval during the test.

At the beginning of drying tests, a vacuum reaching 34 kPa (10” Hg) absolute was applied to each specimen for a short period of time. Then the pressure decreased in the vessel to 1.7 kPa (0.5” Hg) absolute. Since the fresh paste is so fluid at the beginning of the test, reaching ultimate blankoff pressure of the vacuum pump leads to creation of many permanent voids on the surface of the sample. Voids affect on crack characteristics of the sample as obstacles against crack propagation. Also the load cell placed inside the vacuum vessel shows erratic results at the very beginning of the test due to effect of vacuum pressure. A short period of time (i.e. 30 min - 1 h) is required to get stable data from load cell. Hence, the first 30 minutes to one hour was assumed as an offset time supported by the fact that only a mass loss of about 1g was recorded during this period due to very low vacuum pressure.

Data Collection and Transfer Procedure

Step 1- Open the GCTS package and click on the ‘Tests’.

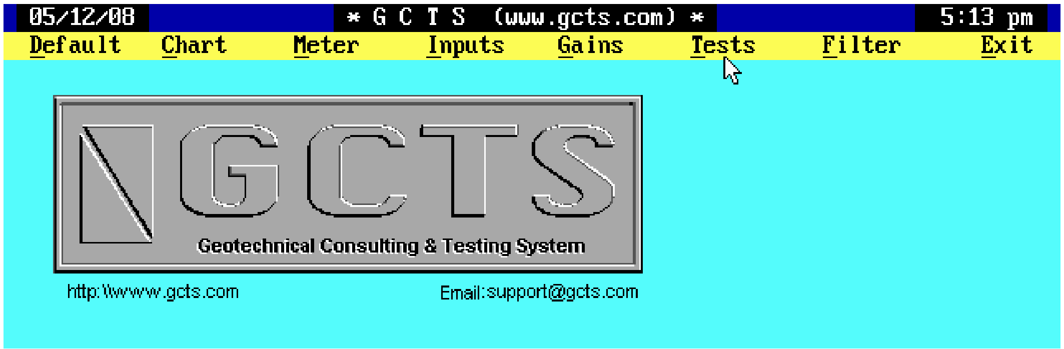

Step 2- Click on the ‘Universal’.

Step 3- Click on the ‘Test-ID’ when in the Transducer column ‘Scale’ is chosen.

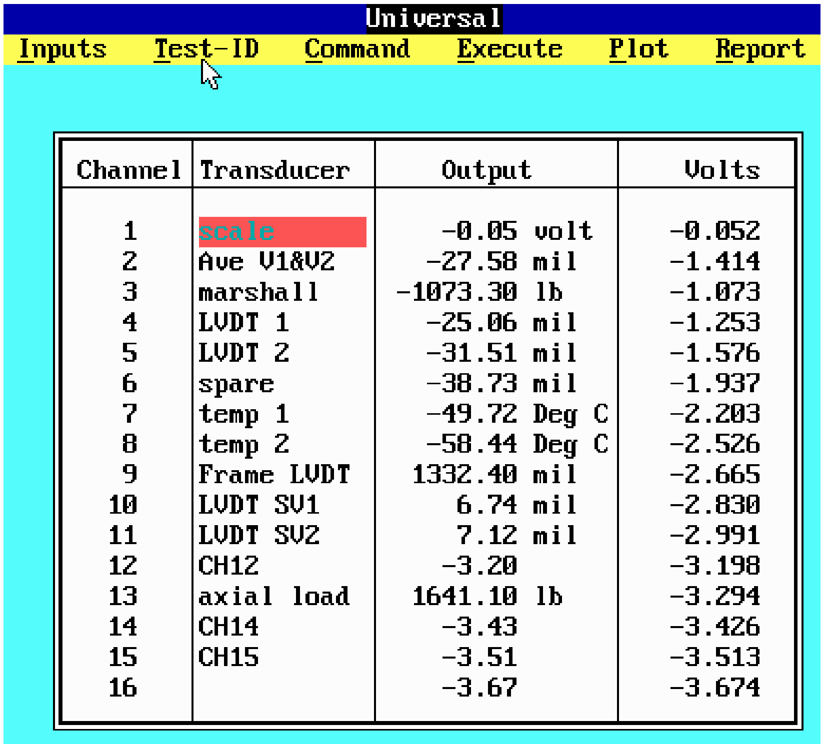

Channel	Transducer	Output	Volts
1	scale	-0.05 volt	-0.052
2	Ave V1&V2	-27.58 mil	-1.414
3	marshall	-1073.30 lb	-1.073
4	LVDT 1	-25.06 mil	-1.253
5	LVDT 2	-31.51 mil	-1.576
6	spare	-38.73 mil	-1.937
7	temp 1	-49.72 Deg C	-2.203
8	temp 2	-58.44 Deg C	-2.526
9	Frame LVDT	1332.40 mil	-2.665
10	LVDT SV1	6.74 mil	-2.830
11	LVDT SV2	7.12 mil	-2.991
12	CH12	-3.20	-3.198
13	axial load	1641.10 lb	-3.294
14	CH14	-3.43	-3.426
15	CH15	-3.51	-3.513
16		-3.67	-3.674

Step 4- Type the Project info and Sample description inside ‘Test-ID’, and press Enter.

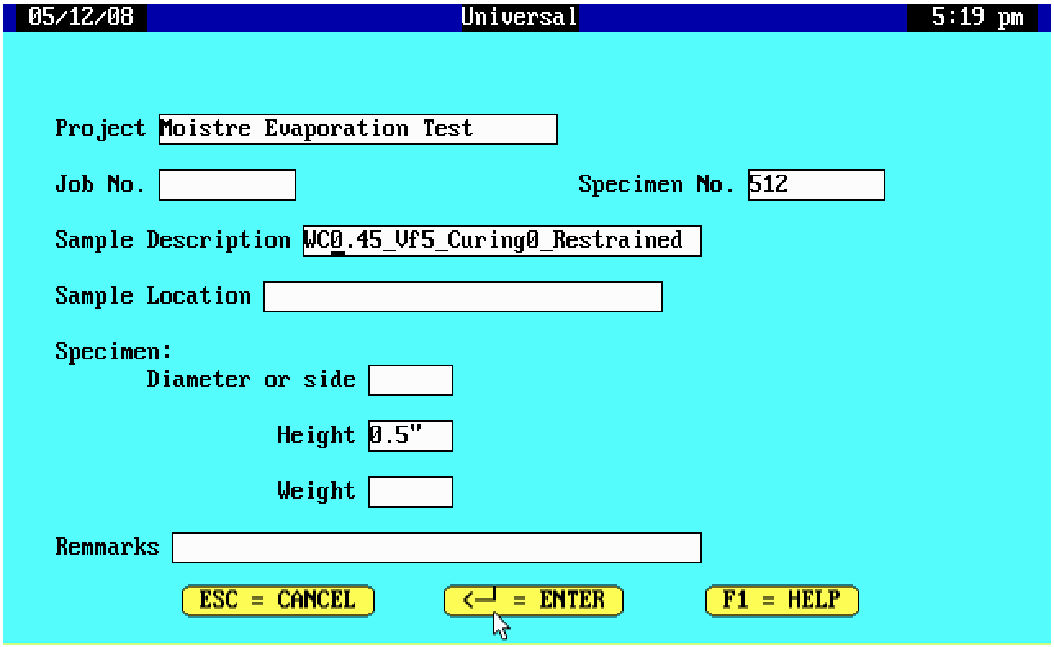

Project Moistre Evaporation Test

Job No.

Specimen No. 512

Sample Description WC0.45_Vf5_Curing0_Restrained

Sample Location

Specimen:

Diameter or side

Height 0.5"

Weight

Remmarks

Step 5- Click on the ‘Command’ and press on ‘F2’ to load a predefined command procedure. You can load ‘MEHDI_1.CMD’ for test duration of 1440 min (24 h).

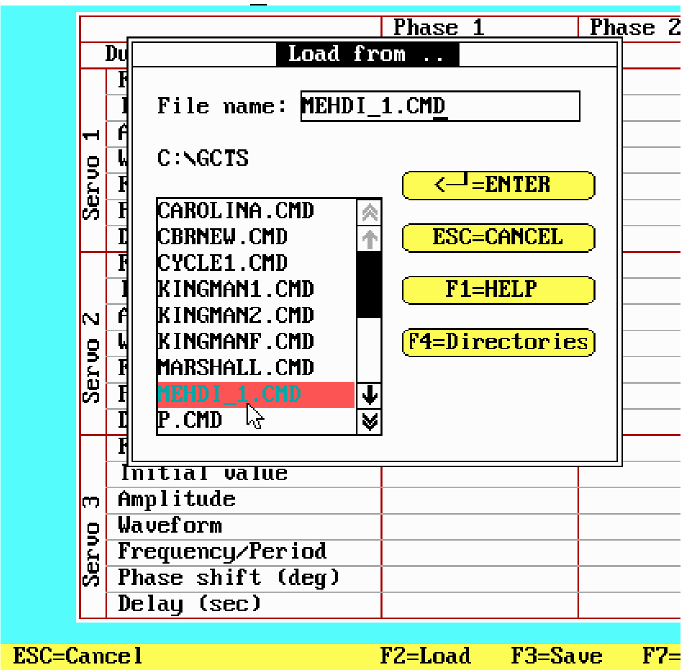

File name: MEHDI_1.CMD

Step 6- In case a new procedure with longer duration or higher frequency is required to be run, a command procedure has to be defined. Click on the ‘Servo-1’ and change the parameters to the desired values. Then click on ‘F3’ to save the command.

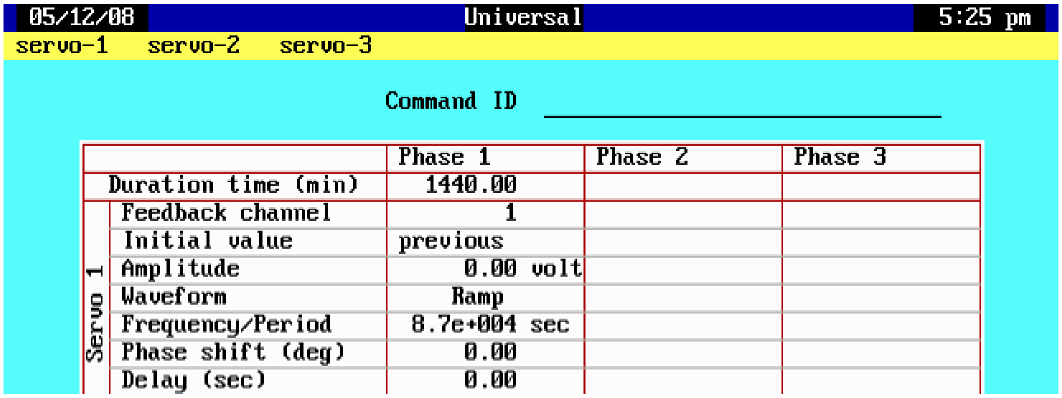

		Phase 1	Phase 2	Phase 3
Duration time (min)		1440.00		
Servo 1	Feedback channel	1		
	Initial value	previous		
	Amplitude	0.00 volt		
	Waveform	Ramp		
	Frequency/Period	8.7e+004 sec		
	Phase shift (deg)	0.00		
	Delay (sec)	0.00		

Step 7- Click on the ‘Execute’ to start the data collection procedure.

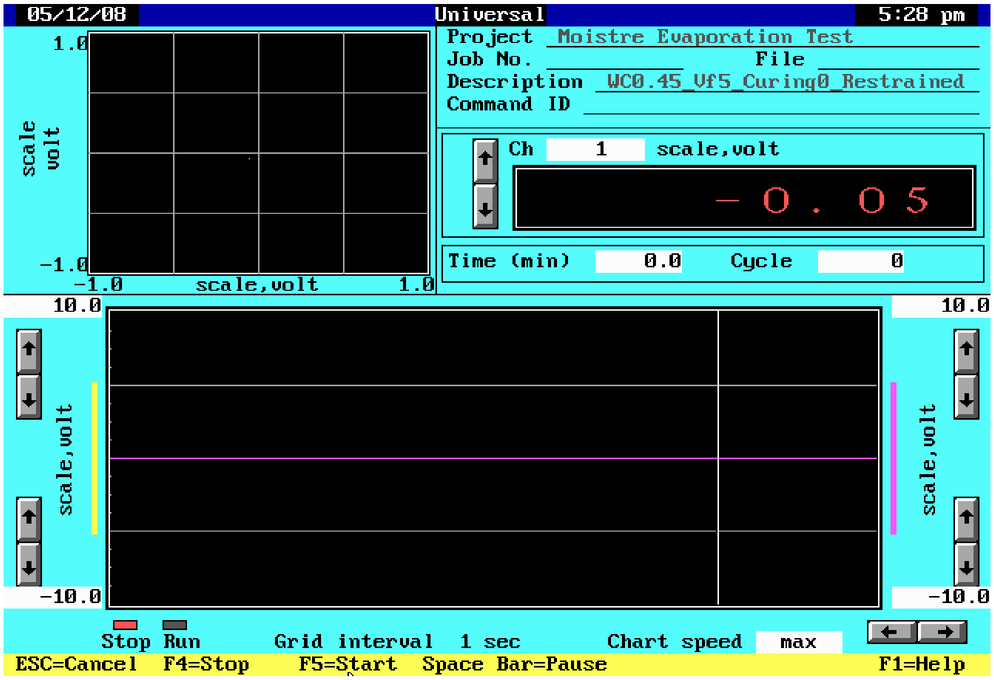

05/12/08 Universal 5:28 pm

Project Moistre Evaporation Test

Job No.

File

Description WC0.45_Vf5_Curing0_Restrained

Command ID

Ch 1 scale,volt

-0.05

Time (min) 0.0

Cycle 0

Grid interval 1 sec

Chart speed max

Step 8- Click on ‘F5’ to start the data collection. A name has to be typed for the name of the generated DAT file.

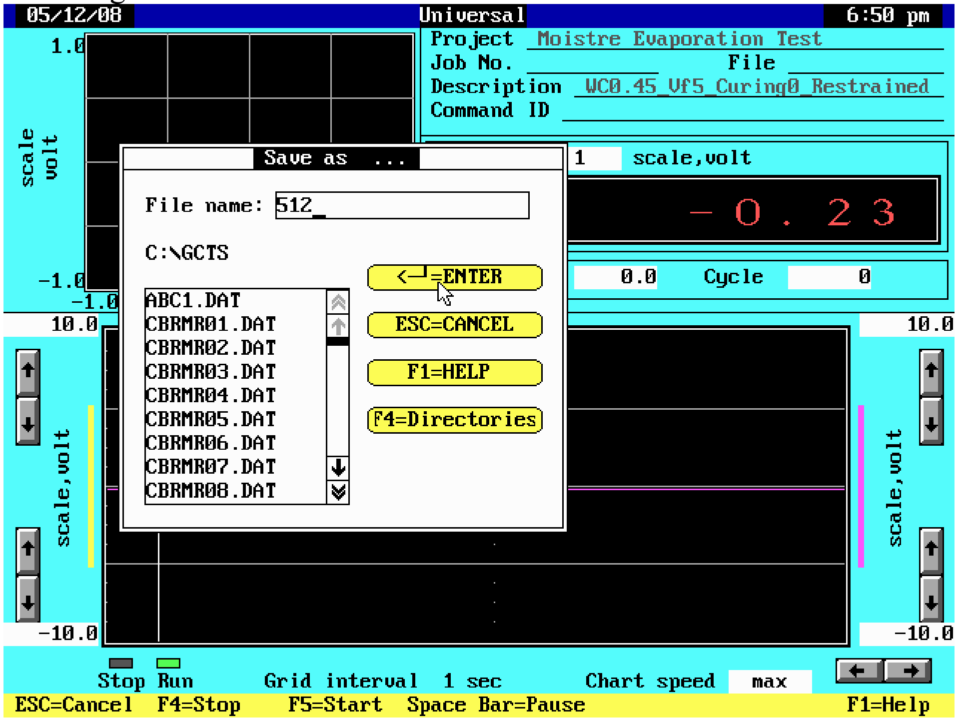

05/12/08 Universal 6:50 pm

Project Moistre Evaporation Test

Job No.

File

Description WC0.45_Vf5_Curing0_Restrained

Command ID

Save as ...

File name: 512_

C:\GCTS

ABC1.DAT
CBRMR01.DAT
CBRMR02.DAT
CBRMR03.DAT
CBRMR04.DAT
CBRMR05.DAT
CBRMR06.DAT
CBRMR07.DAT
CBRMR08.DAT

1 scale,volt

-0.23

0.0 Cycle 0

Grid interval 1 sec

Chart speed max

Step 9- After the test is complete, click on the ‘Report’ to convert the format of the output file from DAT (only readable inside the GCTS package) to Text (ASCII) format.

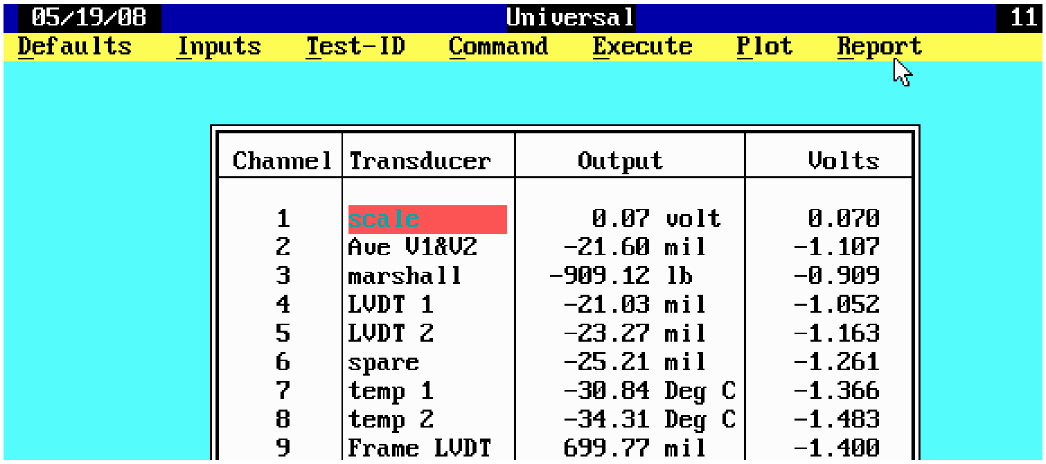

Channel	Transducer	Output	Volts
1	scale	0.07 volt	0.070
2	Ave V1&V2	-21.60 mil	-1.107
3	marshall	-909.12 lb	-0.909
4	LVDT 1	-21.03 mil	-1.052
5	LVDT 2	-23.27 mil	-1.163
6	spare	-25.21 mil	-1.261
7	temp 1	-30.84 Deg C	-1.366
8	temp 2	-34.31 Deg C	-1.483
9	Frame LVDT	699.77 mil	-1.400

Step 10- The DAT file has to be loaded by clicking on or typing the DAT file name and then pressing Enter.

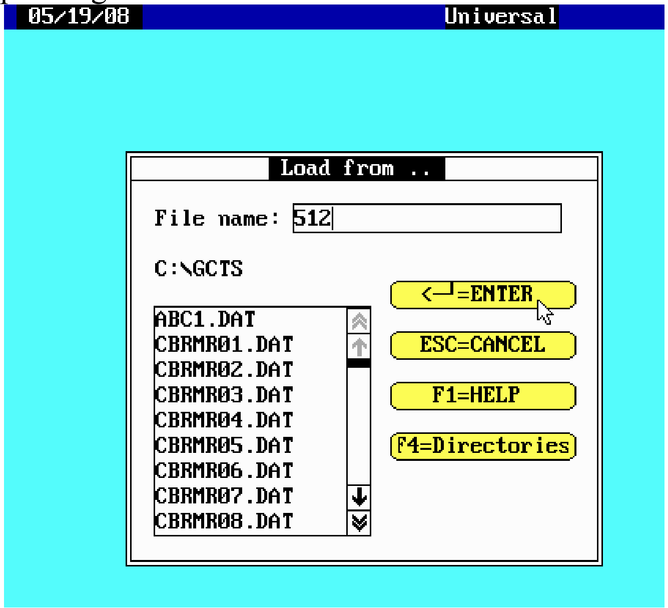

File name: 512

C:\GCTS

ABC1.DAT
CBRMR01.DAT
CBRMR02.DAT
CBRMR03.DAT
CBRMR04.DAT
CBRMR05.DAT
CBRMR06.DAT
CBRMR07.DAT
CBRMR08.DAT

Step 11- Choose ‘File’ and press Enter.

Data File: 512.dat

Report to
○ Printer
● File

Step 12- Type in the file of the ASCII file and press ‘Enter’.

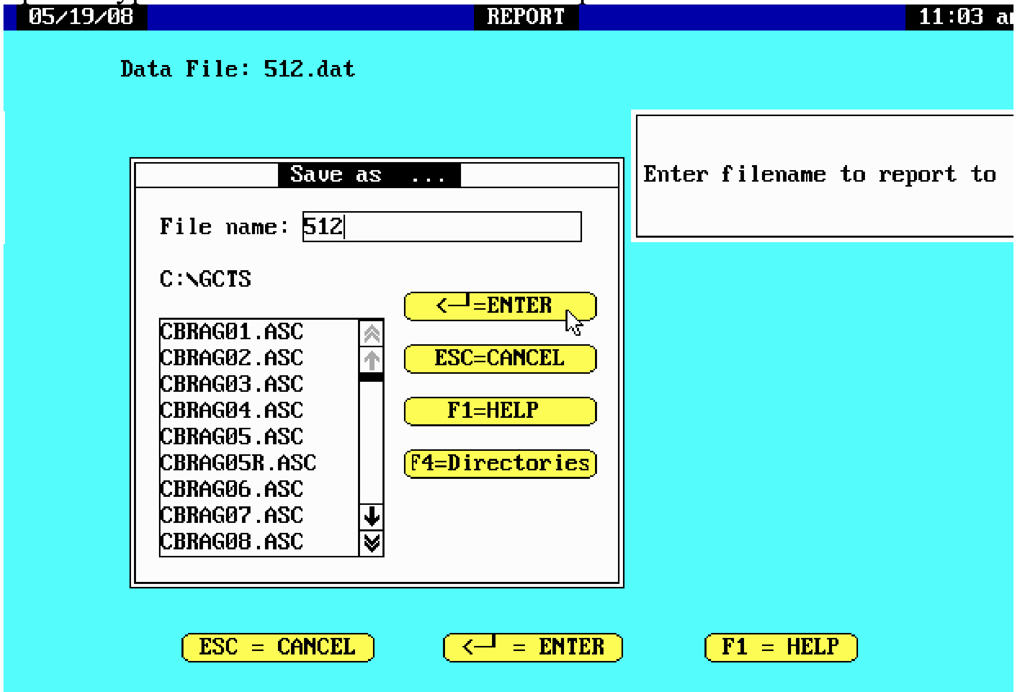

Data File: 512.dat

Save as ...

File name: 512

C:\GCTS

```
CBRAG01.ASC
CBRAG02.ASC
CBRAG03.ASC
CBRAG04.ASC
CBRAG05.ASC
CBRAG05R.ASC
CBRAG06.ASC
CBRAG07.ASC
CBRAG08.ASC
```

Enter filename to report to

Step 13- The data transfer is complete and you can find the ASCII file on: C:\gcts

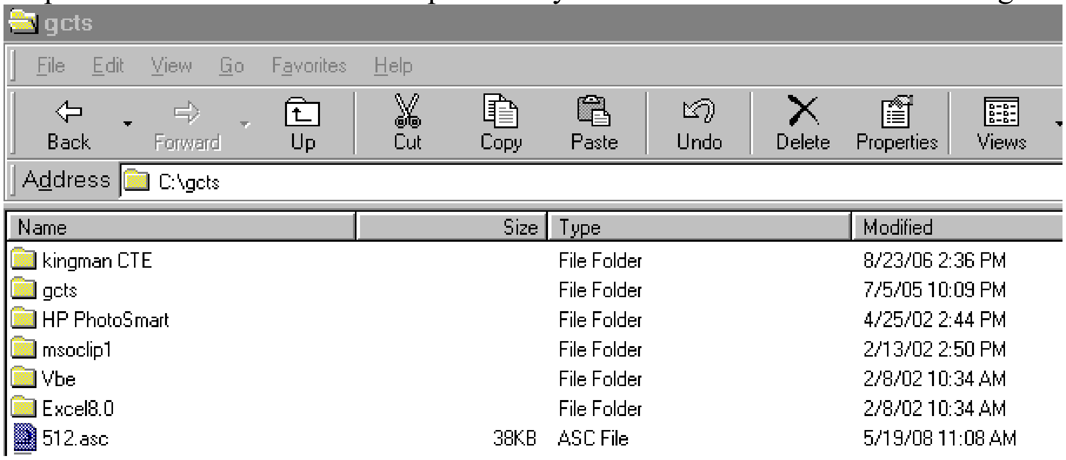

Address C:\gcts

Name	Size	Type	Modified
kingman CTE		File Folder	8/23/06 2:36 PM
gcts		File Folder	7/5/05 10:09 PM
HP PhotoSmart		File Folder	4/25/02 2:44 PM
msoclip1		File Folder	2/13/02 2:50 PM
Vbe		File Folder	2/8/02 10:34 AM
Excel8.0		File Folder	2/8/02 10:34 AM
512.asc	38KB	ASC File	5/19/08 11:08 AM

APPENDIX C
Finite Element Analysis of Evaporation Test Data

Evaporation Problem

A thin concrete slab with the lateral surfaces insulated from moisture removal, is initially saturated with the moisture concentration of 520 kg/m^3. The bottom end of slab is impervious and insulated from moisture removal as well. The top face is exposed to a low-pressure condition using a vacuum pump simulating two different stages of drying. During stage I, the test simulates a roughly constant evaporation rate of 0.42 kg/(m^{2}h) from the top face. However, during stage II drying which starts after 11.5 hours, evaporation can be observed as a convection-type process with zero ambient moisture concentration. The problem is a 1-D moisture transport from bottom end to the top face and therefore, a uniform mesh of n=1,2,.. linear elements is used for this problem. The forward difference method is applied to calculate several steps of the transient solution to the moisture diffusion problem. *L*=0.0125 m, *D(t)* and *$h_2(t)$* are presented as a function of time according to optimization works on analytical solutions as shown in Figure C.2.

A code is written to find the critical step for stable solutions. Moisture loss at each time step is calculated as the difference between the integration of moisture concentration inside the domain, and the initial moisture content. The results are compared with the experimental data and the results of Abaqus analysis.

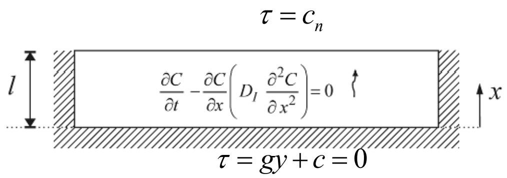

Stage I Drying

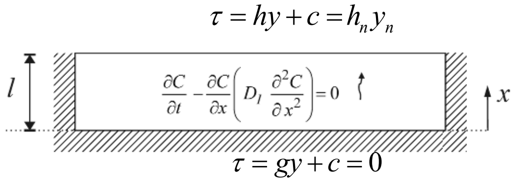

Stage II Drying

Figure C.1. Governing differential equations and boundary conditions of the problem

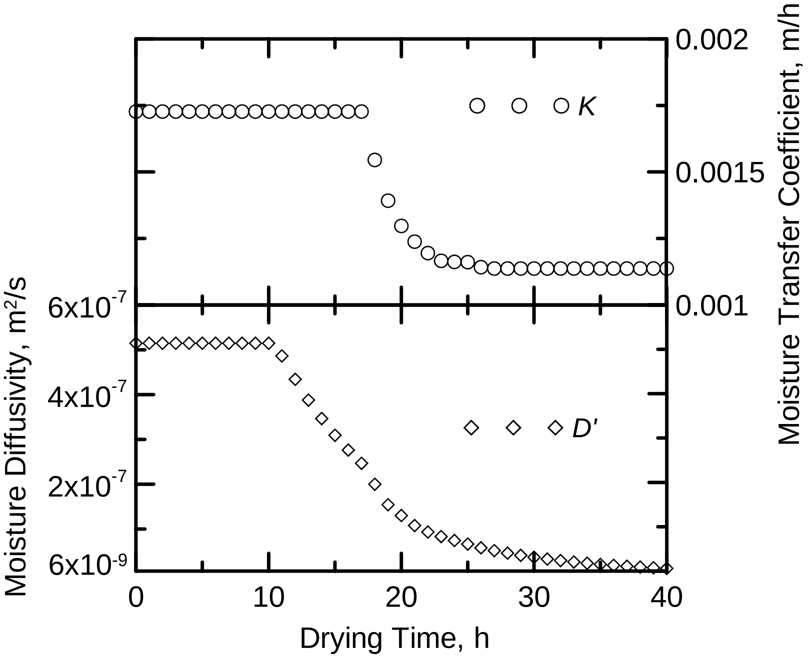

Figure C.2. Input diffusivity and moisture transfer coefficient as a function of time

Solution

General 1D time-dependent problem:

D.E.:

$$\underbrace{\rho(x)\frac{\partial^2 u(x,t)}{\partial t^2}+\mu(x)\frac{\partial u(x,t)}{\partial t}}_{time-dependent\ terms}\underbrace{-\frac{\partial}{\partial x}\left[\alpha(x)\frac{\partial u(x,t)}{\partial x}\right]+\beta(x)u(x,t)=f(x,t)}_{1D\ BVP}$$

B.C.s: mixed $\Rightarrow \tau = gy + c$

I.C.s: $u(x,t_0)=u_0(x)$

Moisture transport problem:

D.E.:

$$\frac{\partial C(x,t)}{\partial t}-\frac{\partial}{\partial x}\left[D\frac{\partial C(x,t)}{\partial x}\right]=0$$

$$\Rightarrow \rho(x)=0,\ \mu(x)=1,\ f(x,t)=0,\ \beta(x)=0,\ \alpha(x)=D$$

Galerkin's method of minimizing residuals:

Trial solution D.E.: $C(x,t;a)=\sum_{j=1}^{n} a_j(t)\phi_j(x)$

$$\int_{\Omega}\left[\frac{\partial C(x,t)}{\partial t}-\frac{\partial}{\partial x}\left(D\frac{\partial C(x,t)}{\partial x}\right)\right]\phi_i(x)dx=0$$

$i=1,2,...,n$

Integration by parts & substituting in residual equation

$$\int_{\Omega}\phi_i(x)\frac{\partial C}{\partial t}dx+\int_{\Omega}\frac{d\phi_i(x)}{dx}D\frac{\partial C}{\partial t}dx=-\left[\left(-D\frac{\partial C}{\partial x}\right)\phi_i(x)\right]_{x_1}^{x_n}$$

$i=1,2,...,n$

$$\frac{\partial C}{\partial x}=\sum_{j=1}^{n}a_j(t)\frac{d\phi(j)}{\partial x}$$

$$\frac{\partial C}{\partial t}=\sum_{j=1}^{n}\frac{da_j}{dt}\phi(j)$$

$$\underbrace{\sum_{j=1}^{n}\left(\int_{\Omega}\phi_i(x)\phi_j(x)dx\right)}_{c}\frac{da_j}{dt}+\underbrace{\sum_{j=1}^{n}\left(\int_{\Omega}\frac{d\phi_i(x)}{dx}D\frac{d\phi_j}{\partial x}dx\right)}_{k}a_j=\underbrace{-\left[\tau(x,t;a)\phi_i(x)\right]_{x_1}^{x_n}}_{f}$$

Forward difference method

In forward difference method all quantities are evaluated at backward end of time, t_{n-1}

$$C\{\dot{a}\}_{n-1}+K\{a\}_{n-1}=F_{n-1}$$

$$\{\dot{a}\}_{n-1}=\frac{\{a\}_n-\{a\}_{n-1}}{\Delta t_n}$$

Moisture transport in forward difference method

$$\left(\frac{1}{\Delta t_n}C\right)a_n=F_{n-1}+\left(\frac{1}{\Delta t_n}C-K\right)a_{n-1}$$

Capacity matrix

C can be diagonalized on the LHS.

$$CL_{ii}=\sum_{j=1}^{n}C_{ij}\ ,\ i=1,2,...,n,\ \ C_{ij}=0\ when\, i\neq j$$

$$[CL]^{-1} = \begin{bmatrix} 1/C_{L11} & 0 & 0 & 0 \\ 0 & 1/C_{L22} & 0 & 0 \\ 0 & 0 & \ddots & 0 \\ 0 & 0 & 0 & 1/C_{Lnn} \end{bmatrix}$$

$$a_n = a_{n-1} + \Delta t_n [CL]^{-1}\left(F_{n-1} - Ka_{n-1}\right)$$

<u>Solution for 1 linear element problem</u>

linear interpolation:

$$\phi_1 = \frac{x_2 - x}{L},\ \phi_2 = \frac{x - x_1}{L}$$

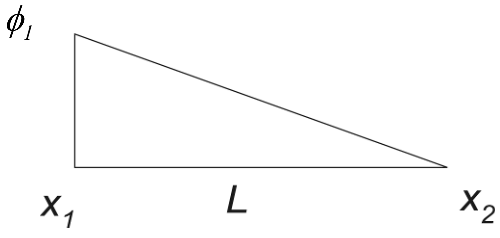

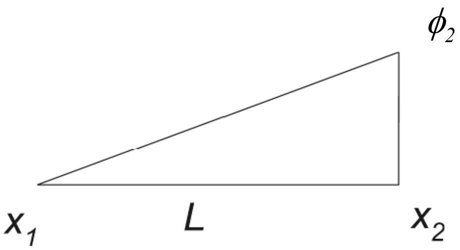

$$k_{ij} = \int_\Omega \frac{d\phi_i(x)}{dx} D \frac{d\phi_j}{\partial x} dx \qquad \Rightarrow K = \begin{bmatrix} D/L & -D/L \\ -D/L & D/L \end{bmatrix}$$

$$c_{ij} = \int_\Omega \phi_i(x)\phi_j(x)dx \qquad \Rightarrow C = L/6 \begin{bmatrix} 2 & 1 \\ 1 & 2 \end{bmatrix} \Rightarrow [CL]^{-1} = \frac{6}{L}\begin{bmatrix} 1/3 & 0 \\ 0 & 1/3 \end{bmatrix}$$

$$f_i = -[\tau\phi_i]_{x_1}^{x_n} \qquad \Rightarrow F_{stageI} = \begin{bmatrix} 0 \\ c_2 \end{bmatrix}$$

$\Rightarrow F_{stageII} = \begin{bmatrix} 0 \\ h_2 a_2 \end{bmatrix}$ but is modified by addition of h_2 term to [K]

Matrix equation at stage I for 1 linear element

$$\begin{bmatrix} a_1 \\ a_2 \end{bmatrix}_n = \begin{bmatrix} a_1 \\ a_2 \end{bmatrix}_{n-1} + \Delta t_n \left(\frac{6}{L}\right) \begin{bmatrix} 1/3 & 0 \\ 0 & 1/3 \end{bmatrix} \left(\begin{bmatrix} 0 \\ c_2 \end{bmatrix} - \begin{bmatrix} 4.12E-5 & -4.12E-5 \\ -4.12E-5 & 4.12E-5 \end{bmatrix} \begin{bmatrix} a_1 \\ a_2 \end{bmatrix}_{n-1} \right)$$

$$L = 0.0125,\ c_2 = -0.42/3600 = 1.667E-4$$

Matrix equation at stage II for one linear element

$$\begin{bmatrix} a_1 \\ a_2 \end{bmatrix}_n = \begin{bmatrix} a_1 \\ a_2 \end{bmatrix}_{n-1} + \Delta t_n \left(\frac{6}{L}\right) \begin{bmatrix} 1/3 & 0 \\ 0 & 1/3 \end{bmatrix} \left(\begin{bmatrix} 0 \\ h_2 a_2 \end{bmatrix} - \begin{bmatrix} 4.12E-5 & -4.12E-5 \\ -4.12E-5 & 4.12E-5 \end{bmatrix} \begin{bmatrix} a_1 \\ a_2 \end{bmatrix}_{n-1} \right)$$

$$\begin{bmatrix} a_1 \\ a_2 \end{bmatrix}_n = \begin{bmatrix} a_1 \\ a_2 \end{bmatrix}_{n-1} + \Delta t_n \left(\frac{6}{L}\right) \begin{bmatrix} 1/3 & 0 \\ 0 & 1/3 \end{bmatrix} \left(- \begin{bmatrix} 4.12E-5 & -4.12E-5 \\ -4.12E-5 & 4.12E-5-h_2 \end{bmatrix} \begin{bmatrix} a_1 \\ a_2 \end{bmatrix}_{n-1} \right)$$

$$L = 0.0125,\ h_2 \textit{ is given as a function of time}$$

Assembled matrices for n elements analysis

$$K_{stageI} = \begin{bmatrix} D/L & -D/L & 0 & & & \\ -D/L & 2D/L & -D/L & 0 & & \\ 0 & -D/L & 2D/L & -D/L & 0 & \\ & 0 & -D/L & \ddots & -D/L & 0 \\ & & 0 & -D/L & 2D/L & -D/L \\ & & & 0 & -D/L & D/L \end{bmatrix}$$

$$K_{stageII} = \begin{bmatrix} D/L & -D/L & 0 & & & \\ -D/L & 2D/L & -D/L & 0 & & \\ 0 & -D/L & 2D/L & -D/L & 0 & \\ & 0 & -D/L & \ddots & -D/L & 0 \\ & & 0 & -D/L & 2D/L & -D/L \\ & & & 0 & -D/L & D/L-h_2 \end{bmatrix}$$

$$[CL]^{-1} = \frac{6}{L}\begin{bmatrix} 1/3 & 0 & & & & \\ 0 & 1/6 & 0 & & & \\ & 0 & 1/6 & 0 & & \\ & & 0 & \ddots & 0 & \\ & & & 0 & 1/6 & 0 \\ & & & & 0 & 1/3 \end{bmatrix}$$

$F_{stageI} = \begin{bmatrix} 0 \\ 0 \\ \vdots \\ c_2 \end{bmatrix}$, $F_{stageII} = \begin{bmatrix} 0 \\ \vdots \\ 0 \end{bmatrix}$ since convection terms have been already added to the [K]

<u>Critical Time Steps</u>

To find out whether the solution technique is stable or not, the behavior of the solution as time $t \to \infty$ is monitored. If the behavior is oscillatory divergence, the solution technique is unstable. In this work, a forward difference method was used. This method is conditionally stable and the critical time step need to be found. The critical time step can be found through trial and error starting by large numbers of time steps and then decreasing it to a number which gives the stable results with no oscillation. The monitored results are the moisture concentration on the bottom, a_1 and moisture concentration on top, a_n which are selected as representative values of moisture concentration through the space domain.

As shown in below Figure C.3, the critical time steps for stage I drying is $152<\Delta t_{crit}<153$. Therefore $\Delta t = 150$ s was chosen for the rest of analysis. Similarly, the critical time step for number of element (n=2) was found to be between 37 and 38 s and therefore, 35 s was chosen for the rest of analysis. As shown in Figures C.3 to C.6, these critical time steps decrease by descretizing the space domain to more but smaller elements. At stage I for n=3, $16<\Delta t_{crit}<17$, and for n=4, $9<\Delta t_{crit}<10$. Similarly at stage II drying, for n=1, $151<\Delta t_{crit}<152$, for n=2, $40<\Delta t_{crit}<41$, for n=3, $17<\Delta t_{crit}<18$, and for n=4, $9<\Delta t_{crit}<10$. The results are in accordance with the formula for critical time step in the forward difference method which is:

$\Delta t_{crit} \cong \frac{2}{d\pi^2}\left((\mu/\alpha)\delta^2\right)$ which can be reduced to $\Delta t_{crit} \cong \frac{2}{\pi^2}\left(\frac{L^2}{D}\right)$

where, d is the spatial dimension of the problem, μ and α are from D.E. and δ is the distance between two adjacent nodes. This formula estimates the critical time step for n=1 as:

$$n = 1 \Rightarrow \left(\Delta t_{crit}\right)_{stageI} \cong \frac{2}{\pi^2}\left(\frac{0.0125^2}{4.12E-7}\right) = 76.85\,\mathrm{s} < 152\,\mathrm{s}$$

and for number of elements n = 2, estimates the critical time step as:

$$n = 2 \Rightarrow \left(\Delta t_{crit}\right)_{stageI} \cong \frac{2}{\pi^2}\left(\frac{0.0125}{2}\right)^2 \Big/ 4.12E-7 = 19.21\,\mathrm{s} < 37\ \mathrm{s}$$

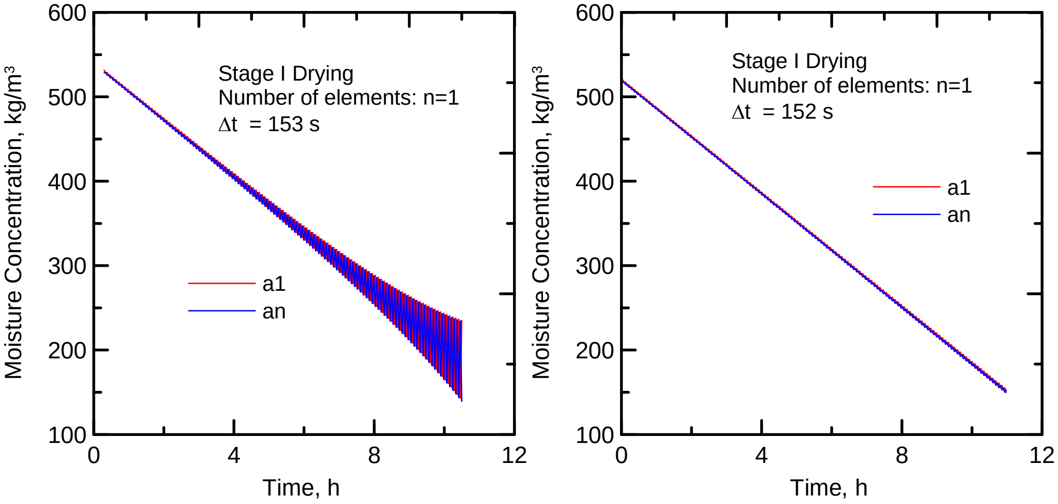

Figure C.3. Finding the critical time step ($152<\Delta t_{crit}<153$) by trial and error for FE analysis with 1 element

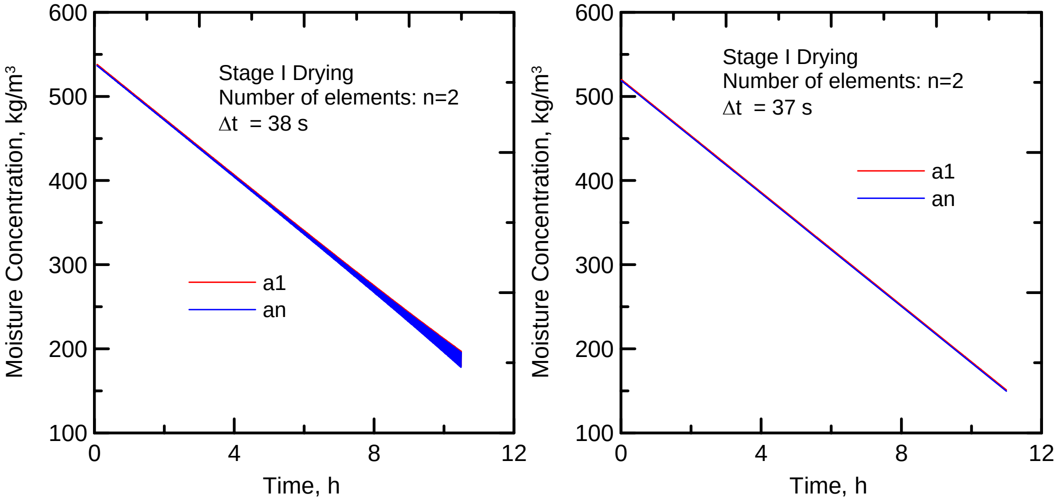

Figure C.4. Finding the critical time step ($37<\Delta t_{crit}<38$) by trial and error for FE analysis with 2 elements

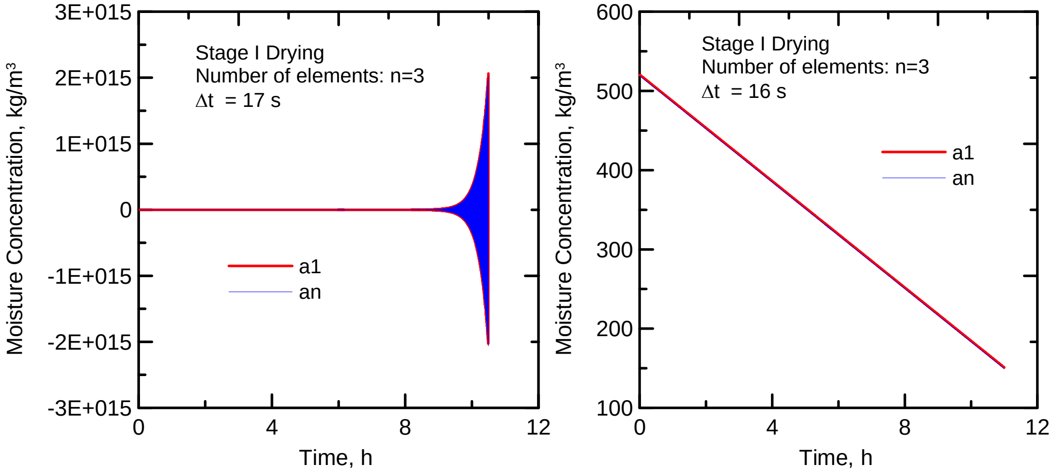

Figure C.5. Finding the critical time step ($16<\Delta t_{crit}<17$) by trial and error for FE analysis with 3 elements

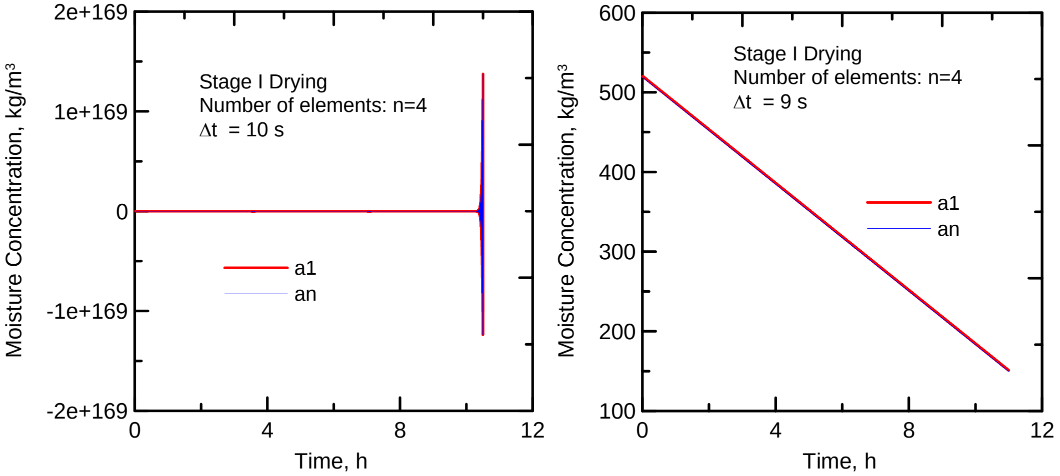

Figure C.6. Finding the critical time step ($9<\Delta t_{crit}<10$) by trial and error for FE analysis with 4 elements

Sensitivity of the 1D Analysis to the Number of Elements

The results of this FE analysis are intended to compare with the experimental data. However, the experimental data are measured as the cumulative moisture loss and not the direct measurement of moisture concentration. Therefore, the integration of moisture concentration over the space domain at each time step is compared with the initial moisture content to find the cumulative moisture loss. For the purpose of analyzing the sensitivity of the results to the number of elements, the cumulative moisture loss at the end of the test is used. The number of elements increases from n=1 to n=5 which translates into increase in the number of nodes from 2 to 6. As shown in Figure C.7, the final cumulative moisture loss are approaching to the asymptotic results from the upper side, but the difference is so insignificant that it may attributed to the noise of the system.

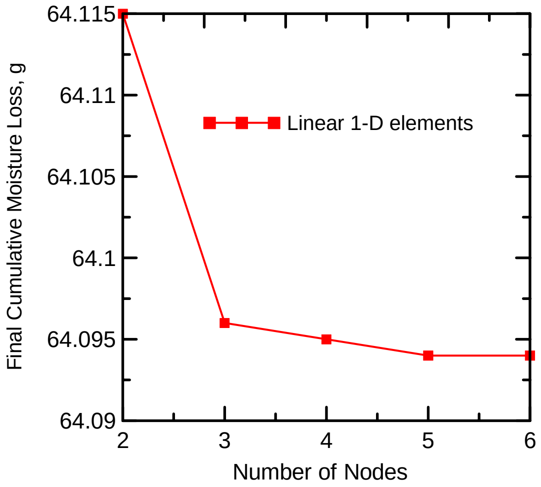

Figure C.7. Tracking the values of cumulative moisture loss at end of the test by increasing number of elements

Results of 1-D FE analysis with the MATLAB code

As shown in Figure C.8, the moisture concentration through the thickness of the sample can be predicted by this method. The FE analysis results show that there is not any significant difference between results of modeling with 1 or 2 elements. Also analyzing with smaller time steps does not have any effect on the predicted results. To verify the results with the experiments, the experimental moisture loss data are compared with the analytical results calculated as the difference between initial total moisture content and the integration of moisture concentration in the domain. The results show that the prediction is within 2% of the experimental results. Slight difference between the results of analysis and experiments is observed at the beginning of the stage II drying which can be due to the transition from stage I to stage II and the nature of proposed different boundary conditions. The comparison between results of 1-D FE analysis by the MATLAB code and the analytical results are shown in Figure C.9.

FE analysis by ABAQUS

The finite element analysis is carried out using ABAQUS v.6.10-1 [70]. The technique utilizes the analogy between the heat transfer and the moisture diffusion. The governing non-linear differential equation for the diffusional moisture transport in the domain of the problem can be written as:

$$\frac{\partial C}{\partial t} = D(C)\left[\frac{\partial^2 C}{\partial x^2} + \frac{\partial^2 C}{\partial y^2}\right]$$

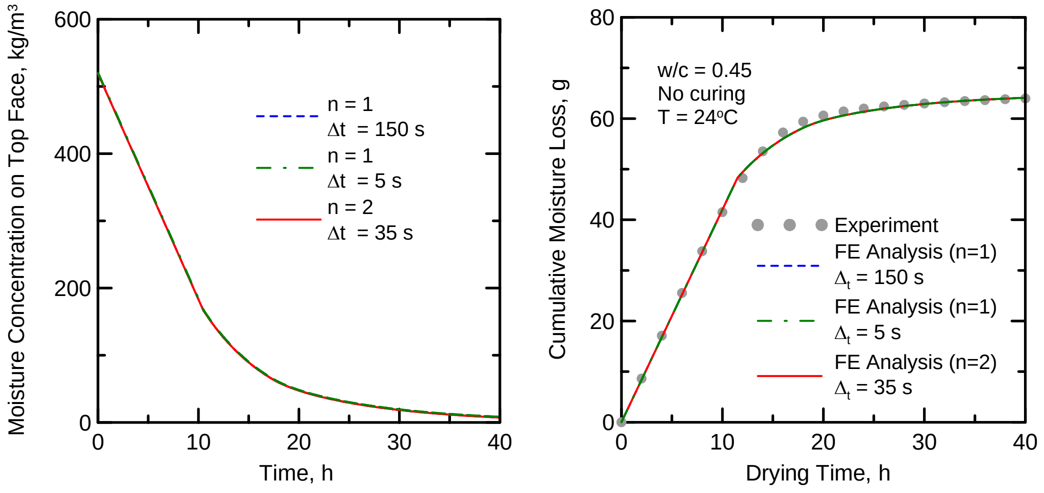

(a) (b)

Figure C.8. (a) Results of FE analysis with different elements and time steps. (b) Comparing the results with experimental data

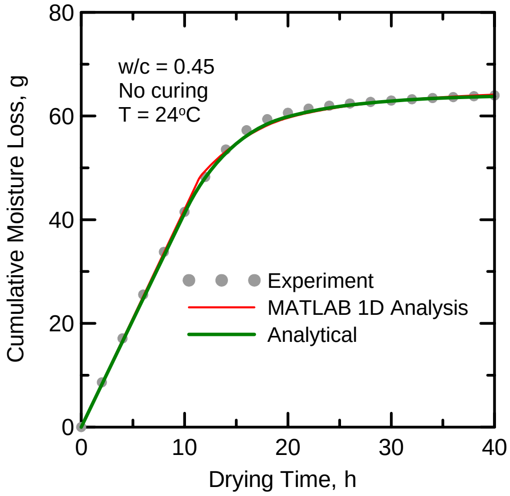

Figure C.9. Comparing results of 1-D FE analysis by the MATLAB code with the analytical results where *C(x,y,t)* is the moisture concentration varying in the domain with time, and *D(C)* is the isotropic moisture diffusivity coefficient which is a function of *C* itself. Moisture diffusivity at the boundary/surface of the sample during stage I drying is in the form of $J=F_0$ and during stage II drying is in the form of a convective boundary condition and can be written as:

$$J = -D(C)\frac{\partial C}{\partial n} = -k\,(C_s - C_*)$$

where

$\frac{\partial C}{\partial n}$ is the moisture gradient at the drying surface with a unit normal "n",

k is the convective moisture transfer coefficient,

Cs is the moisture concentration at the surface and

C* is the ambient moisture concentration.

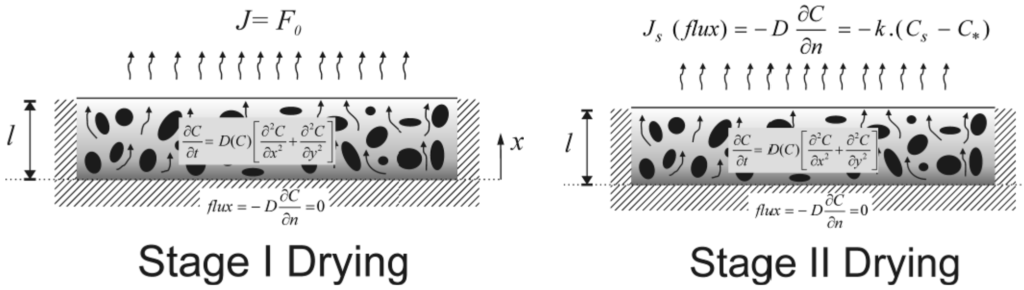

Figure C.10. Cement paste slab subjected to different boundary conditions during stag I and II drying

In equivalent transient thermal problem in 2-D space, the corresponding equations are given by:

$$\frac{\partial T}{\partial t} = \left(\frac{k}{\rho c}\right)\left[\frac{\partial^2 T}{\partial x^2}+\frac{\partial^2 T}{\partial y^2}\right]$$

whrere, *T(x,y,t)* is the temperature varying in the domain with time, and *k* is the isotropic thermal conductivity which may be a function of *T*, ρ is the density and *c* is the specific heat. While corresponding boundary conditions for heat transfer during stage I can be in the same form as diffusion problem ($J=F_0$), the heat convection at the boundary for the stage II drying can be written as:

$$\frac{\partial T}{\partial n} = h_{fT}\,(T_* - T_s)$$

where

$\frac{\partial T}{\partial n}$ is the thermal gradient with a unit normal “n”,

h_{fT} is the convective transfer coefficient for thermal problem,

T_s is the temperature at the boundary,

T_* is the ambient temperature.

Comparing governing and boundary equations of heat transfer and diffusion problems lead us to the conclusion of one-to-one analogy between these two boundary value problems under following correspondences:

Table C.1.
Analogy and corresponding terms between two boundary value problems

Diffusion Problem		Heat Transfer Problem
$C(x,y,t)$	⟷	$T(x,y,t)$
$D(C)$	⟷	$k/\rho c$
k	⟷	h_{fT}
C_*	⟷	T_*
C_s	⟷	T_s

Descriptions and details of the modeling

Due to 1-D flux, a thin slices like the one shown in the Figure C.11 can be a representative of all other slices perpendicular to top surface. In that slice, the concentration and flux will only changes according to the distance from the bottom/surface of sample.

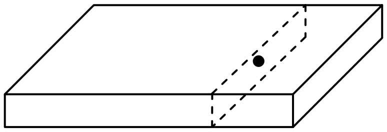

Figure C.11. A representative thin slice cut perpendicular to top surface for modeling 1-D moisture transport

An implicit heat transfer finite element analysis is carried out. The finite element domain is shown in Figure C.12.

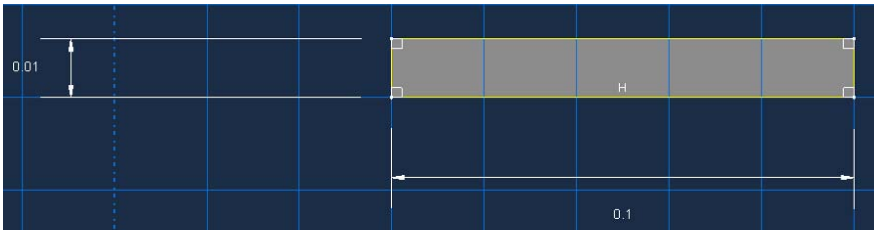

Figure C.12. Finite element domain

Material Properties

The material values used in the analysis are as follows:

(a) The moisture diffusivity of the slab as a function of concentration. The input values come from the analytical works shown in Figure C.2. However, in that figure, the values of diffusivity are shown as a function of time. Considering an average moisture concentration at each time step, the values of diffusivity can be plotted versus moisture concentration. This relationship is shown in Figure C.13 which is well-fitted by the CEB-FIP model [154]. These values can be introduced to Abaqus as isotropic concentration-dependent data in a tabular format.

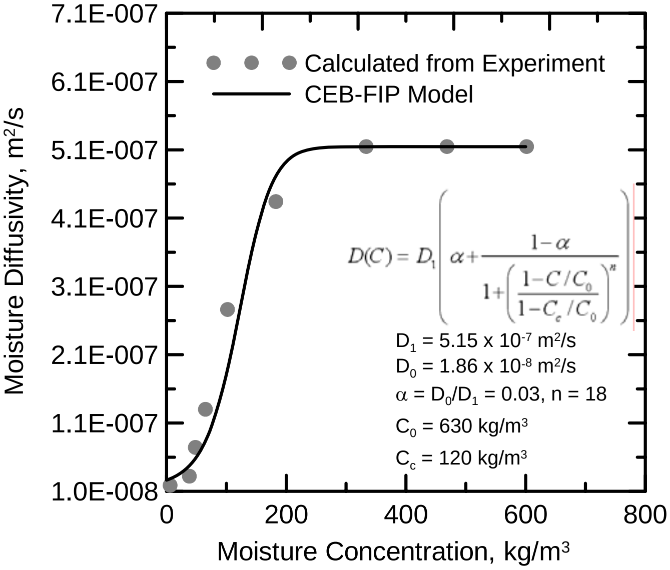

Figure C.13. Input values of diffusivity as a function of moisture concentration

(b) The density and specific heat are 1. Since in the mentioned analogy, *D(C)* corresponds to $k/\rho c$ and the values of moisture diffusivity are introduced for conductivity, the values of density (ρ) and specific heat (c) should be taken as 1.

Steps

Different steps defined for this specific problem are as follows.

(a) Initial step: In the initial step, a pre-defined field is created to be used as initial condition. The initial value of $C_i = 520\ kg/m^3$ is applied to the whole body as the initial condition.

(b) Step-1: This step is defined to simulate stage I drying. Since the top boundary conditions are different in the stage I from the stage II, these two steps have to be created separately.

(c) Step-2: This step is defined to simulate stage II drying. The initial condition in this step is selected as “computed” which refers to the results computed in the previous step.

Loadings

As shown in Figure C.14, the boundary condition of stage I drying (constant flux: $J=F_0$) is defined as a load with the magnitude of -0.42 kg/(m^{2}h). This value comes from the experimental analysis. This load is assigned to step-1 as the boundary condition for stage I. The other boundary conditions which are impermeable surfaces on the sides and bottom of the sample are ignored, since zero flux corresponds to zero load.

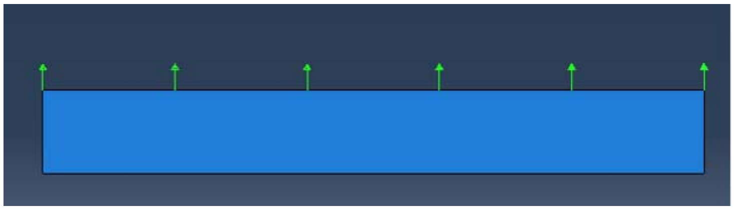

Figure C.14. The boundary condition of stage I drying defined as a load

Interaction

A single interaction is created for the purpose of imposing a convective boundary condition for the step-2. Convective transfer coefficient and ambient temperature are introduced into ABAQUS through defining a “surface film condition” type interaction with time-variable film coefficient presented in a tabular format and ambient temperature as a “sink temperature”. In this problem, the moisture transfer coefficient shown in Figure C.2 is inputted in the table for convective transfer coefficient and the sink temperature is taken 0 corresponding to ambient moisture concentration in the vacuum desiccator. The interaction then assigned to step-2 and the load boundary condition (constant flux for stage I) is inactivated for the step-2.

Convergence Studies on Different FEM Meshes

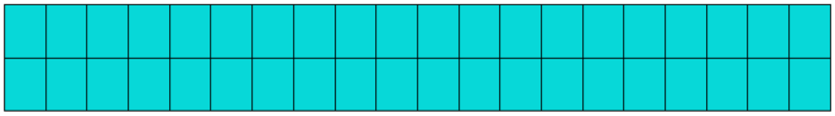

Figure C.15a. Mesh-1: 2 layers

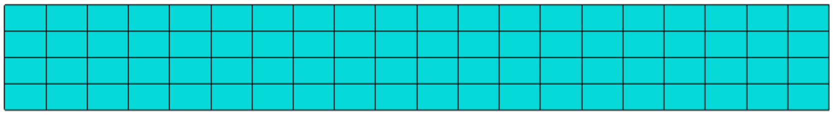

Figure C.15b. Mesh-2: 4 layers

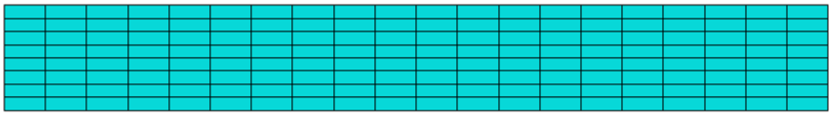

Figure C.15c. Mesh-3: 8 layers

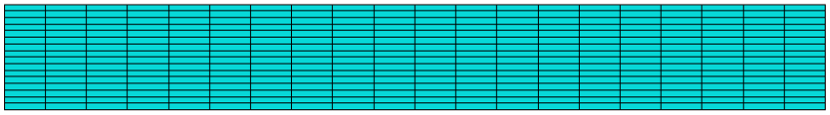

Figure C.15d. Mesh-4: 16 layers

Figure C.15e. Mesh-5: 32 layers

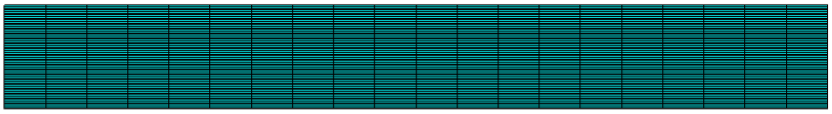

Figure C.15f. Mesh-6: 64 layers

Figure C.15. Different mesh sizes used for convergence studies

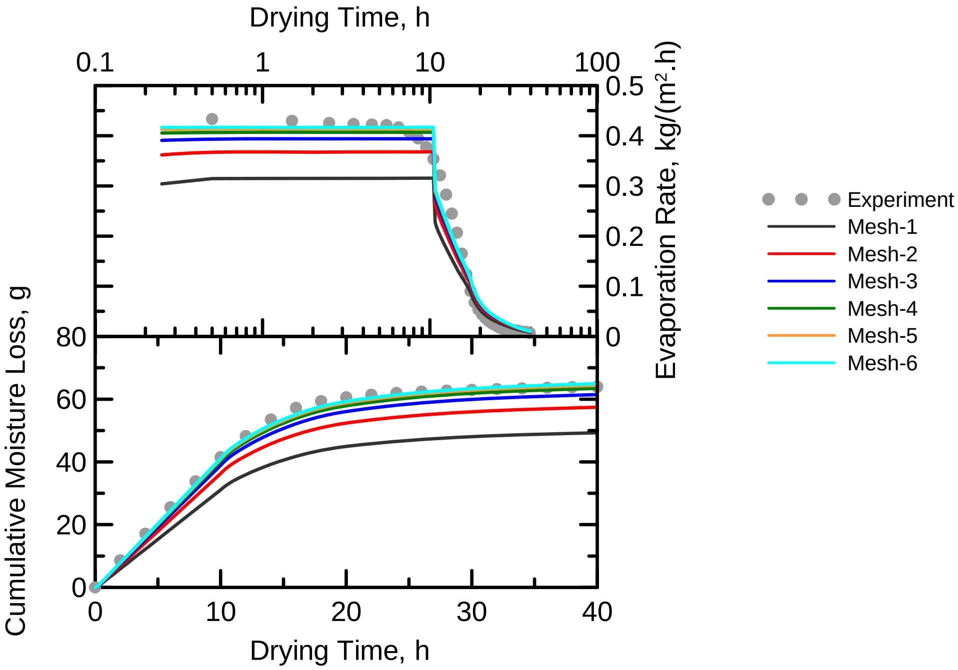

Figure C.16. Convergence studies on the results of evaporation tests with Q4 elements

Table C.2.
Results of FE analysis with ABAQUS using Q4 elements comparing to the experimental results

Model	Element type	Number of nodes	Number of elements	Initial flux (kg/(m^2.h))	Final Cumulative moisture loss (g)
Q4Slab-1	DC2D4	63	40	0.30401	49.2899
Q4Slab-2	DC2D4	105	80	0.36166	57.4078
Q4Slab-3	DC2D4	189	160	0.39079	61.4349
Q4Slab-4	DC2D4	357	320	0.40539	63.4345
Q4Slab-5	DC2D4	693	640	0.41269	64.4335
Q4Slab-6	DC2D4	1365	1280	0.41635	64.9328
Experiment	-	-	-	0.42	65

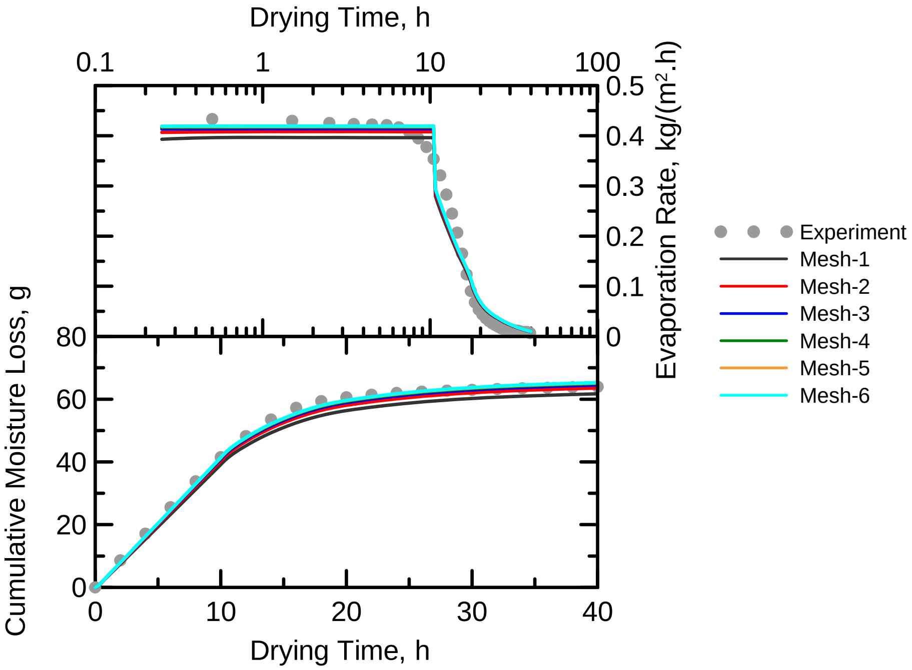

Figure C.17. Convergence studies on the results of evaporation tests with Q8 elements

(DC2D8: An 8-node quadratic heat transfer quadrilateral)

Table C.3.
Results of FE analysis with ABAQUS using Q8 elements comparing to the experimental results

Model	Element type	Number of nodes	Number of elements	Initial flux (kg/(m^2.h))	Final Cumulative moisture loss (g)
Q8Slab-1	DC2D8	165	40	0.39298	61.7196
Q8Slab-2	DC2D8	289	80	0.40662	63.5864
Q8Slab-3	DC2D8	537	160	0.41335	64.5142
Q8Slab-4	DC2D8	1033	320	0.41669	64.9723
Q8Slab-5	DC2D8	2025	640	0.41835	65.2012
Q8Slab-6	DC2D8	4009	1280	0.41918	65.3162
Experiment	-	-	-	0.42	65

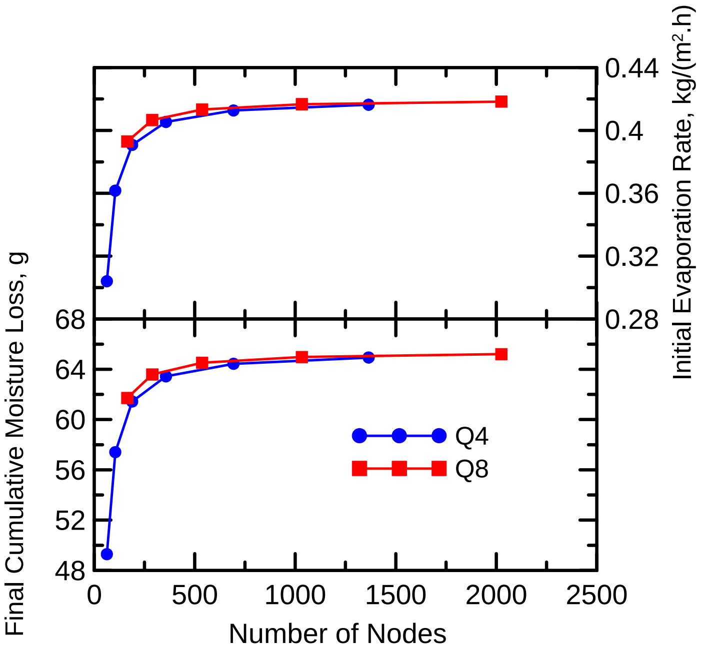

Figure C.18. Final cumulative moisture loss and initial evaporation rates versus number of nodes

Comparing FE Analysis and the Experimental Results

Mesh and Element types

For the purpose of comparison with the analytical analysis which was done in 100 layers, the same number of layers is used for meshing along y-direction (along the direction of external flux). As shown in previous section, this number of element ensures the convergence of the results as well. Since there is no moisture transfer along the x-direction (perpendicular to the direction of external flux), the domain is divided by 20 layers. The type of analysis is an implicit heat transfer analysis. Since the shape of domain is very simple and basic, a 4-node linear heat transfer quadrilateral element (DC2D4) is used in this analysis.

(a) The results of FE analysis regarding moisture concentration at nodes are shown in Figure C.19 in different times ranging from 2 to 40 h.

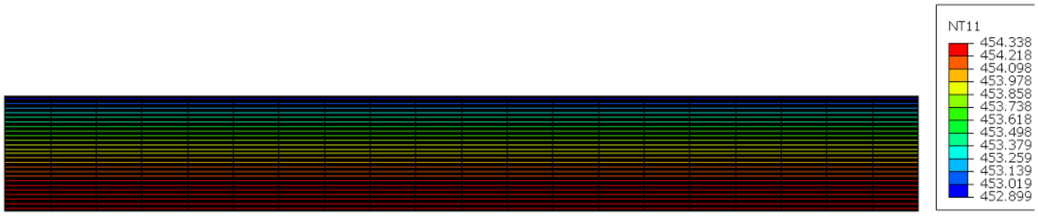

(a) t = 2 h

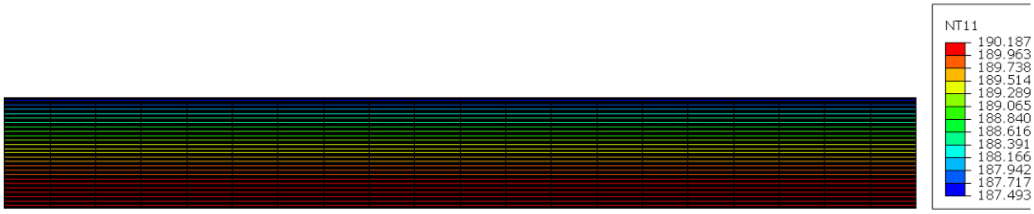

(b) t = 10 h

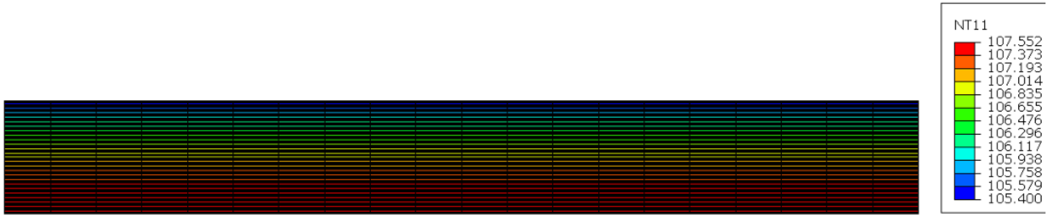

(c) t = 14 h

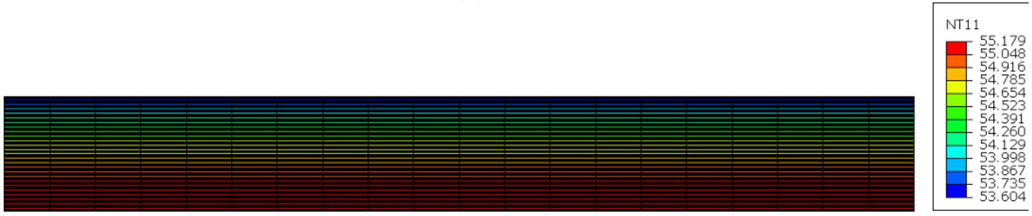

(d) t = 20 h

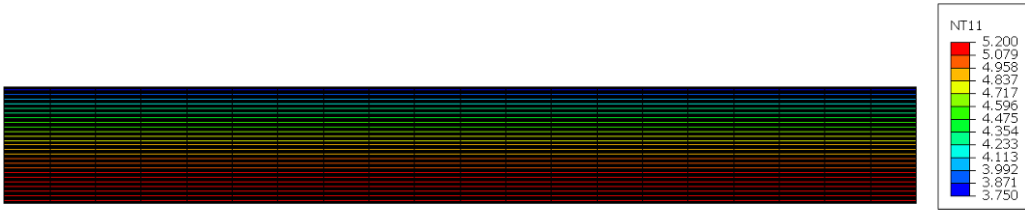

(e) t = 40 h

Figure C.19. Distribution of moisture concentration (kg/m^3) at: a) t=2 h, b) t=10 h, c) t=14 h, d) t=20 h, e) t=40 h

(b) The results of FE analysis regarding the flux at integration points are shown in Figure C.20 at different times ranging from 2 to 40 h.

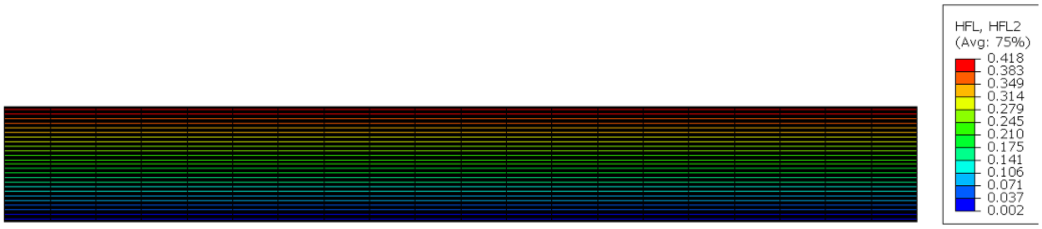

(a) t = 2 h

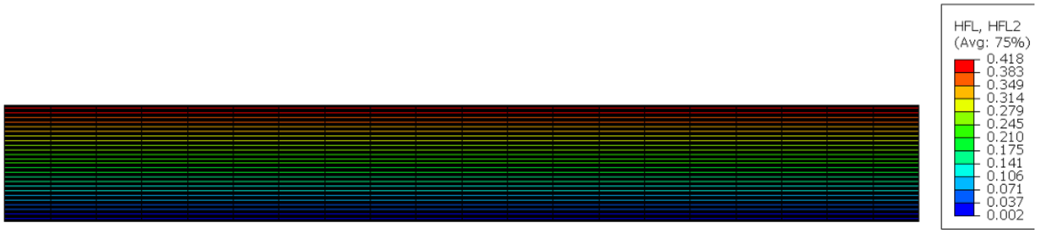

(b) t = 10 h

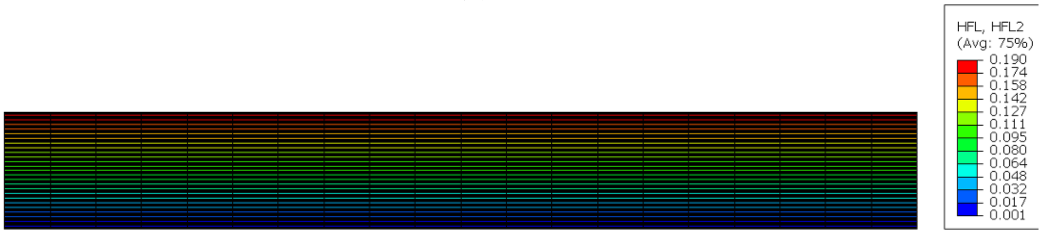

(c) t = 14 h

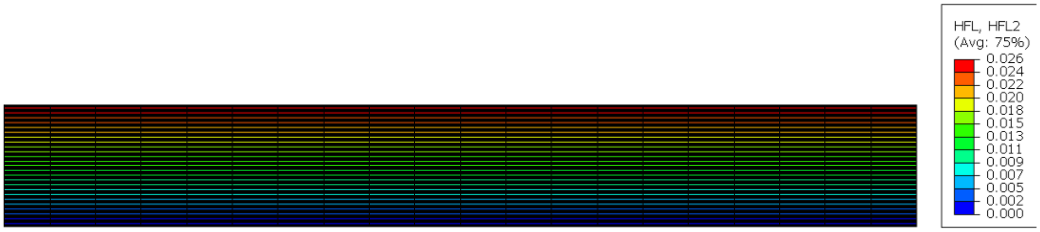

(d) t = 20 h

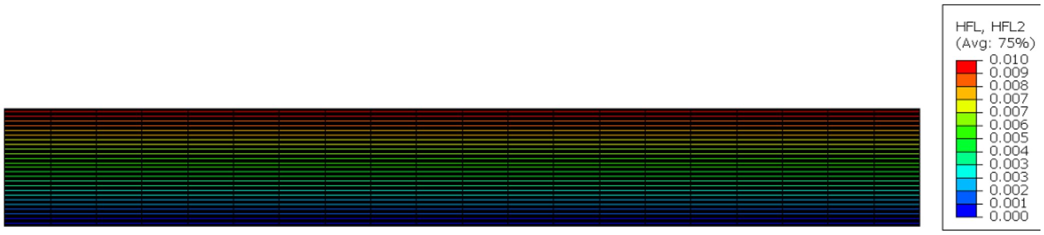

(e) t = 40 h

Figure C.20. Distribution of moisture flux (kg/(m^{2}h)) at: a) t=2 h, b) t=10 h, c) t=14 h, d) t=20 h, e) t=40 h

(c) The results of FE analysis regarding normalized moisture loss can be obtained by the integration of flux at the surface over the time. The total moisture loss however, can be calculated as the product of normalized moisture loss and the surface area. This result along with the results of experimental analysis, analytical works and 1D FE analysis (MATLAB code) is shown in Figure C.21 and C.22.

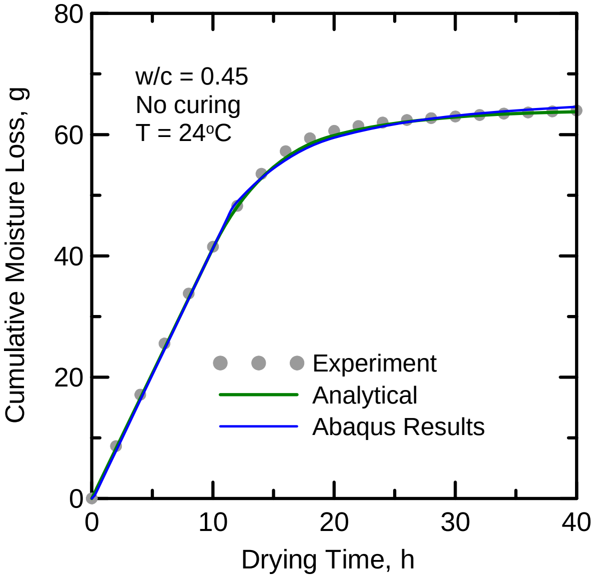

Figure C.21. Comparing results of FE analysis by ABAQUS with the analytical results

As shown in the Figure C.22, the results of 1-D FE analysis are very close to the ABAQUS results. Both results along with analytical results are within 2% of the experimental data (Figure C.9 and C.21). It seems that the proposed 1-D FE method and Abaqus analysis can be used to analyze the drying of cement-based materials in conditions where no analytical solution is available. The examples are:

- Analysis of drying of internally cured concrete materials by pre-soaked lightweight aggregate. In this case the lightweight aggregate acts as an internal volume moisture source.
- Analysis of the slow process of drying in cement-based materials consideration the aging factor. In this case, some amounts of moisture is consumed by the hydration process which can be modeled as an internal volume moisture sink.
- Analysis of drying of concrete element with complex shape, such as a concrete samples with oblique surfaces, etc...
- Analysis of 2-D/3-D moisture transport through concrete elements.

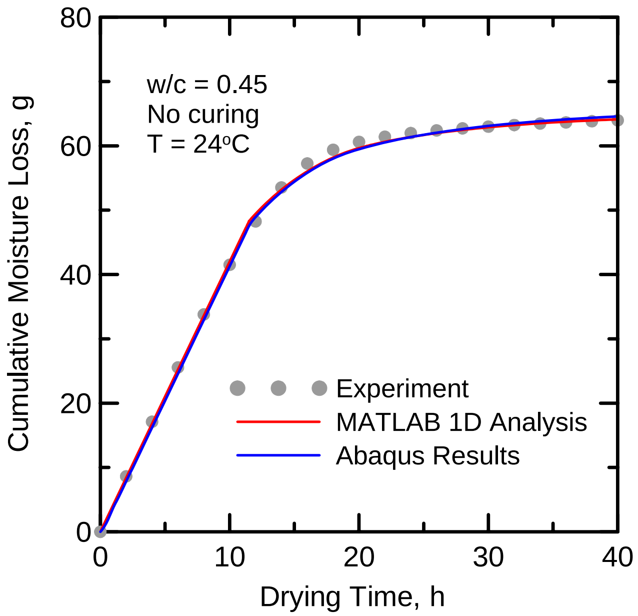

Figure C.22. Comparing results of analysis by ABAQUS with the experimental results and results of 1D analysis by the MATLAB code

Matlab Code

```
close all;clc;clear all;

%--------------------------- inputs -----------------------------
----------
% file and version
fname     = 'n1_delta_t150s.dat';             % result file
colWidth = 14;                      % format column width
digit    = 6;                       % format digit used
progVer   = 'Forward_8 04/10/11';   % program version

% element numbers and size
n =1;
L = 0.0125/n;

% test constants
Area = 0.01;    % surface are (m2)
F0 = 0.42/3600; % evaporation potential at stage I (kg/m2/s)
D_I = 5.15e-7;  % diffusion coefficient (m2/s)
t_trn = 10.5;   % transition time from stage I to II
t_final = 40;   % time of end of the test
ini_content_I = 530;     % in kg/m3

% input D_II and h2 as a function of time (from analytical works)
```

```
t_DII = linspace(0,((t_final-t_trn)*3600),60);
D_II_time =[5.14722E-07,4.86389E-07,4.59444E-07,4.34167E-
07,4.10278E-07,...
    3.87778E-07,3.66389E-07,3.46389E-07,3.27222E-07,3.09167E-
07,...
    2.92222E-07,2.76167E-07,0.000000261,2.46639E-07,2.11417E-
07,...
    1.99778E-07,1.74417E-07,1.54083E-07,1.37528E-07,1.29972E-
07,...
    1.17917E-07,1.07611E-07,9.84722E-08,9.30556E-08,8.79444E-
08,...
    8.31111E-08,7.85278E-08,7.42222E-08,7.01389E-08,6.62778E-
08,...
    6.26389E-08,5.77778E-08,5.46111E-08,5.15833E-08,4.875E-08,...
    4.60833E-08,4.35556E-08,4.11389E-08,3.88889E-08,3.675E-08,...
    3.47222E-08,3.28056E-08,0.000000031,2.93056E-08,2.76944E-
08,...
    2.61694E-08,2.47306E-08,2.33694E-08,2.20861E-08,2.08694E-
08,...
    1.97222E-08,1.86389E-08,1.76139E-08,1.66444E-08,1.57278E-
08,...
    1.48639E-08,1.40472E-08,1.32722E-08,1.25444E-08,1.18528E-08];
h2_time=-
[0.001727,0.001727,0.001727,0.001727,0.001727,0.001727,...

0.001727,0.001727,0.001727,0.001727,0.001727,0.001727,0.001727,..
.

0.001727,0.001648,0.001545,0.00146,0.001392,0.001339,0.001297,...

0.001264,0.001238,0.001215,0.001195,0.001178,0.001166,0.001162,..
.

0.001162,0.001162,0.001161,0.001152,0.001142,0.001137,0.001137,..
.

0.001137,0.001137,0.001137,0.001137,0.001137,0.001137,0.001137,..
.

0.001137,0.001137,0.001137,0.001137,0.001137,0.001137,0.001137,..
.

0.001137,0.001137,0.001137,0.001137,0.001137,0.001137,0.001137,..
.
    0.001137,0.001137,0.001137,0.001137,0.001137]/3600;


% -------------------------Analysis of stage I ------------------
----------
% initial condition for stageI
a_I = ones([(n+1) 1])*ini_content_I;

% time steps for stageI (s)
delta_t_I=150; %n=1:152 %n=2:37 %n=3:16 %n=4:9 %n=5:6 %n=6:4
%n=8:2
```

```
% inverse of lumping capacity matrix (CL-1)
CLm1 = zeros([(n+1) (n+1)]);
for i = 1:n+1
    CLm1(i,i) = 6/L*1/6;
end
CLm1(1,1)=6/L*1/3;
CLm1(n+1,n+1)=6/L*1/3;

% internal force is zero, however because of the mixed boundary
condition
% (i.e. tau1=g1y1+c1 & tau2=h2y2+c2), F_i refers to [c1;..;cn]
% at stage I [c1,...,cn-1] are zeros but cn is equal to outside
flux F0
F_I =zeros ([(n+1) 1]);
F_I(n+1) = -F0;

% K matrix includes the convection coefficient in addition to
alpha terms
% at stage I there is no convection and therefore it just has
alpha terms
K_I = zeros([(n+1) (n+1)]);
for i = 1:n+1
    K_I(i,i) =2*D_I/L;
    if i-1>0
        K_I(i,i-1)=-D_I/L;
    end
    if i+1<n+2
        K_I(i,i+1)=-D_I/L;
    end
end
K_I(1,1)=D_I/L;
K_I(n+1,n+1)=D_I/L;

% number of rounds for time domain of stageI
rounds_I = floor(t_trn*3600/delta_t_I);

% calculate {a}n based on {a}n-1 according to forward difference
a_I_store = [];
for m = 1:rounds_I
    M(m)=m;                 % store round numbers in an array
    a_I = a_I+delta_t_I*CLm1*(F_I-K_I*a_I);
    a_I_store = [a_I_store a_I];% extend the {a}n matrix
    D_I_t(m)=D_I;
    h2_I_t(m)=h2_time(1);
end

% plot the results of {a}n vs. time
T_M=M*delta_t_I/3600;    % convert rounds to actual time
figure(1);plot(T_M,a_I_store(n+1,M),'-r',T_M,a_I_store(1,M),'-b')
legend('a_n','a_1');
title('StageI: Moisture content on top and bottom of sample');
xlabel('Time, h')
ylabel('moisture content, kg/m3')
```

```
% cumulative moisture loss
sum_step_I = sum(a_I_store);
for i = 1:rounds_I
    Integ_a_I(i) = (sum_step_I(i)*2-a_I_store(1,i)-
a_I_store(end,i))*L/2*Area*1000;
    M_loss_I (i) = ini_content_I*(n*L)*Area*1000 - Integ_a_I(i);
end

% plot the CML vs. rounds
figure(2);plot(T_M,M_loss_I(M),'-r')
title('stageI: Cumulative Moisture Loss');
legend('Stage I:CML');
xlabel('rounds')
ylabel('Cumulative Moisture Loss, g')

fprintf(1, 'moisture loss at the end of stage I (g):  %5.4f\n',
M_loss_I(end));
%n=1:43.801, %n=2:44.030, %n=3:44.072 %n=4:44.090 %n=5:44.093
%n=6:44.0953
%%n=8:44.098




% -------------------------Analysis of stage II -----------------
-----------
% initial condition for stageI
a_II = a_I_store(:,end);

% time steps for stageII (s)
delta_t_II=150; %n=1:160 %n=2:50 %n=3:18 %n=4:9 %n=5:6 %n=6:4
%n=8:2

% internal force is zero, and [c1,...,cn] are also zeros
F_II =zeros ([(n+1) 1]);

% number of rounds for time domain of stageII
rounds_II = floor((t_final-t_trn)*3600/delta_t_II);

% calculate {a}n based on {a}n-1 according to forward difference
a_II_store = [];
for q = 1:rounds_II
    D_II = interp1(t_DII,D_II_time,(q*delta_t_II),'spline');   %
diffusivity m2/s
    %D_II = 5.15e-7*(0.03+(1-.03)/(1+((1-
mean(a_II)/ini_content_I)/(1-120/ini_content_I))^18));
    % diffusion m2/s
    h2 = interp1(t_DII,h2_time,(q*delta_t_II),'spline');   %
convection coefficient m/s
    % K matrix includes the convection coefficient in addition to
alpha terms
    % at stage II there is a convection term as "h2" which is
added to the last
```

```
    % term in the K matrix
    K_II = zeros([(n+1) (n+1)]);
    for j = 1:n+1
        K_II(j,j) =2*D_II/L;
        if j-1>0
            K_II(j,j-1)=-D_II/L;
        end
        if j+1<n+2
            K_II(j,j+1)=-D_II/L;
        end
    end
    K_II(1,1)=D_II/L;
    K_II(n+1,n+1)=D_II/L-h2;

    Q(q)=q;                 % store round numbers in an array
    a_II = a_II+delta_t_II*CLm1*(F_II-K_II*a_II);
    a_II_store = [a_II_store a_II];
    D_II_t(q)=D_II;
    h2_II_t(q)=h2;
end

% plot the results of {a}n vs. time
T_Q=Q*delta_t_II/3600+T_M(end);    % convert rounds to actual
time
figure(3);plot(T_Q,a_II_store(n+1,Q),'-r',T_Q,a_II_store(1,Q),'-
b')
title('StageII: Moisture content on top and bottom of sample');
legend('a_n','a_1');
xlabel('Time, h')
ylabel('moisture content, kg/m3')

% cumulative moisture loss
sum_step_II = sum(a_II_store);
for l = 1:rounds_II
    Integ_a_II(l) = (sum_step_II(l)*2-a_II_store(1,l)-
a_II_store(end,l))*L/2*Area*1000;
    M_loss_II (l) = ini_content_I*(n*L)*Area*1000 -
Integ_a_II(l);
end

% plot the CML vs. rounds
figure(4);plot(T_Q,M_loss_II(Q),'-r')
title('satge II: Cumulative Moisture Loss');
legend('Stage II: CML');
xlabel('Time, h')
ylabel('Cumulative Moisture Loss, g')

fprintf(1, 'moisture loss at the end of stage II (g):  %5.4f\n',
M_loss_II(end))
%n=1:


% -------------------------combine two stages -------------------
----------
```

```
a_store =[a_I_store a_II_store];
M_loss = [M_loss_I M_loss_II];
MQ = [M Q+M(end)];
T_MQ = [T_M T_Q];
D_t = [D_I_t D_II_t];
h2_total = [h2_I_t h2_II_t];

% plot the input D vs. time
figure(5); plot(T_MQ,D_t(MQ),'-r')
title('Input moisture diffusivity as a function of time');
legend('D(t)');
xlabel('Time, h')
ylabel('moisture diffusivity, m2/s')

% plot the input h2 vs. time
figure(6); plot(T_Q,-h2_II_t(Q),'-b')
title('Input convective moisture transfer coefficient as a
function of time');
legend('h2(t)');
xlabel('Time, h')
ylabel('convective moisture transfer coefficinet, m/s')

% plot the results of {a}n vs. time
figure(7); plot(T_MQ,a_store(n+1,MQ),'-r',T_MQ,a_store(1,MQ),'-
b')
title('Moisture content on top and bottom of sample');
legend('a_n','a_1');
xlabel('Time, h')
ylabel('moisture content, kg/m3')

% plot the CML vs. rounds
figure(8);plot(T_MQ,M_loss(MQ),'-b')
title('Cumulative Moisture Loss During the Test');
legend('Cumulative Moisture Loss');
xlabel('Time, h')
ylabel('Cumulative Moisture Loss, g')


% ------------------------ plot output results-------------------
----------
% (1.1) print input and output response
fid1 = fopen(fname,'w');
fprintf (fid1,' program version : %30s\n\n',progVer);

% (1.2) print heading of result file
textHeading = {'n';'L';'Area';'F0';'t_trn';'tfinal'};
valHeading  = [n,L,Area,F0,t_trn,t_final];
PrintHeading(fid1,textHeading,valHeading,colWidth,digit);
fprintf
(fid1,'**********************************************************
********************************************\n\n');

% (1.3) print table of result file
```

```
textData       =
{'Time';'D_t';'h2_t';'top_moisture';'bott_moisture';'moist_loss'}
;
data           = {T_MQ,D_t,-
h2_total,a_store(n+1,:),a_store(1,:),M_loss};
NJtableResult = StoreTable(data);
NJ             = NJtableResult{1};
tableResult    = NJtableResult{2};
PrintTable(fid1,textData,tableResult,NJ,colWidth,digit);
fclose all;
```

APPENDIX D

Drying Tests on Clays: An Application of the Developed Test Method

Results of Low-Pressure Drying Experiments on Clay

Wet clay has different microstructure than Portland cement paste including different particle size and distribution, and has no hydration characteristics to change the microstructure by the time. To evaluate the efficiency and applicability of the test method in capturing transport properties and evaporation characteristics of geological materials, two oversaturated clay samples were prepared and subjected to the vacuum drying. According to Attenberg test method, the clay used in this study has Liquid Limit (LL) of 38.16, Plastic Limit (PL) of 21.43, and Plastic Index (PI) of 16.73. Casagrade's plasticity chart distinguishes the mineral as Montmorillonite clay. The clay was passed through sieve No. 30 before placing in an oven maintaining a uniform temperature of 110°C for 24 h. The clay was removed after the material has been dried to a constant mass according to ASTM D 2216-05. The clay was then mixed with water with water-to-solid ratios of 0.45 and 0.6 and labeled by C0.45 and C0.60 samples compared to Portland cement paste P0.45. The mix design is shown in Table D.1.

Table D.1.
Mix proportions of the test series (kg/m^3)

Test series	Portland cement	Water	water-to-solid ratio
P0.45	1450	650	0.45
C0.45	1450	650	0.45
C0.60	1450	650	0.60

As shown in Figure D.1, after 48h drying the cumulative moisture loss of cement paste sample P0.45 was 66 g while the cumulative moisture loss of C0.45 and C0.60 samples were 74 and 77 g. This shows that 95% and 82% of the moisture initially added to the clay samples was evaporated at the end of the tests which confirms the capability of the test method in simulating the drying process.

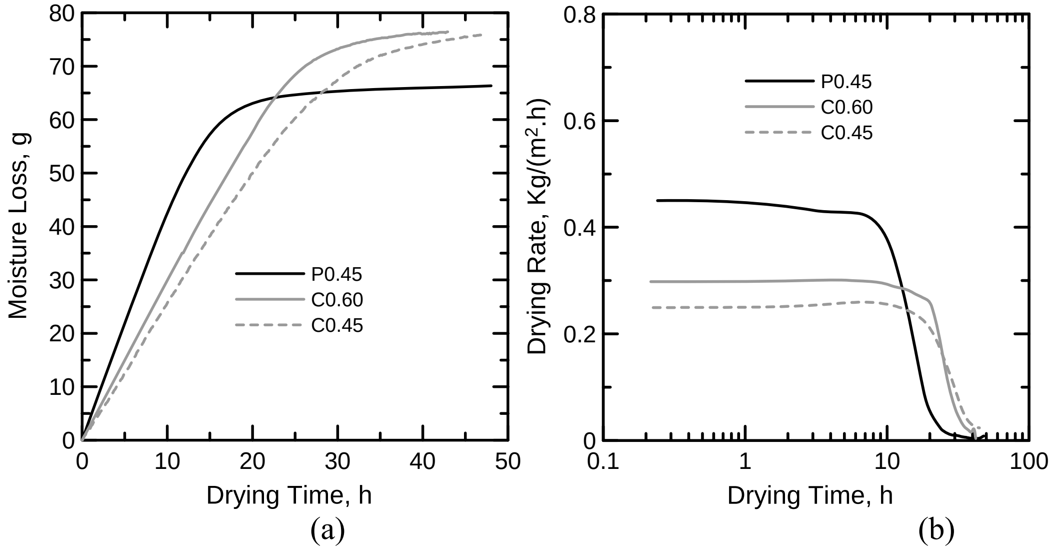

Figure D.1. Results of low-pressure evaporation tests on clay samples and their comparison with plain cement paste sample: (a) cumulative moisture loss curves; (b) drying rate curves

The calculated evaporation rates during drying test are shown in Figure D.1b. The average calculated drying rate at initial stages of drying for clay samples with w/s ratio of 0.45 and 0.6 were 0.25 kg/(m^2h) and 0.28 kg/(m^2h), respectively. Comparing these rates with 0.42 kg/(m^2h) for the plain cement paste sample (P0.45) indicates that clay decreases the initial evaporation rates during early stage of drying. It may be related to the mass transfer at the boundary of the material which appears to be taken place in a thin film inside porous medium under the vacuum condition. This transition layer is defined as the location where the pressure drops from the saturated water vapor pressure to the pressure of the vacuum chamber [189]. This pressure drop induces a gas flux between porous medium and the vacuum chamber, and determines the mass transfer at the boundary of the material. During the drying process, the thickness of this transition layer which controls the intensity of the mass flux is regulated by the physical properties and microstructure of the material [189]. Therefore, the difference in the physical properties and microstructure of clay and Portland cement could be the reason of different initial evaporation rates.

This observation indicates that similar to cement pastes the drying of clay under constant low-pressure conditions occurs in two distinct stages of a constant drying rate period (stage I), and a falling drying rate period (stage II). During stage I drying, the main phase transitions occur at the boundary surface and vapor phase diffusion into the air is determining rate of evaporation. Reaching a critical value of moisture content at the surface, the material is unable to support the necessary flux to the surface and rate of evaporation starts to fall. During stage II drying, the removal of moisture is mainly controlled by diffusion which dominates the capillary forces [106]. The transition time from stage I to stage II drying was significantly altered from 9.7 h for cement paste to 26.8 h and 24.1 h for clays with w/s ratios of 0.45 and 0.60 respectively.

Simplified analysis of drying experiments on clay

In order to simulate the results of drying tests using a dual-stage drying concept, two different boundary conditions at the top surface are required. As shown in Figure D.1, first, a boundary condition of constant flux is applied followed by the boundary condition of constant concentration, that is set to ambient moisture concentration (i. e. zero in this case). The moisture transfer inside the matrix is simulated by Fick's second law of diffusion which governs a majority of moisture transfer problems in porous media [58, 108].

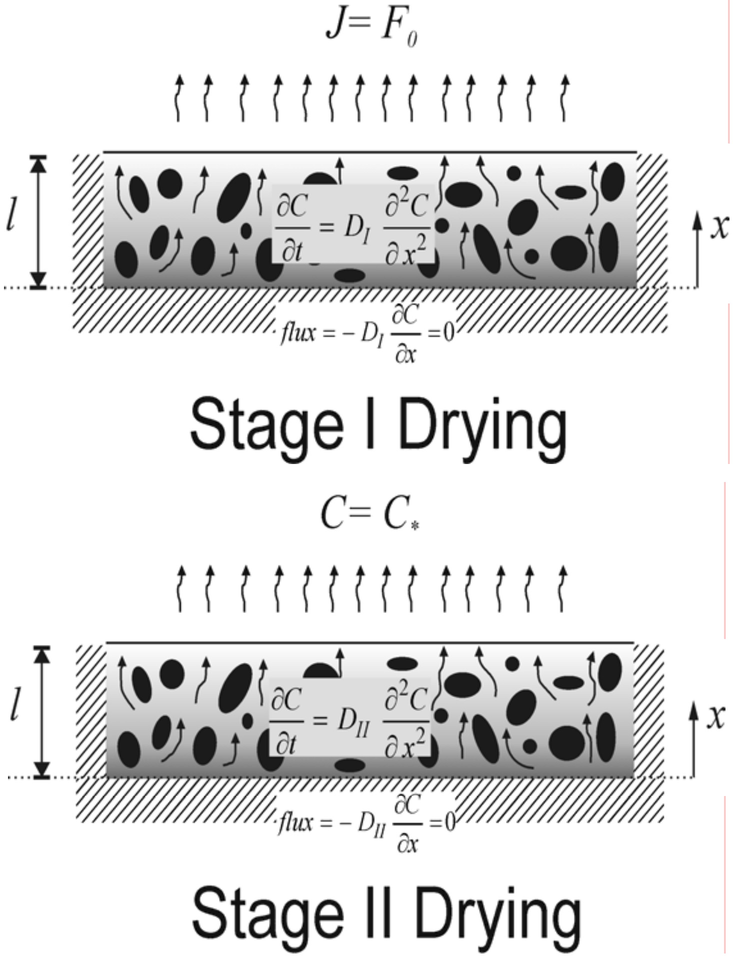

Figure D.2. Boundary conditions and Fick's 2nd law of diffusion for the presented drying problem

The analytical solution for the initial and boundary conditions of stage I drying, assuming a constant diffusivity is given by Eq. (1) [109].

$$C(t,x) = C_i + \frac{F_0 L}{D_I}\left\{\frac{D_I t}{L^2} + \frac{3x^2 - L^2}{6L^2} - \frac{2}{\pi^2}\sum_{n=1}^{\infty}\frac{(-1)^n}{n^2}\exp(\frac{-D_I n^2 \pi^2 t}{L^2})\cos\frac{n\pi x}{L}\right\} \tag{D.1}$$

where C is the moisture concentration (kg/m^3), D is the moisture (liquid and vapor) diffusion coefficient (m^2/s) and t is the time (s). Also, C_i is the initial moisture concentration (kg/m^3), F0 is the constant flux in stage I drying (kg/(m^{2}s)), and L is the thickness of sample (m). Using this solution, moisture concentration at the top surface is obtained providing constant F0 and D_I values. Since stage I drying ends when the surface reaches equilibrium moisture concentration (i. e. zero), moisture diffusivity at stage I drying is calculated as long as the time of transition from stage I to stage II has not lapsed.

For stage II drying, analytical solution can be integrated over the thickness of sample. The total amount of diffusing moisture in stage II drying, M_t (kg), can be obtained from the corresponding quantity after infinite time, M_∞ (kg). Therefore, moisture loss during the advanced phase of drying is given by [109]:

$$\frac{M_t}{M_\infty} = 1 - \sum_{n=0}^{\infty}\frac{8}{(2n+1)^2\pi^2}\exp\{-D_{II}(2n+1)^2\pi^2 t/4L^2\} \tag{D.2}$$

Considering only first term of the series, moisture diffusivity, D_{II} (m^2/s), can be derived by

$$D_{II} = \frac{-4L^2}{\pi^2}\cdot a_{\ln} \quad \text{when} \quad \ln\left(1 - \frac{M_t}{M_\infty}\right) - \ln\frac{8}{\pi^2} = a_{\ln}\, t \tag{D.3}$$

As shown in Table D.23 and Figure D.3, the diffusivities of clay samples C0.45 and C0.60 at the stage I drying were 1.4x10^{-7} and 1.1x10^{-7} m^2/s which are 4 times smaller than the initial diffusivity of cement paste. However, the diffusivities at stage II drying for C0.45 and C0.60 samples were higher by 20% and 140% compared to cement paste. While the difference between the results of clays and cement pastes may be related to their physical and microstructural differences, the difference between the results of two clay samples may be discussed by different amount of moisture concentrations. Unlike the stage I drying, diffusion coefficients in Stage II drying depend on moisture concentration [110]; however, in this analysis diffusivity in stage II is taken constant resulting in calculation of an average diffusivity, which is averaged over space and time.

Table D.2.
Initial evaporation rates, transition time, evaporation rate at 24 h, cumulative moisture loss, and diffusivities of tested samples

Test series	Initial evaporation rate (kg/(m^2.h))	Transition time of drying stages (h)	Evaporation rate at 24 h (kg/(m^2.h))	Cumulative moisture loss at 48 h (g)	Moisture diffusivity at stage I (m^2/s)	Moisture diffusivity at stage II (m^2/s)
P0.45	0.42	9.7	0.024	66	5.1E-07	3.3E-09
C0.45	0.28	26.8	0.167	74	1.4E-07	8.0E-09
C0.60	0.25	24.1	0.176	77	1.1E-07	4.0E-09

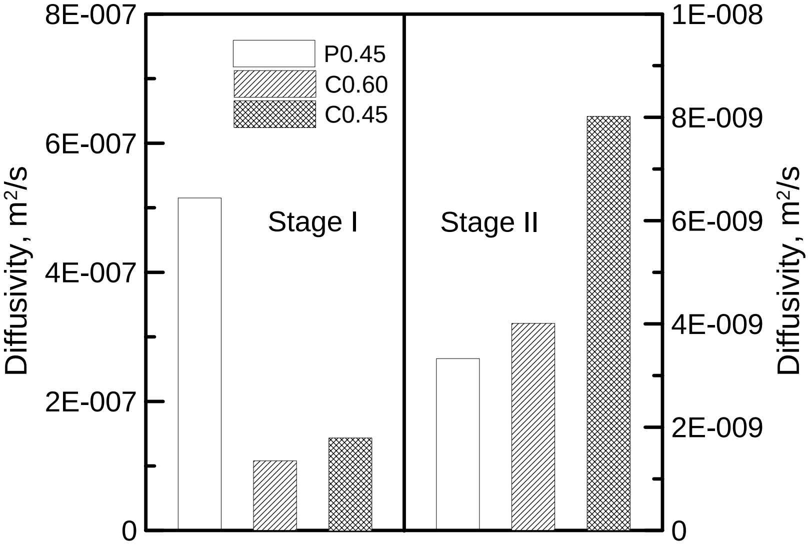

Figure D.3. Results of diffusion analysis on wet clay and cement paste samples

Advanced Moisture Transport Analysis on the Drying Clay

The advanced modeling of drying of cementitious materials as porous media is presented in the Appendix. It first provides an overview of existing theories for the drying of porous media using a single non-linear diffusion equation, which is accounted for all processes namely, Darcian transport of liquid and vapor water, and diffusion of vapor in dry air. The main mechanisms of drying are identified accordingly in two separate stages of drying based on connectivity of liquid and vapor phases inside the pores, observed qualitatively through experiments. Then a quantitative model of drying is proposed, in which each mechanism is accounted for by appropriate equations. It is shown that the developed model can well predict the experimental data of the drying of cement-based materials, and moisture distribution as well as moisture diffusivity and its variations with time. The same analytical method is applied to clay samples. Results of analysis are shown in Figure D.4 which presents a fairly well prediction of the drying data by the variation of diffusivity and slight variation of moisture transfer coefficient. Results of analysis show that the diffusion coefficients vary in the range of 2.2×10^{-7} to 1.34×10^{-8} m^2/s. These results are in good agreement with the results of Ketelaars [190] who reported diffusivity values in the range of 1×10^{-7} to 1×10^{-9} m^2/s for different clay samples.

Image Analysis on Early-Age Cracked Samples

Time-lapse photography shows that visible early-age cracks were detected in the clay samples sample as early as 6 h and it developed throughout the test. The cracking area versus time is shown in Figure D.6 and Figure D.7 shows a cracked clay sample after 48 h of vacuum drying.

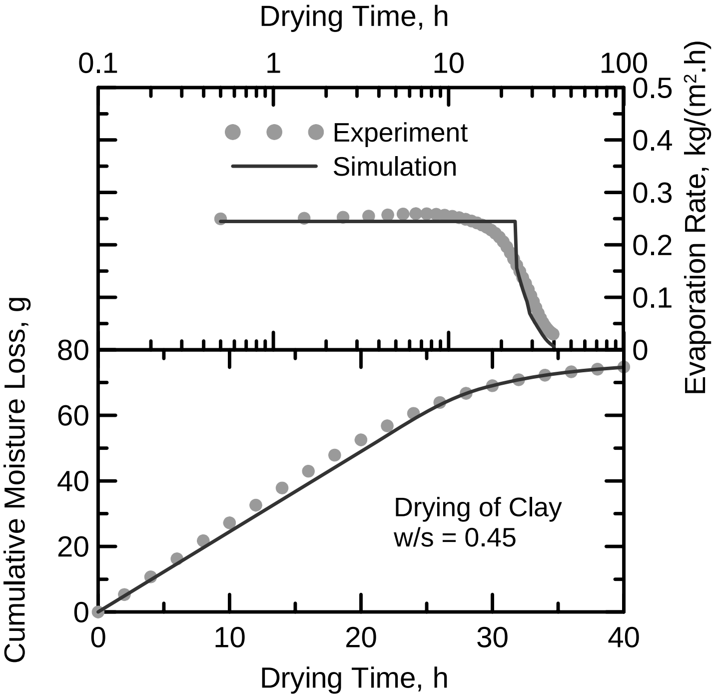

(Figure D.4(a))

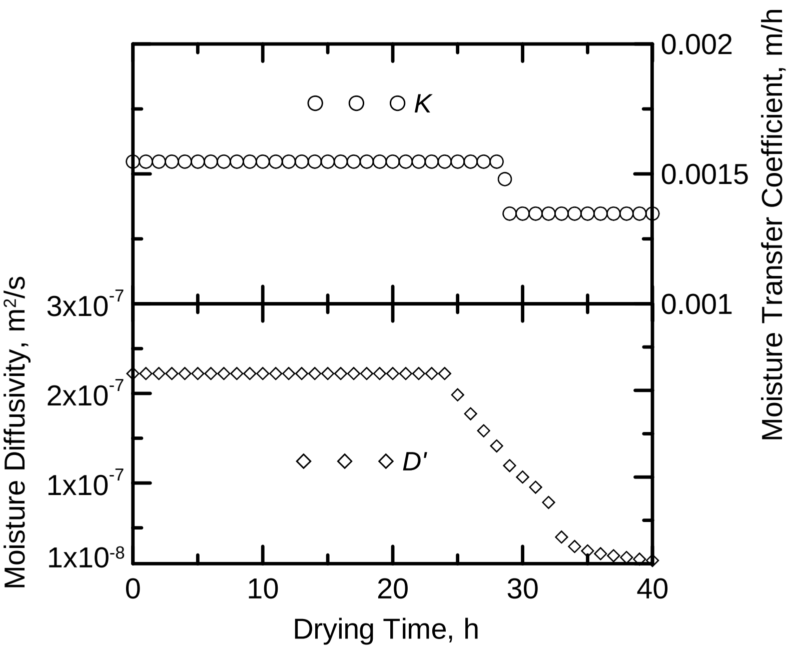

(Figure D.4(b))

Figure D.4. (a) Prediction of cumulative moisture loss and evaporation rate as a function of time for the experimental data of an evaporation test, (b) Back-calculated *D* and *k* for the best fit of data

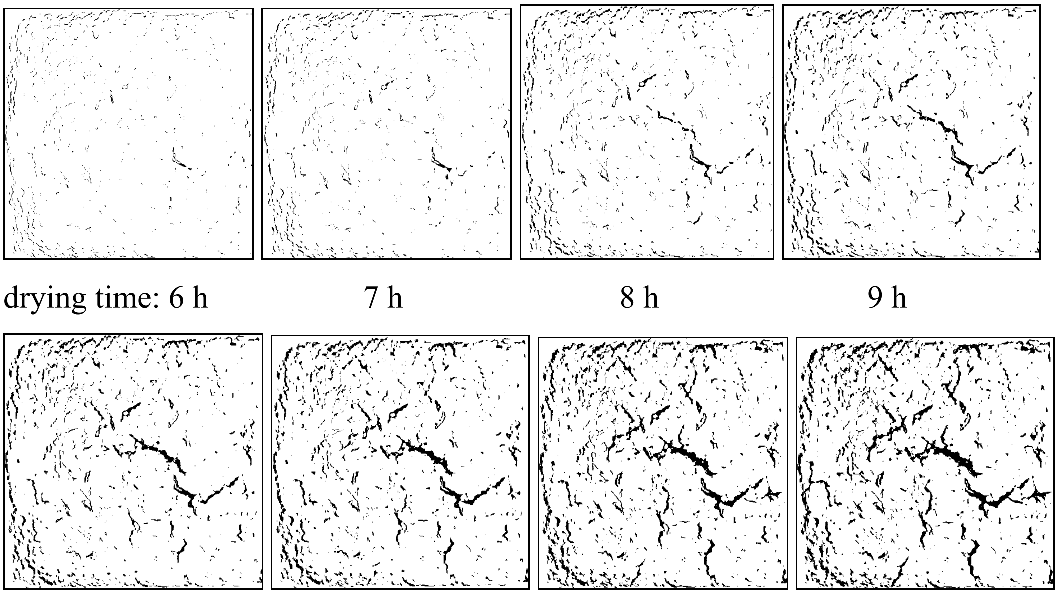

drying time: 6 h 7 h 8 h 9 h

drying time: 10 h 11 h 12 h 13 h

Figure D.5. 2-D Crack development during drying of a clay sample

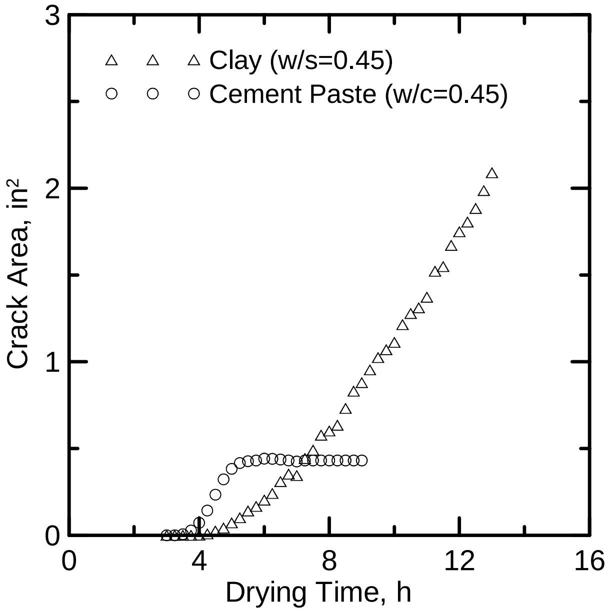

Figure D.6. Comparing cracking area of a clay sample vs. time with a Portland cement paste

Figure D.7. Image of a 2D crack pattern in a clay sample after vacuum drying for 48 h

APPENDIX E

Image Analysis on Early-age Cracks: Quantification and Orientation

Quantification of Crack Parameters

Several parameters for the quantification of crack patterns are presented. The parameters are used to compare shrinkage cracks in different samples. First, these parameters are introduced and then their values for different samples using an automatic procedure developed by a computer code are compared.

Interesting parameters for quantification of cracks in concrete samples

1. Total area of cracks, A (mm^2): A is the total area of cracks on the image.
2. Areal fraction, A_A (mm^2/mm^2): A_A is the ratio between the areas of the counted cracks to the entire area of the image.
3. Total length of cracks, L (mm): L is the total dendritic length of all the skeletonized cracks in the image.
4. Average crack length, L_{mean} (mm): L_{mean} is the mean value of the dendritic length of all cracks in the image.
5. The crack density, L_A (mm/mm^2): L_A is the total dendritic length of cracks per image area.
6. Average width of cracks, W (mm): W is the total area of cracks (A) divided by total dendritic length (L).
7. Total number of cracks, N_{total} (-): N_{total} is the total number of objects in the binary image of cracks.
8. Number of cracks per unit area, N_A ($1/mm^2$): N_A is the total number of features (cracks) divided by the area of image.
9. Total number of crack intersections, N_{Int} (-): N_{Int} is the count of intersection points in the image of crack.
10. Average nearest neighbor distance in plane, Δ_2 (1/mm): Δ_2 presents a measure for the average centre-to-centre distance of randomly dispersed nearest neighbors in a plane which is closely related to the configuration and can be demonstrated as $\Delta_2 = 0.5 / N_A^{1/2}$.

Beside above parameters, length and width of all detected cracks in the image are calculated. The graphs of normal probability density and normal cumulative density present more information of the distribution of crack length and crack width in the image.

Automatic procedures for the quantification of crack parameters

Step 1: make a binary image of crack pattern

Step2: Detect cracks intersection points from skeletonized image of crack

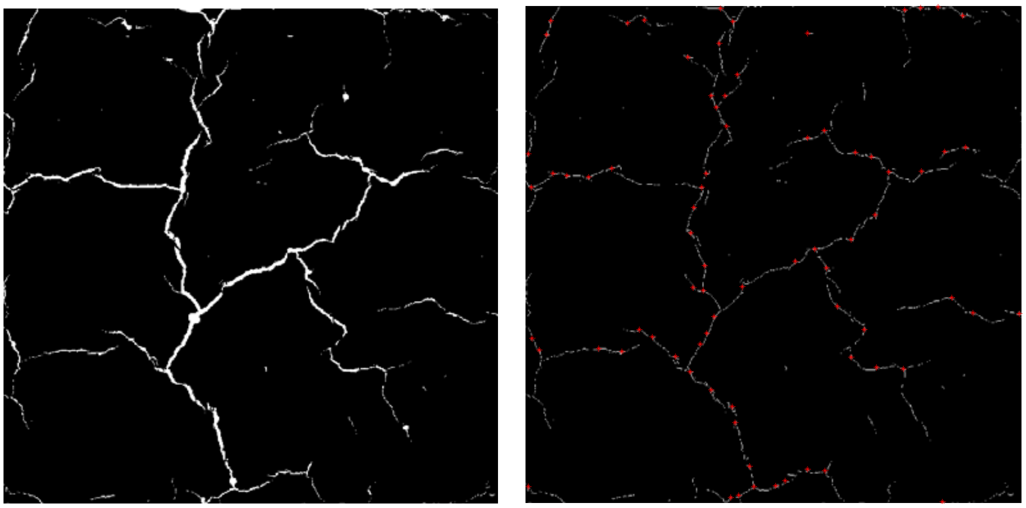

Step 3: Dilate the intersection points

Step 4: Subtract dilated intersection points from the initial binary image

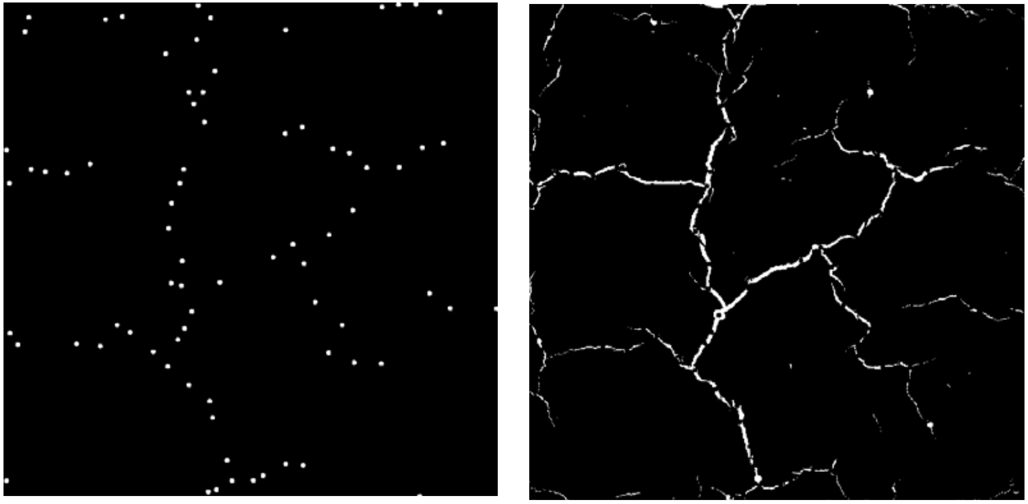

Figure E.1. The process of image analysis on a cracked paste sample

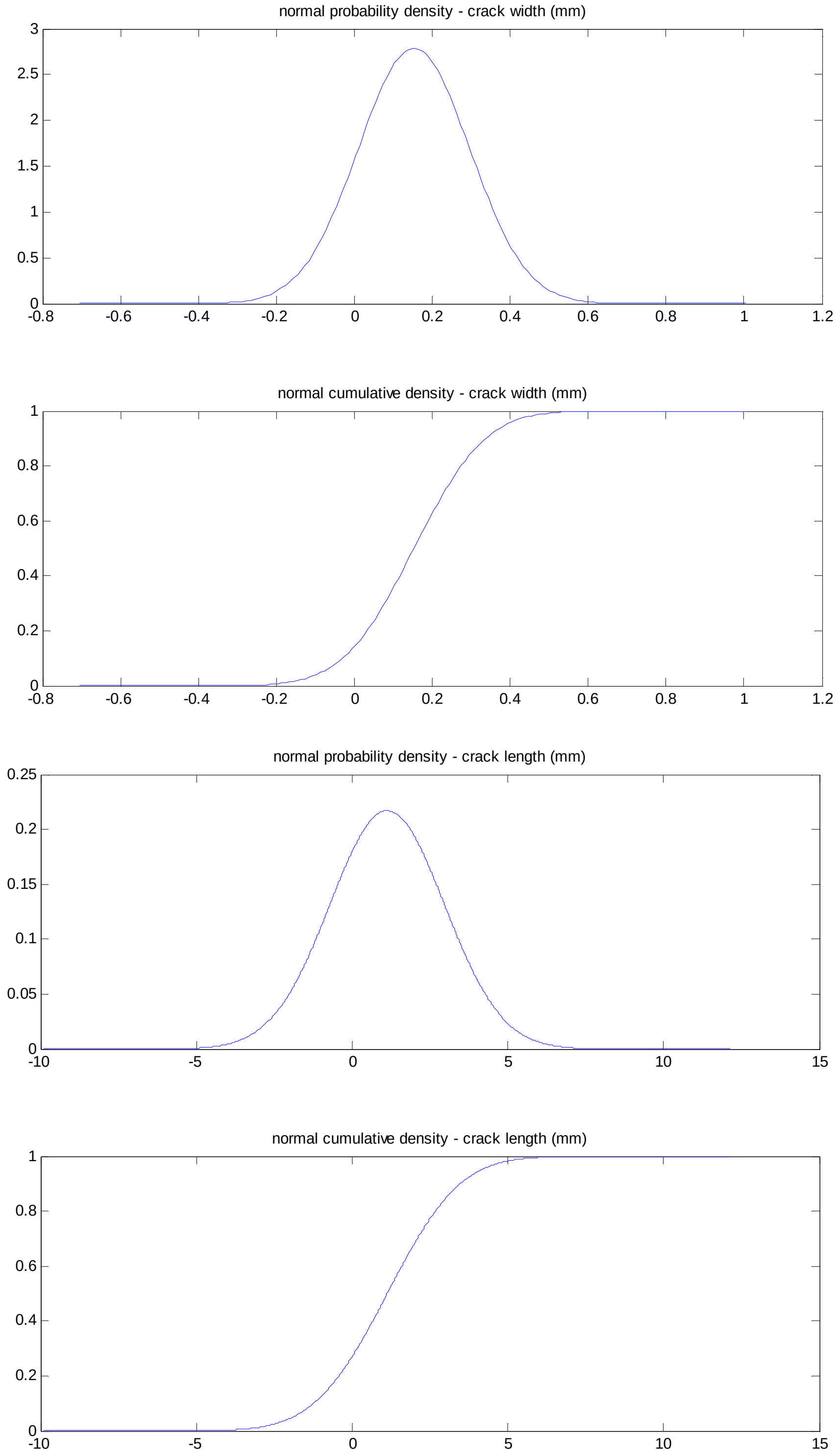

Figure E.2. Normal probability and cumulative density curves of crack width and crack length

Table E.1.
Results of crack analysis on a plain and FRC samples

Parameters obtained from crack analysis	Plain Sample	Glass Fiber Sample
Total length of cracks (mm)	621.0	582.3
Total cracking area of image (mm^2)	200.4	81.7
Density of cracks in image (1/mm)	0.062	0.058
Mean crack length (mm)	1.13	0.60
Total areal fraction of cracks (-)	0.020	0.008
Average width of cracks (mm)	0.32	0.14
Number of cracks per unit area (mm^{-2})	0.05	0.10
Average nearest neighbor distance (mm)	2.13	1.61
Total number of crack intersections (-)	77	55
Total number of cracks in image (-)	551	969
Degree of orientation of cracks (0-1)	0.099	0.084
Average specific number of intersections (1/mm)	0.066	0.053

Determination of Crack Orientations in Early-Age Cracked Cement Pastes

Concept

The degree of crack orientation is determined on the basis of the classical stereological technique of oriented secants on a plane [191, 192, 193, 194]. In this technique, parallel equidistant straight lines cover the view to be analyzed. A count of the intersections of these lines and the cracks network is performed. The number of intersections is divided by the total length developed by the straight lines in order to get the specific number of intersections, which is characteristic of the specific surface of cracking.

N_L = specific number of intersections

S_v = specific surface of cracking = $2N_L$

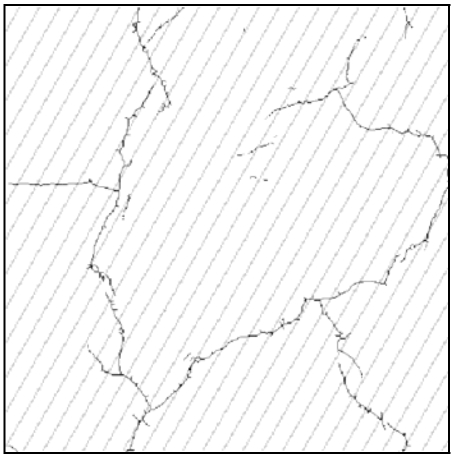

Figure E.3. Analysis by counting number of intersections of cracks network with the oriented secants (parallel equidistant lines)

In case of an anisotropic cracking, these characteristics are calculated by averaging the different values obtained by rotating the family of straight lines.

$N_L(\Theta i)$ = specific number of intersections in the orientation Θi

$$N_L = 1/n \sum_{1}^{n} N_L(\Theta i)$$; where n = number of orientations

$$S_v = 2N_L$$

For the purpose of emphasizing the anisotropy, the different values of $N_L(\Theta i)$ are reported in a polar referenced plane, in a figure which is named "rose of the number of intersections". The anisotropy is characterized by a scalar, called degree of orientation, ω, given as

$$\omega = \frac{(N_{L\max} - N_{L\min})}{N_{L\max} + (\frac{\pi}{2} - 1) \cdot N_{L\min}}$$

where; N_{Lmax} and N_{Lmin} are the maximum and minimum values taken by N_L respectively. Degree of orientation, ω, takes the value 0 for a perfectly isotropic crack pattern and the value 1 when all the cracks have the same orientation (extreme anisotropy).

Automatic Process of Orientation Analysis

The automatic procedure elaborated for the estimation of crack pattern orientation includes;

- Converting grayscale (8-bit unit) images of cracked sample into binary images.
- Reducing the cracks to single pixel lines by binary thinning, known as skeletonization.
- Providing families of equidistant parallel lines in different angles (from 0^o to 180^o, here steps are 15^o) in the format of binary images.
- Superimposition of the image of crack network and image of parallel equidistant lines with a given direction using the logical binary operation "AND".
- Counting the number of intersections of the cracks with the set of lines.
- Measuring total length of parallel lines covering the image.
- Calculating specific number of intersections defined as the number of intersections divided by the total length of parallel lines.
- Doing all above steps for the next incremental angles.
- Calculating average specific number of intersections and degree of orientation for the crack network as given in the previous section.

Testing and Calibration of Crack Orientation Analysis Process

In order to insure the reliability of this image analysis process, a series of trial shapes and figures are analyzed. These trials include; a circle, a series of parallel lines, and four different rectangles. Since the circle is perfectly isotropic and parallel lines are completely oriented to one direction and have extreme anisotropy, the expected results for the orientation degrees are 0 and 1 respectively. The rectangles tested here have different values of length to width ratio as; 1 (square), 2, 3 and 6. The analysis should be capable of capturing the effect of increase in the values of orientation degree by the elongation of rectangle. Here are the results;

1) For a circle:

Degree of orientation: 0.0519

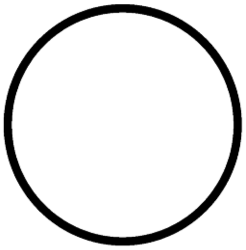

Rose of the number of intersections:

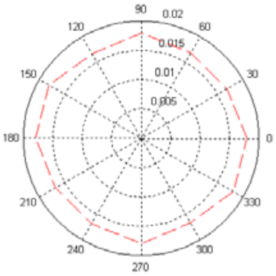

2) For parallel lines:

Degree of orientation: 1.0000

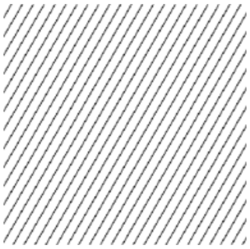

Rose of the number of intersections

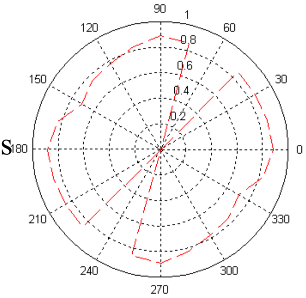

3) For a rectangle with length to width ration of 1 (square):

Degree of orientation: 0.3328

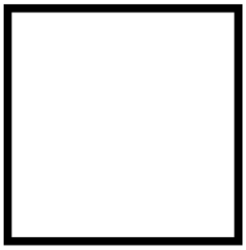

Rose of the number of intersections:

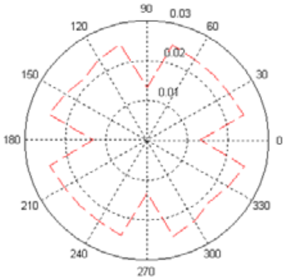

4) For a rectangle with length to width ration of 2:

Degree of orientation: 0.5078

Rose of the number of intersections:

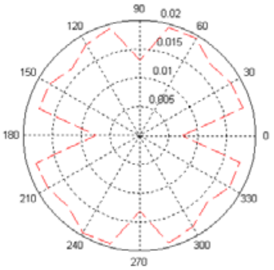

5) For a rectangle with length to width ration of 3:

Degree of orientation: 0.6136

Rose of the number of intersections:

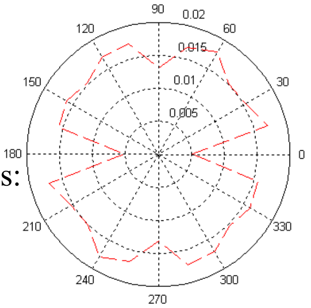

6) For a rectangle with length to width ration of 6:

Degree of orientation: 0.7466

Rose of the number of intersections:

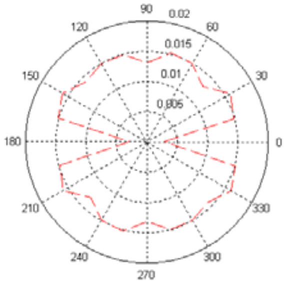

Crack Orientation Analysis on Cement Paste Samples

The process of image analysis on an early-age cracked cement paste sample (plain sample 1) after 24 hours of vacuum drying is shown as below;

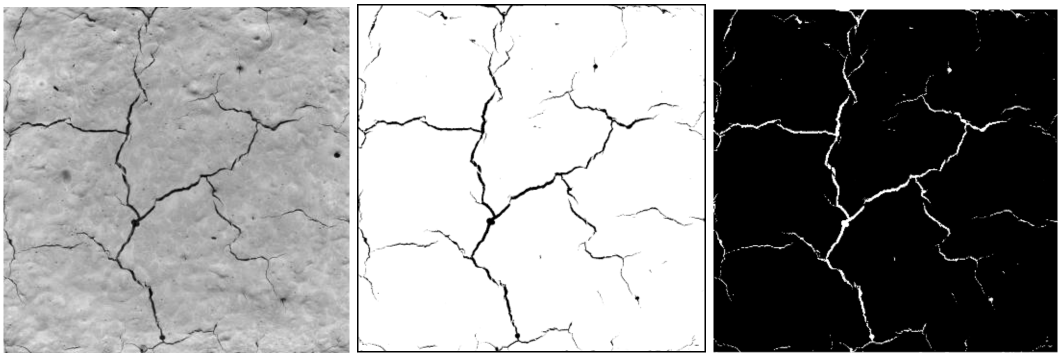

original grayscale image (8-bit unit) → binary image (black and white) → opposite of binary image

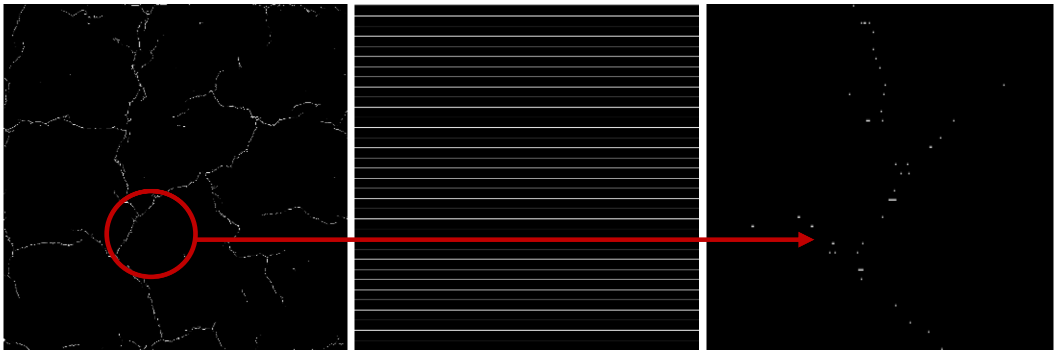

skeletonization of crack network → superimposing secants with crack image → points of intersection

Rose of the number of intersections:

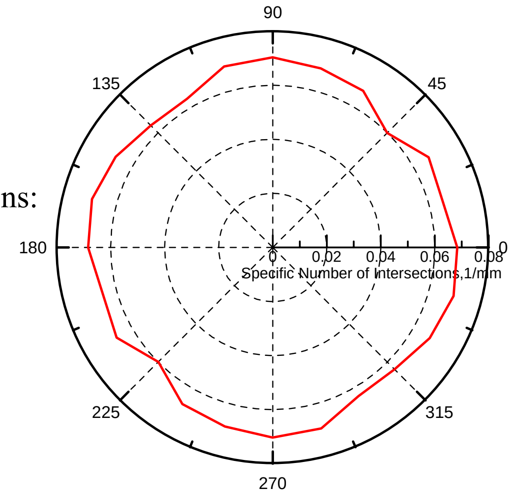

ω: 0.0998

N_L: 0.0666 mm^{-1}

S_v: 0.1333 mm^{-1}

The results of analysis for the other samples are as follow;

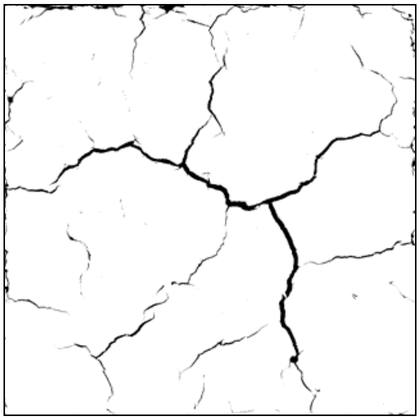

Plain cement paste (sample 2)

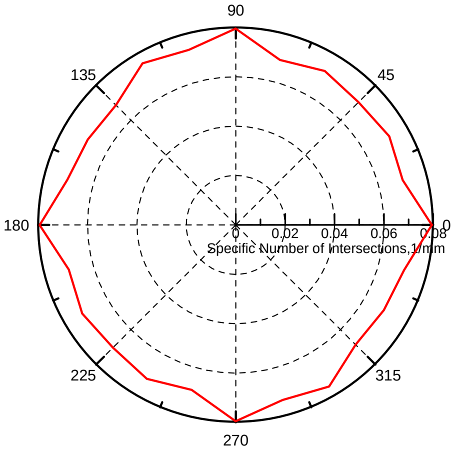

Rose of the number of intersections

ω: 0.0922

N_L: 0.0727 mm^{-1}

S_v: 0.1455 mm^{-1}

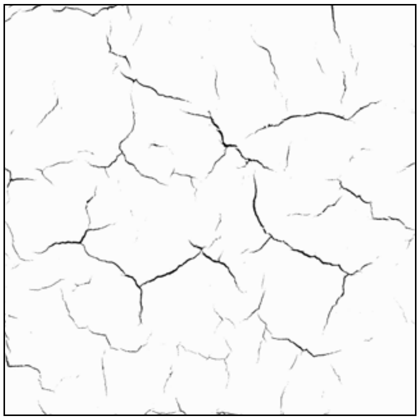

AR-glass fiber cement paste (sample 1)
AR-glass content: 3 kg/m^3

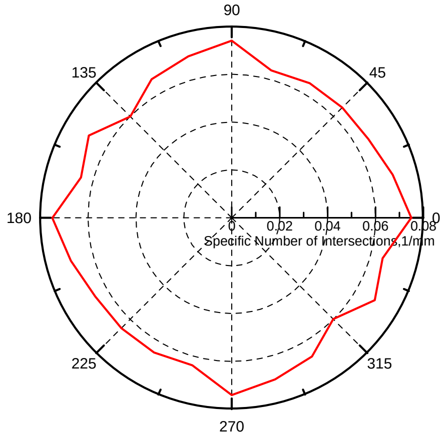

Rose of the number of intersections

ω: 0.1376

N_L: 0.0677 mm^{-1}

S_v: 0.1354 mm^{-1}

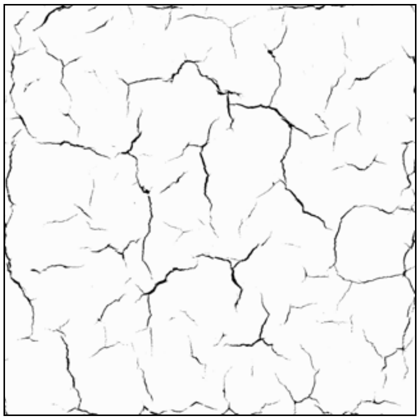

AR-glass fiber cement paste (sample 2)
AR-glass content: 3 kg/m^3

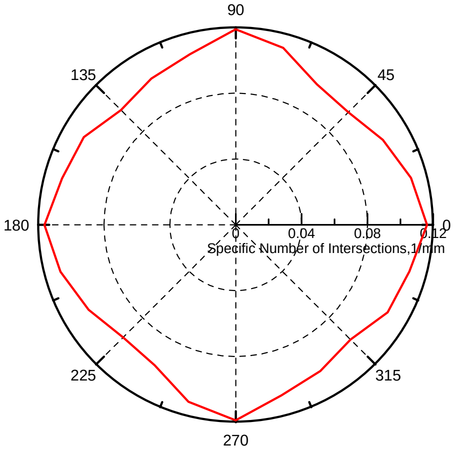

Rose of the number of intersections

ω: 0.1272
N_L: 0.1070 mm^{-1}
S_v: 0.2140 mm^{-1}

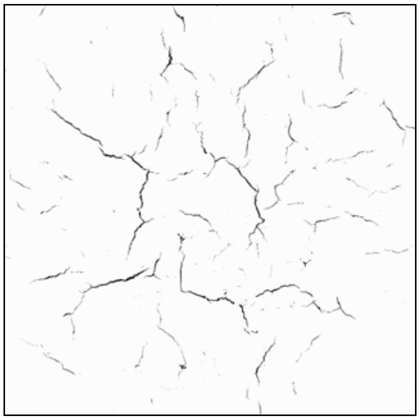

AR-glass fiber cement paste (sample 1)
AR-glass content: 6 kg/m^3

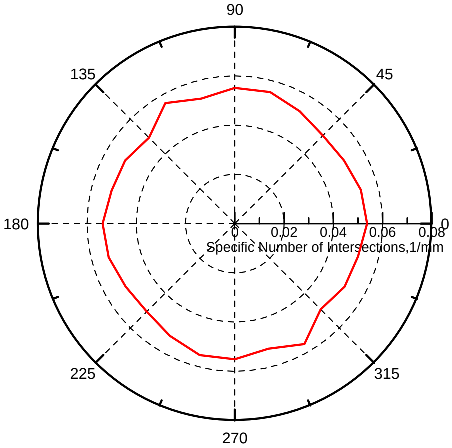

Rose of the number of intersections

ω: 0.0844
N_L: 0.0528 mm^{-1}
S_v: 0.1056 mm^{-1}

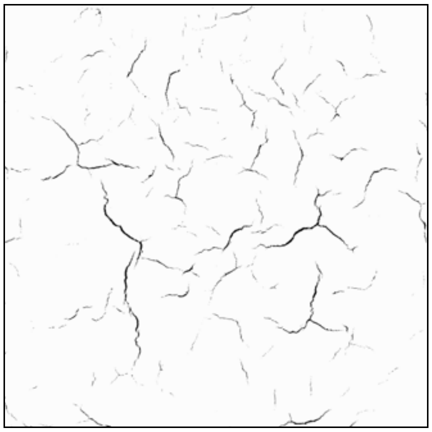

AR-glass fiber cement paste (sample 2)
AR-glass content: 6
kg/m^3

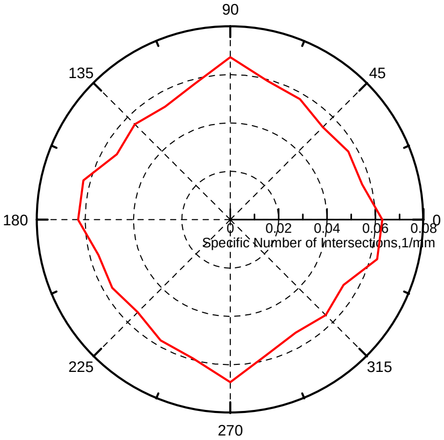

Rose of the number of intersections

ω: 0.1350
N_L: 0.0584 mm^{-1}
S_v: 0.1168 mm^{-1}

Table E.2.
Results of crack analysis and quantifications

Sample	Degree of Orientation, ω	Specific Number of Intersections, N_L (mm^{-1})	Specific Surface of Cracking, S_v (mm^{-1})
Plain cement paste	0.096	0.0697	0.1393
AR-glass cement paste (3 kg/m^3)	0.1324	0.0874	0.1747
AR-glass cement paste (6 kg/m^3)	0.1097	0.0538	0.1076

APPENDIX F

Modeling Early-age Shrinkage of Concrete Due to High Rate of Evaporation

Drying of Cement-Based Materials

Governing Differential Equations

Drying of cement-based materials can be considered as a moisture flow through porous media. Darcy's law can be used to obtain the flux of liquid water in a saturated porous medium. [195]:

$$q_l = -\frac{k_l}{\mu_l}\nabla p \tag{F.1}$$

where q_l is the flux of liquid water, k_l is the liquid permeability, μ_l is the dynamic viscosity of liquid water and p is the macroscopic pressure. However, except in very early stage of drying, the concrete is not fully saturated. In non-saturated state, the liquid water is transported because of gradient of the capillary pressure [160]. The liquid water flux for transport through a non-saturated medium can be obtained by the extended Darcy' law as presented in equation (F.2) In this equation $k_l(\theta)$, the effective permeability of liquid water, is a function of moisture content.

$$q_l = -\frac{k_l(\theta)}{\mu_l}\nabla p_c(\theta) = -K\nabla\Psi \tag{F.2}$$

K is the hydraulic conductivity defined as $K = g\rho k_l(\theta)/\mu_l$ and Ψ is the hydraulic potential presented by $\Psi = p_c(\theta)/g\rho_l$. Defining the liquid diffusivity as $D_{\theta,l} = K(\partial\Psi/\partial\theta_l)$, liquid water transport is presented as

$$q_l = -D_{\theta,l}\nabla\theta_l \tag{F.3}$$

Conservation of mass for liquid water expressed in volumetric quantities can be written as: $\partial\theta_l/\partial t = -\nabla.q_l - E_{l-v} = \nabla.\left(D_{\theta,l}\nabla\theta_l\right) - E_{l-v}$ (F.4)

On the other hand, the vapor transport under isothermal conditions at the microscopic level is given by Fick's law:

$$q_v = -\frac{1}{\rho_l}\frac{M}{RT}D_v\nabla p_v \tag{F.5}$$

where, q_v is the flux of water vapor, ρ_l is the density of liquid water, D_v is the diffusion coefficient of water vapor in air, M is the molecular mass of water, R is the gas constant, T is the absolute temperature, and p_v is the vapor pressure. The term M/RT results from the ideal gas law, whereas ρ_l results from the transformation of the mass flux for vapor into an equivalent volumetric liquid water flux [141]. Pel (1995) showed that at the macroscopic level, macroscopic volumetric flux through a porous medium with only air and vapor is obtained from equation (F.6).

$$q_v = -D_{\theta,v}\nabla\theta_l \tag{F.6}$$

where

$$D_{\theta,v} = \frac{(n-\theta_l)}{\rho_l}\frac{M}{RT}T^*(\theta_l)D_vP_{vs}\left(\frac{\partial h}{\partial\theta_l}\right) \tag{F.7}$$

where n is the porosity, $(n-\theta_l)$ *is* the void-space available for vapor diffusion, T^* is the tortuosity accounting for the extra path length resulting from the tortuous pores, D_v is the vapor diffusivity, p_{vs} is the saturation pressure of water vapor, and h is the relative humidity. The macroscopic conservation of mass for water vapor expressed in volumetric quantities can be written as:

$$\frac{\partial \theta_v}{\partial t} = -\nabla . q_v + E_{l-v} \tag{F.8}$$

where E_{l-v} is the rate of evaporation.

To find a single nonlinear diffusion equation for water in both phases, equation (F.4) and equation (F.8) are combined.

$$\frac{\partial(\theta_v + \theta_l)}{\partial t} = \nabla . \left(D_{\theta,l} + D_{\theta,v}\right)\nabla \theta_l \tag{F.9}$$

Defining moisture diffusivity as $D_\theta = D_{\theta,l} + D_{\theta,v}$, equation (F.9) is represented as:

$$\frac{\partial(\theta_v + \theta_l)}{\partial t} = \nabla . \left(D_\theta \nabla \theta_l\right) \tag{F.10}$$

Assuming equilibrium between water and vapor, the mass density of the vapor in the pores and total moisture content are given as:

$$\frac{\theta_l}{\rho_l} = n\frac{\theta_v}{\rho_v} \Rightarrow \theta = \theta_v + \theta_l = \left(1 + \frac{\rho_v / \rho_l}{n}\right)\theta_l \tag{F.11}$$

At the room temperature, the density of water vapor is 0.74 kg/m^3.

$$\theta = \left(1 + \frac{7.4 \times 10^{-4}}{n}\right)\theta_l \tag{F.12}$$

As one can see from equation (F.12), for liquid water content to vapor content ratio greater than about 10^{-3}, the total moisture content can be appropriately approximated by the liquid water content. Therefore, equation (F.10) can be represented as a non-linear diffusion equation for total moisture as:

$$\frac{\partial \theta}{\partial t} = \nabla . \left(D_\theta \nabla \theta\right) \tag{F.13}$$

Dual-stage Drying Methodology

Studies of drying behavior of clay brick ceramics by Hall et al. [99], Platten [146], Cooling [100], and different wet capillary-porous materials by Kowalski [101] indicate that evaporative flux at the boundary is roughly constant for a period of time at the beginning of the drying referred to as stage I and then falls significantly by the time in the second period or stage II. The same drying behavior was observed for the Portland cement pastes in recent experimental works by authors [148], as well as in mortar [149] and light-weight concrete [66]. In most of early-age drying tests, the moisture transport through the sample is assumed to be one-directional (1-D) due to high surface area-to-depth ratio, and exposing only top surface to the drying condition. For modeling the internal moisture transport in stage I and stage II drying, 1-D form of equation (F.13) is used with the replacement of dimensionless moisture concentration variable, θ (-), with the dimensional variable C (kg/m^3).

$$\frac{\partial C}{\partial t} = \frac{\partial}{\partial x}\left[D(C)\frac{\partial C}{\partial x}\right] = \frac{dD}{dC}\left(\frac{\partial C}{\partial x}\right)^2 + D\frac{\partial^2 C}{\partial x^2} \qquad \text{(F.14)}$$

The only difference in applying this formula in stage I and II, is the constant diffusivity at stage I, while the diffusivity is variable at stage II drying. The assumption is based on experimental observations that concrete is capillary saturated during stage I [105] but unsaturated at later stages of drying and its value will be a strong function of moisture concentration. Therefore, the time of drying is divided into several time steps at stage II and constant diffusivity is applied at each time step with respect to the time and the location. Using this method, the time-varying diffusivity values at stage II are only averaged over the space. This can be acceptable considering high evaporative surface-to-depth ratio of the samples. Consequently, equation (F.14) can be simplified to equation (F.15) for stage I as well as each time step for stage II.

$$\frac{\partial C}{\partial t} = D\frac{\partial^2 C}{\partial x^2} \qquad \text{(F.15)}$$

Hydration of cement and its implications on transport properties need to be taken into account during early-age drying of cementitious materials. With time, liquid water will be chemically bounded into hydration products as well as physically bound water to increasing internal solid surfaces. Both chemically and physically bound water may be assumed to be in local equilibrium with free water due to rapid rate of hydration at the early age. To simplify the concept, the concentration of bound water, *S*, is directly taken proportional to the concentration of the free water, *C*, the substance free to diffuse.

$$S = RC \qquad \text{(F.16)}$$

During early-age drying when the moisture diffusion is accompanied by immobilization of bound water, equation (F.15) is modified as:

$$\frac{\partial C}{\partial t} = D\frac{\partial^2 C}{\partial x^2} - \frac{\partial S}{\partial t} \qquad \text{(F.17)}$$

Equation (F.16) can be presented in a new form by substituting for *S* from equation (F.16).

$$\frac{\partial C}{\partial t} = \frac{D}{1+R}\frac{\partial^2 C}{\partial x^2} = D'\frac{\partial^2 C}{\partial x^2} \qquad \text{(F.18)}$$

Replacing the term *D/(1+R)* with *D'* as the effective moisture diffusion coefficient, the equation is seen in the usual form of diffusion equations. Therefore, *D'* presents the potential for conductivity of free water through the fresh cementitious materials.

The cement paste is assumed to be homogeneous at initial conditions with an impermeable bottom surface. Therefore, the initial and boundary conditions are

$$t = 0, \quad C = C_i \qquad 0 \le x \le L \qquad \text{(F.19)}$$

at $x = 0,$ $$J = -D'\frac{\partial C}{\partial x} = 0 \tag{F.20}$$

where C_i is the initial moisture concentration (kg/m^3), and J is the moisture flux (kg/m^2).

Moisture transport during stage I drying is considered as an external mass transfer control process with a constant drying rate. Thus, the boundary condition at the top surface is

at $x = L,$ $$J = F_0 \tag{F.21}$$

where, F_0 is the constant flux in stage I drying (kg/m^{2}s). Solution to moisture concentration values as a function of time and location during stage I drying based on equations (F.18-21) is [109]

$$C(t,x) = C_i + \frac{F_0 L}{D'}\left\{\frac{D't}{L^2} + \frac{3x^2 - L^2}{6L^2} - \frac{2}{\pi^2}\sum_{n=1}^{\infty}\frac{(-1)^n}{n^2}\exp\left(\frac{-D'n^2\pi^2 t}{L^2}\right)\cos\frac{n\pi x}{L}\right\} \tag{F.22}$$

In this model transition time from stage I to stage II, referring to the loss of continuity in the liquid phase, is defined by the user which may be obtained from experimental data. Prediction of the transition time based on physical grounds requires further studies. For modeling stage II drying based on the concept of convective-diffusive transfer of vapor at the surface, the exchanged flux of moisture, J, can be characterized by the convection equation .

$$J = -D'\frac{\partial C}{\partial x} = k(C_s - C_*) \tag{F.23}$$

where k (m/h) is convective moisture transfer coefficient or surface factor, C_s is the surface moisture concentration and C_* is the ambient moisture concentration (kg/m^3). k parameter takes into account the wind velocity, the surface temperature, and the relative humidity for drying to the atmosphere or in the case of low-pressure drying encompasses vacuum condition and temperature. The analytical solution for equations (F.18-21) during each time step at stage II drying with the convective boundary condition as of equation (F.23) is given by [153]

$$C(t,x) = C_* + (C_i - C_*) + \sum_{n=1}^{\infty}\frac{2\sin(\lambda_n)}{\lambda_n + \sin(\lambda_n)\cos(\lambda_n)}\cos(\lambda_n\frac{x}{L})\, e^{\left(-\lambda_n^2\frac{D't}{L^2}\right)} \tag{F.24}$$

Where,

$$\lambda_n \tan(\lambda_n) = \frac{kL}{D'} \tag{F.25}$$

Geometry, governing equations and boundary conditions during stages I and II drying are presented in Figure (F.1).

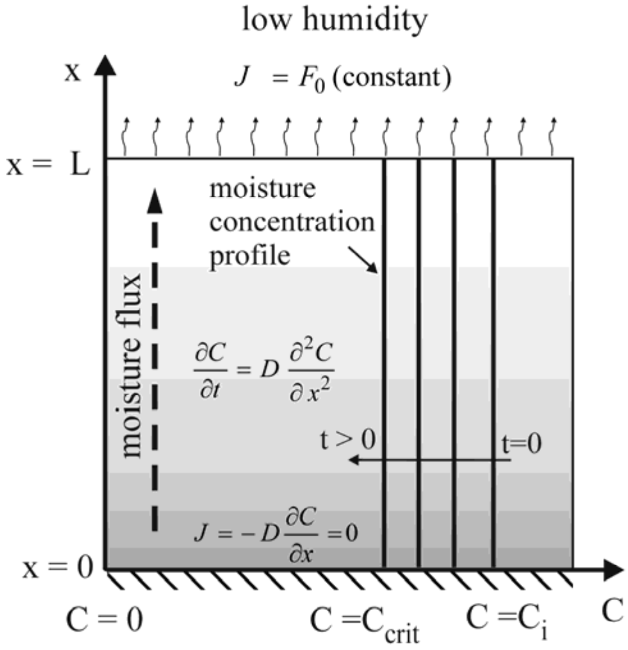

Figure F.1a

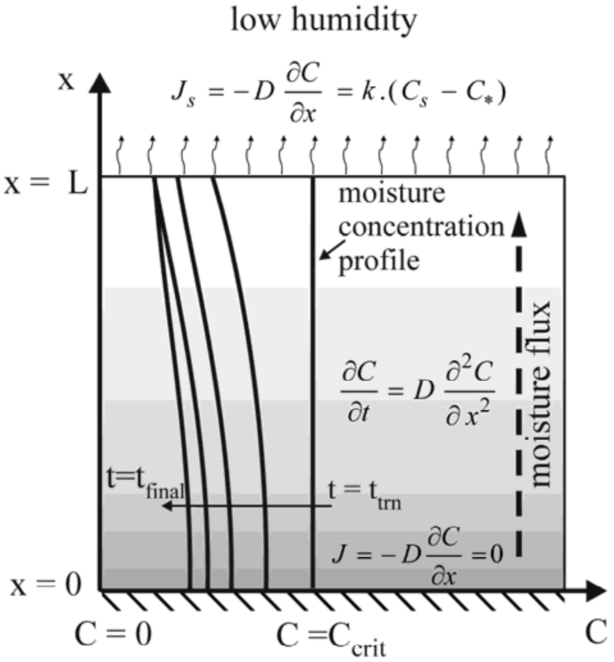

Figure F.1b

Figure. F.1. Geometry, governing equations and boundary conditions during: (a) stage I drying, (b) stage II drying assuming convective moisture flow on the top surface

Back-Calculation Procedures

A back calculation model is used to predict diffusivity and moisture transfer coefficient at any time step based on given cumulative moisture loss and evaporation rate curves. Optimization is implemented to find two best fit parameters, $D'(t)$ and $k(t)$ to predict the experimental results. The objective function for minimization is the weighted sum of two errors of cumulative moisture loss and flux. In optimization algorithm, normalized design variables (D' and k) are used to avoid numerical problems caused by mixing big and small numbers in numerical operations. Thus, diffusion coefficient at the current time step is normalized with its value at previous time step, $D_{norm}=D'_i/D'_{i-1}$, so does the mass transfer coefficient $k_{norm}= k_i/k_{i-1}$. Once the optimal solution D_{norm} and k_{norm} are found, they are reverted back to D' and k. Inequality constraints are imposed to the design variables D' and k in terms of lower and upper bounds. Initial values for D' are obtained from analysis of stage I drying, while initial values for k are estimated from equation (F.26) which is derived by rearranging equation (F.23).

$$k^{(est)} = \frac{J^{(\exp)}(t = t_{trans})}{C_{crit} - C_*} \tag{F.26}$$

where, $k^{(est)}$ is the estimated surface factor (m/h) and $J^{(\exp)}(t = t_{trans})$ is the experimental rate of evaporation at the transition time which is roughly equal to initial evaporation rate. C_{crit} is the surface moisture concentration at end of stage I or critical moisture concentration (kg/m^3) and C_* is the ambient moisture concentration. For other time steps, initial D' values for optimization process, $D^{(est)}$ are estimated by the assumption of proportional decrease of diffusivity with the flux, while initial k values, $k^{(est)}$ are estimated by a convection transport formula.

$$D^{(est)} = D_{i-1}\frac{J^{(\exp)}(t^{(i)})}{J^{(\exp)}(t^{(i-1)})} \tag{F.27}$$

$$k^{(est)} = \frac{J^{(\exp)}(t^{(i)})}{C(t^{(i-1)}, x = L) - C_*} \tag{F.28}$$

In equation (F.27) and (F.28), $t^{(i)}$ is the current time step, while $t^{(i-1)}$ is the previous time step. At each time step, these two initially estimated parameters, $D^{(est)}$ and $k^{(est)}$ are passed to the optimizer and the optimizer calls the function evaluation to calculate the error and update these two parameters several times until optimal solution for D' and k are found. Results of back calculations for the reported data by Selih (1996) are shown in Figure (F.2) and (F.3).

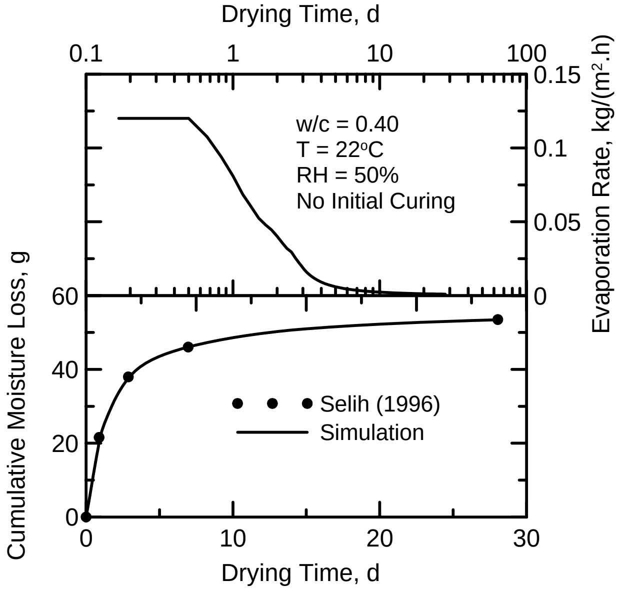

Figure F.2a

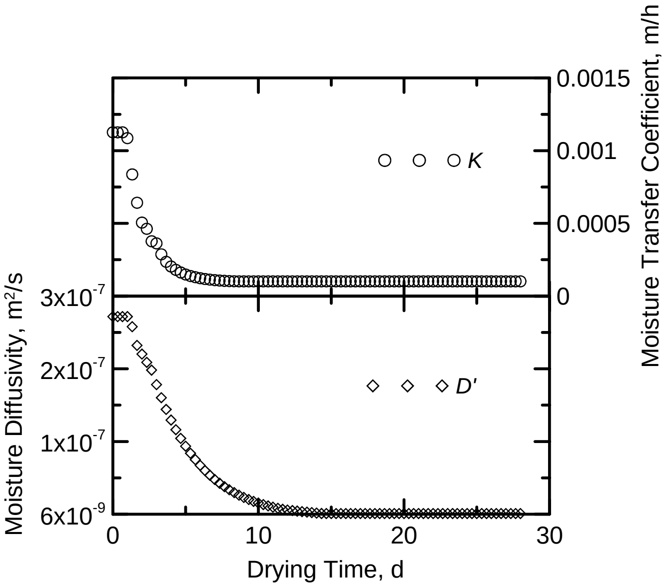

Figure F.2b

Figure F.2. (a) Prediction of cumulative moisture loss and evaporation rate as a function of time for the experiment performed by Šelih (1996), (b) Back-calculated D' and k for the best fit of data

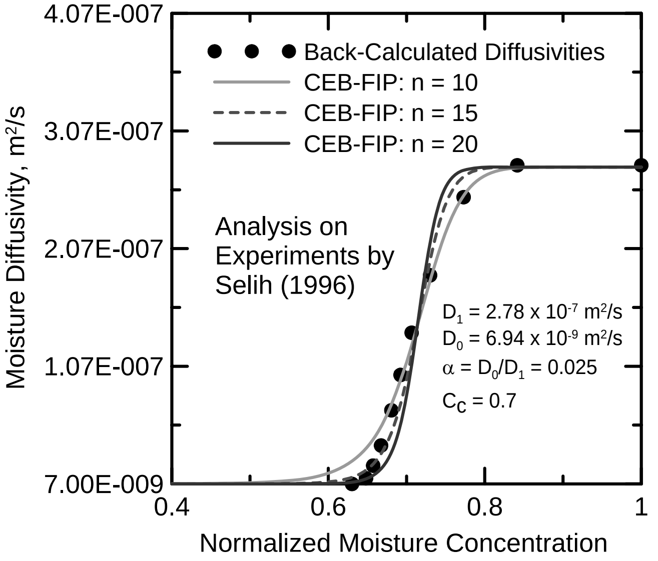

Figure F.3a

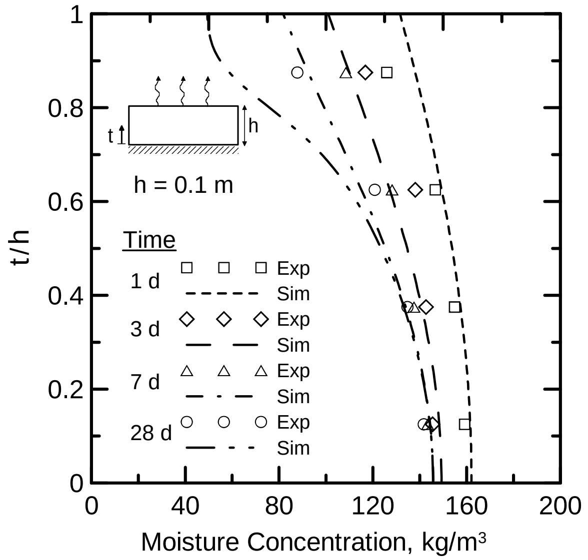

Figure F.3b

Figure F.3. Results of analysis on drying data by Šelih (1996): (a) Moisture diffusivity as a function of normalized moisture concentration expressed by CEB-FIP models, (b) moisture concentration distributions through the thickness of the sample in comparison with experimental results

Shrinkage Strains and Drying

Simplified Models

Some researchers have focused on developing linear relationship between shrinkage strains and the relative humidity. Wittmann and Roelfstra [196] described the unrestrained hygral length change, ε_{sh}, as a function of relative humidity, *h*, by a linear relationship such as:

$$\varepsilon_{sh} = \alpha_{sh}{}^{h}.\Delta h \tag{F.29}$$

where $\alpha_{sh}{}^{h}$ is an empirical shrinkage coefficient depending on concrete composition and maturity. Alvaredo and Wittmann [197] have used this linear relationship with the $\alpha_{sh}{}^{h}$ ranging from 1.5-2.5x10^{-3}. Bazant and Xi [198] and Bazant et al. [199] also introduced the same concept into their models. According to van Zijl [200], the experimental measurement indicate that the empirical shrinkage coefficient, $\alpha_{sh}{}^{h}$ is constant in the range $0.4 < h < 0.99$.

Similar efforts have been made on linearly relating moisture content to the shrinkage strain assuming a quasi-linear relationship between the moisture content and the relative humidity in the range of 50-100% in desorption isotherm curves [201, 202]. Thelandersson et al. [203] modeled the developed strain in the drying concrete according to equation (F.29).

$$\varepsilon_{sh} = \alpha_{sh}{}^{C}.\Delta C \tag{F.30}$$

where *C* is the moisture content (-), and $\alpha_{sh}{}^{C}$ is the coefficient of hygral contraction which can be obtained from the linear part of unrestrained shrinkage versus weight loss curve [204].

The major reason for dealing with water content rather than relative humidity is that water content can be more easily measured by weight loss monitoring [55]. Therefore, there is no requirement for desorption isotherms of the concrete to relate humidity, *h*, to the water content, *C*. Granger et al. [205] and Verbeck [206] showed that particularly when *h* remains above 50 percent, this relationship is confirmed fairly well by experiments. This model has been used in hydro-mechanical models accounting for the full coupling of drying, shrinkage, creep and cracking [207]. Benboudjema et al. [208, 209, 210] used the coefficient of hygral contraction as $\alpha_{sh}{}^{C} = 1.22\times10^{-5}$.

The advantage of these simplified models (equations F.29-30) is an easy implementation in drying models to obtain developed strains and related stresses. Having moisture distributions at different time in drying of a concrete sample, and using a Finite Element Method (FEM), the moisture concentration can be easily translated into an internal stress distribution. This stress distribution can be finally used to calculate the total deformation of a drying specimen [196]. However, the drawback is the lack of a physical interpretation between nature of the porosity in the material and the developed strains.

Capillary Pressure-Based Models

Experimental results [205, 211] and models based on the mechanics of porous media [212, 213, 214] reveal the nonlinearity between the shrinkage strain and relative humidity or water content. This nonlinearity which is more pronounced at the beginning and at the end of the drying process [215] led to suggestions of bilinear and nonlinear relationships [216, 200]. Capillary tension, disjoining pressure, and solid surface tension (Gibbs-Bangham) are among several mechanisms recognized for shrinkage of cement-based materials [217]. However, much of the shrinkage that is observed in early-age concrete can be attributed stresses associated with capillary tension [218]. Kelvin and Laplace equations are used to present the magnitude of capillary pressure developed in the concrete pores due to drying phenomena [219]. According to Baron [219] these equations can be derived from the equilibrium of chemical potentials between liquid and vapor phases of water, under certain assumptions. These assumptions include capillary water forms a single continuous phase, water vapor is an ideal gas, capillary water is homogenous and incompressible, velocity is zero at any point, capillary water is not under any external loads such as gravity, the gas pressure is equal to the atmospheric pressure and the water is in the chemical equilibrium with ambient atmosphere. Kelvin equation presents the capillary pressure as:

$$p_l - p_g = p_c = \frac{\rho_l RT}{M_v}\ln(h) \tag{F.31}$$

where p_l is the pressure of liquid water, p_g is the pressure of the gas phase (dry air and water vapor), p_c is the capillary pressure, ρ_l is the water density (1000 kg/m^3), R is the universal gas constant, T is temperature, M_v is the molar mass of water (0.01801 kg/mol), and h is the fractional relative humidity. This relationship allows the use of internal relative humidity (h) as a parameter for modeling developed stress and strain in concrete due to drying [220]. According to this formulation, the capillary pressure at 300 K (26.8 ^{o}C) and relative humidity of 0.5 (RH = 50%) is -96 MPa, which shows the high magnitude of capillary pressure in the pores. The capillary pressure between humid air (dry air and water vapor) and liquid water should be balanced by the surface tension σ_{lg} at the interface of liquid/gas phase. Assuming a circular meniscus with the radius r_m, the first law of Laplace can be derived as:

$$p_l - p_g = p_c = \frac{2\sigma_{lg}}{r_m} \tag{F.32}$$

where σ_{lg} is surface tension, and r_m is the radius of assumed circular meniscus.

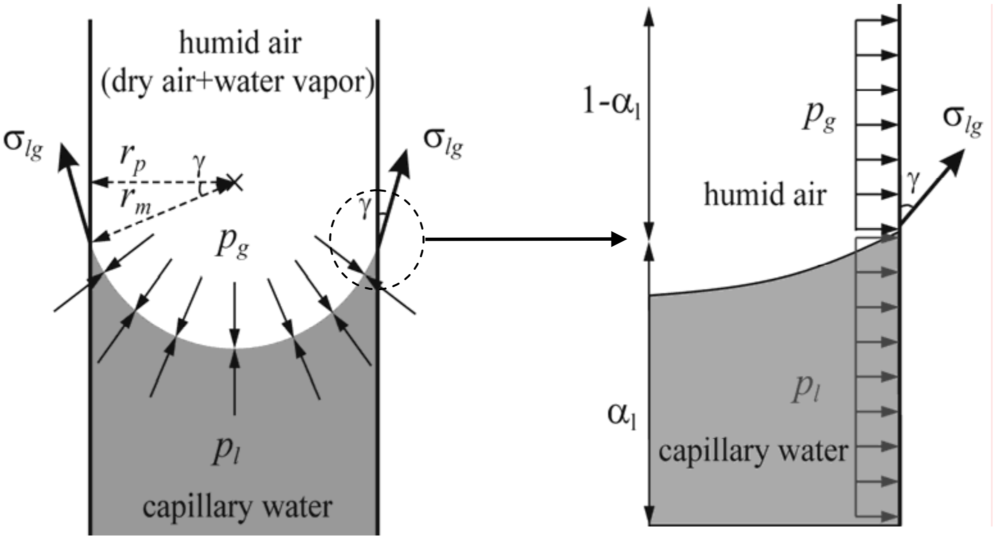

(a) (b)

Figure F. 4. a) Equilibrium between liquid water and humid air at the interface of liquid/gas phase inside a pore in concrete, b) different pressures applied on solid skeleton inside capillary pores [221]

As a reaction to this negative pressure within the pore fluid, compression develops in the solid microstructure [222]. An average pressure on the solid skeleton due to the capillary pressure, p_{sol_c} is calculated as

$$p_{s\_c} = \alpha_l p_l + (1-\alpha_l) p_g + \alpha_{lg} \sin\gamma \, \sigma_{lg} - p_{atm} \tag{F.33}$$

where, α_l is the volumetric fraction of liquid water in the capillary pores, α_{lg} is a coefficient incorporating effect of surface tension (σ_{lg}). Inserting equation (F.32) into equation (F.33) and rearranging gives

$$p_{s\_c} = \alpha_l (p_l - p_g) + p_g + \frac{\alpha_{lg} \sin\gamma r_m}{2} p_c - p_{atm} \tag{F.34}$$

According to Baron's assumption $p_{atm} = p_g$ and therefore

$$p_{s\_c} = \left(\alpha_l + \frac{\alpha_{lg} \sin\gamma r_m}{2} \right) p_c = \alpha_{sol\_c} \, p_c \tag{F.35}$$

Gray and Schrefler [223] replaced the coefficient $\alpha_{sol\text{-}c}$ by the saturation degree of liquid phase, S_l, and therefore, the pressure on solid skeleton can be presented as

$$p_{s\_c} = S_l \, p_c \tag{F.36}$$

While equation (F.36) shows only the microscopic pressure on the solid skeleton due to the capillary pressure, Bazant [224] presented variation of disjoining pressure in a similar fashion to capillary pressure.

$$\Delta p_d = \frac{\rho_a RT}{M_a} \ln(h) \tag{F.37}$$

where, p_d is the disjoining pressure, and ρ_a and M_a are the density and molar mass of adsorbed water, respectively. Similar to the capillary pressure, the variation of the applied pressure on the solid skeleton due to the disjoining pressure can be presented as:

$$\Delta p_{s\_d} = \alpha_{sol\_d} \, \Delta p_c \tag{F.38}$$

Considering equation (F.36) and (F.38), the total applied pressure on the solid skeleton, p_{sol} due to the capillary and the disjoining pressures can be obtained using the saturation degree of liquid phase, S_l, and a homogenization factor, α_s [215] as:

$$p_s = \alpha_d \, S_l \, p_c \tag{F.39}$$

The homogenization factor incorporates effects of both capillary and disjoining pressures as well as the effect of scale change from microscopic to macroscopic levels, and can be obtained from shrinkage tests.

Equation (F.39) can be used to determine the strains induced by the pore pressures due to the drying process. A unit cell approach can be taken to study this effect on porous media such as concrete materials. As shown in Figure (F.5), concrete can be approximated by a square in which the pores are placed in the center and the rest of area is the solid phase. Effective stress $\tilde{\sigma}$ is defined as the stress acting on the solid skeleton which can be obtained from the equilibrium.

$$\sigma = (1-\phi)\tilde{\sigma} - \phi p_s \tag{F.40}$$

where σ is the external stress (restraining effects) and ϕ is the porosity. In unrestrained shrinkage tests, the external stress is zero ($\sigma = 0$). On the other hand, $\tilde{\sigma}$ can be related to the strains due to elastic behavior of solid skeleton.

$$\tilde{\sigma} = E\varepsilon_s \tag{F.41}$$

where, E is the young's modulus, and ε_s is the shrinkage stain.

The shrinkage strain can therefore be obtained by combining equation (F.40) and (F.41).

$$\varepsilon_s = \frac{\phi}{(1-\phi)E} p_s \tag{F.42}$$

To calculate shrinkage strains based on equation (F.42), capillary porosity, ϕ and modulus of elasticity, E has to be modeled, initially. The capillary porosity, ϕ, has been predicted with different models [225, 226, 227, 228]. The model proposed by Bentz and Garboczi [226] is used in this study with the following equation:

$$\phi = \frac{w/c - 0.41\alpha}{w/c + 0.313} \tag{F.43}$$

where w/c is the water-to-cement ratio, and α is the degree of hydration.

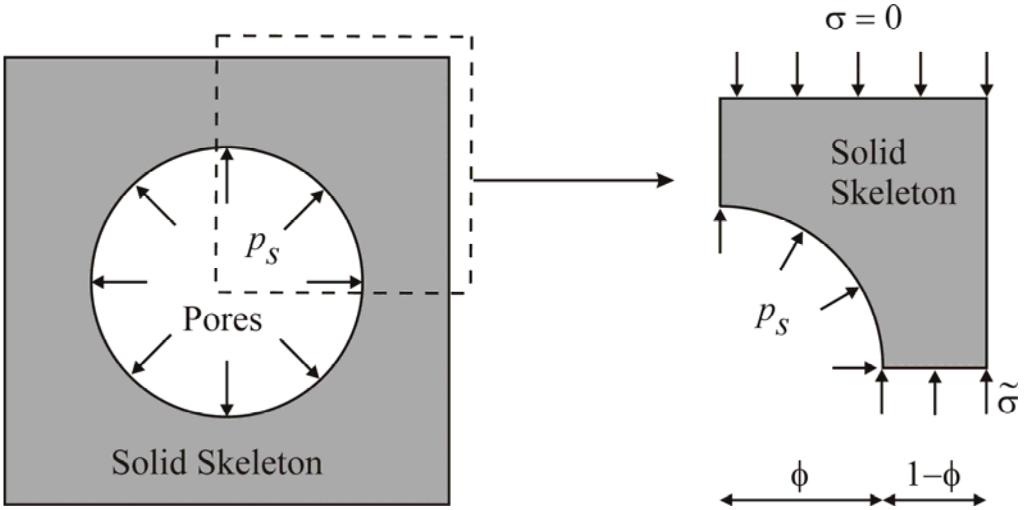

Figure F.5. Effective stress on solid skeleton based on unit cell modeling [221]

The degree of hydration is modeled as a function of time using a power function.

$$\alpha = \left(\frac{t}{t_f}\right)^a \alpha_f \tag{F.44}$$

where, t_f is the final drying time, and α_f is the degree of hydration at the final drying time. Results of simulation of degree of hydration are in good agreement with the experimental data reported by Lamond and Peilert [229] showing that the degree of hydration of ordinary Portland concrete with w/c of about 0.45 at 24 h is about 0.2 (see Figure F.6). This model is used for studying early-age drying shrinkage tests.

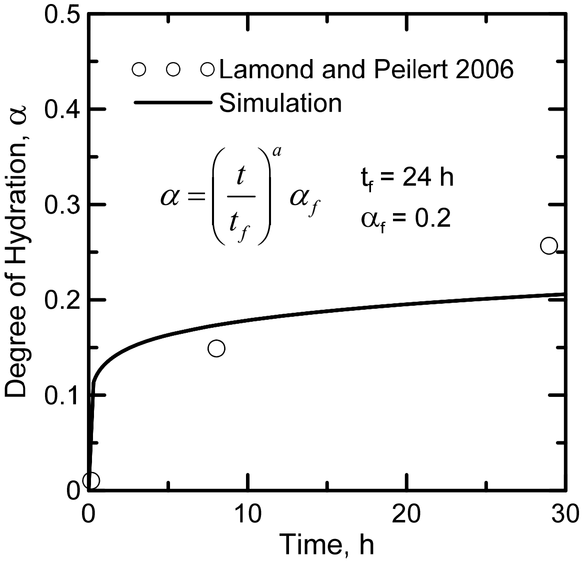

Figure F.6. Simulation of degree of hydration in comparison with experimental data

Elastic modulus development in the early age concrete can be modeled using a two-stage methodology.

$$E=\begin{cases} E_i\left(\dfrac{t}{t_i}\right)^a & ;t\le t_i \\ E_i+(E_f-E_i)\left(\dfrac{t-t_i}{t_f-t_i}\right)^b & ;t>t_i \end{cases} \tag{F.45}$$

where E, E_i, and E_f are the elastic modulus at different times. t, t_i and t_f are the time, initial time of setting, and the final time of drying, respectively. a and b are constants. However, a should be more than 1 and b less than 1 to conform to the experimental data [Dao et al. 2009] and [Van Heyningen and Boon 1973]. As Shown in Figure (F.7), such a model is capable of simulating the development of modulus of elasticity at very early age (<6 h) as well as from very early hours to few days (0-150 h).

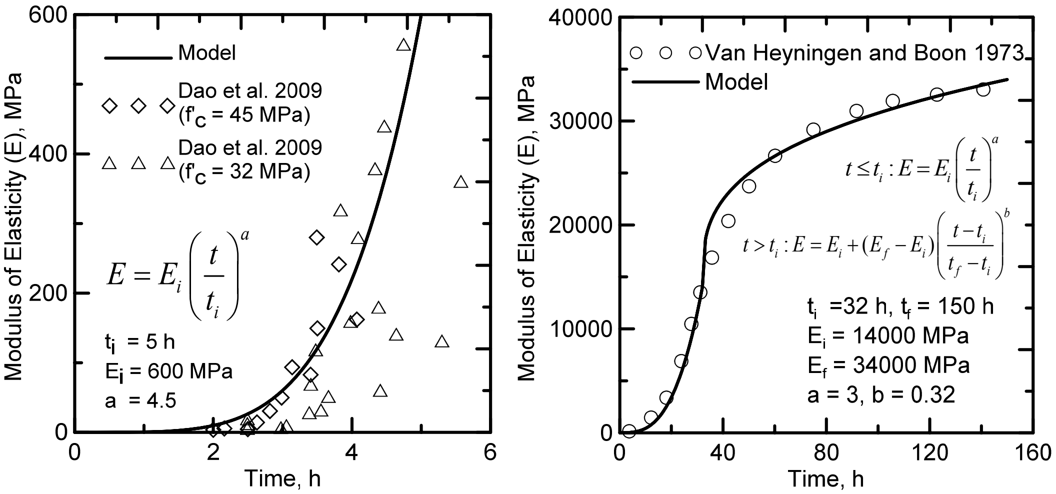

Figure F.7. Modeling development of modulus of elasticity in early ages (0-150 h)

Modeling Early-Age Shrinkage from Drying Data

In order to confirm the soundness of this method in calculating early-age shrinkage from the drying data, the method can be applied to different sets of data with available experimental moisture loss curves and shrinkage versus time curves. The experimental data of Wongtanakitcharoen and Naaman [20] were chosen for this purpose which involve one-dimensional drying of linear prismatic specimens 1000 mm in length and 100×60 mm in cross sectional area, under temperature of 35-40 ^{o}C provided by a radiator heater, and relative humidity of

22.5%. As shown in Figure (F.8) rapid rate of evaporation was insured using a high velocity fan provided constant high flow of air over the specimen's surface.

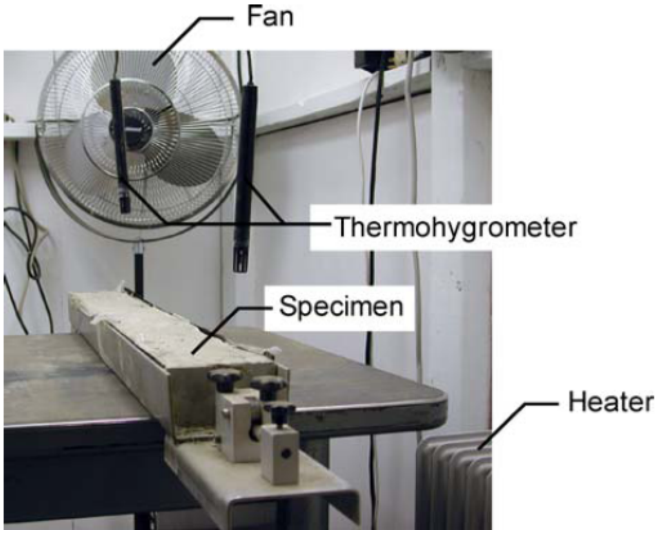

Figure F.8. Unrestrained early-age shrinkage test setup (Wongtanakitcharoen and Naaman 2007)

Among different early-age shrinkage tests performed by Wongtanakitcharoen and Naaman, test results on plain concrete and PVA fiber reinforced concrete with 0.2% volumetric fraction were chosen for analysis. The water to cement ratio by weight was 0.53. ASTM C150 Type III Portland cement was used in the concrete mix and the coarse aggregate was crushed limestone of 9.525mm maximum size, and the fine aggregate was NS-2 sand. The weight ratio of Portland cement to water, sand and coarse aggregate in this mixture were 1-0.53-1-1 and the properties of PVA fiber is shown in Table F.1.

Table F.1.

Properties of PVA fiber used in this study

Fiber type	Denier	Shape	Equivalent dimension(mm)	Length(mm)	Specific gravity	Tensile strength, MPa (ksi)	Elastic modulus, GPa (ksi)
PVA#16		Monofilament (circular)	0.040	12	1.30	1560 (220)	40 (5710)

The ambient moisture concentration, C_* , can be obtained from the desorption isotherm curves which relate internal relative humidity to the water content. Using the BSB model [110], C_* was obtained 56 kg/m^3. As shown in Figure (F.9a), the evaporation rates were computed from cumulative moisture loss data using a numerical differentiation procedure. The drying results were used to back-calculate diffusion and convective moisture transfer coefficients as shown in Figure (F.9b). Similar to author's drying results on plain and glass fiber reinforced concrete [148], the moisture loss curves for these two samples (plain and 0.2%

PVA) are very similar and therefore a single cumulative moisture loss curves is used for the rest of analysis.

A desorption isotherm model, the BSB model [230], is used to relate internal relative humidity to the water content.

$$C^* = \frac{AkV_m H}{(1-kH)[1+(A-1)kH]} \tag{F.46}$$

where, C^* is moisture content (kg of water / kg of solid), H is relative humidity (fraction) and A, k, V_m are three empirical parameters defined as:

$A = \exp(\frac{A_0}{T}), \quad A_0 = 855$

$V_m = 0.024(0.85 + 0.45 w/c)V_{ct}$; for t< 5 d and 0.3 < w/c < 0.7

V_{ct} = 0.9, 1.0, 0.85 and 0.60 for cement type 1 to 4, respectively.

$$k = \frac{(1-\frac{1}{n})A - 1}{A-1}$$

$n = 5.5(0.33 + 2.2 w/c)N_{ct}$; for t > 5 days and 0.3 < w/c < 0.7

N_{ct} = 1.1, 1.0, 1.15 and 1.5 for cement type 1 to 4, respectively.

Results of analysis including simulation of profiles moisture concentration, relative humidity, capillary pores pressure, macroscopic pressure on solid skeleton are shown in Figures (F.10) and (F.11).

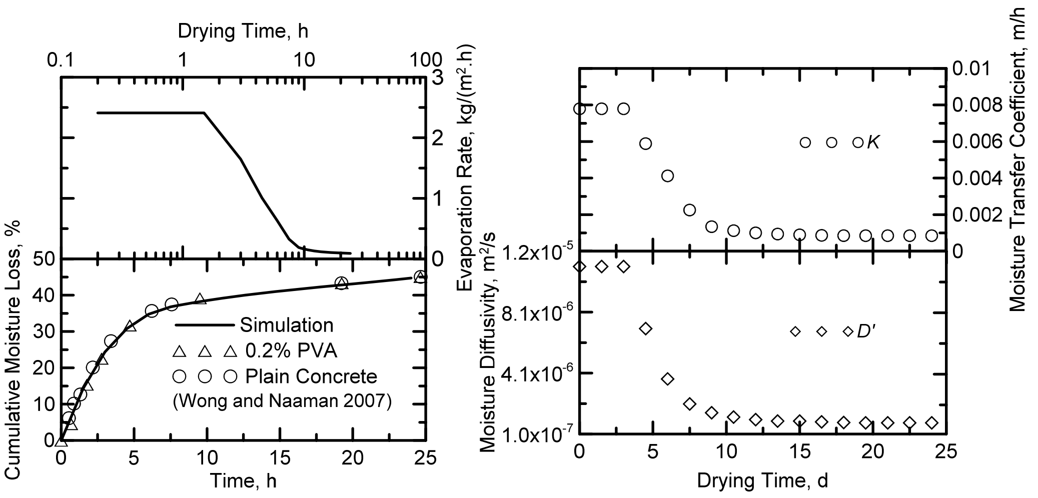

(a) (b)

Figure F.9. (a) Prediction of cumulative moisture loss and evaporation rate as a function of time for the reported experimental data, (b) Back-calculated D’ and k for the best fit of data

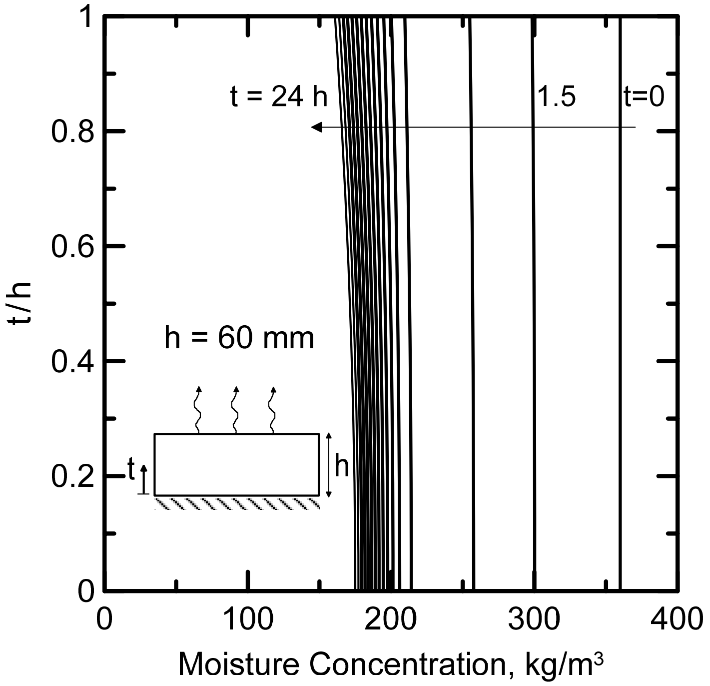

(a)

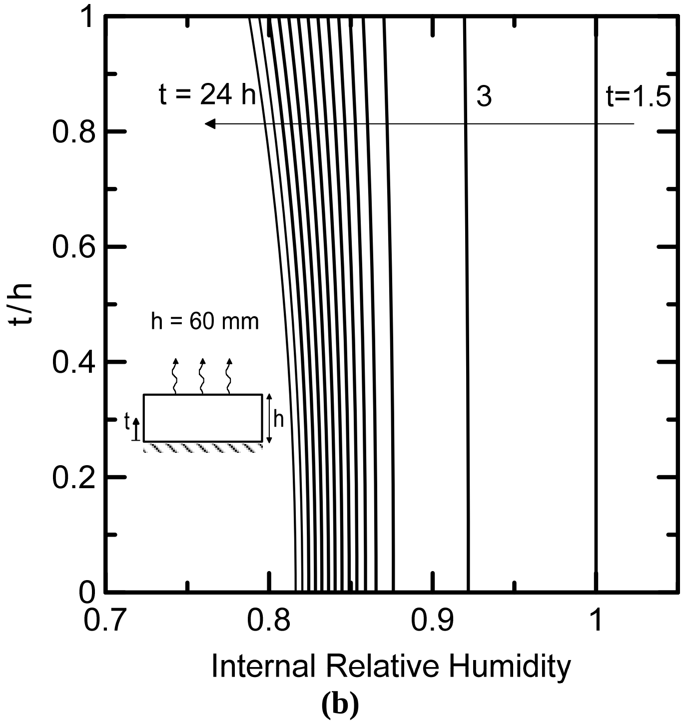

(b)

Figure F.10. (a) Simulation of moisture concentration profiles during drying of plain and PVA0.2% concrete, (b) simulation of relative humidity profiles from desorption isotherms (BSB model)

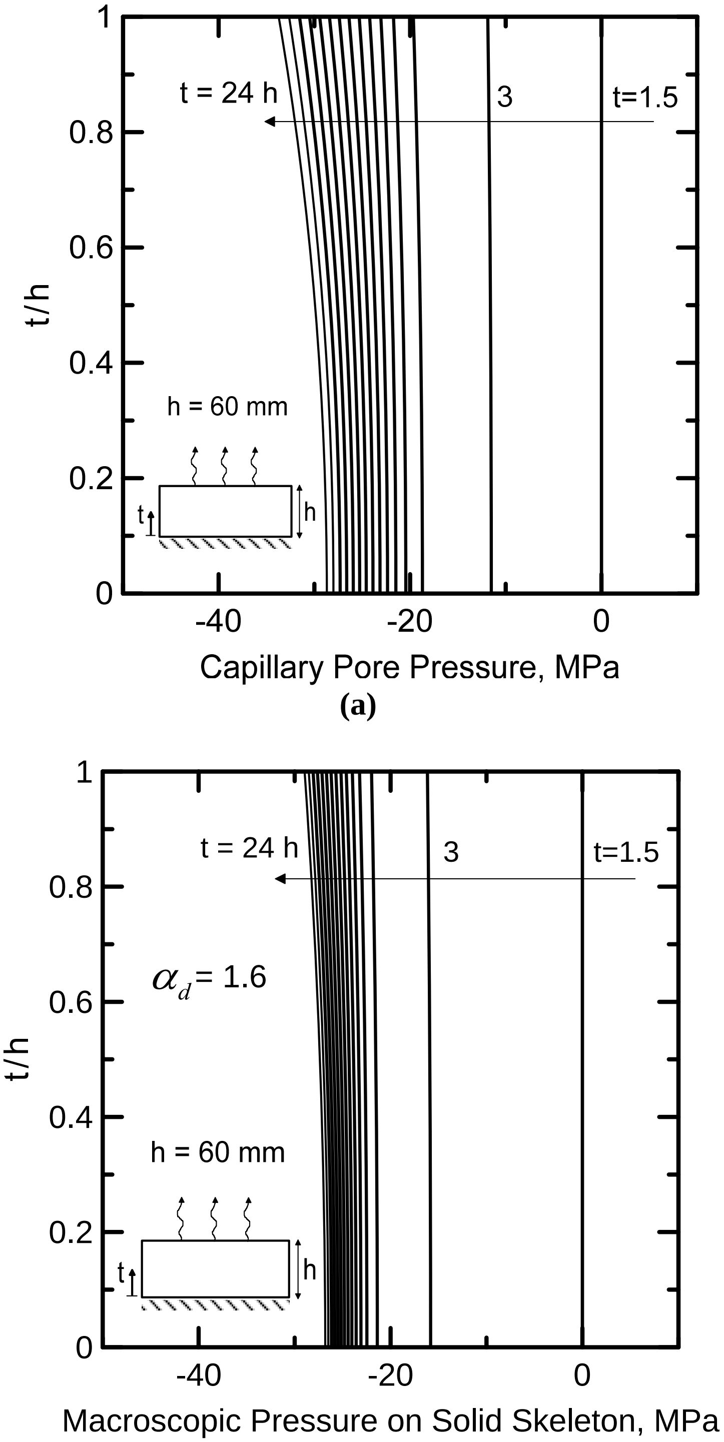

(a)

(b)

Figure F.11. (a) Simulation of capillary pores pressure profiles, (b) simulation of macroscopic pressure on solid skeleton during early-age drying of plain and PVA0.2% concrete

Simulation results for the development of capillary porosity are shown in Figure (F.12). Also elastic modulus development curves introduced the model is shown in Figure (F.13). Based on these data, the profile of shrinkage strains during the drying process is simulated as shown in Figure (F.14).

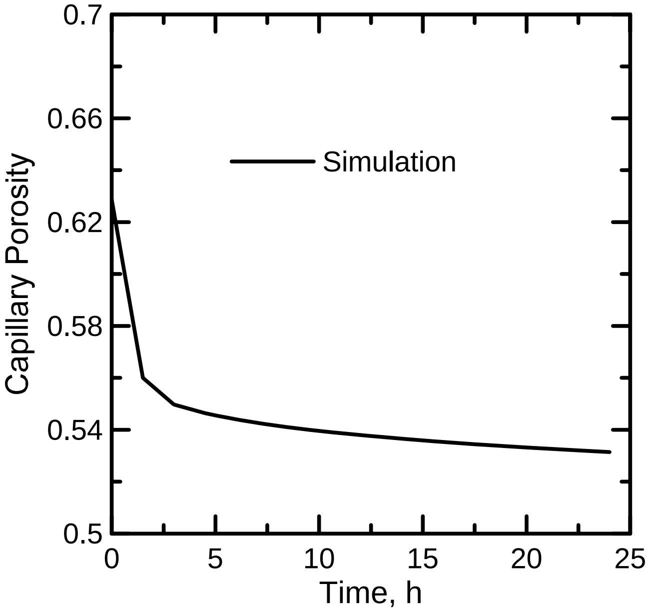

Figure F.12. Change in Capillary porosity according to porosity model by Bentz and Garboczi [226]

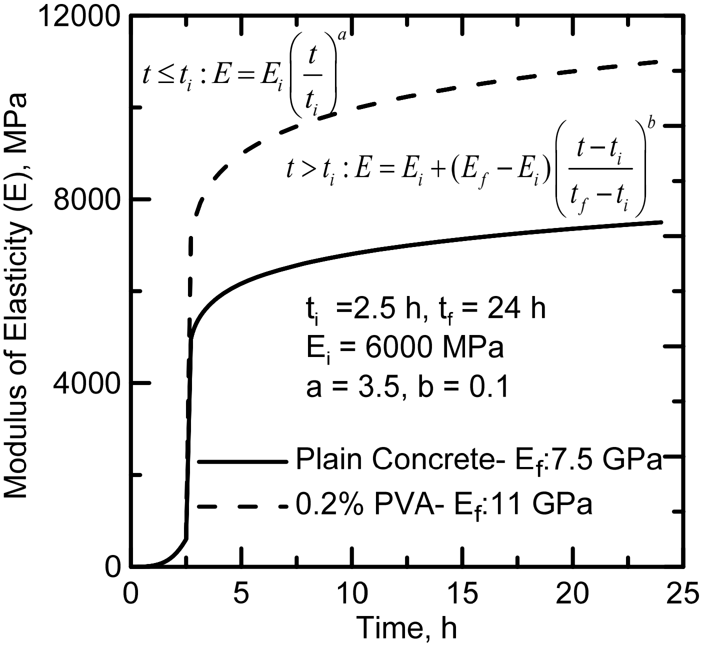

Figure F.13. Introduced elastic modulus for plain and PVA 0.2% concrete

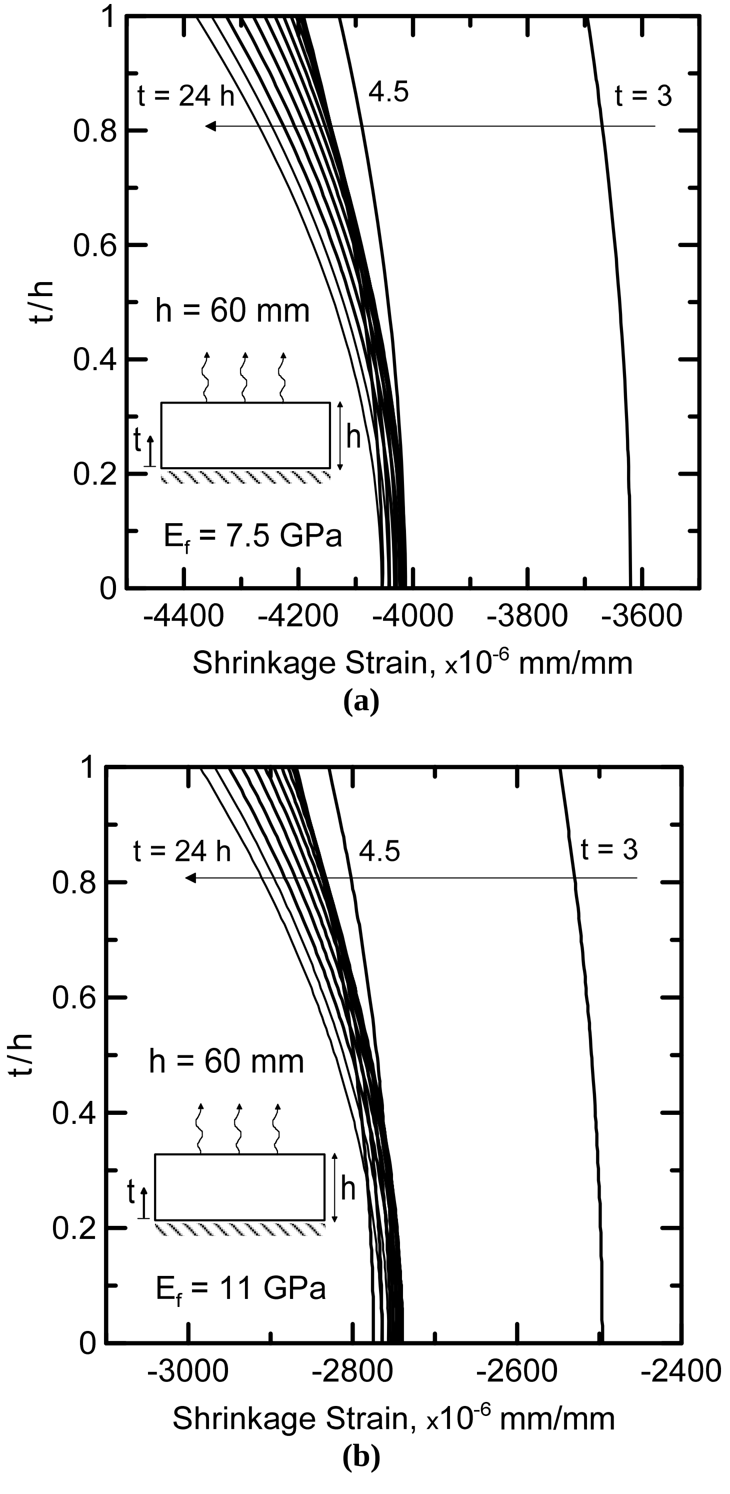

Figure F.14. Simulated early-age shrinkage strain profiles during drying of: a) plain concrete, b) PVA0.2% concrete

Since the reported data by Wongtanakitcharoen and Naaman (2007) are the average shrinkage strains, the simulated shrinkage strains in Figure (F.14) are averaged over the thickness of samples and shown in Figure (F.15). As shown in the figure, simulation results indicate that the proposed method is capable of predicting experimental shrinkage strains during early-age drying process of cement-based materials and presenting the variation of moisture concentration, internal relative humidity, capillary pores pressure and applied macroscopic pressure on the solid skeleton within the time and space domain of the test.

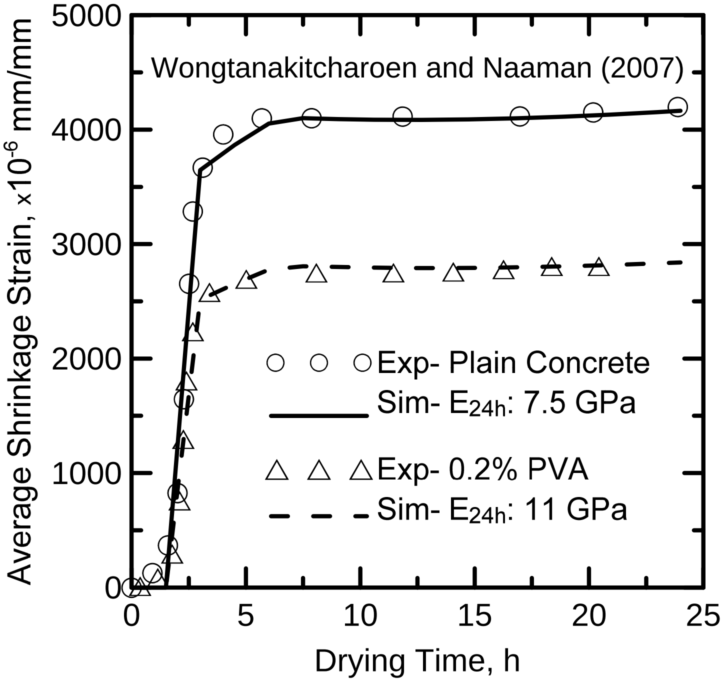

Figure F.15. Simulation of early-age shrinkage strain averaged over the thickness of the sample in comparison with the experimental data reported by Wongtanakitcharoen and Naaman (2007)

References

[1] Horvath A. Construction materials and the environment. Annu Rev Environ Resour 2004; 29: 181-204.

[2] US Central Intelligent Agency. The world factbook. 2003. Washington, DC: CIA.

[3] CEMBUREAU (the European Cement Association), Rue d'Arlon 55, BE-1040 Brussels, Belgium.

[4] Kwon SJ, Na UJ, Park SS, Jung SH. Service life prediction of concrete wharves with early-aged crack: Probabilistic approach for chloride diffusion. Struct Saf 2009;31(1):75-83.

[5] Huang XM, Yang CY. Early-age concrete cover crack and its effects on concrete cover. Key Eng Mater 2006;302-303:630-6.

[6] Tietz, T. The cement industry and climate change challenges. California Nevada Cement Association. 2008. A presentation at American Concrete Institute's Spring Convention, March 30-April 3, Los Angeles, Calif.

[7] Yoon IS, Schlangen E, de Rooij MR, van Breugel K. The effect of cracks on chloride penetration into concrete. Key Eng Mater 2007;348-349:769-72.

[8] Lura P, Pease B, Mazzotta GB, Rajabipour F, Weiss J. Influence of shrinkage-reducing admixtures on development of plastic shrinkage cracks. ACI Mater J 2007;104(2):187-94.

[9] Banthia N, Gupta R. Plastic shrinkage cracking in cementitious repairs and overlays. Mater Struct 2009;42(5):567-79.

[10] Mora-Ruacho J, Gettu R, Aguado A. Influence of shrinkage-reducing admixtures on the reduction of plastic shrinkage cracking in concrete. Cem Concr Res 2009;39(3):141-6.

[11] Cohen MD, Olek J, Dolch WL. Mechanism of plastic cracking in Portland cement and portland cement-silica fume paste and mortar. Cem Concr Res 1990;20(1):103-19.

[12] Slowik V, Schmidt M, Fritzsch R. Capillary pressure in fresh cement-based materials and identification of the air entry value. Cem Concr Compos 2008;30:557–565.

[13] Radocea A. A study on the mechanism of plastic shrinkage of cement-based materials. PhD thesis, Göteborg, Chalmers University of Technology, Göteborg;1992.

[14] Wittmann FH. On the action of capillary pressure in fresh concrete, Cem Concr Res 19766;6(1):49–56.

[15] Esping O. Effect of limestone filler BET(H2O)-area on the fresh and hardened properties of self-compacting concrete, Cem Concr Res 2008;38:938–944.

[16] Morris P, Dux P. Cracking of plastic concrete, Aust J Civ Eng 2003;1(1):17-21.

[17] Aly T, Sanjayan JG. Mechanism of early age shrinkage of concretes, Mater Struct 2009;42:461–468.

[18] Slowik V, Schlattner E, Klink T. Experimental Investigation into early age shrinkage of cement paste by using fiber Bragg gratings. Cem Concr Compos 2004;26(5):473–9.

[19] Hammer TA. Effect of silica fume on the plastic shrinkage and pore water pressure of high-strength concretes, Mater Struct 2001;34:273-278.

[20] Wongtanakitcharoen T, Naaman AE. Unrestrained early age shrinkage of concrete with polypropylene, PVA, and carbon fibers, Mater Struct 2007;40:289-300.

[21] Dao VTN, Dux PF, Morris PH. Tensile properties of early-age concrete. ACI Mater J 2009;106(6): 483-492.

[22] Benboudjema F. Modélisation des déformations différées du béton sous sollicitations biaxiales. Application aux enceintes de confinement de bâtiments réacteurs des centrales nucléaires, PhD dissertation, Université de Marne-la-Vallée, 2002.

[23] ASTM C157-08. Standard test method for length change of hardened hydraulic-cement mortar and concrete, ASTM Book of Standards 2008;04.02.

[24] Grzybowski M, Shah SP. Shrinkage Cracking of Fiber Reinforced Concrete, ACI Mater J 1990; 87(2):138-148.

[25] Paillere AM, Buil M, Serrano JJ. Effect of fiber addition on the autogenous shrinkage of silica fume concrete, ACI Mater J 1989;86(2):139-144.

[26] Kovler, K. Testing system for determining the mechanical behavior of early age concrete under restrained and free uniaxial shrinkage, Mater Struct 1994;27(6):324-330.

[27] Toma G, Pigeon M, Marchand J, Bissonnette B, Bercelo L. Early-age autogenous restrained shrinkage: stress build up and relaxation, Proceedings of the Fourth International Research Seminar on 'Self-Desiccation and its Importance in Concrete Technology', Ed. B. Persson and G. Fagerlund, Lund University. 1999:61–72.

[28] Altoubat AS, Lange DA. Grip-specimen interaction in uniaxial restrained test, ACI SP-206 on Concrete: Material Science to Application, A Tribute to Surendra P. Shah. 2002:189-204.

[29] Aly T, Sanjayan, JG, Collins F. Effect of polypropylene fibers on shrinkage and cracking of concretes, Mater Struct 2008;41(10):1741-1753.

[30] Weiss WJ, Shah SP. Recent trends to reduce shrinkage cracking in concrete pavements, Aircraft/Pavement Technology: In the Midst of Change, Seattle, WA, 1997:217-228.

[31] Kraai PP. A proposed test to determine the cracking potential due to drying shrinkage of concrete. Concr Constr 1985;30(9):775-778.

[32] Shaeles CA, Hover KC. Influence of mix proportions and construction operations on plastic shrinkage cracking in thin slabs. ACI Mater J 1988;85(6):495-504.

[33] Opsahl OA, Kvam SE. Betong med EE-stal-fiber (Concrete with FE-steel fibers), Report No. STF 65 A82036, SINTEF dep, Cement and Concrete Research Institute, Technical University of Norway, Trondheim, June 1982.

[34] Padron I, Zollo RF. Effect of synthetic fibers on volume stability and cracking of Portland cement concrete and mortar. ACI Mater J 1990;87(4):327–332.

[35] Carlson RW, Reading TJ. Model study of shrinkage cracking in concrete building walls. ACI Struct J 1988;85(4):395-404.

[36] Shah SP, Karaguler ME, Sarigaphuti M. Effects of shrinkage reducing admixture on restrained shrinkage cracking of concrete. ACI Mater J 1992;89(3):289-295.

[37] Shah SP, Marikunte S, Yang W, Aldea C. Control of cracking with shrinkage-reducing admixtures. Transp Res Rec 1997;1574:25-36.

[38] Bentur A. Early age cracking in cementitious systems, Chapter 6.5 – RILEM State of the Art Report TC 181-EAS, ed. A. Bentur, RILEM Publications, Bagneux, France. 2003.

[39] Hossain AB, Weiss J. Assessing residual stress development and stress relaxation in restrained concrete ring specimens. Cem Concr Compos 2004;26:531-540.

[40] Turcry P, Loukili A, Haidar K, Pijaudier-Cabot G, Belarbi A. Cracking tendency of self-compacting concrete subjected to restrained shrinkage: experimental study and modeling, J Mater Civ Eng 2006;18(1):46–54.

[41] AASHTO PP 34-99. Standard practice for estimating the crack tendency of concrete. 2004.

[42] ASTM C 1581-04. Standard test method for determining age at cracking and induced tensile stress characteristics of mortar and concrete under restrained shrinkage. 2004.

[43] Turcry P, Loukili A. Evaluation of plastic shrinkage cracking of self-consolidating concrete. ACI Mater J 2006;103(4):272-9.

[44] Sanjuan MA, Moragues A. A testing method for measuring plastic shrinkage in polypropylene fibre reinforced mortars. Mater Lett 1994;21:239-46.

[45] Nanni A, Ludwig DA, Mcgillis MT. Plastic shrinkage cracking of restrained fiber-reinforced concrete. Transp Res Rec 1993;1382:69-72.

[46] Banthia N, Gupta R. Test method for evaluation of plastic shrinkage cracking in fiber-reinforced cementitious materials. Exp Tech 2007;31(6):44-8.

[47] Naaman AE, Wongtanakitcharoen T, Hauser G. Influence of different fibers on plastic shrinkage cracking of concrete. ACI Mater J 2005;102(1):49-58.

---

[48] Ma Y, Zhu B, Tan M, Wu K. Effect of Y-type polypropylene fiber on plastic shrinkage cracking of cement mortar. Mater Struct 2004;37:92-5.

[49] Jacobsen S, Aarseth LI. Effect of wind on drying from wet porous building materials surfaces-A simple model in steady state. Mater Struct 1999;32:38-44.

[50] Shimomura T, Maekawa K. Analysis of the drying shrinkage behaviour of concrete using a micromechanical model based on micropore structure of concrete. Mag Concr Res 1997;49(181):303-322.

[51] Wang K, Shah SP, Phuaksuk P. Plastic shrinkage cracking in concrete materials-Influence of fly ash and fibers", ACI Mater J 2001;98(6):458-64.

[52] Samman TA, Mirza WH, Wafa FF. Plastic shrinkage cracking of normal and high-strength concrete: A comparative study", ACI Mater J 1996;93(1):36-40.

[53] Berhane Z. Evaporation of water from fresh mortar and concrete at different environmental conditions. ACI J Proc 1984;81(6):560-5.

[54] Hall C, Hoff WD. Water transport in brick, stone, and concrete. New York: Taylor & Francis, 2002.

[55] Torrenti JM, Granger L, Diruy M, Genin P. Modeling concrete shrinkage under variable ambient conditions, ACI Mat. J. 1997;96 (1):35-39.

[56] West RP, Holmes N. Predicting moisture movement during the drying of concrete floors using finite elements, Constr Build Mater 2005;19:674-681.

[57] Garbalinska H. Application of √t-type, logarithmic and half-time methods in desorptive measurements of diffusivity in narrow humidity ranges. Cem Concr Res 2006;36 :1294-303.

[58] Huldén M, Hansen CM. Water permeation in coatings. Prog. Org. Coatings. 1985;13(3):171-194.

[59] Kim, JK, Lee CS. Prediction of differential drying shrinkage in concrete. Cem Concr Res 1998;28 (7):985-994.

[60] Bazant ZP, Najjar LJ. Drying of concrete as a nonlinear diffusion problem. Cem Concr Res 1971;1(5):461-73.

---

[61] Bazant ZP, Najjar LJ. Nonlinear water diffusion in non-saturated concrete. Mater Struct 1972;5(1):3-20.

[62] Wilson GW, Fredlund DG, Barbour SL. Coupled soil-atmosphere modelling for soil evaporation. Can Geotech J 1994;31(2):151-161.

[63] Kodikara JK, Chakrabarti S. Modelling of moisture loss in cementitiously stabilised pavement materials. ASCE J Geomech 2005;5 (4):295-303.

[64] Chen D, Mahadevan S. Cracking analysis of plain concrete under coupled heat transfer and moisture transport processes. J Struct Eng 2007;133(3):400-410.

[65] Walton JC, Plansky LE, Smith RW. Models for estimation of service life of concrete barriers in low-level radioactive waste disposal, Rep. Prepared for U.S. Nuclear Regulatory Commission, NUREG/CR-5542 EGG-2597.1990.

[66] Šelih J, Bremner TW. Drying of saturated lightweight concrete: An experimental investigation. Mater Struct 1996;29(7):401-405.

[67] Young JF. Physical mechanisms and their mathematical descriptions. Mathematical modelling of creep and shrinkage of concrete, Ed. ZP Bazant, Wiley, Chichester.1988:63-98.

[68] ACI 305, Hot weather concreting-ACI 305R-99, Farmington Hills, Michigan: American Concrete Institute. 1999.

[69] Uno PJ. Plastic shrinkage cracking and evaporation formulas, ACI Mater J 1998;95(4):365-375.

[70] Dassault Systemes, SIMULIA, Rhode Island, USA, 2010.

[71] Bissonnette B, Therrien Y, Pleau R. Steel fiber reinforced concrete and multiple cracking, Can J Civil Eng 2000;27 (4):774-784.

[72] Swamy RN, Stavarides H. Influence of fiber reinforcement on restrained shrinkage cracking, ACI J 1979;76 (3):443-460.

[73] Hossain AB, Pease B, Weiss WJ. Quantifying restrained shrinkage cracking potential in concrete using the restrained ring test with acoustic emission, Transp Res Rec 2003; Concr Mater Const 1834:24-33.

[74] Mane SA, Desai TK, Kingsbury D, Mobasher B. Modeling of restrained shrinkage cracking in concrete materials, ACI SP206-14 2002:219-242.

[75] Shah HR, Weiss WJ. Quantifying shrinkage cracking in fiber reinforced concrete using the ring test, Mater Struct 2006;39 (9):887-899.

[76] Kim B, Weiss WJ. Using acoustic emission to quantify damage in fiber reinforced cement mortars, Cem Concr Res 2003;33 (2):207-214.

[77] Soranakom C, Bakhshi M, Mobasher B. Role of alkali resistant glass fibers in suppression of restrained shrinkage cracking of concrete materials, Proc 15th International Glass Fibre Reinforced Concrete Association Congress (GRC 2008), Prague, Prague Czech Republic, April 20-23, 2008.

[78] ACI Committee 544.5R-10. Report on physical properties and durability of fiber-reinforced concrete, American Concrete Institute, Farmington Hills, MI, 2010.

[79] Majumdar AJ, Laws V. Glass fibre reinforced cement, Oxford BSP Professional Books, London, UK,1991.

[80] Litherland KL, Oakley DR, Proctor BA. The use of accelerated aging procedures to predict the long term strength of GRC composites, Cem Concr Res 1981;11:455-466.

[81] Bentur A, Diamond S. Fracture of glass fiber reinforced cement, Cem Concr Res 1984;14:31-34.

[82] Bentur A. Mechanisms of potential embrittlement and strength loss of glass fiber reinforced cement composites, Proc Durability of glass fiber reinforced concrete symposium organized by PCI, November 12-15, 1985, Chicago , ed. S. Diamond, 1986, pp. 109-123.

[83] Grzybowski M, Shah SP. A model to predict cracking in fiber reinforced concrete due to restrained shrinkage, Mag Concr Research 1989), Vol. 41, No. 148, pp. 125-135.

[84] Shah SP, Ouyang C, Marikunte S, Yang W, Becq-Giraudon E. A method to predict shrinkage cracking of concrete, ACI Mater J 1998;95 (4): 339-346.3

[85] Tuma JJ. Engineering mathematics handbook, McGraw-Hill, New York, 1970.

[86] Bazant ZP, Panula L. Practical prediction of time-dependent deformation of concrete, part 1: shrinkage, part2: creep, Mater Struct 1978;11 (5): 307-328.

[87] ACI Committee 209. Guide for modeling and calculating shrinkage and creep in hardened concrete (ACI 209.2R-08), American Concrete Institute, Michigan, USA. 2008.

[88] Sultan E, Boudaoud AI, Amar MB. Evaporation of a thin film: diffusion of the vapour and Marangoni instabilities. J Fluid Mech 2005;543:183-202.

[89] Arya SP. Introduction to micrometeorology. San Diego: Academic Press, 2001.

[90] Huang CH. Pasquill's influence: On the evaporation from various liquids into the atmosphere, J Appl Meteorol 1997;36 (8):1021-6.

[91] Brighton PWM. Evaporation from a plane liquid surface into a turbulent boundary layer. J Fluid Mech 1985;159:323-45.

[92] Prata AT, Sparrow EM. Diffusion-driven nonisothermal evaporation. J Heat Transfer 1985;107(1):239-42.

[93] Brutsaert W. A model for evaporation as a molecular diffusion process into a turbulent atmosphere", J Geophys Res 1965;70:5017-24.

[94] Carmeliet J, Hens H, Roels S, Adan O, Brocken H, Cerny R, Pavlik Z, Hall C, Kumaran K, Pel L. Determination of the Liquid Water Diffusivity from Transient Moisture Transfer Experiments. J Therm Envelope Build Sci. 2004;27:277-305.

[95] Janz M. Methods of measuring the moisture diffusivity at high moisture levels. Report TVBM-3076, University of Lund, Lund Institute of Technology, Division of Building Materials, 1997.

[96] Mehta PK, Monteiro PJM. Concrete: Microstructure, Properties and Materials. Boston: McGraw-Hill, 2006.

[97] Soroushian P, Ravanbakhsh S. Control of plastic shrinkage cracking with specialty cellulose fibers, ACI Mater J 1998;95(4):429-35.

[98] Copeland LE, Hayes JC. Determination of non-evaporable water in hardened portland-cement paste. ASTM Bull 1953;194:70-4.

[99] Hall C, Hoff WD, Nixon MR. Water movement in porous building materials-VI. Evaporation and drying in brick and block materials. Build Environ 1984;19(1):13-20.

[100] Cooling LF. Contribution to the study of florescence. II. The evaporation of water from bricks. Trans Br Ceram Soc 1930;29:39-54.

[101] Kowalski SJ. Thermomechanics of drying processes. New York: Springer, 2003.

[102] Scherer GW. Theory of drying. J Am Ceram Soc 1990;73(1):3-14.

[103] Plumb OA, Gu L, Webb SW. Drying of porous materials at low moisture content. Drying Technol 1999;17(10):1999-2011.

[104] Kowalski SJ. Thermomechanical approach to shrinkage and cracking phenomena in drying. Drying Technol 2001;19(5):731-65.

[105] Garrabrants AC, Kosson DS. Modeling moisture transport from a portland cement-based material during storage in reactive and inert atmospheres. Drying Technol 2003;21(5):775-805.

[106] Vu TH. Influence of pore size distribution on drying behaviour of porous media by a continuous model. MS Thesis, Otto-von-Guericke-Universität Magdeburg, Germany, 2006.

[107] Simunek J, Van Genuchten M, and Sejna M. The Hydrus-1d Software Package for Simulating the One-Dimensional Movement of Water, Heat, and Multiple Solutes in Variably-Saturated Media. Version 3.0, Agriculture Research Service, US Department of Agrriculture, Riverside, CA, 2005.

[108] Blandin HP, David JC, Vergnaud JM, Illien JP, Malizewicz M. Modelling of drying of coatings: effect of the thickness, temperature and concentration of solvent. Prog Org Coat 1987;15:163-72.

[109] Crank J. The mathematics of diffusion. New York: Oxford Science Publications, 1989.

[110] Xi Y, Bažant Z, Molina L, and Jennings HM. Moisture diffusion in cementitious materials- Moisture capacity and diffusivity. Adv Cem Bas Mater 1994;1:258-266.

[111] Cussler EL. Diffusion: mass transfer in fluid systems. 3rd edition, New York: Cambridge University Press, 2009.

[112] American Society for Testing Materials. Standard Specification for Fiber-Reinforced Concrete, ASTM C1116/C1116M-10. Annual Book of ASTM Standards 2010. Section 4. Constrcution. 04.02.

[113] Tsotsas E, Mujumdar AS. Modern drying technology: Computational tools at different scales. Darmstadt, Germany: Wiley-VCH, 2007.

[114] Sebastian P, Turner IW. An investigation of the boundary conditions for a vacuum drying problem-Introducing the transition layer concept. Drying Technol 1994;12(4):717-60.

[115] Ramon G, Agnon Y, Dosoretz G. Heat transfer in vacuum membrane distillation: Effect of velocity slip. J Membr Sci 2009;331:117-25.

[116] Bažant ZP, Raftshol WJ. Effect of cracking in drying and shrinkage specimens. Cem Concr Res 1982;12:209-226.

[117] Aldea C-M, Shah SP, Karr A. Effect of cracking on water and chloride permeability of concrete. J. Mat. in Civ. Engrg 1999; 11(3):181-187.

[118] Bažant ZP, Sener S, Kim JK. Effect of cracking on drying permeability and diffusivity of concrete, ACI Mater J 1987;84(5):351–358.

[119] Vejmelková E, Padevet P, Cerny. Effect of cracks on hygric and thermal characteristics of concrete. Bauphysik 2008;30(6):438–44.

[120] Torrijos MC, Giaccio G, Zerbino, R. Internal cracking and transport properties in damaged concretes. Mater Struct 2010;43:109–21.

[121] Brutsaert W. Evaporation into the atmosphere: theory, history, and applications, D. Reidel Publishing Co., Boston, 1982.

[122] Hisatake K, Tanaka S, Aizawaa Y. Evaporation rate of water in a vessel, J Appl Phys 1993;73 (11):7395-401.

[123] Kimpton DD, Wall FT. Determination of diffusion coefficients from rates of evaporation, J Phys Chem 1952;56 (6):715-717.

[124] Lugg GA. Diffusion coefficients of some organic and other vapors in air, Anal Chem 1968;40 (7):1072-1077.

[125] Kwon KC, Ibrahim TH, Park Y, Simmons CM, Pseudo-binary molecular diffusion of vapors into air, Adv Environ Res 2004; 8:667-678.

[126] Kwon KC, Park Y, Simmons CM, Tibere GL, Ibrahim TH, Molecular diffusion of volatile-liquid vapors into air, Chem Eng Commun 2003;190:1449-67.

[127] Prandtl L. On fluid motions with very small friction (in German), Third International Mathematical Congress, Heidelberg, Germany, (1904) 484-491.

[128] Hisatake K, Fukuda M, Kimura J, Maeda M, Fukuda Y. Experimental and theoretical study of evaporation of water in a vessel, J Appl Phys 1995;77 (12): 6664-74.

[129] Davies JT, Rideal EK. Interfacial phenomena, Academic Press, New York, 1961.

[130] Wiederhold PR. Water vapor measurement: Methods and instrumentation, Marcel Dekker Inc, New York, 1997.

[131] Tuve GL, Bolz RE. Handbook of tables for applied engineering science, 2nd edition, CRC Press, Cleveland, 1976.

[132] Nellis G, Klein S, Heat Transfer, Cambridge University Press, New York, 2008.

[133] Buckingham E. Studies on the movement of soil moisture, Bulletin No. 38, US Department of Agriculture, Washington, 1907.

[134] Philip JR. Flow in porous media, Annu Rev Fluid Mech 1970; 2:177-204.

[135] Sposito G. The ‘Physics’ of Soil Water Physics, Water Resour Res 1986; 22 (9S):83S-88S.

[136] Bear J, Bachmat Y. Introduction to modeling of transport phenomena in porous media. Kluwer, Dordrecht, 1991.

[137] Lewis RW, Schrefler BA. The finite element method in the static and dynamic deformation and consolidation of porous media. Wiley, New York, 1998.

[138] Coussy O. Poromechanics. Wiley, New York, 2004.

[139] Mainguy M, Coussy O, Baroghel-Bouny V. Role of air pressure in drying of weakly permeable materials. ASCE J Eng Mech 2001;127:582–592.

[140] Idiart AE, Lopez CM, Carol I. Modeling of drying shrinkage of concrete specimens at the meso-level, Mater. Struct. 2011; 44:415–435.

[141] Pel L. Moisture transport in porous building materials, PhD thesis, Technische Universiteit Eindhoven, Eindhoven, Netherlands, 1995.

[142] Samson E, Marchand J, Snyder K, Beaudoin J. Modeling ion and fluid transport in unsaturated cement systems in isothermal conditions, Cem Concr Res 2005;35:141–153.

[143] Richards LA. Capillary conduction of liquids through porous mediums, Physics 1931;1:318-333.

[144] Sposito G. Lie group invariance of the Richard equation, in J.H. Cushman (ed.), Dynamics of Fluids in Hierarchical Porous Media, Academic Press, London, 1990: 93-98.

[145] Coussot P. Scaling approach of the convective drying of a porous medium. Eur. Phys. J. B 2000;15:557-566.

[146] Platten AK. A study of evaporation and drying in porous building materials, PhD thesis, University of Manchester Institute of Science and Technology (UMIST), Manchester, UK, 1985.

[147] Kowalski SJ. Thermomechanics of drying processes, Springer, New York, 2003.

[148] Bakhshi M, Mobasher B. Experimental observations of early-age drying of Portland cement paste under low-pressure conditions, Cem Concr Compos 2011;33 (4): 474-484.

[149] Azenha M, Maekawa K, Ishida T, Faria R. Drying induced moisture losses from mortar to the environment- Part I -experimental research, Mat. Struct. 2007;40 (8) :801-811.

[150] Rogers JA, Kaviany M. Funicular and evaporative-front regimes in convective drying of granular beds, Int. J. Heat Mass Transfer 1992;35 (2): 469-480.

[151] Rahman MK, Baluch MH, Al-Gadhib AH, Modeling of shrinkage and creep stress in concrete repair, ACI Mater J 1999;96 (5):542-550.

[152] Akita H, Fujiwara T, Ozaka Y, A practical procedure for the analysis of moisture transfer within concrete due to drying, Mag Concr Res 1997;49 (179): 129-137.

[153] Demirkol E, Erdoğdu F, Palazoğlu TK, Analysis of mass transfer parameters (changes in mass flux, diffusion coefficient and mass transfer coefficient) during baking of cookies, J Food Eng 2006;72:364-371.

[154] Comite Euro-International du Beton, CEB-FIP model code 1990, EPF Lausanne, Switzerland, 1998.

[155] Kim JK, Lee CS. Moisture diffusion of concrete considering self-desiccation at early ages, Cem Concr Res 1999;29 (12):1921–1927.

[156] Baluch MH, Rahman MK, Al-Gadhib AH, Raza A, Zafar S. Crack minimization model for Hot Weather Concreting, Arabian J Sci Eng 2006;31 (1C):77-91.

[157] Sakata K. A study on moisture diffusion in drying and drying shrinkage of concrete, Cem Concr Res 1983;13:216-224.

[158] Šelih J, Sousa ACM, Bremner TW. Moisture transport in initially fully saturated concrete during drying, Transp Porous Media 1996;24 (1):81-106.

[159] Šelih J. Movement of water during drying of fully saturated concrete, PhD Dissertation, The University of New Brunswick, Canada, 1995.

[160] Bakhshi M, Mobasher B, Soranakom C. Early-age drying of cementitious materials: theory and modeling, Construct Build Mater, under Review, 2011.

[161] Azenha M, Maekawa K, Ishida T, Faria R. Drying induced moisture losses from mortar to the environment. Part II: numerical implementation, Mater Struct 2007;40:813–825.

[162] TM 5-822-7, Standard Practice for Concrete Pavements, U.S. Army Corps of Engineers, USACE, 1987, http://www.usace.army.mil/inet/usace-docs/.

---

[163] CSA Standard A23.1. Design and control of mixes, 5th Canadian Metric ed., Canadian Portland Cement Association, 1991.

[164] Australian Technical Bulletin, Cracks in concrete due to plastic shrinkage and plastic settlement, Technical Bulletin 95/1, Australian Pre-Mixed Concrete Association, Oct. 1995.

[165] Hover KC. Evaporation of water from concrete surfaces, ACI Mater J 2006;103 (5):384-389.

[166] Menzel CA. Causes and prevention of crack development in plastic concrete, Proc Portland Cement Association Annual Meeting, 1954:130-136.

[167] Dalton J. Experimental essays on evaporation, Proc Manchester Literary and Philosophical Society, 1802;5:536-602.

[168] ACI Committee 308, Guide to curing concrete, Committee Report ACI 308R-01, ACI Manual of Concrete Practice, American Concrete Institute, Farmington Hills, MI, 2001.

[169] Al-Fadhala M, Hover KC. Rapid evaporation from freshly cast concrete and the Gulf environment, Const Build Mate 2001;15:1-7.

[170] Kohler, MA. Lake and pan evaporation, Water Loss Investigations: Lake Hefner Studies, Technical Report, Geological Survey Professional Paper 269, U.S. Government Printing Office, Washington, D.C., 1954:127-148.

[171] Kohler, MA, Nordenson, TJ, Fox WE. Evaporation from pans and lakes, Research Paper No. 38, U.S. Department of Commerce, Washington, D.C., May 1955.

[172] Shuttleworth WJ. Evaporation, Handbook of Hydrology, DR Maidment, ed, McGraw-Hill, 1993:4.1-4.53.

[173] Veihmeyer FJ. Evapotranspiration, Handbook of Appl Hydrol, VT Chow, ed, McGraw Hill, 1964:11-1 to 11-38.

[174] Churchill SW, Ozoe H, A correlation for laminar free convection from a vertical plate, J Heat Transfer 1973;95C:540–541.

[175] Incropera FP, DeWitt DP. Introduction to heat transfer, 5th Ed, Wiley, John Wiley & Sons, New York, USA, 2007.

[176] Thibodeaux LJ. Chemodynamics: environmental movement of chemical in air, water, and soil; John Wiley and Sons: New York, 1979:160-163.

[177] Crawford M. Air pollution control theory; McGraw Hill: New York, 1976.

[178] Friedlander SK. Smoke, dust, and haze: Fundamentals of aerosol behavior; John Wiley and Sons: New York, 1977.

[179] Reist PC. Aerosol science and technology, 2nd ed; John Wiley and Sons, Inc: New York, 1993.

[180] Yi SM, Holsen T, Noll K. Comparison of dry deposition predicted from models and measured with a water surface sampler. Environ Sci Technol 1997; 31:272-278.

[181] Lienhard IV JH, Lienhard V JH. A heat transfer textbook, 3rd Edition, Phlogiston Press, Cambridge, MA, 2008.

[182] Touloukian YS, Saxena SC, Hestermans P. Thermophysical properties of matter;11: Viscosity, IFI/Plenun, NY, 1970.

[183] Poling BE, Prausnitz JM, O'Connell J.P. The properties of gases and liquids, 5th ed, McGraw-Hill, New York, 2000.

[184] Poole TS. Guide for curing Portland cement concrete pavements;II: FHWA-HRT-05-038. Federal Highway Administration, McLean, VA, 2006.

[185] Nonhebel G, Moss AAH. Drying of solids in the chemical industry, Butterworth & Co Ltd, London, England, 1971.

[186] Green D, Perry R. Psychrometry, evaporative cooling, and solids drying, Perry's Chemical Engineers' Handbook, 8th Ed, McGraw-Hill, New York, US, 2007.

[187] Branson DE, Christiason ML. Time dependent concrete properties related to design-strength and elastic properties, creep and shrinkage, SP-27: Creep, Shrinkage and Temperature Effects, American Concrete Institute, Farmington Hills, MI, 1971: 257-277.

[188] ACI Committee 209. Prediction of creep, shrinkage and temperature effects in concrete structures, ACI SP-76: Designing for Creep and Shrinkage in Concrete Structures - A Tribute to Adrian Pauw, American Concrete Institute, Farmington Hills, MI, 1982:193-300.

[189] Perre P. Drying with internal vaporisation: Introducing the concept of identity drying card (IDC), Drying Technol 1995;13 (5-7):1077-1097.

[190] Ketelaars AAJ. Drying deformable media: kinetics, shrinkage and stresses. PhD dissertation, Eindhoven University of Technology, Netherland, 1992.

[191] Salytkov SA. Stereometrische metallographie, VEB Deutscher Verlag für Grundstoffindustrie, Leipzig, 1974.

[192] Stroeven P. Some aspects of micromechanics of concrete, PhD Dissertation, Stevin Laboratory, Technological University of Delft, Netherland, 1973.

[193] Stroeven P. Geometric probability approach to the examination of microcracking in plain concrete, J Mater Sci 1979;14 (5):1141-1151.

[194] Litorowicz A. Identification and quantification of cracks in concrete by optical fluorescent microscopy, Cem Concr Res 2006;36:1508-1515.

[195] Darcy HPG. Les fontaines publiques de la ville de Dijon. Exposition et application á suivre et des formules á employer dans les questions de duistribution d'eau. Victor Dalamont, Paris, France, 1856.

[196] Wittmann FH, Roelfstra PE. Total deformation of loaded drying concrete, Cem Concr Res 1980;10: 601-610.

[197] Alvaredo AM, Wittmann FH. Shrinkage as influenced by strain softening and crack formation, RILEM Proc 5th Int Symp Creep and Shrinkage of Concrete-Mathematical Modeling, 1993:103-113, Barcelona, Spain.

[198] Bazant ZP, Xi Y. Drying creep of concrete: Constitutive model and new experiments separating its mechanisms, Mater Struct 1997;27: 3–14.

[199] Bazant ZP, Hauggaard AB, Baweja S, Ulm FJ. Microprestress-solidification theory for concrete creep. I: aging and drying effects, J Engrg Mech 1997;123(11):1188-1194 .

[200] van Zijl GPAG. Computational modelling of masonry creep and shrinkage, PhD dissertation, Delft University, 1999.

[201] Pihlajavaara SE. A review of some of the main results of a research on the aging phenomena of concrete: Effect of moisture conditions on strength, shrinkage and creep of mature concrete, Cem Concr Res 1974;4:761-771.

[202] Baroghel-Bouny V, Mainguya M, Lassabatereb T, Coussy O. Characterization and identification of equilibrium and transfer moisture properties for ordinary and high-performance cementitious materials, Cem Concr Res 1999;29(8):1225-1238.

[203] Thelandersson S, Matensson A, Dahlblom O. Tension softening and cracking in drying concrete, Mater Struct 1988;21:416-24.

[204] Granger L. Comportement différé du béton dans les enceintes de centrales nucléaires: analyse et modélisation. Ph.D. thesis, 1996. Ecole Nationale des Ponts et Chaussées, Marne-La-Vallée, France [in French].

[205] Granger L, Torrenti JM, Acker P. Thoughts about drying shrinkage: Experimental results and quantification of structural drying creep, Mater Struct 1997;30:588-598.

[206] Verbeck GJ, Hehnuth RH. Structures and physical properties of cement paste, Proc. 5th Int. Symp. on Chemistry of Cement, Tokyo, Japan, 1968, 1-32.

[207] Benboudjema F, Meftah F, Torrenti JM. Interaction between drying, shrinkage, creep and cracking phenomena in concrete, Eng Struct 2005;27: 239–250.

[208] Benboudjema F, Heinfling G, Meftah F, Sellier A, Torrenti JM. On the prediction of delayed strains for concrete subjected to drying and loading simultaneously, Proc. of CONCREEP 6: Creep, shrinkage and durability mechanics of concrete and other quasi-brittle materials 2001:245–250.

[209] Benboudjema, F, Meftah F, Torrenti, JM. Drying creep: An elastoplastic damage approach of the structural effect, Fracture Mechanics of Concrete Structures, R. de Borst, J. Mazars, G. Pijaudier-Cabot, and J. G. M. van Mier, eds. Lisse, The Netherlands, 2001;1:169–176.

[210] Benboudjema F, Meftah F, Torrenti JM. Structural effects of drying shrinkage, J Eng Mech 2005;131 (11):1195-1199.

[211] Day RL, Cuffaro P, Illston JM. The effect of drying on the drying creep of hardened cement paste. Cem Concr Res 1984;14(3):329–338.

---

[212] Bourgeois F, Burlion N, Shao JF. Modelling of elastoplastic damage in concrete due to desiccation shrinkage. Int J Numer Anal Methods Geomech 2002; 26:759–774.

[213] Gawin D, Pesavento F, Schrefler BA. Modelling of deformations of high strength concrete at elevated temperature. Mater Struct 2004;37:218–236.

[214] Grasberger S, Meschke G. Thermo-hygro-mechanical degradation of concrete: From coupled 3D material modeling to durability oriented multifield structural analyses. Mater Struct 2004;37:244–256.

[215] Benboudjema F, Meftah F, Torrenti JM. A viscoelastic approach for the assessment of the drying shrinkage behaviour of cementitious materials, Mater Struct 2007;40:163–174.

[216] Obeid W, Mounajed G, Alliche A. Experimental identification of Biot's hydro-mechanical coupling coefficient for cement mortar. Mater Struct 2002;35:229–236.

[217] Grasley ZC, Lange DA. Thermal dilation and internal relative humidity of hardened cement paste, Mater Struct 2007;40:311–317.

[218] Mindess S, Young JF. Concrete, Prentice-Hall, New Jersey, 1981.

[219] Baron J. le béton hydraulique, ENPC Press, Paris, France, 1982.

[220] Grasley ZC, Lange DA. Modeling drying Shrinkage stress gradients in concrete, ASTM J Test Eval 2003;26(2): 115-122.

[221] Benboudjema F. Modélisation des déformations différées du béton sous sollicitations biaxiales. Application aux enceintes de confinement de bâtiments réacteurs des centrales nucléaires, PhD dissertation, Université de Marne-la-Vallée, 2002 [in French].

[222] Bissonnette B, Marchand J, Charron JP, Delagrave A, Barcelo L. Early age behavior of cement-based materials, Mater Sci Concr VI, J. Skalny, S. Mindess, Ed, American Ceramic Society, 2001:243-326.

[223] Gray WG, Schrefler B.A. Thermodynamic approach to effective stress in partially saturated porous media, Eur J Mech A/Solids 2001; 20:521–538.

[224] Bažant ZP. Thermodynamics of hindered adsorption and its implications for hardened cement paste and concrete, Cement and Concrete Research, 2(1), 1972:1-16.

[225] Gallé C. Effect of drying on cement-based materials pore structure as identified by mercury intrusion porosimetry: A comparative study between oven-, vacuum-, and freeze-drying, Cem Concr Res 2001;31 (10):1467-1477.

[226] Bentz DP, Garboczi EJ. Percolation of phases in a three-dimensional cement paste microstructural model, Cem Concr Res 1991;21(2-3):325-344.

[227] Powers TC, Brownyard TL. Studies of the physical properties of hardened Portland cement paste, J Am Concr Inst 1947; 22(9):971-992.

[228] Hansen TC. Physical structure of hardened cement paste. A classical approach, Mater Struct 1986;19 (6):423-436.

[229] Lamond J, Peilert J. Significance of tests and properties of concrete and concrete-making materials- STP169D, ASTM International, Philadelphia, PA, 2006.

[230] Xi Y, Bažant ZP, Molina L, Jennings HM. Moisture diffusion in cementitous materials-Adsorption isotherms, Adv Cem Based Mater 1994;1:248-257.